

DYNAMICS MODELING OF AGILE FIXED-WING UNMANNED AERIAL VEHICLES

Waqas Khan

Department of Mechanical Engineering

McGill University

Montreal, Quebec, Canada

April 2016

A thesis submitted to McGill University
in partial fulfillment of the requirements of the degree of

Doctor of Philosophy

© Waqas Khan, 2016

Acknowledgements

First and foremost, I would like to thank my supervisor Prof. Meyer Nahon for his sincere guidance, constructive criticism and unwavering support over the course of my research. I have always found him to be a motivating mentor and a patient person.

I would also like to acknowledge my parents and my family for their love, support, prayers, patience, as well as for their encouragement that helped me to complete this research.

Additionally, I am thankful to all my friends and colleagues working at the Aerospace Mechatronics Lab, who have helped me on several occasions. This particularly extends to Patrick Abouzakhm, Pierre-Yves Breches, Eitan Bulka, and Mikael Persson. In their presence, the work environment became interesting and fruitful.

Finally, I would like to express my heartfelt gratitude to all the people and institutions without whom this research would not have been possible. I would like to specifically thank Prof. Nahon, the Natural Sciences and Engineering Research Council (NSERC), the Fonds de recherche du Québec – Nature et technologies (FRQNT), and McGill University’s Faculty of Engineering, for their financial support during this work.

Abstract

Recent emergence of a special class of small fixed-wing UAVs called agile UAVs or highly maneuverable UAVs, has led to a renewed interest in modeling and understanding full-envelope fixed-wing aircraft dynamics. Agile UAVs are characterized by low weight and inertia, low aspect ratio surfaces with big control surfaces and large deflections, and a powerful thruster producing high thrust-to-weight ratio and a strong slipstream. Owing to this unique configuration, agile UAVs attain maneuverability that parallels that of rotary-wing and flapping-wing UAVs, therefore making them suitable for a wide range of tasks involving both conventional and extreme aerobatic flight.

While RC pilots have long demonstrated the potential of agile UAVs, mimicking these capabilities autonomously remains at large a challenge, mainly because the behavior of these UAVs is not well understood. This work takes a first step towards understanding and simulating the behavior of agile UAVs for their full flight envelope. To this end, a six degree-of-freedom nonlinear dynamics model is presented. The model is validated for a *YAK54 ARF Electric 3D Aerobat* test platform having a wing span of 0.82 m. The inertial and geometric parameters are determined from measurements and a detailed CAD model.

The agile UAV model incorporates aerodynamics based on a component breakdown approach. The full ± 180 deg. angle of attack and sideslip range is captured while also taking into account low aspect ratio as well as large control surface deflection effects both pre-stall and post-stall. The effect of quasi-steady and unsteady aerodynamics is also investigated. Aerodynamic interference between different components such as the wing, tail etc. is introduced in a simple fashion.

Most of the aerobatic maneuvers of agile UAVs are possible due to its powerful thruster because it supports the aircraft weight, while its slipstream provides air over the aerodynamic and control surfaces to help maintain lift and control. In lieu of this, a detailed

mathematical treatment for the thruster dynamics and the propeller slipstream effects have also been undertaken in the current work. A thruster dynamics model is developed by considering its components namely the battery, ESC, brushless DC motor, and propeller. Gyroscopic effects arising from large pitching and yawing of the thruster are also taken into account. For the slipstream, the effects of both axial and swirl components are considered. A novel model is presented to predict the axial velocity up to far downstream of the propeller.

The last aspect of this work is the validation of the agile UAV model (implemented in Simulink). A multitude of experiments comprising of static bench tests and wind-tunnel tests are performed. A thorough validation is carried out against experimental data for the individual components as well as the overall agile UAV model. In general, the simulated results are in good agreement with experimental data. A final qualitative validation is also done by configuring the model to run in real-time with the pilot-in-loop and visual feedback provided through X-Plane. A professional RC pilot who has experience flying the real aircraft, tested the simulation by flying various RC maneuvers. His overall comments were that the simulation behaves much like the real aircraft.

Abrégé

L'émergence récente d'une classe spéciale de petits véhicules aériens sans pilote (UAV) à voilure fixe appelés drones agiles ou drones très maniables a conduit à un regain d'intérêt pour la modélisation et la compréhension des dynamiques de ces véhicules. Les drones agiles sont caractérisés par leur faible poids et leurs faibles moments d'inertie, leurs surfaces à faible rapport hauteur/largeur, une grande déviation des surfaces de contrôle, un propulseur puissant produisant un rapport élevé force/poids et un sillage aérodynamique puissant. Grâce à cette configuration unique, les drones agiles atteignent une maniabilité comparable à celles de voilures tournantes et de voilures de battement, ce qui les rend adaptés pour un large éventail de tâches impliquant une voltige à la fois classique et extrême.

Alors que les pilotes de RC ont longtemps démontré le potentiel des drones agiles, imiter ses capacités avec l'autonomie reste encore un grand défi, surtout dû au fait que le comportement de ces drones n'est pas bien compris. Ce travail fait un premier pas vers la compréhension et la simulation du comportement des drones agiles pour leur enveloppe de vol complet. Un modèle dynamique non linéaire à six degrés de liberté est ici présenté. Le modèle est validé pour une plateforme de test YAK54 ARF 3D électrique Aerobat avec une envergure de 0.82 m. Les paramètres inertiels et géométriques sont déterminés en utilisant les mesures du véhicule et un modèle CAO détaillé.

Le modèle de drone agile utilise une approche de répartition des composantes intégrant l'aérodynamique. Les ± 180 degrés de l'angle d'attaque complet et la gamme de glissade sur l'aile sont capturés tout en prenant compte d'un faible rapport hauteur/largeur, ainsi que des grands effets de déviations des surfaces de contrôle à la fois pré-arrêt et post-arrêt. L'effet de l'aérodynamique quasi soutenu et non-soutenu est également étudié. L'interférence aérodynamique entre différentes composantes telles que l'aile, la queue, etc. est aussi simplement introduite.

La plupart des manœuvres de voltige des drones agiles sont possibles grâce à leurs puissants propulseurs, puisqu'il supporte le poids de l'avion, tandis que son sillage aérodynamique fournit de l'air aux surfaces aérodynamiques et de contrôle pour aider à maintenir une capacité de s'élever et la capacité de contrôle. Ainsi, un traitement mathématique détaillé de la dynamique des propulseurs et les effets de l'hélice de sillage aérodynamique ont également exploré dans les travaux présentés. Un modèle de dynamique de propulseur est développé en tenant compte de ses composantes, spécifiquement la batterie, ESC, moteur DC sans balais et l'hélice. Les effets gyroscopiques résultant de grands tangages et lacet du propulseur sont également pris en compte. Pour le sillage aérodynamique, les effets des axiaux et les tourbillonnements sont considérés. Un nouveau modèle est présenté pour prédire la vitesse axiale présente en aval de l'hélice.

Le dernier aspect de ce travail est la validation du modèle de drone agile (mis en œuvre dans Simulink). Une multitude d'expériences comprenant des bancs d'essai statiques et des tunnels aérodynamiques sont effectuées. Une validation approfondie est accomplie en rapport aux données expérimentales pour les composantes individuelles ainsi que le modèle global de drone agile. En général, les résultats simulés sont en accord avec les données expérimentales. Une validation qualitative finale se fait aussi par la configuration du modèle afin de fonctionner en temps réel avec le pilote en boucle et une rétroaction visuelle fournie par X-Plane. Un pilote professionnel de RC qui a de l'expérience de vol avec la plateforme réelle a testé la simulation en effectuant diverses manœuvres de RC. Ses commentaires généraux étaient que la simulation agit comme l'avion réel.

Table of Contents

ACKNOWLEDGMENTS	ii
ABSTRACT	iii
ABRÉGÉ	v
LIST OF TABLES	x
LIST OF FIGURES	xi
NOMENCLATURE	xv
1 Introduction	1
1.1 Literature review	3
1.1.1 Modeling techniques for maneuvering flight	3
1.1.2 Kinematics	7
1.1.3 Aerodynamics	7
1.1.4 Thruster dynamics	13
1.1.5 Propeller slipstream effect	15
1.2 Dissertation contribution	17
1.3 Thesis organization	18
2 Dynamics and Kinematics	19
2.1 Reference frames	19
2.1.1 Attitude representation	20
2.1.2 Transformation between inertial and body frames	21
2.2 State variables	22
2.3 Rigid body dynamics	22
2.4 Kinematics	24
2.5 Test platform	25
2.5.1 Description of the test platform	25
2.5.2 Mass and inertial parameters	26
2.5.3 Input-to-deflection relationships	27
3 Aerodynamics	29
3.1 Component breakdown approach	30
3.1.1 Segment velocity and angle of attack	32
3.1.2 Segment forces and moments	33
3.1.3 Total aerodynamic force and moment	34
3.2 Low-alpha aerodynamics	34
3.2.1 Effect of low aspect ratio	35

3.2.2	Effect of stall	38
3.2.3	Effect of control surface deflection	40
3.3	High-alpha aerodynamics	42
3.3.1	Effect of low aspect ratio	43
3.3.2	Effect of control surface deflection	43
3.4	Aerodynamic interaction	45
3.4.1	Effect of bound vortex	46
3.4.2	Effect of trailing vortices	47
3.5	Unsteady aerodynamics	48
3.5.1	Reduced frequency	49
3.5.2	Time-dependant unsteady effects	50
3.6	Experiments and validation	52
3.6.1	Validation of the low aspect ratio effect	52
3.6.2	Validation of the control surface deflection effect	54
3.6.3	Full range aerodynamic curves	55
3.6.4	Validation for the test platform	56
4	Thruster dynamics	62
4.1	Thruster model	63
4.1.1	Operation	63
4.1.2	Thruster force and moment	64
4.2	Battery dynamics	64
4.2.1	Operation	65
4.2.2	Mathematical model	65
4.3	Brushless DC motor dynamics	66
4.3.1	Operation	66
4.3.2	Mathematical model	66
4.4	ESC model	68
4.5	Propeller aerodynamics	69
4.5.1	Propeller frame	70
4.5.2	In-plane velocity components	71
4.5.3	Blade element theory	71
4.5.4	2D aerodynamic coefficients	74
4.5.5	Momentum theory	75
4.5.6	Inflow model	76
4.5.7	Induced velocity distribution	77
4.5.8	Propeller forces and moments	77
4.5.9	Propeller forces and moments in the body frame	79
4.5.10	Working states of the propeller	79
4.6	Gyroscopic moments	82
4.7	Experiments and validation	82
4.7.1	Determination of system parameters	82
4.7.2	Experimental setup and procedure	87
4.7.3	Steady-state validation	88
4.7.4	Comparison with existing models	94

4.7.5	Analysis and discussion	95
4.7.6	Dynamic validation	98
5	Propeller slipstream effect	102
5.1	Propeller slipstream model	104
5.1.1	Swirl velocity effect	104
5.1.2	Time-dependent slipstream	105
5.2	Slipstream in various operating states	105
5.3	Propeller slipstream mechanism	106
5.3.1	Acceleration and diffusion in the slipstream	106
5.3.2	Propeller jets from marine propellers	107
5.4	Axial slipstream velocity	108
5.4.1	Slipstream velocity in the near-field region	110
5.4.2	Transition from near-field to far-field region	110
5.4.3	Slipstream velocity in the far-field region	112
5.5	Axial slipstream velocity coefficients	114
5.5.1	Experimental setup and procedure	114
5.5.2	Determination of the coefficients	115
5.6	Validation	119
5.6.1	Validation at different rotational speeds	119
5.6.2	Validation with different geometry	121
5.6.3	Validation with different configuration	122
5.6.4	Analysis and discussion	125
6	Validation	129
6.1	Agile UAV dynamics model	130
6.2	Static bench tests	131
6.2.1	Experimental setup	131
6.2.2	Results and discussion	132
6.3	Real-time pilot-in-loop simulations	138
6.3.1	Simulation environment	138
6.3.2	Simulated maneuver results	139
6.4	Unsteady aerodynamics during maneuvers	151
7	Conclusions	153
7.1	Aerodynamics	155
7.2	Thruster dynamics	156
7.3	Propeller slipstream effect	156
7.4	Future works and recommendations	157
References	160

List of Tables

<u>Table</u>	<u>Page</u>
2.1 YAK54 Test Platform Mass and Inertial Parameters	27
3.1 Semi-empirical Coefficients for Rectangular Flat Plates	40
3.2 YAK54 Starboard Wing Segments	58
4.1 Electrify 10x4.5 Propeller Parameters	87
6.1 YAK54 Segments	131

List of Figures

<u>Figure</u>	<u>Page</u>
1.1 Examples of fixed-wing, rotary-wing, and flapping-wing UAVs	1
1.2 Agile UAV performing aerobatics	2
2.1 Body and inertial frames	19
2.2 YAK54 electric 3D aerobat RC plane [101]	25
2.3 Fully assembled YAK54 plane and its CAD model	26
2.4 Input-deflection relationships	28
3.1 An agile UAV performing aerobatics, and perch maneuver [102]	29
3.2 Decomposition of the YAK54 platform, and segment velocity and angle of attack	31
3.3 (a) Leading and side-edge vortices [29], (b) leading-edge vortex at $\alpha = 10$ deg. [38], and (c) lift coefficient for a LAR wing of $AR = 2$	36
3.4 (a) Leading-edge vortex breakdown and trailing-edge separation, and (b) effect of $\dot{\alpha}$ on f_{TE} and C_L	38
3.5 Flap deflection in low-alpha regime	41
3.6 Comparison of high-alpha expressions	42
3.7 Flap deflection in high-alpha regime	44
3.8 (a) Vortex system of the wing, and (b) effect of bound vortex filament ..	46
3.9 Effect of trailing vortex filament on (a) horizontal tail, and (b) vertical tail	48
3.10 Simulated vs experimental aerodynamic coefficients for various AR	53
3.11 Simulated vs experimental lift coefficient for various flap deflections	54
3.12 Full range aerodynamic curves for a rectangular flat plate	55
3.13 Simulated aerodynamic coefficients under quasi-steady conditions	56

3.14	Experimental setup	57
3.15	Simulated vs experimental aerodynamic forces/moments for $\alpha = 0$ deg. ..	59
3.16	Simulated vs experimental aerodynamic forces and moments for various angles of attack	60
4.1	Schematic of the thruster model	64
4.2	Electrical and mechanical system of a BLDC motor	67
4.3	(a) A propeller in general forward flight, and (b) propeller frame	70
4.4	Resultant flow to a propeller blade section	72
4.5	Instantaneous thrust of propeller blades	73
4.6	(a) Propeller slipstream, (b) differential segment, and (c) mass flow rate.	75
4.7	Propeller forces and moments	78
4.8	(a) Vortex-ring, (b) turbulent-wake, and (c) windmill-brake states	80
4.9	Armature voltage drop for moderate discharge rate	83
4.10	Back EMF vs rotational speed	84
4.11	CAD model of the thruster	85
4.12	Segmented Electrify 10x4.5 propeller	86
4.13	Schematic of the experimental setup	88
4.14	Steady-state thrust and torque for Electrify 10x4.5 under static condition	89
4.15	Steady-state thrust and torque for APC 10x4.7 under axial flow condition	90
4.16	Steady-state aerodynamic forces and moments for oblique flow condition.	92
4.17	Comparison with existing models	94
4.18	Induced velocity and thrust distribution on the propeller disc	96
4.19	Effective angle of attack on the propeller disc	97
4.20	Step input response for PW: (a) 1100 μ s, (b) 1500 μ s, and (c) 2000 μ s ...	98
4.21	Step input response for PW train	100

4.22	Random input response	101
5.1	Propeller slipstream on a small fixed-wing UAV	102
5.2	Marine propeller jet	107
5.3	Axial slipstream velocity	109
5.4	Momentum-averaged slipstream velocity and radius	111
5.5	Experimental setup	114
5.6	(a) Maximum slipstream velocity, (b) its radial location, and (c) velocity at the slipstream core	116
5.7	Gaussian curve fits to experimentally measured velocity profiles	117
5.8	Simulation vs experiments at (a) 1750 RPM, and (b) 6425 RPM. Detailed comparison is shown in (c) for $d_s/D_p = 1.58$ and 4.33	120
5.9	Slipstream velocity comparison for APC 11x5.5 and APC 14x4.7	122
5.10	Slipstream velocity comparison for GWS 9x5 at $d_s/D_p = 1$ and 1.5	123
5.11	Slipstream velocity comparison for GWS 5x4.3	123
5.12	Slipstream velocity comparison for coaxial contra-rotating APC propellers	124
5.13	Variation of slipstream velocity with aircraft forward speed	125
5.14	Mass flow rate and entrainment rate vs axial distance	127
6.1	Schematic of the agile UAV model	130
6.2	Experimental setup	132
6.3	Simulated vs experimental slipstream velocity	133
6.4	Simulated vs experimental force and moment for elevator tests	134
6.5	Simulated vs experimental force and moment for rudder tests	135
6.6	(a) Experimental setup, and (b) simulated vs experimental force and moment for aileron tests	136
6.7	Simulated vs experimental force and moment for aileron-elevator tests ...	137

6.8	Tailslide maneuver (aircraft scale = $3.3 \times$ actual size; time step = 0.7 s)...	140
6.9	Aircraft states for the tailslide maneuver	141
6.10	Harrier maneuver (aircraft scale = $2.5 \times$ actual size; time step = 1.5 s) ...	142
6.11	Aircraft states for the harrier maneuver	143
6.12	Hover maneuver (aircraft scale = $2.5 \times$ actual size; time step = 0.9 s	144
6.13	Aircraft states for the harrier maneuver	144
6.14	Knife-edge maneuver (aircraft scale = $2.5 \times$ actual size; time step = 1 s) .	145
6.15	Aircraft states for the knife-edge maneuver	146
6.16	Rolling harrier maneuver (scale = $1.43 \times$ actual size; time step = 0.8 s) ...	148
6.17	Aircraft states for the rolling harrier maneuver	148
6.18	Blender/inverted spin maneuver (scale = 1.67; time step = 0.8 s)	149
6.19	Aircraft states for the blender/inverted spin maneuver	150
6.20	Reduced frequencies during various maneuvers	152

Nomenclature

SYMBOLS

α	Angle of attack from zero-lift line
α'	Effective angle of attack
α_0	Zero-lift angle of attack due to geometric camber
α'_0	Effective zero-lift angle of attack due to flap deflection
α_f	Angle induced due to flap deflection
$\alpha_{high,S}$	Start angle of high-alpha regime
$\alpha_{stall,P}$ and $\alpha_{stall,N}$	Positive and negative stall angles for propeller airfoils
β	Sideslip angle of the aircraft
χ	Wake skew angle of the slipstream
$\delta_f, \delta_a, \delta_e,$ and δ_r	Deflection (flap, aileron, elevator and rudder)
δ_t	Thruster input (in RPM)
η_f	Flap efficiency
Γ_{BV} and Γ_{TV}	Strength of bound and trailing vortices
λ	Gain for cost minimizing function
$\boldsymbol{\Omega}^B \in \mathbb{R}^3$	Aircraft angular velocity in body frame; components $[p, q, r]^T$
$\boldsymbol{\Omega}_{thr} \in \mathbb{R}^3$	Rate of change of orientation of the spinning thruster
$\boldsymbol{\omega}_{thr} \in \mathbb{R}^3$	Spin velocity of the thruster; components $[\omega, 0, 0]^T$
ω and n	Propeller rotational speed in rad/s and rev/s
ϕ_{inflow}	Inflow angle to blade section
ϕ, θ, ψ	Roll, pitch and yaw of aircraft
φ_p	Propeller tilt angle
ψ_p	Propeller blade azimuth angle
Ψ	Entrainment in the slipstream

τ_{arm}	BLDC motor armature torque
τ_{damp}	Magnetic damping torque
τ_e	Electrical time constant of the motor
τ_f	Flap effectiveness factor
τ_{LE} and τ_{TE}	Quasi-steady time constants for LEV breakdown and TE separation
$\tau_{LE,1}$, $\tau_{LE,2}$, $\tau_{TE,1}$, and $\tau_{TE,2}$	Unsteady time constants for LEV breakdown and TE separation
θ_p	Geometric pitch angle of blade section
$\theta_{P/B}$	Rotation angle between propeller and body frames
A_{disc}	Propeller disc area
$B(s)$	Transfer function for the battery with zero z_{batt} and pole p_{batt}
b	Segment span
$C(\bar{s})$	Generalized Theodorsen function
$\mathbf{CF}_{seg} \in \mathbb{R}^3$	Segment force coefficient; components $[\mathbf{CF}_{seg,x}, \mathbf{CF}_{seg,y}, \mathbf{CF}_{seg,z}]^T$
$\mathbf{CF}_{thr}, \mathbf{CM}_{thr} \in \mathbb{R}^3$	Thruster force and moment coefficients
$C_{L,p}$ and $C_{L,v}$	Potential (linear) and vortex (nonlinear) lift coefficient
C_T and C_Q	Thrust and torque coefficient
C_a and C_A	2D and 3D axial force coefficient
C_d and C_D	2D and 3D drag coefficient
$C_{d,0}$ and $C_{d,90}$	2D Drag coefficient at 0 and 90 deg. angle of attack
$C'_{d,90}$	Effective 2D drag coefficient at 90 deg. angle of attack
C_l and C_L	2D and 3D lift coefficient
$C_{l\alpha}$ and $C_{L\alpha}$	2D and 3D lift curve slope
$C_{m,ac}$ and $C_{M,ac}$	2D and 3D pitching moment coefficient
C_n and C_N	2D and 3D normal force coefficient

c, c' and c_f	Chord, effective chord, and flap-chord
$c_{0.75}$	Chord at 75% blade location
dA	Differential area
dL, dD and dM	Differential lift, drag and moment
dT'	Differential thrust on a segment of an annulus
d_{ZFE}	Length of zone of flow establishment
$d\dot{m}_a$	Mass flow rate of air through differential segment
d_s and r_s	Axial and radial coordinate of the slipstream
$e \in \mathbb{R}^4$	Attitude quaternion; components $[e_0, e_1, e_2, e_3]^T$
$F, M \in \mathbb{R}^3$	Total force and moment at the aircraft c.g.
$F_{aero}, M_{aero} \in \mathbb{R}^3$	Aerodynamic force and moment at the aircraft c.g.
$F_{grav} \in \mathbb{R}^3$	Gravitational force at the aircraft c.g.
$F_p, M_p \in \mathbb{R}^3$	Propeller aerodynamic force and moment
$F_{seg}, M_{seg} \in \mathbb{R}^3$	Segment aerodynamic force and moment at its a.c.
$F_{thr}, M_{thr} \in \mathbb{R}^3$	Thruster force and moment at the c.g.
f_{LE} and f_{TE}	Normalized chordwise locations of LEV breakdown and TE separation
H and $H_{thr} \in \mathbb{R}^3$	Angular momentum of the aircraft and thruster
\dot{h} and \ddot{h}	Plunge velocity and acceleration
I and $I_{thr} \in \mathbb{R}^{3 \times 3}$	Inertia tensor of the aircraft and thruster
I_{rot}	Rotational inertia of the thruster
J	Propeller advance ratio based on total velocity ($= V/nD_p$)
K_T and K_Q	Thrust and torque constants
K_{ind}	Longitudinal slope of the induced velocity
K_p and K_v	Potential and vortex lift parameters
K_{vel}, K_{tor} and K_{damp}	Velocity, torque and damping constants of the motor

$k_{\dot{\alpha}}$ and $k_{\dot{\beta}}$	Reduced frequencies based on $\dot{\alpha}$ and $\dot{\beta}$
k_O	Oswald efficiency factor
k_r	Reduced frequency
$\mathbf{M}_{gyro} \in \mathbb{R}^3$	Gyroscopic moment of the thruster
$\mathbf{M}_{mot} \in \mathbb{R}^3$	Reaction moment of BLDC motor
M_P and N_P	Pitching moment and yaw moment (or P-factor)
m	Aircraft mass
\dot{m}_s and \dot{m}_{s0}	Mass flow rate across the slipstream, and at the propeller plane
N	Number of propeller blades
P_N and S_F	Normal force and Side force
$\mathbf{p}^I \in \mathbb{R}^3$	Position of aircraft c.g. in inertial frame; components $[p_N, p_E, p_D]^T$
\mathfrak{R}_B^I , \mathfrak{R}_I^B and $\mathfrak{R}_P^B \in \mathbb{R}^{3 \times 3}$	Transformation matrices (body to inertial, inertial to body, and propeller to body frames)
R_0 and D_0	Contracted radius and diameter
R_h	Propeller hub radius
R_{l-l} and \mathbb{V}_{l-l}	Line-to-line resistance and voltage
R_p and D_p	Propeller radius and diameter
R_{phase} and \mathbb{V}_{phase}	Phase resistance and voltage
$\mathbf{r} \in \mathbb{R}^3$	Position of segment a.c. from c.g.; components $[r_x, r_y, r_z]^T$
$\mathbf{r}_p \in \mathbb{R}^3$	Position of propeller center from c.g.; components $[r_{p,x}, r_{p,y}, r_{p,z}]^T$
r	Radial location of the propeller blade segment
T and Q	Aerodynamic thrust and torque
T_{avg}	Average thrust of blade for one revolution
T_{inst} and HB_{inst}	Instantaneous thrust and hub force
t_{max} and $x_{t,max}$	Airfoil maximum thickness ratio and its location
$\mathbb{V}_{R,arm}$ and $\mathbb{V}_{L,arm}$	Voltage drop across armature resistance and inductance

$\mathbb{V}_{arm}, i_{arm}, R_{arm},$ and	Armature voltage, current, resistance and inductance
L_{arm}	
\mathbb{V}_{back}	Back EMF
\mathbb{V}_{des}	Desired voltage
$\mathbf{V} \in \mathbb{R}^3$	External velocity at the segment a.c.; components $[V_x, V_y, V_z]^T$
V_0 and d_0	Efflux velocity and its axial location
$\mathbf{V}_{cg} \in \mathbb{R}^3$	Translational velocity of aircraft c.g.; components $[u, v, w]^T$ in the body frame and $[\dot{p}_N, \dot{p}_E, \dot{p}_D]^T$ in the inertial frame
V_{disc}	Axial velocity at the propeller disc
V_{ia}	Axial induced velocity at the propeller disc
$V_{ia,0}$	Axial induced velocity at the propeller disc center
$V_{ia,avg}$	Momentum-averaged axial induced velocity at the propeller disc
$\mathbf{V}_{ind} \in \mathbb{R}^3$	Velocity induced due to aerodynamic interference
$\mathbf{V}_{ind,BV}$ and $\mathbf{V}_{ind,TV} \in \mathbb{R}^3$	Induced velocity due to bound and trailing vortices
V_{out}	Axial velocity far downstream of the propeller
$\mathbf{V}_p \in \mathbb{R}^3$	Propeller velocity at its center; components $[V_{p,x}, V_{p,y}, V_{p,z}]^T$
$V_{p,\parallel}$ and $V_{p,\perp}$	Parallel and perpendicular components of $V_{p,IP}$
$V_{p,A}$ and $V_{p,IP}$	Axial and in-plane components of \mathbf{V}_p
$\mathbf{V}_{QS} \in \mathbb{R}^3$	Velocity perturbation due to quasi-steady effects
V_R	Resultant velocity to a propeller blade section
$\mathbf{V}_s \in \mathbb{R}^3$	Slipstream velocity at the segment a.c.
V_s and R_s	Axial slipstream velocity and slipstream radius
$V_{s,avg}$	Momentum-averaged axial slipstream velocity
$V_{s,max}$ and R_{max}	Maximum slipstream velocity and its radial location
V_{tot}	Total flow velocity through a differential segment
$\mathbf{V}_{wind} \in \mathbb{R}^3$	Wind velocity in body frame

$[x_{cg}, y_{cg}, z_{cg}]^T$	Location of c.g. from propeller plane measured in body frame
x_p and x_e	Normalized chordwise locations of potential and vortex lift
z_{\max} and $x_{z,\max}$	Airfoil maximum camber ratio and its location

SUPERSCRIPTS

<i>B</i>	Body frame
<i>I</i>	Inertial frame
<i>P</i>	Propeller frame
<i>S</i>	Sensor frame
<i>QS</i>	Quasi-steady
<i>AM</i>	Added mass
<i>dyn</i>	Dynamic
<i>circ</i>	Circulatory

ABBREVIATIONS

<i>AR</i>	Aspect ratio
a.c.	Aerodynamic center
BV and TV	Bound Vortex and Trailing Vortices
c.g.	Center of gravity
LAR	Low aspect ratio
LE, SE, and TE	Leading-Edge, Side-Edge and Trailing-Edge
LEV	Leading-Edge Vortices
LP and TP	Leading-Point and Trailing-Point
PW	Pulse Width
ZFE and ZEF	Zone-of-Flow-Establishment and Zone-of-Established-Flow

Chapter 1

Introduction

The past few decades have seen tremendous growth in unmanned aerial vehicles (UAVs) that have demonstrated their widespread utility in many roles. While they are now well established in the military sphere, they have also begun penetrating civilian applications including surveillance, search and rescue, patrolling/monitoring operations, etc. Coupled with the technological revolution in hardware equipment and miniature sensors, and the advancements in algorithms and software, a whole new horizon of applications have now become possible with small unmanned aerial vehicles.

Although various types and configurations of UAVs have been deployed over time to suit the needs of specific applications, these can be broadly classified into fixed-wing (conventional), rotorcraft (helicopter, quadcopter etc.), and flapping-wing UAVs. An example of each class is shown in Fig. 1.1. The fixed-wing class has long been associated with conventional cruise flight, and only the latter two classes have been thought to be suited for applications requiring maneuverability. This perception is no longer true with the recent emergence of a special class of small fixed-wing UAVs called agile UAVs or highly maneuverable UAVs. As the name suggests, agile UAVs, owing to their low weight and inertia, control surfaces as big as 50% chord, large deflections up to 50 deg., and powerful



Figure 1.1: Examples of fixed-wing (left), rotary-wing (center), and flapping-wing (right) UAVs.

thrusters producing high thrust-to-weight ratios of around 2, and a strong slipstream, attain maneuverability paralleling that of rotorcraft and flapping-wing UAVs, while retaining their capability of long-distance flight. As such, agile UAVs are able to exploit both the efficient cruise flight of fixed-wing UAVs and the maneuvering capabilities of rotorcraft and flapping-wing UAVs.



Figure 1.2: Agile UAV performing aerobatics.

Remote control (RC) pilots routinely perform impressive aerobatic feats with small fixed-wing RC planes that fall in the category of agile UAVs (see Fig. 1.2). The desire to mimic these capabilities autonomously has led to a renewed interest in fixed-wing UAVs with a focus on understanding and modeling their dynamics for the full flight envelope, i.e. complete ± 180 deg. angle of attack and sideslip range. Realization of such autonomous capabilities will make them the ideal aerial platform for a broad spectrum of applications including flight in constrained environments and limited spaces such as indoors, caves etc., flight that require rapid maneuvers like evasion, perching, stop and stare etc., and in general, applications that require a long transit before executing maneuvers at the target destination. Whereas conventional flight of fixed-wing UAVs have been studied for quite long now and have become a standard textbook topic, the behavior of agile fixed-wing UAVs is not well understood and remains largely a challenge till today. The primary objective of this thesis

is to understand and model the flight dynamics of agile UAVs for their entire working envelope covering conventional flight, high angle of attack flight, aerobatics and extreme maneuvers. The work in this thesis is part of the long-term goal of autonomous maneuvering capability for agile UAVs.

1.1 Literature Review

Despite being a relatively new field of interest, a plethora of work has already been undertaken for agile UAVs, their dynamics modeling and control. Efforts in the literature are mostly vested on specific maneuvers; hover (or perching), in particular, seems to be a spotlight maneuver. A brief literature review relevant to this thesis is presented in these major areas: modeling techniques, kinematics, aerodynamics, propulsion, and slipstream.

1.1.1 Modeling Techniques for Maneuvering Flight

The flight dynamics of agile UAVs are quite different from conventional fixed-wing aircraft and are complicated by the nonlinear and unsteady aerodynamics, as well as thruster dynamics and other effects like the propeller slipstream etc., encountered during maneuvering flight. The outcome is a highly nonlinear dynamics model for agile UAVs with strong coupling between its states.

Maneuvering (unconventional) flight may not have been studied much for agile UAVs yet, but it has remained a central topic of research for fixed-wing combat aircraft that need to satisfy stringent maneuverability requirements e.g. that of quick evasion and pursuit. However, dynamic models for these aircraft are developed on a case-by-case basis with extensive wind-tunnel testing, e.g. [1], or computationally expensive CFD methods, e.g. [2]. While these methods may be feasible for military-grade aircraft, they are less practical for small UAVs which may be better addressed via identification techniques or first principles.

System Identification Techniques

System identification techniques have become popular for identifying models of small unmanned vehicles including agile UAVs, especially in maneuvering flight. Such popularity

stems from the fact that flight test data for identification can be gathered relatively easily by flying these small, inexpensive and readily available off-the-shelf UAVs. While Ref. [3, 4] detail the main concepts of system identification for aerial vehicles, its importance is summed up in a brief statement by Ciecinski et al. [4],

“Identification of the model of an aircraft dynamics is the most reliable method to obtain a model of motion. Theoretical analysis and laboratory (wind tunnel) tests are costly and do not include effects of some phenomena occurring in real flight.”

In general, system identification requires actual flight data containing recorded control inputs of the pilot as well as the aircraft behavior (output). Advanced mathematical tools are employed to determine the input-to-output relationship or unknown parameters of arbitrary transfer functions that represent the agile UAV model. Many existing works in the literature are based on this approach as it seems relatively simple and may result in more accurate models. For example, Johnson et al. [5] presents a model for small fixed-wing UAVs at high angles of attack, obtained entirely from extensive flight test data. Least-square regression curve fitting is used to identify transfer functions from aileron, elevator, and rudder commands to roll, pitch and yaw rates respectively. In another similar work [6], the aerodynamic model of a Micro Aerial Vehicle (MAV) is identified from flight test data. Although the system identification approach may result in a more accurate aircraft model, and eliminates the need of evaluating complex aerodynamic forces and other nonlinear effects in maneuvering flight, the downside is that the identified model is based purely on the input-output relationship having no physical basis and is a black box for further development of the model itself and possibly for controllers. A more serious drawback is the lack of generality in the identified model, i.e. the model found is only valid for the particular aircraft tested and cannot be adapted to other aircraft. Moreover, reasonable output is not guaranteed for inputs/conditions other than the test inputs/conditions that were used to identify the model. This implies that exhaustive experimental testing must be carried out

before the model can even come close to being general. Hence system ID techniques may well be used only for specific maneuvers and not to cover the entire flight envelope.

First Principles of Physics

Comprehensive physics-based models that cover the full flight envelope of agile UAVs are scarce in the literature. This is not surprising since most works on autonomous control of agile UAVs are limited to specific maneuvers and as such the flight dynamics are determined either via system ID techniques discussed above, or by first principles that simplify drastically for the specific maneuver. Green et al. [7, 8], for instance, presents a controller for the hover maneuver of a small fixed-wing MAV whose dynamics are modeled using first principles and simplified since nonlinear or unsteady aerodynamics are not involved therein. A more detailed treatment is carried out in [9–11] for the hover and transition (cruise-to-hover or vice versa) of small fixed-wing UAVs. A major advantage of physics-based models is that they are general and the effect of each model parameter on the overall aircraft behavior is well understood.

Agile UAVs in hover/perch or transition maneuvers closely resemble vertical takeoff and landing (VTOL) aircraft, also called tail-sitters, and as such benefit from the standard modeling techniques for VTOLs, see [12], for these particular maneuvers. Stone [13] presents a nonlinear dynamics model for his wing-in-propeller-slipstream tail-sitter UAV. To a large extent, the model is physics-based, i.e. based on 6-dof rigid body equations of motion with aerodynamic and thruster forces/moments, and propeller slipstream effect. Other works for VTOL configuration include those by Kubo [14] and Roy et al. [15].

The most relevant works to this thesis are the works undertaken at the University of Illinois at Urbana-Champaign by Selig [16, 17] that aim to model maneuvering capabilities of small fixed-wing UAVs as realistically as possible through first principles. This comprehensive work models aerodynamics for the full angle of attack and sideslip range, and takes into account various effects present during maneuvering flight such as the flow shadowing effect

(the shielding of one surface by another), flow curvature effect (flow deflection due to induced downwash), slipstream swirl effect, propeller wake lag effect (delay in the propeller wake reaching the aft surfaces like the tail), pitch and yaw damping of the propeller etc. As such the developed UAV model is extremely detailed and is shown to successfully capture well-known RC pilot maneuvers like tail-slide, knife-edge, harrier, hover, and even more involved and sophisticated ones like knife-edge spins, rolling harriers, inverted flat spins etc. The dynamics model is integrated into the framework of a commercial simulator FS One [18], and though Ref. [16, 17] provide some insight to the underlying dynamics and operation, it does not allow further development and use in path/maneuver planning, trajectory generation or controller development. Furthermore, the natural commercial goal of the FS One simulator is to be as realistic as possible and therefore the various effects discussed above, no matter how small, are modeled. This leads to a vast number of parameters, constants, weighing and scaling factors (some semi-empirical in nature) which in turn require tuning/refinement for different aircraft in lieu of their actual flight behavior. Considering the long-term goal of autonomous maneuvering, it is felt necessary to develop a dynamics model for agile UAVs that may not necessarily be as comprehensive as Selig's, but captures reasonably well the maneuvering capabilities of agile UAVs. The works by Selig [16, 17] are key to this thesis and serve as guide on various effects that exist during maneuvering flight.

More often, physics-based modeling is used together with system identification techniques to identify entities that are difficult to evaluate otherwise in the six-dof equations of motion, from simple experiments with the aircraft. Usually, these include the nonlinear post-stall and unsteady aerodynamic coefficients. For example, the dynamics model presented in [19] for an agile fixed-wing UAV is based on the six-dof equations of motion with aerodynamic coefficients identified via simple experiments and wind-tunnel tests. Validity of the model is demonstrated for different inputs and is found to be sufficiently accurate. Motion-tracking

has also been used [20–22] for identification of aerodynamic coefficients, in particular unsteady aerodynamic coefficients for pitch-up maneuvers of lightweight aircraft.

1.1.2 Kinematics

When using first principles, the six-dof rigid body equations must be complemented by kinematic relationships that relate the attitude of the agile UAV to its motion. Depending on the preferred attitude representation, appropriate kinematic relationships can be used.

Euler angle representation (roll ϕ , pitch θ , and yaw ψ) is widely used for conventional fixed-wing aircraft mainly because it is easy to visualize, and intuitive for controller development. It has a deficiency at $\theta = \pm 90$ deg. where it suffers a mathematical singularity (gimbal lock) and fails to distinguish between roll and yaw. Nonetheless it suffices for conventional flight where such large excursions in pitch are never encountered except for unusual upset conditions. For agile UAVs however, Euler angles are clearly unsuitable, and the singularity problem must be addressed before the representation can be used for maneuvering flight. In some works, this is done by bounding the pitch angle ($-90^\circ < \theta < 90^\circ$) e.g. [15], and in others [11, 13] by using a dual-representation: Euler angles at low pitch angles and vertical Euler angles at high pitch angles. The vertical Euler angles are similar to Euler angles, but measured from a reference vertical hover position, see [13].

Quaternion representation is the most popular choice for attitude representation for maneuvering flight [8–10, 16–19]. Even though they are less intuitive for visualization and control than Euler angles, they do not have any mathematical singularity. As well, formulating the dynamics model in terms of quaternions is computationally more efficient since it results in linear and algebraic equations, unlike formulation with Euler angles that involves trigonometric functions.

1.1.3 Aerodynamics

Different approaches are used in the literature to model aerodynamics in maneuvering flight with the simplest one being the stability derivatives approach. In this approach,

aerodynamic terms that indicate the aircraft stability are determined based on geometry, external flow and motion about a particular operating condition of the aircraft. It is used often for conventional fixed-wing aircraft whose flight does not deviate too much from its normal operating condition.

In contrast, agile UAV operation spans over the full ± 180 deg. angle of attack and sideslip range leading to nonlinear dynamics as well as strong coupling between the aircraft states. Stability derivatives approach may therefore not be well-suited for agile UAVs. Exceptionally if the UAV dynamics are linearized about multiple operating conditions, stability derivatives can be used in each of the resulting linear models. The obvious consequence then is having to deal with more than one model and devising an intelligent switching scheme between the models. An example of the stability derivative approach used for agile UAVs is Ref. [11], wherein two linear independent models are presented – one obtained by linearizing about level flight condition and the other about hover condition. Aerodynamic forces are computed using stability derivatives in each model. Based on a pre-set criterion, a control algorithm switches intelligently between the models in real-time.

A more suitable approach for agile UAVs is the component breakdown approach also known as the strip theory approach [15–17]. The various components of the aircraft (wing, tail, fuselage etc.) are divided into segments, each producing lift, drag and moment about the aircraft center of gravity (c.g.). The breakdown approach allows modeling each segment independently with its own aerodynamics as well as the possibility to model almost every geometric detail of the aerodynamic surfaces. More so, this approach results in a single unified model that by design considers realistic phenomena (adverse yaw, induced roll etc.).

Full Angle of Attack Range Aerodynamics

Aerodynamic data covering the full ± 180 deg. angle of attack range is needed for each segment of the aircraft (defined in the component breakdown approach above). Such data is not readily available for all airfoils, and researchers have used various techniques to

generate the full-range data for their airfoils. Kubo [14], for example, generated full angle of attack range aerodynamic curves for NACA4412 airfoil by combining the NACA4412 up-to-stall data with modified ± 180 deg. NACA0012 data. In Ref. [15], aerodynamic curves are modeled in parametric form using nonlinear lifting line theory for the pre-stall angle of attack range. For post-stall aerodynamics, the aircraft is assumed to behave like a flat plate (bluff body) producing only form drag. Smooth transition from streamlined aerodynamics to bluff body aerodynamics is achieved by using a weighting function. Selig [16–17] also uses full range aerodynamic curves developed from available experimental data fused with XFOIL [23] for low angles of attack, and semi-empirical methods for high angles of attack. A low-order panel method is used by Stone [13] to model aerodynamics for his wing-in-propeller-slipstream tail-sitter UAV.

Mathematical treatment of post-stall aerodynamics (also called high angle of attack aerodynamics) is also present in the literature. It is well known that beyond stall, the profile of an airfoil has negligible effect on its aerodynamic performance and thus the airfoil behaves, more or less, like a flat plate. Several expressions for post-stall aerodynamic coefficients of flat plates can be found in the literature [24–28].

Low Aspect Ratio Surfaces at Low Reynolds Number

One of the challenges in modeling aerodynamics of small fixed-wing UAVs is its low aspect ratio (LAR) surfaces operating at low Reynolds number (around 70,000 to 200,000 based on the UAV mean wing chord and cruise speed [29]). For agile UAVs, the low aspect ratio surfaces are a design consequence of keeping the aerodynamic and control surfaces, as much as possible, within the propeller slipstream, see Fig. 1.2. This allows lift and control of the agile UAV at low/zero forward speed flight as well as maneuvering flight wherein the external flow is largely detached from the surfaces.

The issue of LAR surfaces at low Reynolds numbers has been recently addressed for MAVs through experimental studies undertaken at the University of Notre Dame [29–32]. Several

aspect ratios between 0.5 and 2, and Reynolds number ranging from 70,000 to 200,000 were tested for various planforms. The experimental data clearly showed the additional vortex lift associated with low aspect ratio wings [33]. Comparison between experimental results and LAR theory by Polhamus [34–35] for delta wings and its extension by Lamar [36] for non-delta planforms, concluded that even at low Reynolds numbers, these theories reasonably predict the lift, drag and moment for low aspect ratio wings prior to stall. Ref. [37] also compared experimental and CFD results to the LAR theory, and found a reasonable agreement between the two.

Another important work is by Okamoto et al. [38] wherein low aspect ratio wing planforms are tested at a low Reynolds number of 10,000. Surprisingly, the LAR theory by Polhamus and Lamar still agrees quite well with experimental data at such low Reynolds numbers. An interesting observation is that, for the same aspect ratio and planform, the experimental data by Okamoto et al. [38] match closely with the experimental data from the University of Notre Dame [30], even though both were obtained at very different Reynolds numbers (the former at 10,000, and the latter at 100,000). This implies that for low aspect ratio wings, there is little effect of Reynolds number below 100,000, as also noted in [30]. Ref. [38] is quite useful since it provides experimental data up to 90 deg. angle of attack, as opposed to the experimental data of University of Notre Dame [29–32] which is only up to around stall.

Another useful experimental study is done in [39] for slightly higher aspect ratios (2 to 5) at Reynolds numbers 40,000 to 160,000. An even more wider range of aspect ratios (0.4–9) is tested in [40] where the aerodynamic characteristics of LAR surfaces at low Reynolds number is researched to determine wind loads on solar panels and its holding structure. The tests were conducted at Reynolds numbers between 60,000 to 200,000 and since the wind can hit the panels from any direction, the angle of attack was varied up to 90 deg. An in-depth discussion and mathematical treatment of LAR wings is also presented in [25].

Large Control Surfaces and Deflections

As alluded earlier, agile UAVs are characterized by control surfaces as large as 50% chord capable of deflecting as high as 50 deg., see Fig. 1.2. This adds complexity to the aerodynamics modeling since not many works address very large control surfaces and deflections, especially for the complete ± 180 deg. angle of attack range.

It is experimentally established that a flap deflection offsets the C_l versus α curve, and this effect is comparable to changing the camber of the airfoil. In most standard aerodynamic textbooks, e.g. [33], simple mathematical expressions can be found to account for the effect of control surface deflection but only in the linear aerodynamics region, i.e. up to stall. A compilation of experimental results and a basic mathematical treatment up to stall is also presented in [25]. In general, mathematical treatments in the literature deal with small flap-to-chord ratios (around 20%), and small deflections (around 20 to 30 deg.).

To understand the effect of large control surfaces and deflections on aerodynamic performance, an experimental study was recently undertaken [41]. Wings with up to 30% flap-to-chord ratios and deflections as large as 65 deg. were tested. Again, only up-to-stall testing was done. To the best of author's knowledge, there exists no experimental work in the literature that deals with the effect of large control surfaces and deflections in the post-stall region. The only works that semi-empirically model this effect are by Selig [16, 17]. For small control surface deflections at low angles of attack, available experimental data is fused with XFOIL [23], and for large deflections at higher angles of attack, other semi-empirical techniques are employed.

Unsteady Aerodynamics

Looking at the impressive aerobatics feats performed by agile UAVs, it is natural to conclude that unsteady aerodynamics play a part in achieving such maneuvers. It is therefore worthwhile to review works in the literature pertaining to unsteady aerodynamic characteristics of aircraft, and in particular agile UAVs.

Experimental and theoretical studies on unsteady airfoil aerodynamics go a long way back to the classical unsteady model by Theodorsen [42] that forms the basis of analysis for fixed-wing aircraft in the attached flow regime. The model extends the quasi-steady thin airfoil theory, see [28], by incorporating the effects of added mass (reaction forces due to accelerating the surrounding fluid) and wake vorticity (induced circulation due to the vorticity in wake). A more comprehensive subsequent model is by Beddoes and Leishman (B-L) for attached flow conditions [43], and with dynamic stall [44] in state-space representation. In the latter, dynamic stall is modeled using trailing edge separation based on Kirchhoff's theory of separated flows. The B-L model is widely used to predict unsteady lift, drag and moment. Another similar model is presented in [45] that deals with unsteadiness in aircraft dynamics due to high angle of attack maneuvers. In addition to trailing edge separation, leading edge vortex breakdown is also considered in this work.

The models discussed above are quite useful since they are developed in state-space form and can be integrated into any simulation with ease. However, they contain a few parameters that need to be determined experimentally for a given aircraft. System identification has been used to identify these parameters for full-scale aircraft [46, 47] and more recently for conventional fixed-wing UAVs [48]. An effort to make the Theodorsen's lift model useful at lower Reynolds numbers is also undertaken [49]. An empirical version of the model is presented for a flat plate pitching at a Reynolds number of $Re = 100$.

Application of the above unsteady models for agile UAVs are not found in the literature. Instead, unsteady aerodynamic characteristics of maneuvering flight are determined directly via system identification from motion tracking data [20, 21]. It was found in Ref. [20] that significant unsteady aerodynamic effects exist in a pitch-up maneuver of a very lightweight MAV (around 14.5 g). On the other hand, Ref. [21] based on 240 flight tests, found that although individual tests showed time-varying aerodynamic coefficients, their average was in good agreement with those predicted by flat plate theory. Thus the unsteady effects were

deemed not-too-large for the pitch-up maneuver. This is also aligned with the fact that Selig’s model [16, 17] is able to capture extremely dynamic maneuvers like blenders and snap rolls, even though no unsteady aerodynamic effects are modeled.

1.1.4 Thruster Dynamics

As alluded earlier, agile UAVs are strongly thruster-dominated due to their high thrust-to-weight ratios (around 2–3), and therefore the dynamics of an agile UAV thruster must be modeled as accurately as possible, particularly when the thruster experiences different flow conditions throughout the maneuvering flight.

Even though considerable work has been carried out on dynamics modeling of small fixed-wing UAVs [50–53], relatively little attention has been paid specifically to their thruster models. Most of the related literature utilize simple algebraic models like $T = \rho n^2 D_p^4 C_T = K_T n^2$ and $Q = \rho n^2 D_p^5 C_Q = K_Q n^2$ [7, 9, 19, 50–53] for predicting the aerodynamic thrust T and torque Q , with the thrust and torque coefficients, C_T and C_Q , determined from experiments, propeller database [54, 55], or using analytical methods such as the widely used Blade Element Momentum Theory (BEMT) [33]. The aforementioned models are steady-state and as such do not predict the transient behavior of the thruster which may be significant during rapid maneuvering. In contrast, Pounds et al. [56] proposed a dynamics model for his thruster, which lumped battery dynamics, motor dynamics and aerodynamics in a single transfer function. In Ref. [57], a more detailed thruster dynamics model is developed by successively applying first principles to the two main components of the thruster namely the brushless DC (BLDC) motor and the propeller. Another work [58] implements a first order nonlinear transfer function to model the dynamics of the thruster, whose parameters were identified through experimentation.

The thrusters on agile UAVs are highly likely to experience various flow conditions including static (i.e. not moving through air), axial flow (i.e. flow aligned with the thruster rotation axis), oblique flow (i.e. flow at an angle to the thruster rotation axis), and even reverse flow.

In light of this, several works have been undertaken to understand the thruster dynamics in these unusual flow conditions. These include studies on the effects of Reynolds number [59, 60], descent flight [61–63], and oblique flow [64, 65] on thruster performance. An attempt to comprehensively model thruster dynamics for maneuvering flight of small UAVs is undertaken in [66]. The model predicts propeller forces and moments in general forward flight conditions (including oblique flow), propeller pitch and yaw damping, and gyroscopic moments.

As the use of propeller-driven UAVs for unconventional applications has been established recently, not much work has been done pertaining to oblique flow effects (i.e. flow coming at an angle to the thruster rotation axis) on UAV thrusters. However this topic has been studied extensively for turboprop aircraft and helicopters. Early works on turboprop aircraft targeted the influence of the angle of attack (pitch), or sideslip (yaw) on propeller performance both experimentally [67, 68] and theoretically [69–72]. Approximate formulae and graphical charts were presented; but applicable only to small pitch and yaw angles (up to around 15 deg.). Also, in a more recent work [33], expressions can be found for lateral force and yaw moment (called the normal force and P-factor respectively for fixed-wing aircraft), but again these have been derived assuming the flow to be at a small angle to the thruster rotation axis.

Works involving flow at large angles to the thruster rotation axis can be found in the literature pertaining to helicopter rotors in forward flight. The earliest work can be traced back to Glauert [73] who realized that a rotor disc in forward flight behaves as a circular wing and, according to the lifting line theory, should produce an upwash at disc leading edge and a downwash at the disc trailing edge with a varying mean induced velocity. Accordingly, Glauert proposed a simple inflow model to account for this variation. Subsequently, many efforts [74, 75] were made to further Glauert’s model and have resulted in a multitude of inflow models, a review of which is presented in [76]. These have been

used to supplement the blade element momentum theory to predict the performance of helicopter rotors.

Oblique flow is also becoming a topic of interest in the naval hydrodynamics research area as large forces and moments are generated by a ship propulsor particularly during steering. Several experimental works have been undertaken to characterize the static and dynamic effects of the incoming flow angle on the performance of a ship propulsor [77]. Also in [78], experimental measurements have been made for the six axis forces and moments on a ship propulsor under oblique flow condition.

1.1.5 Propeller Slipstream Effect

Being characterized by a powerful thruster that allows maneuvering flight, agile UAVs also benefit from the strong airflow known as propeller slipstream or propwash, produced by the thruster. While the external flow is largely detached from the aerodynamic surfaces during extreme maneuvers, the propeller slipstream keeps the immersed aerodynamic and control surfaces effective, thereby maintaining lift and control of agile UAVs in these maneuvers.

Early works [79–81] on propeller slipstream were more focused on analytical methods to determine the induced velocity within the slipstream and subsequently, the propeller-airframe interaction based on conventional theories such as the momentum theory, lifting-line theory, blade element theory etc. A good correlation between theoretical and experimental results was reported for wings mounted in the vicinity of the propeller. A recent work by Stone [13] includes the propeller-slipstream effect for a tail-sitter UAV. The author used a full azimuthal blade-element solution combined with fixed wake to predict, in real-time, slipstream velocities over the wing located within one propeller diameter downstream. The slipstream velocities are then superimposed on the external flow velocity for more accurate estimates of the aerodynamic and control forces/moments.

Momentum theory is widely used for fixed-wing aircraft to predict slipstream velocity downstream of the propeller [12, 51, 53, 66]. Since the theory does not consider slipstream

diffusion with ambient flow, its applicability is limited to regions near the propeller. In contrast, the diffusion of propeller slipstreams have been researched thoroughly for marine propellers, where the effect of the propeller jets on nearby structures, like seabed scouring etc., is studied [82–84]. Researchers in this area are interested in these propeller jet effects up to large axial distances of several propeller diameters from the propeller plane and as such, take into account the diffusion phenomenon using semi-empirical equations that have been developed for marine propellers from detailed experimental investigations. The efforts in this research area are summarized in a comprehensive review by Lam et al. [85].

The inherently complex flow field of the propeller slipstream and its even-more-complicated aerodynamic interference with the airframe has also led to a large body of experimental work in the literature. Gamble [86], for example, presents detailed experiments to quantify the aerodynamic effect of the propeller slipstream on a MAV wing, particularly with varying wing position, and rigid vs. flexible wing configurations. Another similar work [87] presents experimentally measured velocity profiles within the propeller slipstream and its effect on the lift and drag coefficients of a MAV. A detailed experimental study is undertaken in [88–90] for slipstream characteristics of small UAV propellers. Measurements for slipstream velocity are taken using a 7-hole Pitot tube for several propellers to identify the characteristics and trends in the evolution of the slipstream up to several diameters downstream of the propeller. These works are particularly useful since they address both axial and rotational slipstream velocities, as well as the slipstream effect on wings of different aspect ratios. It is observed in [88] that similar to marine propeller jets, propeller slipstreams start to spread out some distance downstream of the propeller due to diffusion caused by viscous/shear forces and turbulence. Thus the slipstream behaves as a turbulent jet for which entrainment is one of the essential phenomena responsible for increase in mass flow rate and the spread with downstream distance [91–93].

Advanced experimental techniques like Particle Image Velocimetry (PIV), Background Oriented Schlieren (BOS) etc. have also been used to investigate the propeller slipstream velocity distribution [94–96]. Nowadays computational fluid dynamics (CFD) is being employed to predict the complex propeller airframe interaction [97, 98], but it is computationally expensive and applicable only on a case-by-case basis.

1.2 Dissertation Contribution

In the present work, dynamics modeling of an agile UAV for its complete flight envelope is undertaken through first principles. Three major components of the UAV (aerodynamics, thruster dynamics, and propeller slipstream effect) that affect its dynamics are studied individually, and improved modeling techniques are presented and validated. The individual models are embedded into the overall UAV simulation that is configured to run both offline and in real-time with the pilot-in-loop. Quantitative and qualitative validation supports the presented six-dof agile UAV model and the underlying modeling techniques.

The main contribution of this work is a physics-based dynamics model for agile UAVs that covers their full flight envelope and successfully captures their behavior in conventional, unconventional/high-angle-of-attack flight, as well as in extreme maneuvers and aerobatics. The individual achievements of this thesis are:

- An agile UAV simulation platform that is open to further development and allows use for motion planning including maneuver construction and trajectory generation, as well as controller development for path following.
- A validated methodology for modeling dynamics of agile UAVs. The methodology can be easily applied to any agile UAV to predict its behavior for its complete working envelope.
- Simple yet accurate model for nonlinear aerodynamics including both post-stall and unsteady aerodynamics. The unique aerodynamics of the aircraft surfaces like low

aspect ratio, low Reynolds number, and large control surfaces capable of high deflections, are all addressed in the presented aerodynamics model.

- Physics-based thruster model for small UAVs that is able to predict all six-axis aerodynamic forces and moments in general flight conditions including static, axial flow, oblique flow and reverse flow conditions. The model also predicts transient behavior of UAV thrusters due to included battery and motor dynamics.
- A novel propeller slipstream model that accounts for both the acceleration and diffusion of the slipstream, and as such has applicability up to downstream distances as large as 5 propeller diameters.

1.3 Thesis Organization

This thesis is presented as follows. In Chap. 2, the kinematics and rigid body equations of motion are derived for agile UAVs. The test platform – *YAK54 ARF Electric 3D Aerobat* RC plane, is introduced, and parameters in the equations of motion are determined for this platform using both experiments and a CAD model. The overall simulation framework established in MATLAB/Simulink is discussed.

Modeling of the aerodynamics, thruster dynamics and propeller slipstream effect is done in Chaps. 3, 4 and 5 respectively. Each chapter presents an introduction to the problem and the challenges associated with modeling. The chapters conclude with experimental validation of the respective models.

The overall model validation is undertaken in Chap. 6. Details on the experiments performed are given, followed by quantitative validation against results from these experiments. For qualitative validation, the simulation framework is expanded to run in real-time with the pilot-in-loop, and interlinked to X-Plane for visual feedback to the pilot. Simulation results for several well-known RC maneuvers flown by the pilot are presented. Finally, Chap. 7 provides conclusions of the work performed as well as a list of suggested future works related to this topic.

Dynamics and Kinematics

In this chapter, kinematics and rigid-body dynamics equations are presented that form the framework of the high-fidelity simulation of agile UAVs. As a first step, reference frames and state variables used to define the aircraft motion are discussed. The equations of motion for the vehicle dynamics are then assembled, followed by parameter identification for a test platform.

2.1 Reference Frames

Multiple reference frames are usually required to define the motion of an aircraft, with the two most common frames being the body and inertial frames. The need for these two frames arise because: 1) the Newton's equations of motion are derived in the inertial frame while the motion of the aircraft is relatively easily represented in the body frame, and 2) some sensors onboard the aircraft like the GPS, sonar etc., measure the aircraft motion in the inertial frame, while others like the Inertial Measurement Unit (IMU) measure it in the body frame. Shown in Fig. 2.1 are the body frame (superscript B) and inertial frame (superscript I) used in the current work.

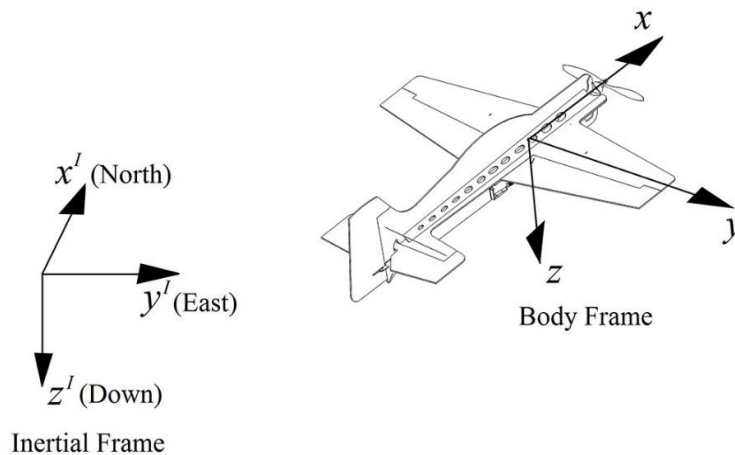


Figure 2.1: Body and inertial frames.

The body frame is defined as per the convention for fixed-wing aircraft: the origin is placed at the aircraft center of gravity (c.g.); the x axis is along the fuselage and points out of the nose; y axis is along the wing and points out of the starboard wing (right side of the airplane when viewed from rear); and z axis points down from the belly of the aircraft. For small aircraft, the earth's gravitational field can be assumed constant over its body and therefore its c.g. is coincident with its center of mass.

Although the inertial frame can be any arbitrary fixed reference frame, it is quite common to choose the earth North-East-Down (NED) frame as the inertial frame. The origin is fixed at any point on the surface of the earth, e.g. starting point of the flight; the x^I axis points in the North direction, y^I points in the East direction, and z^I points vertically downwards towards the earth center. One of the benefits of choosing NED frame as the inertial frame is that GPS sensor measurements (such as ground speed, ground course etc.) are in the NED frame.

At any instant, the body and inertial frames can be related by a translation plus rotation transformation, implying that quantities in one frame can be easily expressed in the other frame. The rotation transformation matrix can be defined depending upon the choice of attitude representation such as Euler angles, quaternion etc.

2.1.1 Attitude Representation

Based on the discussion in the previous chapter (Sec. 1.1.2), the present work will use quaternion representation for the agile UAV attitude, so as to avoid the singularity problem associated with the Euler angles.

A quaternion is a four parameter representation defined as:

$$e = e_0 + e_1 \mathbf{i}^I + e_2 \mathbf{j}^I + e_3 \mathbf{k}^I = \cos(\Theta/2) + \mathbf{e} \sin(\Theta/2) \quad (2.1)$$

and can be interpreted as a single rotation about an axis in space. The first element e_0 is the scalar part defining the angle of rotation Θ , while the other three elements e_1 , e_2 and e_3 , define the unit vector \mathbf{e} of the axis of rotation in the inertial frame. For a proper rotation,

the quaternion must be of unit magnitude, i.e. $\|e\| = (e_0^2 + e_1^2 + e_2^2 + e_3^2)^{0.5} = 1$. Reference [99] is a good reference on quaternion mathematics, while a more application-specific discussion on quaternion is given by Phillips [100].

It is frequently required to transform quaternion to Euler angles and vice versa since quaternion representation is neither intuitive nor immediately evident for compound rotations that involve a combination of Euler angles (roll, pitch and yaw) [50]. Therefore, the following relationships are useful to get Euler angles from quaternion:

$$\begin{aligned}\phi &= \text{atan2}\left[2(e_0e_1 + e_2e_3), (e_0^2 + e_3^2 - e_1^2 - e_2^2)\right] \\ \theta &= \text{asin}\left[2(e_0e_2 - e_1e_3)\right] \\ \psi &= \text{atan2}\left[2(e_0e_3 + e_1e_2), (e_0^2 + e_1^2 - e_2^2 - e_3^2)\right]\end{aligned}\tag{2.2}$$

and the inverse relationships:

$$\begin{aligned}e_0 &= \cos(\phi/2)\cos(\theta/2)\cos(\psi/2) + \sin(\phi/2)\sin(\theta/2)\sin(\psi/2) \\ e_1 &= \sin(\phi/2)\cos(\theta/2)\cos(\psi/2) - \cos(\phi/2)\sin(\theta/2)\sin(\psi/2) \\ e_2 &= \cos(\phi/2)\sin(\theta/2)\cos(\psi/2) + \sin(\phi/2)\cos(\theta/2)\sin(\psi/2) \\ e_3 &= \cos(\phi/2)\cos(\theta/2)\sin(\psi/2) - \sin(\phi/2)\sin(\theta/2)\cos(\psi/2)\end{aligned}\tag{2.3}$$

Transformation between quaternion and other attitude representations such as direction cosine matrix (DCM), vertical Euler angles etc. can be found readily in the literature [11, 19, 99, 100].

2.1.2 Transformation between Inertial and Body Frames

With quaternion attitude representation, the rotation transformation from the body to inertial frame is given as:

$$\mathfrak{R}_B^I = \begin{bmatrix} e_0^2 + e_1^2 - e_2^2 - e_3^2 & 2(e_1e_2 - e_0e_3) & 2(e_1e_3 + e_0e_2) \\ 2(e_1e_2 + e_0e_3) & e_0^2 + e_2^2 - e_1^2 - e_3^2 & 2(e_2e_3 - e_0e_1) \\ 2(e_1e_3 - e_0e_2) & 2(e_2e_3 + e_0e_1) & e_0^2 + e_3^2 - e_1^2 - e_2^2 \end{bmatrix}\tag{2.4}$$

The inverse transformation from the inertial frame to the body frame is simply the transpose of the above rotation matrix, i.e. $\mathfrak{R}_I^B = (\mathfrak{R}_B^I)^T$.

2.2 State Variables

In assembling the equations of motion, 13 state variables will be introduced. These are:

- | | | |
|---|---|--|
| <ul style="list-style-type: none"> • Three position states $\mathbf{p}^I = [p_N, p_E, p_D]^T$: the North-East-Down position of the aircraft c.g. in the inertial frame. • Three velocity states $\mathbf{V}_{cg}^B = [u, v, w]^T$: translation velocity of the aircraft c.g. in the body frame (also called body velocity). | } | <p>Related to translational motion of the aircraft</p> |
| <ul style="list-style-type: none"> • Four angular position states $e = [e_0, e_1, e_2, e_3]^T$: attitude of the aircraft defined in terms of quaternions. • Three angular velocity states $\mathbf{\Omega}^B = [p, q, r]^T$: rotational velocity of the aircraft in the body frame (also called body rates). | } | <p>Related to rotational motion of the aircraft</p> |

Additional states may be introduced in the next chapters. In particular, when modeling unsteady aerodynamics, additional states such as the trailing-edge separation point (refer to [43–48]), will be appended to the above listed states.

2.3 Rigid Body Dynamics

The rigid body equations for the aircraft dynamics can be found in any aircraft textbook [50–53]. Starting with the Newton’s second law for translational motion: $\Sigma \mathbf{F}^I = m d\mathbf{V}_{cg}^I/dt$ in the inertial frame, the equation is expressed in the body frame as:

$$\Sigma \mathbf{F}^B = m \left(d\mathbf{V}_{cg}^B/dt + \mathbf{\Omega}^B \times \mathbf{V}_{cg}^B \right) \quad (2.5)$$

Equation (2.5) is expressed at the c.g. since it is coincident with the center of mass. The transformation to body frame is done since it is easier to analyze the aircraft motion in that frame. The first term on the R.H.S. is the rate of change of velocity’s magnitude observed in the body frame, i.e. $[\dot{u}, \dot{v}, \dot{w}]^T$, while the second term is the rate of change in the velocity direction, and is given by a cross product of the angular velocity $\mathbf{\Omega}^B = [p, q, r]^T$ and linear velocity $\mathbf{V}_{cg}^B = [u, v, w]^T$ both expressed in the body frame.

The L.H.S of Eq. (2.5) is the vector sum of all external forces, namely gravitational, aerodynamic and thruster forces, in the body frame, i.e. $\Sigma \mathbf{F}^B = \mathbf{F}_{grav}^B + \mathbf{F}_{aero}^B + \mathbf{F}_{thr}^B$. Whereas

the aerodynamic and propulsive forces are usually in the body frame, the gravitational force is the inertial frame and must be transformed into the body frame according to:

$$\mathbf{F}_{grav}^B = mg \begin{bmatrix} 2(e_1e_3 - e_0e_2) \\ 2(e_2e_3 + e_0e_1) \\ e_0^2 + e_3^2 - e_1^2 - e_2^2 \end{bmatrix} \quad (2.6)$$

Equation (2.5) is then expanded to give:

$$\begin{bmatrix} \dot{u} \\ \dot{v} \\ \dot{w} \end{bmatrix} = \begin{bmatrix} rv - qw \\ pw - ru \\ qu - pv \end{bmatrix} + g \begin{bmatrix} 2(e_1e_3 - e_0e_2) \\ 2(e_2e_3 + e_0e_1) \\ e_0^2 + e_3^2 - e_1^2 - e_2^2 \end{bmatrix} + \frac{1}{m} (\mathbf{F}_{aero}^B + \mathbf{F}_{thr}^B) \quad (2.7)$$

A detailed treatment of the aerodynamic and thruster forces, \mathbf{F}_{aero}^B and \mathbf{F}_{thr}^B , is carried out in Chaps. 3 and 4 respectively.

Likewise for the rotational motion, starting with $\Sigma \mathbf{M}^I = d\mathbf{H}^I/dt$ in the inertial frame, and expressing it in the body frame to get:

$$\Sigma \mathbf{M}^B = d\mathbf{H}^B/dt + \boldsymbol{\Omega}^B \times \mathbf{H}^B \quad (2.8)$$

The sum of external moments on the L.H.S. includes the aerodynamic and thruster moments (\mathbf{M}_{aero}^B and \mathbf{M}_{thr}^B). The gravitational force acting at the aircraft c.g. does not create any moment. The angular momentum \mathbf{H} of a rigid body is the product of its inertia matrix and angular velocity, where the inertia matrix about the body axes with origin at the c.g. is:

$$\mathbf{I}^B = \begin{bmatrix} I_x & -I_{xy} & -I_{xz} \\ -I_{xy} & I_y & -I_{yz} \\ -I_{xz} & -I_{yz} & I_z \end{bmatrix} \approx \begin{bmatrix} I_x & 0 & -I_{xz} \\ 0 & I_y & 0 \\ -I_{xz} & 0 & I_z \end{bmatrix} \quad (2.9)$$

In the above equation, the inertia matrix is simplified for an aircraft due to symmetric mass distribution and geometry about the xz plane. The angular momentum in the body frame is therefore: $\mathbf{H}^B = \mathbf{I}^B \boldsymbol{\Omega}^B$, and its time derivative becomes: $d\mathbf{H}^B/dt = \mathbf{I}^B \dot{\boldsymbol{\Omega}}^B$ since the inertia matrix remains constant in the body frame.

Expanding Eq. (2.8) results in,

$$\begin{bmatrix} \dot{p} \\ \dot{q} \\ \dot{r} \end{bmatrix} = (\mathbf{I}^B)^{-1} \begin{bmatrix} (I_y - I_z)qr + I_{xz}pq \\ (I_z - I_x)pr + I_{xz}(r^2 - p^2) \\ (I_x - I_y)pq - I_{xz}qr \end{bmatrix} + \mathbf{M}_{aero}^B + \mathbf{M}_{thr}^B \quad (2.10)$$

The aerodynamic and thruster moments are evaluated later in Chaps. 3 and 4 respectively.

2.4 Kinematics

Equations (2.7) and (2.10) are the rigid body equations that define the aircraft dynamics, but are insufficient in themselves for a solution of the motion. Hence, these must be supplemented with a kinematic relationship between the aircraft attitude and its motion.

In quaternion representation,

$$\begin{bmatrix} \dot{e}_0 \\ \dot{e}_1 \\ \dot{e}_2 \\ \dot{e}_3 \end{bmatrix} = \frac{1}{2} \begin{bmatrix} \lambda(1 - \|e\|^2) & -p & -q & -r \\ p & \lambda(1 - \|e\|^2) & r & -q \\ q & -r & \lambda(1 - \|e\|^2) & p \\ r & q & -p & \lambda(1 - \|e\|^2) \end{bmatrix} \begin{bmatrix} e_0 \\ e_1 \\ e_2 \\ e_3 \end{bmatrix} \quad (2.11)$$

where the diagonal term $\lambda(1 - \|e\|^2)$ is a cost minimizing function that tries to maintain $\|e\| = 1$ when propagating Eq. (2.11), so that the resulting quaternion always represents a proper rotation. A value of $\lambda = 1000$ is deemed to work well in Ref. [50], but may be changed depending on the solver used.

To complete the equations of motion for an agile UAV, the position state propagation may be written as,

$$\begin{bmatrix} \dot{P}_N \\ \dot{P}_E \\ \dot{P}_D \end{bmatrix} = \begin{bmatrix} e_0^2 + e_1^2 - e_2^2 - e_3^2 & 2(e_1e_2 - e_0e_3) & 2(e_1e_3 + e_0e_2) \\ 2(e_1e_2 + e_0e_3) & e_0^2 + e_2^2 - e_1^2 - e_3^2 & 2(e_2e_3 - e_0e_1) \\ 2(e_1e_3 - e_0e_2) & 2(e_2e_3 + e_0e_1) & e_0^2 + e_3^2 - e_1^2 - e_2^2 \end{bmatrix} \begin{bmatrix} u \\ v \\ w \end{bmatrix} = \mathfrak{R}_B^I \begin{bmatrix} u \\ v \\ w \end{bmatrix} \quad (2.12)$$

Equations (2.12), (2.7), (2.11), and (2.10) constitute the six-dof 13-state dynamics model for the agile UAV, which is implemented in Simulink for the test platform discussed in the section that follows. A variable time-step Runge-Kutta integrator (ODE45) is used to propagate the equations.

2.5 Test Platform

This section describes the test platform used in the current work. The mass and inertial parameters in the equations of motion are determined for this test platform, along with the input-to-control surface deflection relationships.

2.5.1 Description of the Test Platform

The test platform is the *YAK54 Electric 3D Aerobat* – an off-the-shelf high performance RC plane by Great Planes [101], see below.



Figure 2.2: *YAK54 Electric 3D Aerobat* RC plane [101].

From among the plethora of available RC planes, the YAK54 was chosen because on top of its capability to perform extreme 3D aerobatics, it is very lightweight (bare-frame weight = 155 to 190 g) making it suitable for indoor flight. Furthermore, these foam planes are quick to assemble and upon accidents/crashes, they absorb most of the impact, leaving the onboard electronic equipment and sensors intact.

The YAK54 was strengthened with a carbon-fiber structure (see Fig. 2.3), to allow it to carry a custom-designed data acquisition (DAQ) system. This will in future facilitate the data collection process during flight tests which could be useful for validation purposes as well as controller development.

The thruster system consists of a *RimFire 400 Outrunner Brushless DC Motor* by Great Planes, powered by an 11.1 V Lithium Polymer (LiPo) battery through an *Electrifly Silver Series 25A* brushless Electronic Speed Control (ESC) unit. An *Electrifly PowerFlow 10x4.5* propeller is coupled to the BLDC motor. The ESC controls the speed of the motor-propeller by varying the voltage (applied to the motor) in proportion to the user's commanded pulse width (PW) signal, whose range is from 1000 to 2000 μs . For RC planes, the input PW signal is sent to the ESC at a fixed frequency of 400 Hz.

2.5.2 Mass and Inertial Parameters

The mass of the ready-to-fly test platform shown in Fig. 2.3, was measured to be 465 g. This includes the weight of the bare aircraft frame (with carbon-fiber structure), thruster unit, and all the hardware for the DAQ system. The thruster unit mentioned above is able to produce a maximum thrust of around 9.9 N (for a maximum PW input of 2000 μs). This gives a thrust-to-weight ratio of around 2.17 for the test platform.

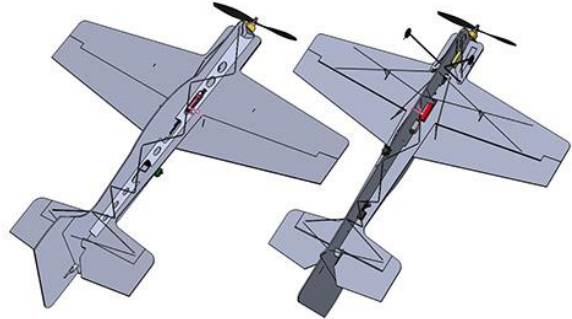


Figure 2.3: Fully assembled YAK54 plane (left) and its CAD model (right).

The inertial parameters were evaluated from a detailed CAD model developed in SolidWorks (see Fig. 2.3). All individual components were modeled with their respective measured masses, so that the CAD model is as accurate as possible. Also, the location of the center of gravity (from the propeller plane) is obtained from the CAD model. Table 2.1 summarizes the mass and inertial properties for the YAK54 test platform.

TABLE 2.1
YAK54 TEST PLATFORM MASS AND INERTIAL PARAMETERS

Parameter	Symbol	Value	Unit
Mass	m	0.465	kg
Moments of Inertia	I_x	2.45×10^{-3}	kg.m ²
	I_y	2.07×10^{-2}	kg.m ²
	I_z	2.25×10^{-2}	kg.m ²
Product of Inertia	I_{xz}	1.7×10^{-4}	kg.m ²
Location of c.g. (measured from propeller plane)	x_{cg}	-0.293	m
	y_{cg}	0	m
	z_{cg}	0.007	m

2.5.3 Input-to-Deflection Relationships

A *Hitec HS-65HB* servo is connected to each of the control surfaces (ailerons, elevator and rudder) and produces deflections in proportion to the user’s commanded PW signals (sent to the servos at a fixed frequency of 50 Hz). As noted by Peddiraju [58], servos can be characterized by two main dynamic effects namely an operational speed saturation, and a delay in response. The former effect is taken into account by the manufacturer’s rated speed which, for HS-65HB servos, is 428 deg/s, while the latter could be experimentally measured [58]. However, from the measured delay (around 48 ms) for a similar but relatively heavier and powerful servo (HS-322HD) in Ref. [58], it is speculated that for the current servos, the delay would be even smaller and hence the delay in servo response is neglected in the present work.

To obtain the steady-state relationships from the commanded PW signals to actual control surface deflections, simple experiments were performed. An Arduino board was programmed to send PW signals to the servos ranging from 1100 to 1900 μs in steps of 50 μs . Control surface deflections were measured using a highly accurate *MicroStrain 3DM-GX3-25* IMU mounted on the control surfaces. The sign convention for control surface deflection follows the standard convention for fixed-wing aircraft, according to which a positive deflection is defined so that it creates a negative moment [33].

- Ailerons deflection $\delta_a = (\delta_{a,R} - \delta_{a,L})/2$: positive right-aileron trailing-edge down, creating negative roll moment.

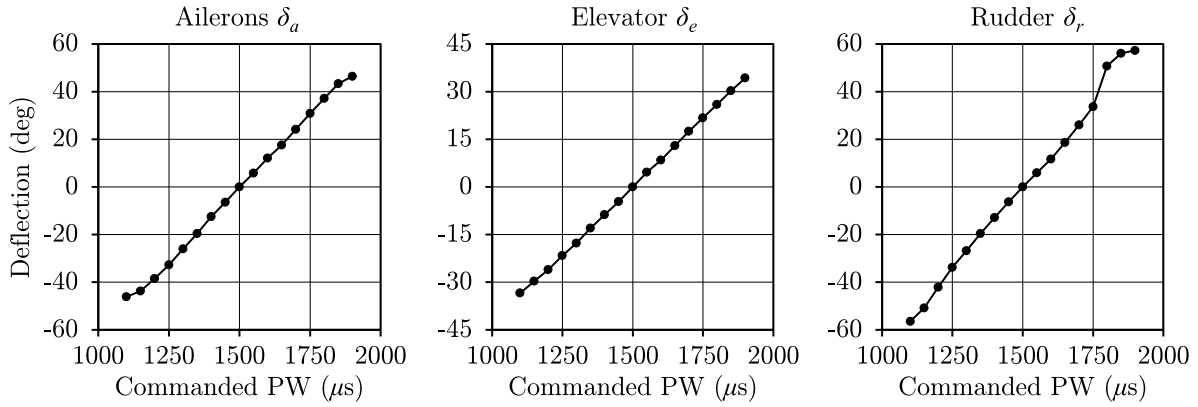


Figure 2.4: Input-deflection relationships.

- Elevator deflection δ_e : positive trailing-edge down creating negative pitch moment.
- Rudder deflection δ_r : positive trailing-edge left (when viewed from rear), creating negative yaw moment.

Figure 2.4 plots the results of the experiments. The control surfaces are level (zero deflection) at $PW = 1500 \mu s$, and vary almost linearly for small inputs around this central PW value. Near the extremes (1100 μs and 1900 μs), the deflection becomes nonlinear. The peak deflections are: ± 46 deg. for the ailerons, ± 34 deg. for the elevator and ± 57 deg. for the rudder.

Chapter 3

Aerodynamics

Agile UAVs rely on unconventional, nonlinear, post-stall and unsteady aerodynamics to perform aerobatic maneuvers and achieve flight conditions that are otherwise impossible with conventional fixed-wing aerodynamics. As an example, consider the perch maneuver in Fig. 3.1 where an agile UAV pitches up quickly to 90 deg. so that part of its aerodynamic surfaces, lying outside the propwash, stall. The partially stalled surfaces act as bluff bodies and help to slow down the UAV from 9 m/s to 2 m/s to make the perch possible [102]. Clearly, to capture such behavior of agile UAVs for their entire working envelope and in particular during extreme maneuvers, it is necessary to model their aerodynamics as completely and comprehensively as possible. The current chapter focusses on this.



Figure 3.1: An agile UAV performing aerobatics (left), and perch maneuver [102] (right).

The challenging task of modeling agile UAV aerodynamics includes modeling:

- 1) the full flight envelope, i.e. ± 180 deg. angle of attack and sideslip range,
- 2) partial flow conditions over the aerodynamic surfaces, e.g. in the case of a partially stalled wing,
- 3) low aspect ratio surfaces ($AR \leq 4$) operating at low Reynolds numbers ($\leq 150,000$),
- 4) large control surfaces (up to 50% flap-to-chord ratios) and deflections (up to 50 deg.),

- 5) realistic phenomena such as adverse yaw, induced roll etc.,
- 6) aerodynamic interaction between aircraft components such as wing, tail etc., and
- 7) unsteady aerodynamic effects particularly during rapid maneuvering.

Many works in the literature resort to system identification techniques to identify the complex aerodynamics of maneuvering flight [19–22]. But, as alluded in Chap. 1, it is not a feasible approach to cover the entire flight envelope of agile UAVs due to the sheer volume of testing required. Also, the stability derivatives approach found often in the literature for conventional fixed-wing aircraft and some agile UAV maneuvers [11], is unsuitable for the current purposes as it would result in multiple linear models adding the complexity of having to devise algorithms to intelligently switch between those models. In the present work, the aerodynamics model for agile UAVs is based on a component breakdown approach as it can be used to easily model aerodynamic surfaces in detail [16, 17]. A discussion on the component breakdown approach follows in the next section.

Despite the aforementioned complexities, this chapter aims to develop an aerodynamics model that captures the behavior of agile UAVs reasonably well, while being as mathematically simple as possible and hence computationally inexpensive. This will facilitate real-time implementation of the overall UAV simulation as well as pilot-in-loop simulations for the purposes of qualitative validation.

3.1 Component Breakdown Approach

The component breakdown approach, also known as strip theory, requires the decomposition of the aircraft components (wing, tail etc.) into a number of segments each producing lift, drag and moment about its aerodynamic center (a.c.). Their forces and moments are transferred to the aircraft center of gravity (c.g.) using kinematics and summed up to give the total aerodynamic force and moment acting on the aircraft. The decomposition process allows modeling each segment independently with its own aerodynamics, as well as the possibility of modeling almost every geometric detail of the individual segment. This means,

for example, that some segments can be modeled with different velocity due to the propwash over them, some segments may be modeled as 100% control surfaces while others can be partial control surfaces, and so on. As opposed to the other approaches discussed earlier, this approach is most befitting for agile UAV aerodynamics because:

- it has the ability to model unique geometry of the agile UAV surfaces, like the elevator shown in Fig. 3.1,
- it can model partially stalled surfaces like part of the wing immersed in the propwash that stalls later than the rest of the wing, and
- the resultant model is a single unified model that, by design, predicts realistic phenomena such as adverse yaw, induced roll etc.

Figure 3.2 shows the decomposition of the YAK54 test platform. The segments are defined keeping in view the aircraft geometry and other constraints like propwash etc. For example, the starboard wing is divided into seven segments such that the first three segments from the wing root lie within the propeller slipstream. More so, the first segment at the wing root has no control surface, while the last segment at the tip has a different configuration with an aileron horn. Similarly, segments can be defined on all components of the aircraft. Based on their geometry and flow conditions, they will each produce aerodynamic forces and moments about their a.c.

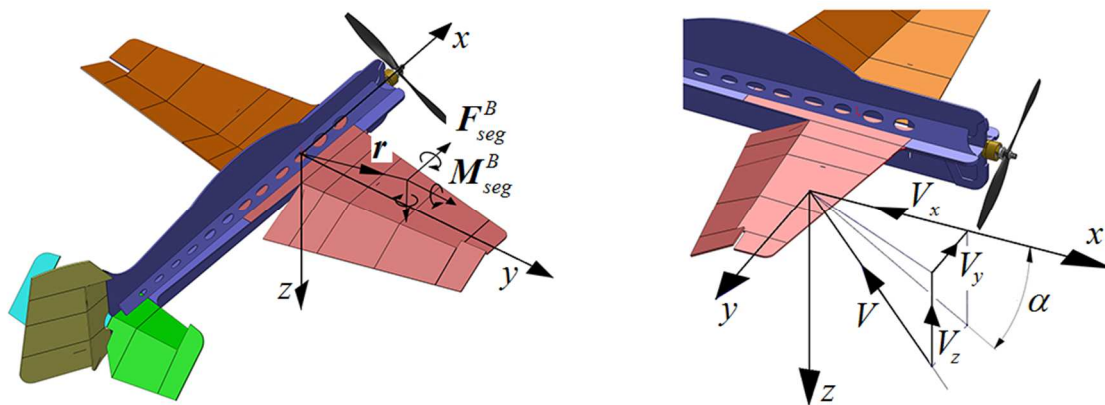


Figure 3.2: Decomposition of the YAK54 platform (left), and segment velocity and angle of attack (right).

3.1.1 Segment Velocity and Angle of Attack

To determine the flow conditions of each aircraft segment, its velocity is calculated at its a.c. using kinematics and appropriate contributions of propwash, wind etc. In general, Eq. (3.1) is used to calculate the velocity of each segment.

$$\mathbf{V} = \mathbf{V}_{cg}^B + \boldsymbol{\Omega}^B \times \mathbf{r} + \mathbf{V}_s + \mathbf{V}_{ind} + \mathbf{V}_{QS} + \mathbf{V}_{wind} \quad (3.1)$$

The first two terms come from the translation and rotation of the aircraft defined by the body velocity $\mathbf{V}_{cg}^B = [u, v, w]^T$ and body rate $\boldsymbol{\Omega}^B = [p, q, r]^T$ respectively. The position vector $\mathbf{r} = [r_x, r_y, r_z]^T$ is from the aircraft c.g. to the aerodynamic center of the segment, measured in the body frame.

The velocity \mathbf{V}_s due to the propeller slipstream is calculated for each segment at its a.c. using the slipstream model from Chap. 5. The induced velocity \mathbf{V}_{ind} on the segment due to aerodynamic interference from other segments is considered in Sec. 3.4. This is particularly important for the vertical and horizontal tail segments which have considerable downwash from the upstream wing segments. Any external wind contribution (given in the body frame) is also added in Eq. (3.1).

Furthermore, the maneuvers performed by agile UAVs are quite rapid, and hence unsteady aerodynamic effects on the segment must be considered. From the works in the literature [16, 17, 21, 22], it is concluded that even aggressive maneuvers like blenders, perching etc. may be reasonably modeled using quasi-steady aerodynamics, i.e. time-dependent unsteady effects may be neglected but other effects due to pitching (rate of change of angle of attack $\dot{\alpha}$) and plunging (change in downward velocity \dot{h}) must be considered. The quasi-steady effect of plunging is already accounted for when using Eq. (3.1), while for the effect of $\dot{\alpha}$, the velocity perturbation $\mathbf{V}_{QS} = 0.5\dot{\alpha}c \mathbf{k}$ [28] is explicitly added in Eq. (3.1). A detailed discussion on the unsteady aerodynamics is given later in Sec. 3.5.

The angle of attack of each segment is calculated from its velocity. For segments on the horizontal surfaces (see Fig. 3.2), the angle of attack is:

$$\alpha = \text{atan2}(V_z, V_x) - \alpha_0 \quad (3.2)$$

while for those on vertical surfaces, it is:

$$\alpha = \text{atan2}(V_y, V_x) - \alpha_0 \quad (3.3)$$

The geometric zero-lift angle α_0 is included so that the angle of attack is measured from the zero-lift line. For symmetric airfoils like those of the test platform, $\alpha_0 = 0$.

It is assumed that the aerodynamic contribution of the spanwise velocity component is negligible. This means that the y direction flow for horizontal surfaces, such as the wing, and the z direction flow for vertical surfaces, such as the rudder, produce only skin friction drag and is thus neglected. Depending on the angle of attack of each segment, its aerodynamics can fall either in the low-alpha regime or in the high-alpha regime, discussed later in Secs. 3.2 and 3.3 respectively.

3.1.2 Segment Forces and Moments

The aerodynamic forces and moments on each horizontal segment are written as:

$$\begin{aligned} \mathbf{F}_{seg}^B &= \frac{1}{2} \rho b c V_{xz}^2 [CF_{seg,x}, 0, CF_{seg,z}]^T \\ \mathbf{M}_{seg}^B &= \frac{1}{2} \rho b c^2 V_{xz}^2 [0, C_{M,ac}, 0]^T \end{aligned} \quad (3.4)$$

and similarly, for vertical segments:

$$\begin{aligned} \mathbf{F}_{seg}^B &= \frac{1}{2} \rho b c V_{xy}^2 [CF_{seg,x}, CF_{seg,y}, 0]^T \\ \mathbf{M}_{seg}^B &= \frac{1}{2} \rho b c^2 V_{xy}^2 [0, 0, -C_{M,ac}]^T \end{aligned} \quad (3.5)$$

Here b and c are the span and mean aerodynamic chord (m.a.c.) of the segment. The segment force coefficients are obtained from its lift and drag coefficients according to,

$$\begin{aligned} CF_{seg,x} &= C_L \sin \alpha - C_D \cos \alpha \\ CF_{seg,y} &= CF_{seg,z} = -C_L \cos \alpha - C_D \sin \alpha \end{aligned} \quad (3.6)$$

The quasi-steady aerodynamic coefficients C_L , C_D and $C_{M,ac}$ are determined in the next sections, depending on whether the segment under consideration is in the low-alpha or high-

alpha regime, with corrections for aspect ratio and control surface deflection. When considering time-dependent unsteady effects (see Sec. 3.5), dynamic coefficients C_L^{dyn} , C_D^{dyn} and $C_{M,ac}^{dyn}$ may be used in Eq. (3.6) above.

3.1.3 Total Aerodynamic Force and Moment

The forces and moments obtained for each segment via Eqs. (3.4) and (3.5), are transferred to the aircraft c.g. using kinematics, and added as follows:

$$\begin{aligned} \mathbf{F}_{aero}^B &= \Sigma \mathbf{F}_{seg}^B \\ \mathbf{M}_{aero}^B &= \Sigma (\mathbf{M}_{seg}^B + \mathbf{r} \times \mathbf{F}_{seg}^B) \end{aligned} \quad (3.7)$$

The above equation represents the net aerodynamic force and moment acting at the aircraft c.g. and is used in the equations of motion.

3.2 Low-Alpha Aerodynamics

In the current work, low-alpha aerodynamics refer to the aerodynamics that exist up to the point where the flow separates from the upper surface starting from the leading-edge (LE) with no reattachment downstream. As such, the complex stall phenomenon is included in the low-alpha regime.

In the linear range, prior to stalling, the lift, drag and moment coefficients may be calculated using the vast airfoil data available in the literature [103, 104], XFOIL [23], or standard equations [33]:

$$\begin{aligned} C_L &= C_{L\alpha} \alpha \\ C_D &= C_{d,0} + C_L^2 / (\pi k_O AR) \\ C_{M,ac} &= -\text{const.} \end{aligned} \quad (3.8)$$

where α is measured from the zero-lift line, $C_{L\alpha}$ is the lift-curve slope of a finite surface, $C_{d,0}$ is the drag coefficient due to skin friction (usually 0.02 to 0.04), k_O is the Oswald's efficiency factor (typically 0.85 – 0.9). The moment at the aerodynamic center is usually negative (i.e. pitch down) and constant in the low-alpha regime. For thin flat plates, the a.c. and the center of pressure are coincident and hence $C_{M,ac} = 0$ [33].

The aerodynamic coefficients in Eq. (3.8) are influenced by a number of factors including airfoil shape/thickness, aspect ratio, Reynolds number, Mach number, control surface deflection, and unsteady flow conditions. For the range of operational speeds of agile UAVs, Mach number has little effect on the aerodynamic performance [30, 50]. Also, for low aspect ratio wings, there is little effect of Reynolds number below $\sim 140,000$, as noted in [30, 50]. This is also evident from the close match between experimentally measured aerodynamic coefficients at various Reynolds numbers, see for e.g. Okamoto et al. [38] at $Re = 10,000$, experimental data of University of Notre Dame [29–32] at $Re = 100,000$ to $140,000$, Krishnan [39] at $Re = 40,000$ to $160,000$, and Ortiz et al. [40] at $Re = 60,000$ to $200,000$.

3.2.1 Effect of Low Aspect Ratio

Agile UAVs are designed to keep most of the aerodynamic and control surfaces immersed in the propwash to maintain lift and control under zero/low forward speed flight and extreme maneuvers, wherein the external flow (i.e. all flow outside the slipstream) is largely detached from the surfaces. As a result of this design constraint, the aerodynamic and control surfaces of agile UAVs are low aspect ratio, typically 1.5 to 4.

The effect of aspect ratio to reduce lift and increase drag is well-known [33]. This degradation in aerodynamic performance may be explained via the generation of two contrarotating vortices at the sides (tips) of a finite wing, which induce downwash and reduce the angle of attack. This results in lower lift and higher drag. The effect can be accounted for by decreasing the lift-curve slope, for which several expressions are available in the literature, though they agree within a few percent [33]. Presently, the expression given in [12] is used:

$$C_{L\alpha} = C_{l\alpha} \left(\frac{AR}{AR + 2(AR + 4)/(AR + 2)} \right) \quad (3.9)$$

where $C_{l\alpha}$ is the 2D lift-curve slope and may be taken as 2π for thin flat plates.

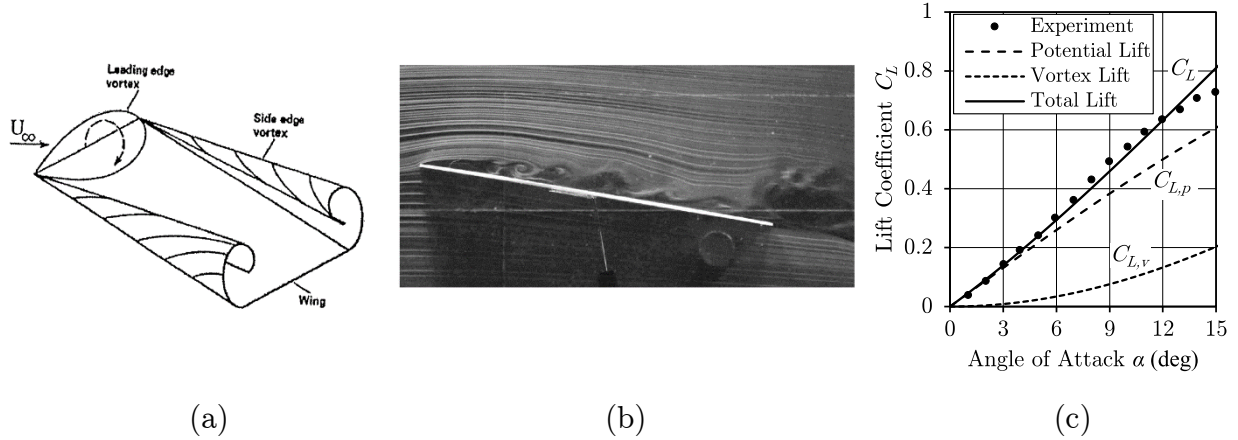


Figure 3.3: (a) Leading and side-edge vortices [29], (b) leading-edge vortex at $\alpha = 10$ deg. [38], and (c) lift coefficient for a LAR wing of $AR = 2$.

Special attention is required when the aspect ratio is below 2, and/or if the airfoil sections are thin with sharp leading and side edges, see for example the test platform in Fig. 3.1. This is because as the aspect ratio becomes lower, the side (tip) vortices engulf more and more of the upper surface as shown in Fig. 3.3 (a). Additionally, if the leading-edge is sharp, flow separation from the leading-edge and consequently leading-edge vortices (LEVs) will form with increasing angle of attack, see Fig. 3.3 (a) and (b). In the low-alpha regime, both the leading-edge and side-edge vortices essentially reattach on the upper surface of the wing, further reducing pressure there, and thus give rise to an additional vortex lift. The total lift for a LAR wing is therefore the sum of potential and vortex lift, as shown in Fig. 3.3 (c). The former may be calculated using potential flow theories such as the Prandtl's lifting line theory, while an expression for the latter for delta wings was proposed by Polhamus [34, 35] using the leading-edge suction analogy. According to Polhamus, the total pressure force required to stabilize and reattach the separated leading-edge vortex is provided by the leading-edge suction force. Later, Lamar [36] extended Polhamus' theory to other non-delta planforms with sharp leading and side edges, using the suction analogy for side-edge vortices. Recent experimental investigations in relation to MAVs [29–32, 37–40] thoroughly discuss the effect of such low aspect ratio surfaces, see Sec. 1.1.3. The main effects include: 1) presence of vortex lift, 2) higher maximum lift coefficient C_{Lmax} , 3) high stall angles up to

38 deg. [30], and 4) nonlinear aerodynamics even in the pre-stall region. The effects are more pronounced for aspect ratios smaller than 1.5 [30]. The mathematical expressions given by Polhamus and Lamar are shown to agree well with experimental data. For the YAK54 test platform shown in Fig. 3.1, the aerodynamic surfaces are thin flat plates (3 – 5% thickness-to-chord ratios) with sharp leading and side edges. Furthermore, the aspect ratio of the YAK54 surfaces are low: $AR = 3.8, 2.5, 1.6,$ and 0.2 for the wing, horizontal tail, vertical tail and fuselage respectively. As a result, Eq. (3.8) is not well suited; instead the nonlinear equations for the lift, drag and moment coefficients given by Polhamus and Lamar [34–36] are used:

$$\begin{aligned}
C_L &= C_{L,p} + C_{L,v} = K_p \sin \alpha \cos^2 \alpha + K_v |\sin \alpha| \sin \alpha \cos \alpha \\
C_D &= C_{d,0} + C_L |\tan \alpha| = C_{d,0} + K_p |\sin \alpha| \sin \alpha \cos \alpha + K_v \sin^3 \alpha \\
C_{M,ac} &= -(x_p - 0.25)K_p \sin \alpha \cos \alpha - (x_e - 0.25)K_v |\sin \alpha| \sin \alpha
\end{aligned} \tag{3.10}$$

The potential (linear) and vortex (nonlinear) lift contributions are represented by the coefficients $C_{L,p}$ and $C_{L,v}$, and parameters K_p and K_v . For LAR rectangular surfaces, K_p is equal to the lift-curve slope $C_{L\alpha}$ [33]. The vortex lift comes from both the leading and side edges, represented by parameters $K_{v,LE}$ and $K_{v,SE}$ respectively. While these individual parameters also vary with aspect ratio, the total vortex lift parameter $K_v = K_{v,LE} + K_{v,SE}$ remains nearly constant, within $\pm 10\%$ of π [36], and is thus used in Eq. (3.10) instead of the individual parameters. Therefore,

$$\begin{aligned}
K_p = C_{L\alpha} &= C_{l\alpha} \left(\frac{AR}{AR + 2(AR + 4)/(AR + 2)} \right) \\
K_v &\simeq \pi
\end{aligned} \tag{3.11}$$

In the pitching moment coefficient of Eq. (3.10), x_p and x_e represent the normalized chordwise locations of the potential and vortex lifts respectively. For rectangular flat plate surfaces, such as those of the YAK54 platform, the center of pressure for potential lift is at quarter-chord location, i.e. $x_p = 0.25$, while x_e is determined from the experimental results of [30] to be nearly constant at 0.42.

3.2.2 Effect of Stall

The low-alpha regime is extended to cover the stall phenomenon by including the effect of trailing-edge (TE) separation and leading-edge vortex (LEV) breakdown. These stall mechanisms are briefly discussed next.

Trailing-Edge Separation

The conventional mechanism for stalling is the progressive separation of flow from the upper surface starting from the trailing-edge. This causes the loss of lift associated with the stall phenomenon. The normalized chordwise location of the TE separation is represented by f_{TE} as shown in Fig. 3.4 (a), such that for fully attached flow, $f_{TE} = 1$. As the angle of attack increases, f_{TE} decreases and becomes zero for fully separated flow from the LE at the start of high-alpha regime (i.e. at $\alpha = \alpha_{high,S}$). For thick wings, the transition from $f_{TE} = 1$ (fully attached) to 0 (fully separated) is progressive and occurs over a range of angle of attack. On the other hand, for thin wings, this transition from fully attached to fully separated flow is abrupt.

Leading-Edge Vortex Breakdown

A thin wing with sharp leading-edge is also characterized by the formation of LE vortices that reattach and travel along the upper surface of the wing. However, at a certain distance

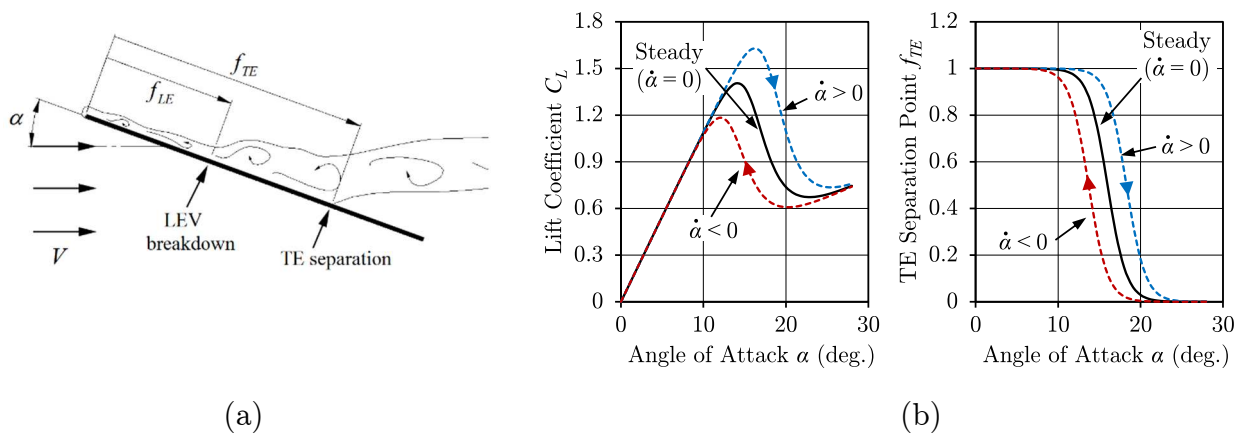


Figure 3.4: (a) Leading-edge vortex breakdown and trailing-edge separation, and (b) effect of $\dot{\alpha}$ on f_{TE} and C_L .

downstream of the leading-edge, these LEVs breakdown due to turbulence etc., thereby causing a loss in the vortex lift. The normalized chordwise position of the LEV breakdown is represented by f_{LE} as shown in Fig. 3.4 (a). At low angles of attack, the LEV breakdown down occurs at the trailing-edge (i.e. $f_{LE} = 1$); as the angle of attack increases f_{LE} starts to decrease and becomes zero at higher angles of attack with the LEV breakdown occurring at the leading-edge.

Aerodynamic Coefficients in the Stall Regime

For thin airfoils with sharp leading-edge, both the TE separation and LEV breakdown are responsible for loss in lift during stall. Following the work of Goman et al. [45], it is possible to extend the low-alpha regime equation (3.10) to cover the stall phenomenon, by including the effect of f_{TE} and f_{LE} on the aerodynamic coefficients:

$$\begin{aligned}
C_L &= 0.25 \left(1 + \sqrt{f_{TE}}\right)^2 \left(K_p \sin \alpha \cos^2 \alpha + f_{LE}^2 K_v |\sin \alpha| \sin \alpha \cos \alpha\right) \\
C_D &= C_{d,0} + C_L |\tan \alpha| \\
C_{M,ac} &= -0.25 \left(1 + \sqrt{f_{TE}}\right)^2 \left[0.0625 \left(-1 + 6\sqrt{f_{TE}} - 5f_{TE}\right) K_p \sin \alpha \cos \alpha\right. \\
&\quad \left.+ 0.17 f_{LE}^2 K_v |\sin \alpha| \sin \alpha\right]
\end{aligned} \tag{3.12}$$

From Eq. (3.12), the LEV breakdown affects only the vortex lift, but the TE separation affects the total lift. Under quasi-steady condition f_{TE} and f_{LE} depend upon α and $\dot{\alpha}$, and may be written from [45–47] as:

$$\begin{aligned}
f_{TE} &= 0.5 \left[1 - \tanh \left\{a_{TE} (\alpha - \tau_{TE} \dot{\alpha} - \alpha_{TE})\right\}\right] \\
f_{LE} &= 0.5 \left[1 - \tanh \left\{a_{LE} (\alpha - \tau_{LE} \dot{\alpha} - \alpha_{LE})\right\}\right]
\end{aligned} \tag{3.13}$$

The semi-empirical coefficients a_{TE} , a_{LE} , α_{TE} , and α_{LE} may be determined from static lift data available in the literature. In this work, these coefficients have been obtained for rectangular flat plates by curve fitting Eq. (3.12) to the static lift coefficient data taken from Refs. [30, 38–40, 105, 106]. A wide range of aspect ratios (0.17 to 6) is covered so that it suffices for any small UAV. Table 3.1 lists these semi-empirical parameters for rectangular flat plates of various aspect ratios.

TABLE 3.1
SEMI-EMPIRICAL COEFFICIENTS FOR RECTANGULAR FLAT PLATES

Aspect ratio	0.167	0.333	0.5	0.75	1	1.25	1.5	1.75	2	3	4	6
a_{LE}	3	3.64	4.48	7.18	10.2	13.38	14.84	14.49	9.95	12.93	15	15
a_{TE}	5.9	15.51	32.57	39.44	48.22	59.29	21.55	7.74	7.05	5.26	6.5	6.5
a_{LE}	59	58.6	58.2	50	41.53	26.7	23.44	21	18.63	14.28	11.6	10
a_{TE}	59	58.6	58.2	51.85	41.46	28.09	39.4	35.86	26.76	19.76	16.43	14
$a_{high,S}$	49	54	56	48	40	29	27	25	24	22	22	20

The quasi-steady time constants, τ_{TE} and τ_{LE} , must be determined from dynamic test data which, for various AR wings, is scarce in the literature. Due to this lack of data, the time constants are presently set to $\tau_{TE} = 4.5c/V$ and $\tau_{LE} = 0.5c/V$ from Goman et al. [45] wherein these are determined for a NACA0015 airfoil and a delta wing of $AR = 1.5$.

Figure 3.4 (b) shows the effect of the rate of change of angle of attack $\dot{\alpha}$ on the trailing-edge separation and lift coefficient. It is seen that for increasing α (i.e. positive $\dot{\alpha}$), f_{TE} and hence stall is delayed. This increases lift from its steady-state ($\dot{\alpha} = 0$) value. Similarly on decreasing α (i.e. negative $\dot{\alpha}$), flow reattachment is delayed and hence the lift coefficient is lower than its steady-state value. Therefore, Eqs. (3.12) and (3.13) capture the well-known hysteresis effect in the aerodynamic coefficients under quasi-steady conditions. The effect of $\dot{\alpha}$ on LEV breakdown is similar. Further details on the effects of the various semi-empirical coefficients can be found in [45–48].

3.2.3 Effect of Control Surface Deflection

In the low-alpha regime, the general effect of control surface deflection is to change the camber of an airfoil and shift the lift curve. By convention, a positive deflection increases the camber and shifts the curve upwards. To account for flap deflection, an effective angle of attack $\alpha' = \alpha - \alpha'_0$ is used in Eq. (3.12), where α'_0 is the effective zero-lift angle of attack due to flap deflection and by convention is taken negative for a positive deflection.

Effective Zero-Lift Angle of Attack

To determine α'_0 , consider a segment with control surface deflected through $+\delta_f$ (see Fig. 3.5). The increase in lift coefficient is written from [33] as,

$$\Delta C_L = C_{L\alpha} \tau_f \eta_f \delta_f \quad (3.14)$$

where $\tau_f = 1 - (\theta_f - \sin\theta_f)/\pi$ is the flap effectiveness factor that accounts for the geometric change due to deflection, and $\theta_f = \arccos(2c_f/c - 1)$ with c_f and c being the segment flap chord and chord respectively. The empirical factor η_f accounts for the effects of viscosity and can be found from [33] against flap deflection. On top of being simple, there are two advantages of using Eq. (3.14) over other methods in the literature: 1) it accounts for the effect of aspect ratio through the $C_{L\alpha}$ term, refer to Eq. (3.9), and 2) it is valid for deflections as large as 70 deg.

At $\alpha = 0$ deg., the effective angle of attack is: $\alpha' = -\alpha'_0$, while the new lift coefficient is $C_L = \Delta C_L$, see Fig. 3.5. Then using the lift expression for the new curve we get:

$$\frac{\Delta C_L}{0.25(1 + \sqrt{f_{TE}})^2} = K_p \sin(-\alpha'_0) \cos^2(-\alpha'_0) + f_{LE}^2 K_v |\sin(-\alpha'_0)| \sin(-\alpha'_0) \cos(-\alpha'_0) \quad (3.15)$$

This nonlinear equation is solved for α'_0 , which will be negative for a positive deflection.

Effective Maximum-Lift Angle of Attack

A positive flap deflection will also affect the maximum-lift angle of attack α_{CLmax} , since the actual stall angle of an airfoil with a deflected control surface is lower than that with no deflection [33]. To determine the effective maximum-lift angle α'_{CLmax} , the new maximum lift coefficient is first calculated using $C'_{Lmax} = C_{Lmax} + \Delta C_{Lmax}$, where ΔC_{Lmax} may be obtained

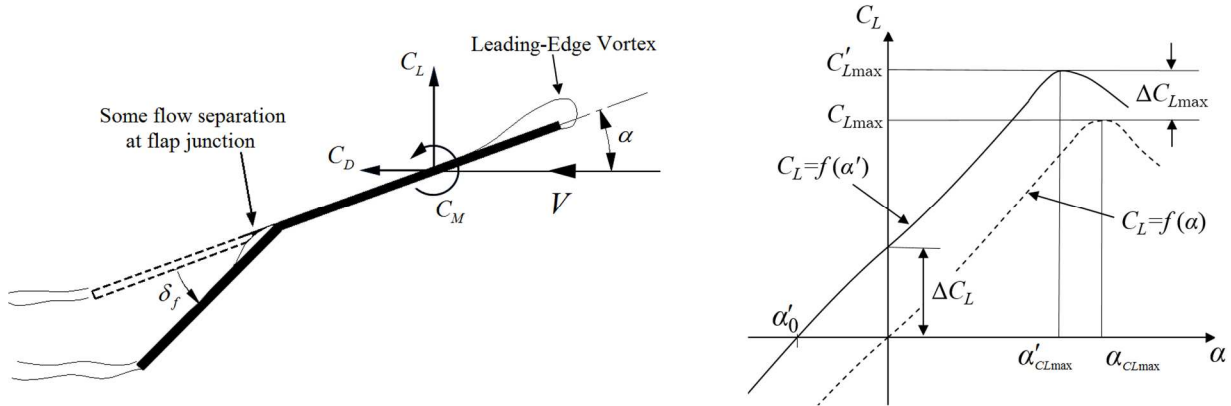


Figure 3.5: Flap deflection in low-alpha regime.

from [33] against flap-to-chord ratio. For this new maximum lift coefficient, the corresponding $\alpha'_{CL_{\max}}$ is found using Eq. (3.12):

$$0.25 \left(1 + \sqrt{f_{TE}}\right)^2 \left[K_p \sin(\alpha'_{CL_{\max}} - \alpha'_0) \cos^2(\alpha'_{CL_{\max}} - \alpha'_0) + f_{LE}^2 K_v \left| \sin(\alpha'_{CL_{\max}} - \alpha'_0) \right| \sin(\alpha'_{CL_{\max}} - \alpha'_0) \cos(\alpha'_{CL_{\max}} - \alpha'_0) \right] = C'_{L_{\max}} \quad (3.16)$$

The above nonlinear equation is solved for the effective maximum-lift angle of attack.

3.3 High-Alpha Aerodynamics

The high-alpha regime starts when the flow is completely separated from the upper surface starting from the leading-edge with no reattachment downstream. This occurs at an angle of attack $\alpha_{high,S}$. Thereafter, the airfoil profile has negligible effect, and it acts as a flat plate for which the aerodynamic coefficients may be calculated using flat plate theory [24] or expressions provided by Hoerner et al. [25], Young et al. [27], or Leishman [28]. In general, these references provide expressions for the normal force coefficient C_n , which may be decomposed into the lift and drag coefficients. The two commonly used expressions (flat plate theory and Hoerner's) are compared in Fig. 3.6 against 2D experimental data for the NACA0012 [107] and NACA63-215 [108] airfoil sections. It is evident that subsequent to flow separation, the two airfoils show similar behavior. Also, both the expressions correlate to the experimental data very well.

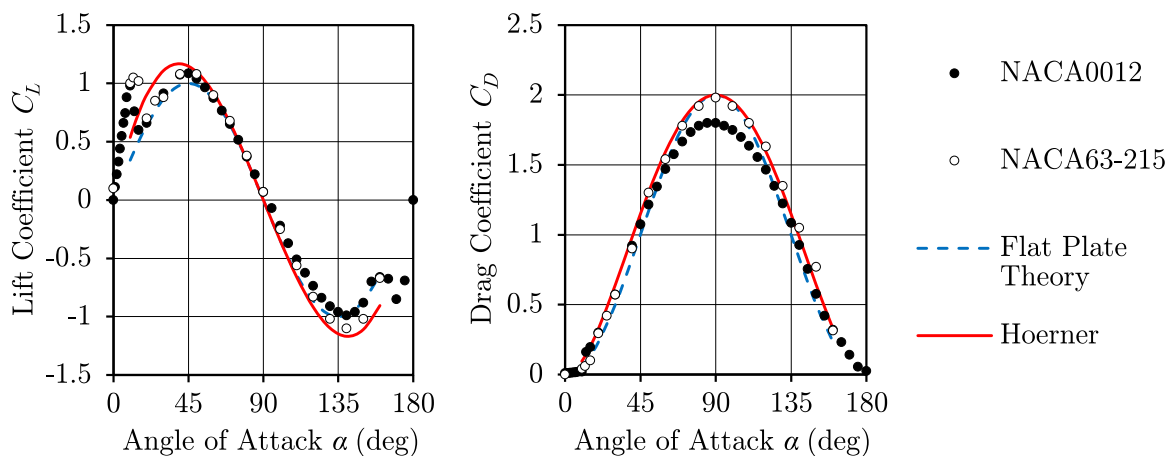


Figure 3.6: Comparison of high-alpha expressions.

In the current work, the expression by Hoerner et al. [25] is used in the high-alpha regime. Accordingly, the normal force coefficient for an infinitely long flat plate is given by,

$$C_n = C_{d,90} \frac{\sin \alpha}{0.56 + 0.44 \sin \alpha} \quad (3.17)$$

The 2D drag coefficient $C_{d,90}$ of a flat plate normal to flow is around 1.98.

3.3.1 Effect of Low Aspect Ratio

A correction for aspect ratio has been made to Hoerner's equation by Lindenburt [26]:

$$C_N = C_{d,90} \sin \alpha \left\{ \frac{1}{0.56 + 0.44 \sin \alpha} - 0.41 [1 - \exp(-17/AR)] \right\} \quad (3.18)$$

The lift, drag and moment coefficients are then written as:

$$\begin{aligned} C_L &= C_N \cos \alpha - C_A \sin \alpha \\ C_D &= C_N \sin \alpha + C_A \cos \alpha \\ C_{M,ac} &= -C_N [0.25 - 0.175(1 - 2\alpha/\pi)] \end{aligned} \quad (3.19)$$

where the axial force coefficient $C_A = 0.5C_{d,0} \cos \alpha$ [26] with $C_{d,0} \approx 0.02 - 0.04$ for flat plates at low Reynolds numbers. The pitching moment coefficient equation is also taken from [26] and is found to fit well for high angles of attack.

3.3.2 Effect of Control Surface Deflection

No mathematical treatment is found in the literature for the effect of control surface deflection at high angles of attack. Even more so, there exists no experimental work on this topic. Therefore, a simple but effective approach is proposed in the current work to account for control surface deflection in the high-alpha regime.

It was pointed out earlier that after complete separation of the flow from the upper surface, an airfoil behaves like a flat plate. Keeping this in view, it is proposed that an airfoil with a positive flap deflection in the high-alpha regime is also equivalent to a flat plate but with a higher drag coefficient $C'_{d,90}$ and at a higher effective angle of attack α' , as shown in Fig. 3.7. Thus the high-alpha expressions, Eqs. (3.18) and (3.19), are used with $C'_{d,90}$ instead of $C_{d,90}$, and α' instead of α .

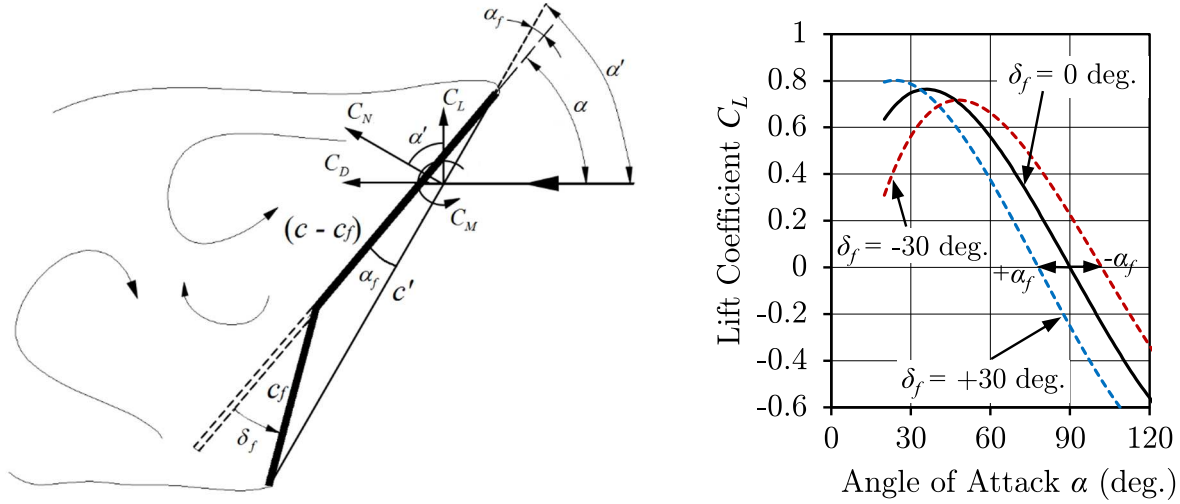


Figure 3.7: Flap deflection in high-alpha regime.

Effective Angle of Attack

Expression for α' in the high-alpha regime may be written from the geometry of Fig. 3.7,

$$\alpha' = \alpha + \alpha_f \quad (3.20)$$

where $\alpha_f = \text{asin}[(c_f/c') \sin \delta_f]$ and $c' = \sqrt{(c - c_f)^2 + c_f^2 + 2c_f(c - c_f) \cos \delta_f}$. The sign of α_f will be positive for a positive deflection.

Due to the flap deflection, the aerodynamics curves in the high-alpha regime are shifted horizontally by the angle α_f , see Fig. 3.7. But, it is assumed that the deflection has no influence on the start of the high-alpha regime ($\alpha_{high,S}$) because this angle depends on the geometric angle of attack with the leading-edge which does not change with flap deflection.

Effective Drag Coefficient

The 2D drag coefficient of the “equivalent” flat plate (normal to flow) is changed with control surface deflection knowing that the airfoil becomes convex or concave to the flow depending on whether the deflection is positive or negative.

A qualitative estimate of drag for 2D shapes is given in Ref. [33]. The 2D drag coefficient (normal to flow) for a 90 deg. concave is 2.2, for a flat plate is 1.98, and for a 90 deg. convex is 1.55. A segment of the YAK54 platform is limited by the maximum possible deflection,

and thus may, at most, form a 50 deg. convex or concave to the flow. In lieu of this, the data from [33] is curve-fitted to predict $C'_{d,90}$ for other deflections:

$$C'_{d,90} = -4.26 \times 10^{-2} \delta_f^2 + 2.1 \times 10^{-1} \delta_f + 1.98 \quad (3.21)$$

For a positive 50 deg. deflection, the airfoil becomes concave to the flow for which Eq. (3.21) gives $C'_{d,90} = 2.1$, while for a negative 50 deg. deflection, the airfoil becomes convex with $C'_{d,90} = 1.8$. For zero deflection, the 2D drag coefficient attains the standard value of 1.98 for a flat plate normal to flow.

3.4 Aerodynamic Interaction

Apart from having their own aerodynamics, the segments of an agile UAV affect each other aerodynamically. It is well known for conventional fixed-wing aircraft that the vortex system associated with finite wings induce a downwash on the horizontal tail, reducing the tail's angle of attack and lift [33]. Similar aerodynamic interactions exist for an agile UAV particularly in the low-alpha regime [16, 17].

In the present work, only the aerodynamic effect of the wing segments on the horizontal and vertical tail segments are considered important, and that too only when the wing segment under consideration is operating in the low-alpha regime. The latter condition is because the effect comes primarily from the vortex system of the wing which is well-defined only for the low-alpha regime. More so, at high alpha, the tail segments can be reasonably considered to be outside of the downwash.

The vortex system of a UAV wing includes bound and trailing vortices, as shown in Fig. 3.8 (a). The bound vortex remains attached to the wing, while the trailing vortices are assumed to shed off at the aileron-flap junction [16, 17] aligned with the flow. Eventually, the trailing vortices roll up to form two big vortices, see Fig. 3.8 (a). Thus when using Eq. (3.1) to calculate velocity for segments on the wing and fuselage: $\mathbf{V}_{ind} = 0$; but for segments on the horizontal and vertical tail,

$$\mathbf{V}_{ind} = \mathbf{V}_{ind,BV} + \mathbf{V}_{ind,TV} \quad (3.22)$$

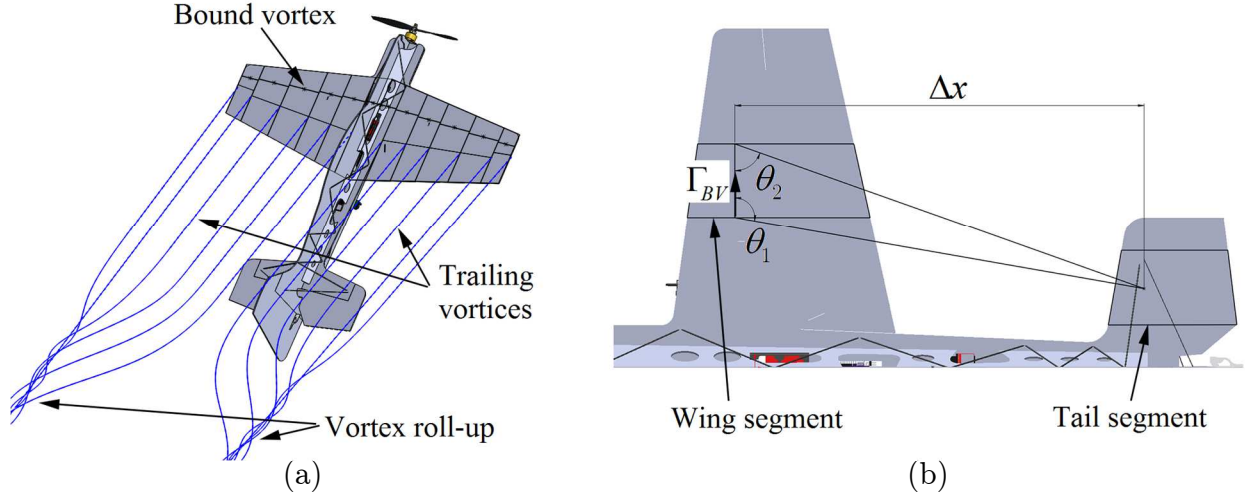


Figure 3.8: (a) Vortex system of the wing, and (b) effect of bound vortex filament.

One might also expect that the reverse interaction of the tail on the wing is important when the agile UAV flies rearwards, as in the case of a tail-slide maneuver where a hovering agile UAV gradually lowers to touch the ground with the tip of its rudder. However, this tail-to-wing interaction is very weak since an agile UAV moves very slowly in the rearward direction to remain stable, and that too for very short duration.

3.4.1 Effect of Bound Vortex

To account for the effect of bound vortex, consider Fig. 3.8 (b). A finite bound vortex (BV) filament is associated with each wing segment operating in the low-alpha regime. The strength of this BV filament is calculated using:

$$\Gamma_{BV} = \frac{1}{2} c C_L V_{xz} \quad (3.23)$$

For a wing segment operating in the high-alpha regime, Γ_{BV} may be taken as zero. The induced velocity on a horizontal tail segment by the bound vortex filaments is found using the Biot-Savart law, and can be written from [33] as:

$$\mathbf{V}_{ind,BV} = -\frac{\Gamma_{BV}}{4\pi\Delta x} (\cos\theta_1 + \cos\theta_2) \mathbf{k} \quad (3.24)$$

The quantities Δx , θ_1 and θ_2 depend on the wing-to-horizontal tail geometry, as shown in Fig. 3.8 (b). For the test platform, the wing and tail are in the same plane (xy), and therefore

the induced velocity given by Eq. (3.24) is only in the z direction. The effect of all individual bound vortex filaments of the wing are added to give the total induced velocity on a tail segment.

The effect of bound vortex on the vertical tail segments is neglected because the induced downwash is mainly in the z direction which is assumed to cause only friction drag for vertical surfaces (as discussed in Sec. 3.1.1). Due to the wing-to-vertical tail geometry, there is also a small induced velocity component in the x direction which is neglected.

3.4.2 Effect of Trailing Vortices

The effect of the trailing vortices (TV) requires a more in-depth geometrical analysis since these vortices are not fixed but rather align with the incoming flow. It is assumed that the vortices are shed off from a spanwise location at the intersection of wing segments, and from a chordwise location at the aileron-flap junction, see Fig. 3.8 (a). Although, these trailing vortex filaments roll up into two big vortices, it is assumed that this happens far downstream and thus the TV filaments are assumed aligned with the incoming flow.

The strength of the shed vortex filament is given as:

$$\Gamma_{TV} = \Delta\Gamma_{BV} \quad (3.25)$$

where $\Delta\Gamma_{BV}$ is the difference between the BV filament strengths of the adjacent wing segments. By convention, Γ_{TV} is taken positive if it is feeding into the bound vortex system of the wing. The magnitude of the induced velocity by the semi-infinite trailing vortex filament is written as [33]:

$$V_{ind,TV} = -\frac{\Gamma_{TV}}{4\pi d'} (\cos\theta_3 + 1) \quad (3.26)$$

For horizontal tail segments in Fig. 3.9 (a):

$d' = s_2 \sin\theta_3$, and $\theta_3 = \arccos(s_1^2 + s_2^2 - s_3^2)/2s_1s_2$, with $s_1 = (\Delta x/V_x)(V_z^2 + V_{xy}^2)^{0.5}$, $s_2 = (\Delta x^2 + \Delta y^2)^{0.5}$, and $s_3 = (\Delta x/V_x)[V_z^2 + (V_y + V_x\Delta y/\Delta x)^2]^{0.5}$.

This induced velocity has all three components which may be written from geometry as:

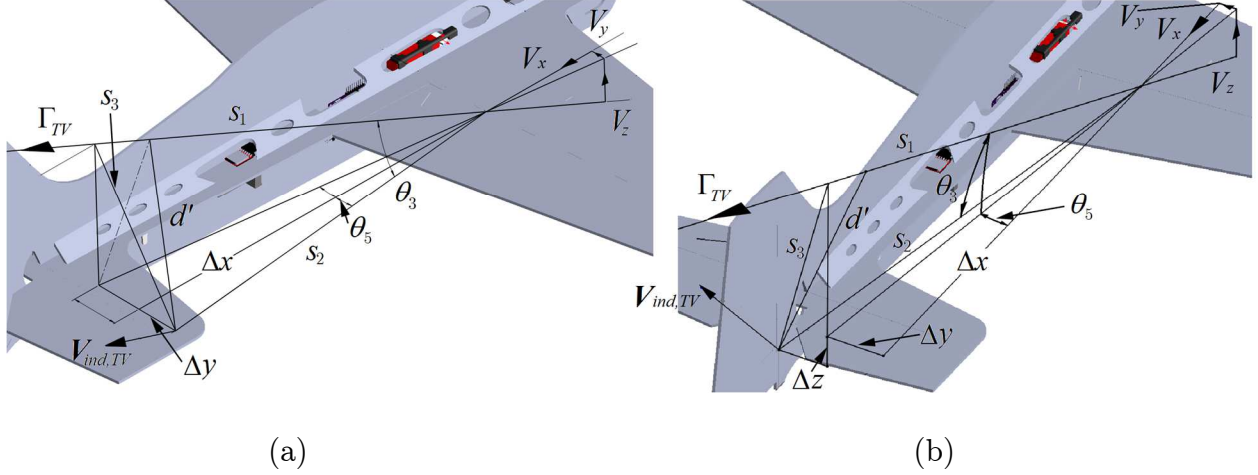


Figure 3.9: Effect of trailing vortex filament on (a) horizontal tail, and (b) vertical tail.

$$\mathbf{V}_{ind,TV} = -V_{ind,TV} \cos \theta_4 \cos \theta_5 \mathbf{i} - V_{ind,TV} \cos \theta_4 \sin \theta_5 \mathbf{j} + V_{ind,TV} \sin \theta_4 \mathbf{k} \quad (3.27)$$

where $\theta_4 = \text{atan}(\cos \theta_5 \tan \theta_6)$, $\theta_5 = \text{atan}(\Delta y / \Delta x)$, and $\theta_6 = \text{atan}[(\Delta y V_x + \Delta x V_y) / \Delta x V_z]$.

For vertical tail segments in Fig. 3.9 (b):

$d' = s_2 \sin \theta_3$, and $\theta_3 = \text{acos}(s_1^2 + s_2^2 - s_3^2) / 2s_1 s_2$, with $s_1 = (\Delta x / V_x)(V_z^2 + V_{xy}^2)^{0.5}$, $s_2 = (\Delta x^2 + \Delta y^2 + \Delta z^2)^{0.5}$, and $s_3 = (\Delta x / V_x)[(V_z + V_x \Delta z / \Delta x)^2 + (V_y + V_x \Delta y / \Delta x)^2]^{0.5}$.

The three components of the induced velocity are:

$$\mathbf{V}_{ind,TV} = V_{ind,TV} \cos \theta_4 \cos \theta_5 \mathbf{i} - V_{ind,TV} \cos \theta_4 \sin \theta_5 \mathbf{j} - V_{ind,TV} \sin \theta_4 \mathbf{k} \quad (3.28)$$

where $\theta_4 = \text{atan}(\cos \theta_5 \tan \theta_6)$, $\theta_5 = \text{atan}(\Delta y / \Delta x)$, and $\theta_6 = \text{atan}[(\Delta y V_x + \Delta x V_y) / (\Delta z V_x + \Delta x V_z)]$.

The effect of all individual trailing vortices may be summed up to give the total induced velocity on a given horizontal or vertical tail segment.

3.5 Unsteady Aerodynamics

Some of the impressive aerobatic maneuvers performed by agile UAVs are very rapid and therefore it seems appropriate to consider the time-dependent unsteady aerodynamic contributions in achieving these maneuvers. Essentially, unsteady aerodynamics come into play with sudden changes in the aircraft motion and even with wind gusts. These changes must be fast enough so that the flow does not have sufficient time to adjust to the motion, leading to the unsteady manifestations of apparent mass, circulation, and dynamic stall.

3.5.1 Reduced Frequency

It is particularly useful to characterize the degree of unsteadiness during maneuvering flight. This is done by the reduced frequency parameter which in general is defined as $k_r = fc/2V$ where f is the angular frequency at which the airfoil is oscillating. For agile UAV segments, it may be defined based on their rate of change of angle of attack [20] to give:

$$k_\alpha = \frac{\dot{\alpha}c}{2V} \quad (3.29)$$

According to Ref. [28], $k_\alpha = 0$ represents steady flow, $0 \leq k_\alpha \leq 0.05$ represents quasi-steady flow, i.e. the time-dependent effects are small enough to be neglected, and $k_\alpha > 0.05$ represents unsteady flow for which time-dependent effects become dominant and must be considered.

For agile UAVs with an average chord of 0.3 m and an average cruise speed of 5 m/s, a maneuver must produce at least $\dot{\alpha} \approx 100$ deg/s, from Eq. (3.29), in order to be unsteady. Even with the most dynamic maneuvers like blenders and snap rolls, it is difficult to achieve such high rates in the angle-of-attack. Thus most maneuvers of agile UAVs do not qualify as unsteady and may be dealt with the quasi-steady treatment as is done in the previous sections. This conclusion is consistent with the experimental observations of Ref. [21] wherein the motion of an agile UAV undergoing an aggressive perch maneuver was captured via motion tracking. The data from 240 flight tests revealed that the average aerodynamic coefficients matched closely to those predicted by the flat plate theory. Thus even an aggressive perch maneuver could be treated as quasi-steady. More so, the simulation in Refs. [16, 17] is shown to successfully capture extremely dynamic maneuvers with only quasi-steady modeling.

On the other hand, significant unsteady aerodynamic effects were observed in [20] during pitch-up maneuver of a lightweight MAV. The reduced frequency was found to be as high as 0.4 in some tests. In light of this, an unsteady aerodynamics model is included in the present work.

3.5.2 Time-Dependent Unsteady Effects

The time-dependent unsteady aerodynamic effects become important for extremely rapid maneuvers during which the reduced frequency exceeds 0.05. Several models exist in the literature to account for these unsteady effects including the well-known Beddoes-Leishman (B-L) [44], Risø [109], and Larsen [110] models. The Beddoes-Leishman model is thoroughly comprehensive and accounts for various effects such as compressibility etc. that are important for helicopter rotors. The inherent drawback is that it has 12 semi-empirical constants that require calibration. On the other hand, the Risø model is targeted towards wind-turbine applications and hence the compressibility effects are not included. Also considering the thick wind-turbine blades, the effect of leading-edge separation is excluded, resulting in a 6-parameter model. The Larsen model [110] is a 7 parameter model that excludes compressibility effects but includes dynamic leading-edge separation.

Unfortunately, the formulation of the aforementioned unsteady models is not suitable for the current work since they are unable to take into account the previously obtained quasi-steady aerodynamic curves which pre-include the effect of low AR, control surface deflection and aerodynamic interference. Therefore, with the help of existing models, an unsteady model suitable for agile UAVs is presented here.

The four main time dependent effects that must be included are: 1) added mass, 2) circulatory response, 3) dynamic trailing-edge separation, and 4) dynamic leading-edge vortex breakdown. The first two effects are related to the attached flow condition ($f_{TE} = 1$), while the latter two are related to the stalled flow condition ($0 < f_{TE} < 1$).

Attached Flow Condition

- Added Mass: Added mass (also called apparent mass) effect arises when the fluid surrounding the segment is suddenly accelerated along with it. The effect may be modeled as added mass terms to account for the reaction forces required to accelerate

the fluid mass. From [111], the increase in lift and moment coefficients due to added mass effect may be given as:

$$\begin{aligned} C_L^{AM} &= \frac{\pi c}{2V^2} \left[V\dot{\alpha} + \ddot{h} + \frac{1}{4}c\ddot{\alpha} \right] \\ C_{M,ac}^{AM} &= -\frac{\pi c}{2V^2} \left[\frac{1}{4}\ddot{h} + \frac{3}{32}c\ddot{\alpha} \right] \end{aligned} \quad (3.30)$$

The above equation has been simplified for the pitching axis located at the segment aerodynamic center. Eq. (3.30) when expressed in dimensional form (i.e. lift and moment) contains the $(\pi/4)\rho c^2$ term that represents the added mass.

- Circulatory Response: The time varying wake shed from the airfoil induces downwash and affects circulation, leading to an overall delayed response to a change in angle of attack. The classical unsteady model of Theodorsen [42] accounts for this effect by multiplying the quasi-steady lift and moment with the Theodorsen transfer function. The original Theodorsen formulation assumed pure harmonic motion of the airfoil and is extended to the entire complex plane by using a generalized Theodorsen function $C(\bar{s})$, where $\bar{s} = (c/2V)s$. Thus from [111],

$$\begin{aligned} C_L^{circ} &= C_L C(\bar{s}) \\ C_{M,ac}^{circ} &= 2C_{M,ac} \end{aligned} \quad (3.31)$$

The moment expression has been simplified since the pitching axis is located at the segment aerodynamic center. For the pitching axis location other than the a.c., the moment expression would contain an additional term multiplied with $C(\bar{s})$, see [28]. A number of approximations for $C(\bar{s})$ exist in the literature, see [49]. The two pole approximation by Jones [112] is used here:

$$C(\bar{s}) \simeq \frac{0.5\bar{s}^2 + 0.2808\bar{s} + 0.01365}{\bar{s}^2 + 0.3455\bar{s} + 0.01365} \quad (3.32)$$

The state-space realization of Jones approximation may also be found in the literature [49]. Equation (3.32) is solved via two first-order differential equations, thereby introducing two additional states in the simulation.

- Total Unsteady Response: Under attached flow conditions, the total unsteady response is the sum of added mass and circulatory terms.

$$\begin{aligned} C_L^{dyn} &= C_L^{AM} + C_L^{circ} \\ C_{M,ac}^{dyn} &= C_{M,ac}^{AM} + C_{M,ac}^{circ} \end{aligned} \quad (3.33)$$

Stalled Flow Condition

For unsteady flow conditions, the chordwise locations of the trailing-edge separation and leading-edge vortex breakdown become time-dependent and represented via first order differential equations [45–47]:

$$\begin{aligned} \tau_{TE,1} \dot{f}_{TE}^{dyn} + f_{TE}^{dyn} &= 0.5 \left[1 - \tanh \left\{ a_{TE} \left(\alpha - \tau_{TE,2} \dot{\alpha} - \alpha_{TE} \right) \right\} \right] \\ \tau_{LE,1} \dot{f}_{LE}^{dyn} + f_{LE}^{dyn} &= 0.5 \left[1 - \tanh \left\{ a_{LE} \left(\alpha - \tau_{LE,2} \dot{\alpha} - \alpha_{LE} \right) \right\} \right] \end{aligned} \quad (3.34)$$

Again the time constants ($\tau_{LE,1}$, $\tau_{LE,2}$, $\tau_{TE,1}$, and $\tau_{TE,2}$) must be determined from dynamic test data of the airfoil. Due to lack of experimental data, these are set to $\tau_{LE,1} = 1.5c/V$, $\tau_{LE,2} = 0.5c/V$, $\tau_{TE,1} = 0.52c/V$, and $\tau_{TE,2} = 4.5c/V$ from [45].

Under stalled flow conditions, the unsteady aerodynamic coefficients C_L^{dyn} , C_D^{dyn} , and $C_{M,ac}^{dyn}$ are determined from Eq. (3.12) but using dynamic TE separation and LEV breakdown locations, i.e. f_{TE}^{dyn} and f_{LE}^{dyn} , instead of quasi-steady ones given by Eq. (3.13).

3.6 Experiments and Validation

In this section, we first present validation for the low aspect ratio and flap deflection effects followed by the full ± 180 deg. angle of attack aerodynamic curves. The proposed aerodynamics model is then applied to the YAK54 platform and validated against experimental data obtained from wind-tunnel tests.

3.6.1 Validation of the Low Aspect Ratio Effect

Figure 3.10 shows the aerodynamic coefficients for rectangular flat plates of $AR = 0.167$, 2, and 4, without any flap deflection. The experimental values are taken from various sources in the literature, see Sec. 3.21, while the simulated coefficients are obtained using the

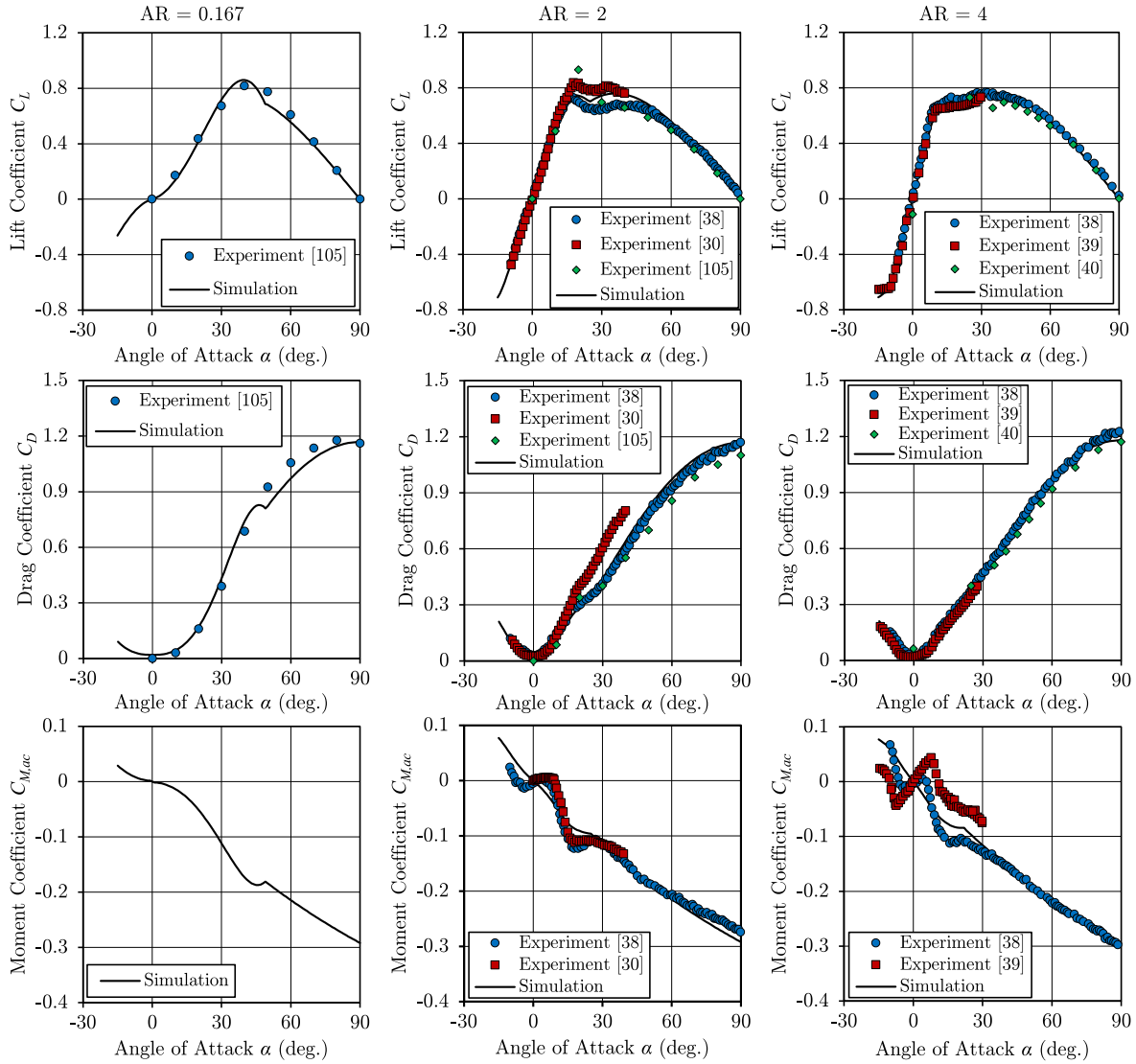


Figure 3.10: Simulated vs experimental aerodynamic coefficients for various AR.

aerodynamics model presented in this chapter. For the lowest AR (i.e. 0.167), experimental measurements for the pitching moment coefficient $C_{M,ac}$ were not available.

For all three aspect ratios, the correlation between the simulation results and experiments is very good indicating that the presented aerodynamics model is able to account for the effect of aspect ratio in both low-alpha and high-alpha regimes. The discrepancy in the moment coefficients at low angles of attack (i.e. in the low-alpha regime) is attributed to the nonlinear variation of the center of pressures of the potential and vortex lifts with angle of attack, which is not modeled in the present work. This is justified considering that the

discrepancy is small, and it further reduces to zero at higher angles of attack (i.e. in the high-alpha regime).

3.6.2 Validation of the Control Surface Deflection Effect

In order to validate the control surface deflection effect, experimental data from Hoerner et al. [25] is used. In that work, lift coefficient data is presented for a rectangular wing ($AR = 6$) with a Clark Y airfoil section and a 20% flap-to-chord ratio.

Since the aspect ratio is large and the leading-edge is not sharp, therefore Eq. (3.8) will be used to calculate the lift coefficient in the low-alpha regime. From [25], the lift curve slope $C_{L\alpha}$ is 4.15 per rad. while the zero-lift angle α_0 is -5.4 deg. Note that using Eq. (3.9) for an aspect ratio of 6, gives $C_{L\alpha} \approx 4.43$ per rad. which is very close to the experimental value. To account for the control surface deflection effect, the method outlined in Sec. 3.2.3 is used.

A comparison between the simulation and experimental results is shown in Fig. 3.11. An excellent match between the two demonstrates the validity of the presented aerodynamics model to account for the effect of flap deflection in the low-alpha regime. As stated earlier, there exists no experimental work in the literature that deals with the effect of flap deflection in the high-alpha regime. Therefore, this effect is validated later in Sec. 3.6.4, wherein wind-

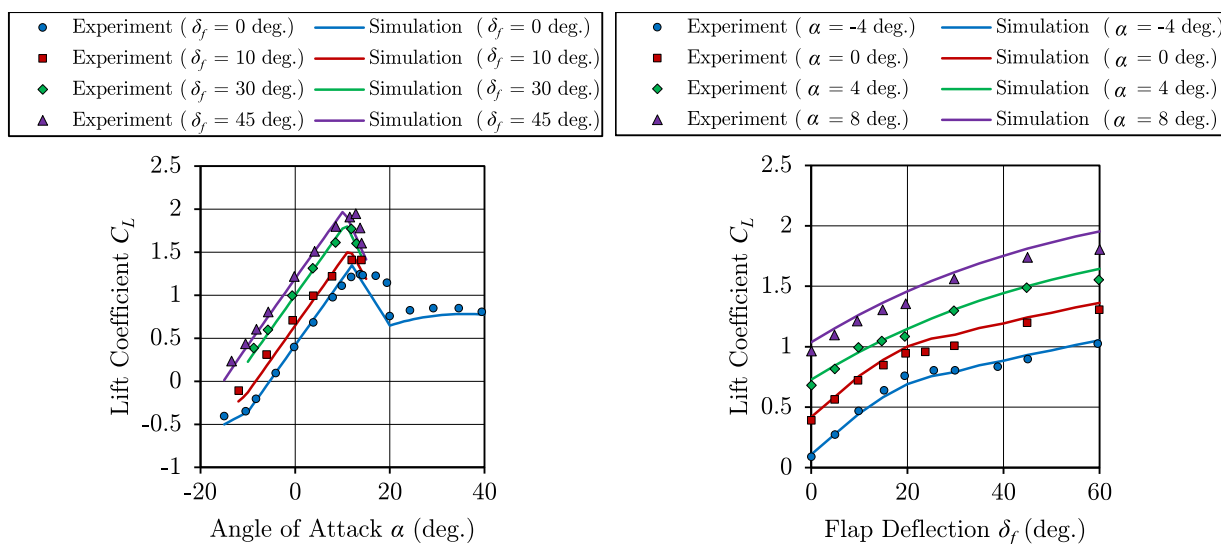


Figure 3.11: Simulated vs experimental lift coefficient for various flap deflections.

tunnel experiments are performed for the test platform wing at two high angles of attack (20 deg. and 50 deg.).

3.6.3 Full Range Aerodynamic Curves

It is worthwhile to plot the full range aerodynamic curves obtained using the presented aerodynamics model. This is done in Fig. 3.12 for a rectangular flat plate wing with $AR = 2$ and $c_f/c = 0.4$. The curves are plotted for deflections: $\delta_f = 0, \pm 25$, and ± 50 deg.

The curves show similar trends to the full range aerodynamic curves presented for a different wing in Refs. [16, 17]. It is interesting to note that for positive deflections, the drag coefficient is higher if α is positive (making the airfoil concave to flow with higher $C_{d,90}$), and lower if α is negative (making airfoil convex with lower $C_{d,90}$). A reverse trend is seen for negative deflections. Furthermore, the bounds of the moment coefficient (around ± 0.4) are consistent with the results of Refs. [16, 17].

Quasi-Steady Effect

Another plot of interest is Fig. 3.13 which shows the hysteresis in the aerodynamic coefficients due to the quasi-steady effect of $\dot{\alpha}$. The curves are simulated for a rectangular flat plate of $AR = 2$ and no flap deflection. As stated in Sec. 3.2.2, the quasi-steady time constants are set to $\tau_{LE} = 0.5c/V$ and $\tau_{TE} = 4.5c/V$, where c is taken as 0.3 m and V is set to 5 m/s which are typical values for small UAVs. For these, $\dot{\alpha}$ must remain within ± 100 deg/s to be considered as quasi-steady ($k_{\dot{\alpha}} \leq 0.05$). For higher $\dot{\alpha}$, time-dependent effects

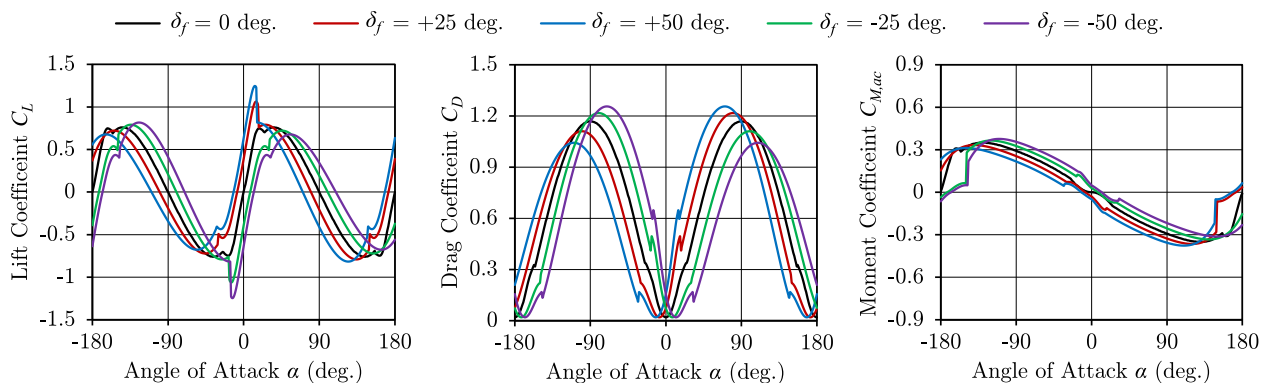


Figure 3.12: Full range aerodynamic curves for a rectangular flat plate.

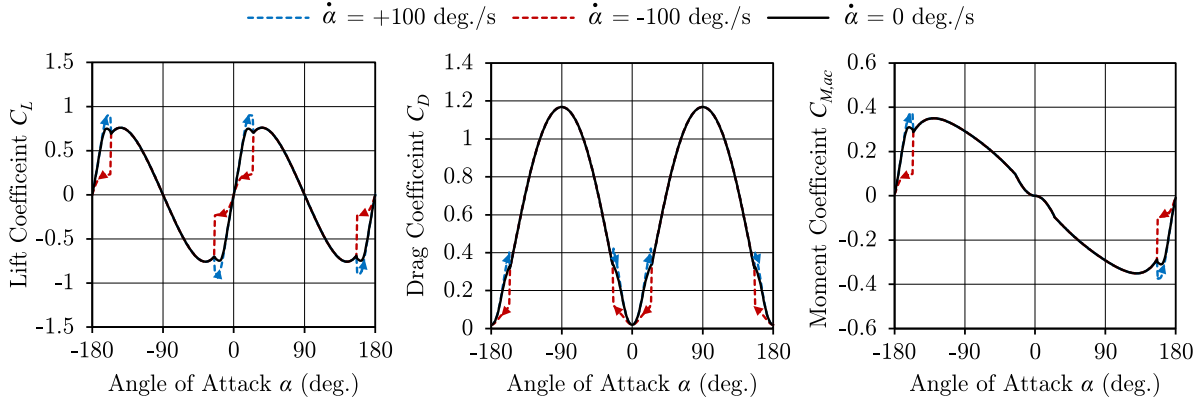


Figure 3.13: Simulated aerodynamic coefficients under quasi-steady conditions.

will become important. As expected, the aerodynamic coefficients are higher for increasing α (i.e. positive $\dot{\alpha}$), and lower for decreasing α (i.e. negative $\dot{\alpha}$).

3.6.4 Validation for the Test Platform

Experimental Setup and Test Procedure

For preliminary validation, it is deemed best to perform wind-tunnel experiments because the aerodynamic forces/moments can be reliably measured in a controlled environment. Although the intent was to mount the entire test platform in the wind-tunnel, only the starboard wing of the YAK54 platform could be tested because the available wind-tunnel had a small 2 ft. x 3 ft. test section. Nonetheless, a major part of the aerodynamics model (component breakdown approach, low and high-alpha aerodynamics, effects of LAR and control surface deflection) can be validated via testing of the wing alone. Other surfaces of the aircraft (horizontal and vertical tail, fuselage etc.) are aerodynamically similar to the wing (i.e. low AR flat plates with big control surfaces and deflections) and therefore the starboard wing validation is sufficient. The remaining aspects of the aerodynamics model (aerodynamic interference and unsteady effects) are covered later in Chap. 6 while validating the overall aircraft model.

The experimental setup is shown in Fig. 3.14. The starboard wing was fastened to an ATI Gamma force/torque (F/T) transducer which measures force and torque in the sensor frame (superscript S) with a high resolution (0.028 N in the x^S and y^S forces, 0.056 N in the z^S

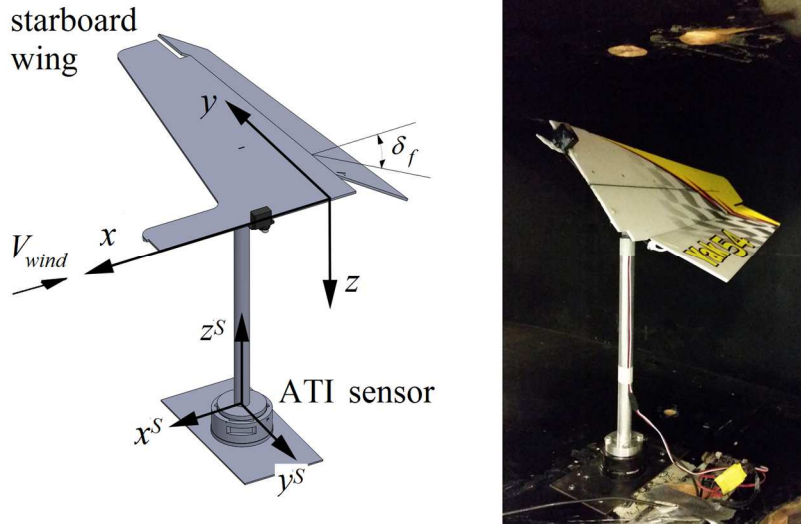


Figure 3.14: Experimental setup.

force, and 0.0014 N.m in torque) and sampling rate of 1 kHz. Wind speeds were measured in the test section using a Reed hotwire anemometer which has a sampling rate of 1 Hz, and a resolution of 0.01 m/s in the range 0.2 to 5 m/s, and 0.1 m/s in the range 5.1 to 25 m/s. An Arduino board was used to send PW signals to a Hitec HS-65HB servo to produce the desired control surface deflection.

Experiments are performed at two wind speeds: 4 m/s and 8 m/s, and angles of attack: 0, 20, 50 and 180 deg. At a given wind speed and angle of attack, the control surface (in this case the aileron) is deflected from -50 deg. to $+50$ deg. with 10 deg. steps. Only a few cases at 180 deg. could be tested since the YAK54 wing, made of depron foam, bent considerably at that angle of attack. Post-processing of the F/T data includes: 1) removing measurement noise via a third-order zero-phase Butterworth low-pass filter with a cut-off frequency of 10 Hz, 2) removing the setup drag from the measurements, and 3) transformation of forces and moments from the F/T sensor frame to the body frame (see Fig. 3.14).

Results and Discussion

For simulation, the aspect ratio of the YAK54 starboard wing is taken to be $AR \approx 1.93$. This is based on half of the wing span (starboard side only) and therefore the aspect ratio is half of that given for the entire wing in Sec. 3.2.1. This accounts for the 3D flow effects

TABLE 3.2
YAK54 STARBOARD WING SEGMENTS

Segment No.	Span (m) b	Chord (m) c	Flap chord (m) c_f	Position vector (m) $\mathbf{r} = [r_x, r_y, r_z]^T$
1	0.046	0.278	0	[0.083, 0.021, -0.007]
2	0.068	0.258	0.109	[0.080, 0.078, -0.007]
3	0.068	0.233	0.100	[0.078, 0.145, -0.007]
4	0.089	0.205	0.090	[0.073, 0.223, -0.007]
5	0.089	0.173	0.078	[0.068, 0.312, -0.007]
6	0.050	0.064	0	[0.065, 0.383, -0.007]
7	0.050	0.083	0.083	[0.028, 0.383, -0.007]

on the starboard wing root that exist under the current test condition. The wing is divided into 7 segments as shown in Fig. 3.2, such that the first three segments lie within the propeller slipstream. The slipstream radius at the wing location is determined using the slipstream model presented later in Chap. 5.

For each segment, its mean aerodynamic chord (m.a.c.) is located using standard techniques [33]. Chord c and flap chord c_f are measured on the m.a.c., and the aerodynamic center is located at quarter chord from its leading edge. The position of the aerodynamic center is measured from the aircraft c.g. in the body frame. Table 3.2 lists the parameters of the wing segments used in simulation.

The velocity for each segment is calculated using Eq. (3.1) with $\mathbf{V}_{cg}^B = \boldsymbol{\Omega}^B = [0, 0, 0]^T$, and also setting \mathbf{V}_S , \mathbf{V}_{QS} and \mathbf{V}_{ind} to zero. The wind velocity in the body frame is calculated from wind-tunnel speed V_{wind} and angle of attack α as: $\mathbf{V}_{wind} = [V_{wind} \cos\alpha, 0, V_{wind} \sin\alpha]^T$. Simulations are run for the experimental test conditions given in the previous section. The results are compared in Figs. 3.15 and 3.16.

- At Zero Angle of Attack

Figure 3.15 shows the simulation results compared with experimental data for the zero degree angle of attack case. The force in the y direction is omitted from the plots because it is zero in both experiments and simulation. The overall match between the simulation

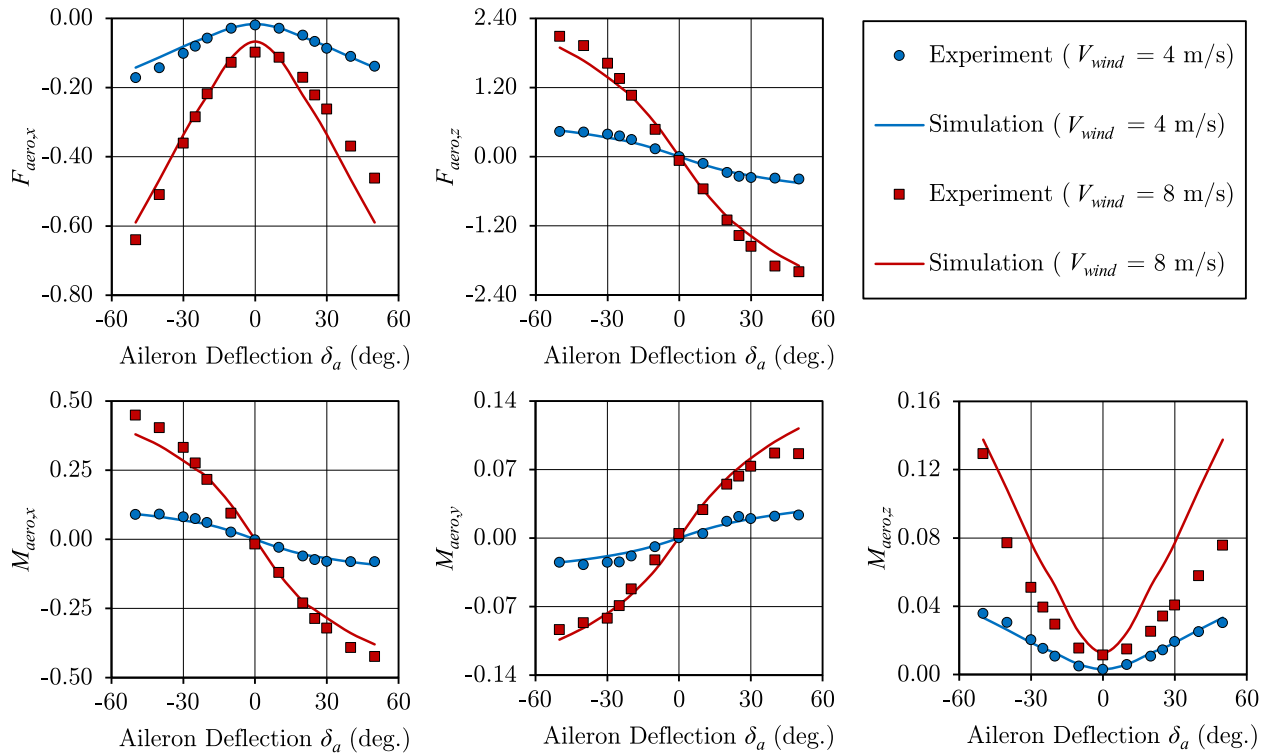


Figure 3.15: Simulated vs experimental aerodynamic forces/moments for $\alpha = 0$ deg.

and experiments is good, with rms errors of 0.036 N in $F_{aero,x}$, 0.10 N in $F_{aero,z}$, 0.024 N.m in $M_{aero,x}$, 0.007 N.m in $M_{aero,y}$, and 0.016 N.m in $M_{aero,z}$.

The drag force acts in the $-x$ direction. For zero aileron deflection, it is minimum and only due to skin friction. Both positive and negative deflections increase drag, but from experimental measurements, the drag increment for positive deflections is lower than that for corresponding negative deflections. This is due to the design-cut spanning the entire length of the underside of the aileron for its movement. On negative deflections, this cut does not allow the flow to remain attached to the deflected aileron; rather it causes flow separation at the wing-aileron junction, resulting in higher drag. The simulation does not include this effect and thus predicts the same drag increment for both positive and negative deflections.

The lift force acts in the $-z$ direction and is zero for no deflection which is expected of a flat plate wing. A positive aileron deflection introduces a positive camber and generates an

upward lift force, while a negative deflection results in a downward force. The roll and pitch moments ($M_{aero,x}$ and $M_{aero,y}$) are caused by the lift forces acting at the segment a.c. away from the aircraft c.g. For positive deflections, an upward lift force gives rise to a negative roll moment and a positive pitch moment. On the other hand, the drag forces on the segments cause a yaw moment $M_{aero,z}$ about the c.g. A positive drag force causes a positive yaw moment.

- At Other Angles of Attack

Figure 3.16 presents the variation of the aerodynamic forces and moments with control surface deflection for different angles of attack. For the completely reversed flow condition, i.e. 180 deg. angle of attack, not all deflections could be tested due to severe deformation of the foam wing. More so, the results are shown only for the wind speed of 4 m/s for clarity.

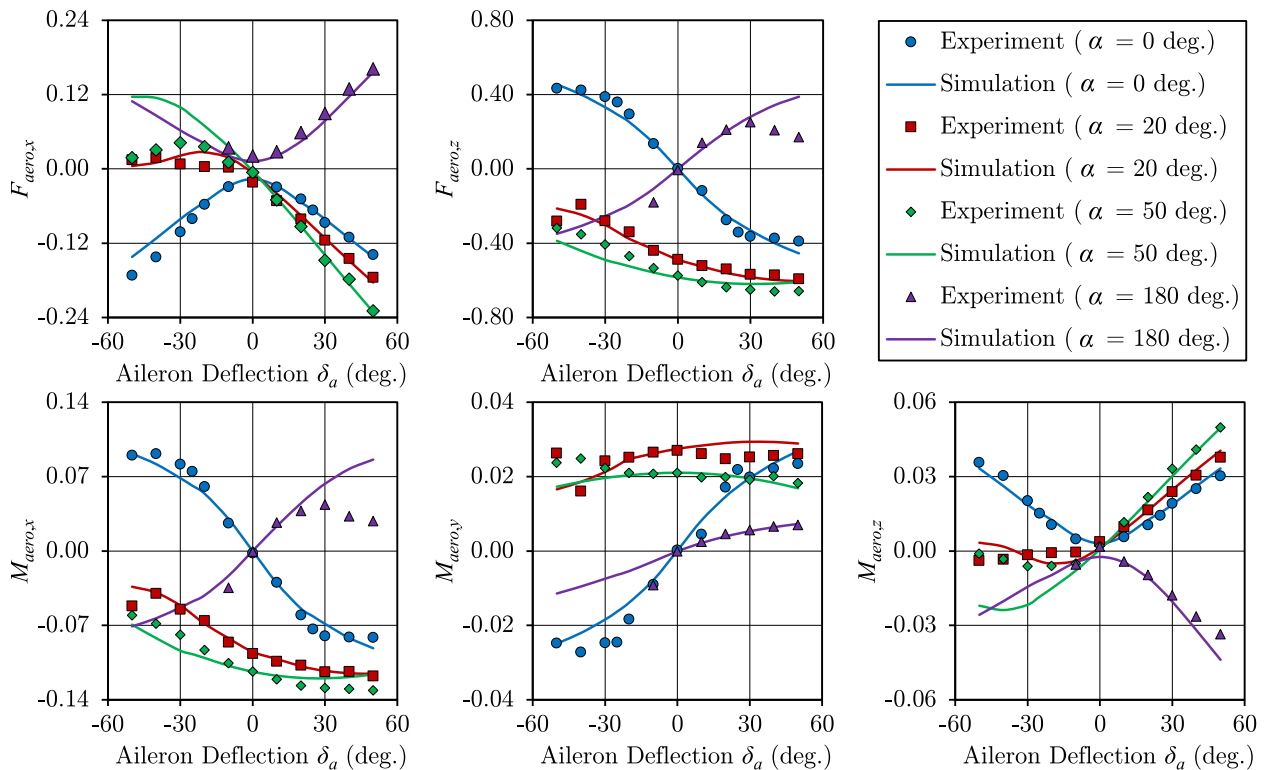


Figure 3.16: Simulated vs experimental aerodynamic forces and moments for various angles of attack.

At zero angle of attack, the change in the aerodynamic forces and moments for positive and negative deflections is more or less equal, i.e. symmetric variation with positive and negative deflections. However, at other angles of attack (e.g. 20 deg. and 50 deg.), the forces and moments vary asymmetrically for positive and negative deflections. Consider $\alpha = 20$ deg.: the drag increases to -0.17 N for $+50$ deg. deflection, while for -50 deg. deflection, it is 0.014 N. Similarly, from its zero-deflection value (-0.49 N), the lift force increases by 0.10 N for $+50$ deg. deflection, while reduces by 0.70 N for -50 deg. deflection. Since the roll, pitch and yaw moments are consequences of the lift and drag forces, these also exhibit asymmetric trends similar to those of the lift and drag forces.

The asymmetric variation of the aerodynamic forces and moments gives rise to the phenomena of adverse yaw, induced roll etc. Consider for example, an agile UAV with differentially-moving ailerons on the starboard and port sides of the wing. From Fig. 3.16, it is seen that at $\alpha = 0$ deg., for any aileron deflection, the complete wing will produce a zero net lift force and yaw moment, because the two sides (starboard and port) produce equal and opposite lift forces and yaw moments that cancel out. But at other angles of attack, any aileron deflection will also produce a net lift force and yaw moment, since the two sides produce opposite but unequal lift forces and yaw moments that do not cancel each other completely. The undesired yaw moment produced by the ailerons is a phenomenon encountered in real-world and is commonly referred to as adverse yaw.

It may also be noted from Fig. 3.16 that for $\alpha = 180$ deg., all the forces and moments are reversed compared to those for 0 deg. angle of attack: the drag force acts in the $+x$ direction, while a positive deflection produce a downward force. Also, the symmetric variation of the aerodynamic forces and moments is expected.

Overall, the simulation results show a good match with experimental data at all angles of attack. The average rms errors are 0.02 N in $F_{aero,x}$, 0.04 N in $F_{aero,z}$, 0.0086 N.m in $M_{aero,x}$, 0.0034 N.m in $M_{aero,y}$, and 0.0045 N.m in $M_{aero,z}$.

Chapter 4

Thruster Dynamics

An agile UAV is typically equipped with a propeller driven thruster to achieve high thrust-to-weight ratio, around 2 – 3, enabling it to perform thrust-borne maneuvers wherein most or all of the UAV weight is supported by the thruster rather than the lift of its wings. A common hover maneuver is an example of the limiting case, i.e. completely thrust-borne flight. Owing to the high thrust-to-weight ratio, the motion of the agile UAV is strongly dominated by its thruster dynamics. Furthermore, in unconventional flight like rapid maneuvering, aerobatics etc., the thruster of the agile UAV is subjected to varying flow conditions during flight namely:

- Static: The thruster is stationary, i.e. not moving forward such as during a hover maneuver.
- Axial Flow: The thruster experiences pure axial flow, i.e. flow aligned with its rotation axis, like that encountered during level flight or vertical takeoff.
- Oblique Flow: The thruster encounters oblique flow, i.e. flow at an angle to its rotation axis. Such a situation arises, for example, during aerobatics and even during random wind gusts.
- Reverse Flow: The thruster experiences reverse flow as a result of a maneuver or accident.

Under these various flow conditions, the thruster generates different aerodynamic thrust and torque and may even generate other secondary forces and moments which can significantly affect the UAV dynamics.

Most of the related literature on propeller driven UAVs uses simple steady-state models like $T = \rho n^2 D_p^4 C_T$ and $Q = \rho n^2 D_p^5 C_Q$ [7, 9, 19, 50–53] including works that also take into account

the effect of forward speed on the thrust and torque coefficients (C_T and C_Q) [33, 55]. Oblique flow condition is considered in very few works, e.g. [33], but limited to small angles to the thruster rotation axis, and therefore unsuitable for the current purpose. Furthermore, dynamic models for UAV thrusters are also rare in the literature and those that are available such as [56, 57], are meant for stationary conditions and rely on experimental testing.

This chapter presents a dynamics model for an agile UAV thruster that predicts all the aerodynamic forces and moments generated under the aforementioned general flight conditions. The goal is to use first principles of physics so that the model does not rely on experimental testing. A brief overview of the thruster hardware and operation is given in the next section, followed by model development. Validation is carried out for the test platform thruster in Sec. 4.7 against experimental data, while a comparison with existing models is also done in Sec. 4.7.4.

4.1 Thruster Model

A thruster unit for UAVs, typically consists of a brushless DC (BLDC) motor coupled with a propeller and driven by an electronic speed controller (ESC). The entire system is powered by a Lithium-Polymer (LiPo) battery. The speed of the motor-propeller is controlled via the ESC which varies the voltage applied to the motor in proportion to the user's commanded pulse width (PW) signal. The generic system is shown diagrammatically in Fig. 4.1 along with the inputs and outputs of the individual sub-models.

4.1.1 Operation

For a desired thrust output, a PW command (ranging from $1000 \mu\text{s}$ to $2000 \mu\text{s}$) is issued to the ESC which then provides a corresponding voltage to the BLDC motor. Since the thruster is run by a small LiPo battery whose power drains quickly, the actual voltage applied to the BLDC motor (called the armature voltage) drops over time even for a constant user command. This is taken into account by the battery model. On applying the armature voltage, the motor starts rotating the propeller which then generates aerodynamic forces

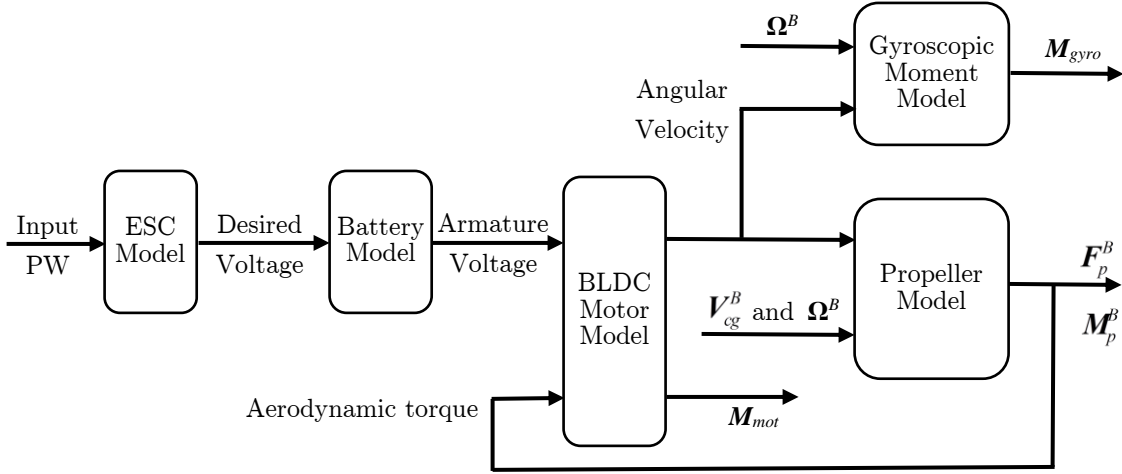


Figure 4.1: Schematic of the thruster model.

and moments that depend upon the external flow condition (UAV body velocity and body rates). The aerodynamic drag generated by the propeller acts as an external load to the BLDC motor. The gyroscopic moment model takes one additional input (UAV body rates) and outputs the gyroscopic moment.

4.1.2 Thruster Force and Moment

The complete thruster model requires three inputs: pulse width (PW) command, UAV velocity V_{cg}^B and body rate Ω^B . The output of the thruster model are the thruster force and moment which may be written as:

$$\begin{aligned} \mathbf{F}_{thr}^B &= \mathbf{F}_p^B \\ \mathbf{M}_{thr}^B &= \mathbf{M}_{mot} + \mathbf{M}_p^B + \mathbf{M}_{gyro} \end{aligned} \quad (4.1)$$

The thruster force is solely due to the propeller (expressed in the body frame) \mathbf{F}_p^B , whereas the thruster moment is due to the motor \mathbf{M}_{mot} , propeller \mathbf{M}_p^B and gyroscopic effects \mathbf{M}_{gyro} . The individual components are modeled next in light of their operation.

4.2 Battery Dynamics

Most small UAVs are electric powered and use LiPo/Lithium ion (Li-ion) batteries as their primary source of power due to their high energy density and long life. The operation of a LiPo battery is briefly discussed and then its mathematical model is presented.

4.2.1 Operation

A LiPo battery, when connected to a circuit having an electric load such as a motor, provides a potential difference across its terminals allowing a current to flow in the circuit. As the current flows, the amount of active material available in the electrodes of the battery reduces and the battery is said to be discharging. Owing to this discharge phenomenon, the available potential at the battery terminals also decreases with time. The rate of discharge depends primarily on the amount of current being drawn and the temperature of the battery.

4.2.2 Mathematical Model

Several mathematical models of LiPo and Li-ion batteries are available in the literature. For example, Gao et al. [113] derived mathematical equations for a Li-ion battery and identified its parameters by curve fitting data from the manufacturer. A more complete mathematical model is presented in [114] which also takes into account temperature dependent effect and battery capacity fading effect. However, these models are quite complex and the identification of their parameters needs either manufacturer's data or extensive experimental testing. A much simpler battery model is implemented in the present work based on the work of Pounds et al. [56]. The battery dynamics are modeled as a high-pass filter for which the transfer function is of the form:

$$B(s) = \frac{s + z_{batt}}{s + p_{batt}} \quad (4.2)$$

with a zero z_{batt} and pole p_{batt} . Equation (4.2) represents a linear battery model and any nonlinearity in the system is neglected for simplicity. This implies that variation in voltage drop due to varying discharge rates, temperature effects, capacity fading effects [114] and other effects [113] are not taken into consideration. The battery model has two parameters namely z_{batt} and p_{batt} , while its input is the desired voltage \mathbb{V}_{des} and its output is the armature voltage \mathbb{V}_{arm} .

4.3 Brushless DC Motor Dynamics

The most common type of motor employed for small UAVs is a brushless DC (BLDC) motor, which has several advantages over its brushed counterpart including no/little maintenance, lower noise, higher efficiency and smoother operation.

4.3.1 Operation

A BLDC motor, in general, consists of two components: a moving part called the rotor containing permanent magnets, and a stationary part called the stator or armature consisting of coils wound around a core. As opposed to conventional DC motors, a BLDC motor armature consists of three-phase winding, and while the armature itself remains stationary, the phase of the current is rotated within the coils. This phase rotation is done by the ESC.

When a potential difference V_{arm} is applied, a current i_{arm} flows in the coils and causes a torque τ_{arm} on the rotor according to the electromagnetic theory of DC motors. This torque creates an angular acceleration $\dot{\omega}$ of the rotor. As the rotor starts rotating, the coils start developing an additional potential called the back EMF whose magnitude is directly proportional to the rotor rotational speed and which opposes the applied potential. As the rotor speeds up, the difference between the applied potential and back EMF decreases to zero. Since the net potential goes to zero, no more current flows in the armature, and thereby the torque and acceleration also become zero. At this point the rotor achieves steady state and rotates at a constant angular velocity ω . In reality, a small current flows in the armature providing torque to overcome friction and the external aerodynamic drag from the propeller.

4.3.2 Mathematical Model

Many models for a BLDC motor can be found in the literature. An application report from Texas Instruments [115] contains a fairly simple motor model and provides a corresponding transfer function. Al-Mashakbeh [116] and Ali et al. [117] present more detailed BLDC motor models in their works and design PID controllers to maintain a desired rotational

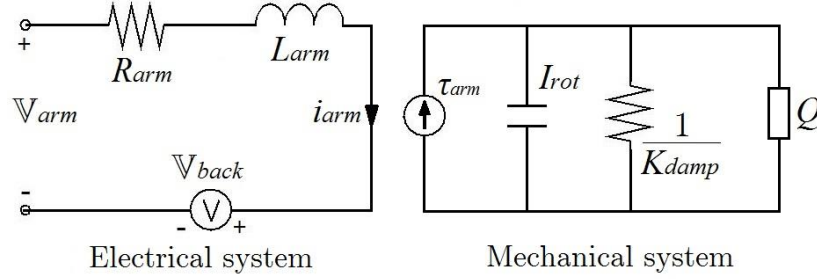


Figure 4.2: Electrical and mechanical system of a BLDC motor.

speed. Likewise, a simple BLDC motor model can easily be assembled considering the electrical and mechanical system of the motor. By applying Kirchhoff's current law to the motor electrical system and Newton's second law to the motor mechanical system, two equations can be derived that constitute the BLDC motor model.

First, consider the electrical circuit of a BLDC motor shown in Fig. 4.2. The voltage \mathbb{V}_{arm} is applied to the motor armature that has a resistance R_{arm} and inductance L_{arm} . The back EMF produced by the rotation of the rotor is represented by \mathbb{V}_{back} . The net voltage ($\mathbb{V}_{arm} - \mathbb{V}_{back}$) causes a current i_{arm} to flow in the circuit. Applying Kirchhoff's law we get: $\mathbb{V}_{arm} - \mathbb{V}_{R,arm} - \mathbb{V}_{L,arm} - \mathbb{V}_{back} = 0$, where $\mathbb{V}_{R,arm} = i_{arm}R_{arm}$ is the voltage drop across the resistance, $\mathbb{V}_{L,arm} = L_{arm}di_{arm}/dt$ is the voltage drop across the inductance, and $\mathbb{V}_{back} = K_{vel}\omega$ is the back EMF that is proportional to the rotational speed of the motor. The constant K_{vel} , referred to as the velocity constant, indicates how much voltage is generated per rad/s of the motor and is usually provided by the manufacturer. Putting all these into Kirchhoff's equation, taking the Laplace transform and solving for the armature current gives:

$$i_{arm} = \frac{\mathbb{V}_{arm} - K_{vel}\omega}{L_{arm}s + R_{arm}} \quad (4.3)$$

Now consider the mechanical system of Fig. 4.2 where the current given by Eq. (4.3) flows in the armature to produce an electromagnetic driving torque τ_{arm} . This torque has to overcome the rotational inertia of the moving parts, the magnetic damping and friction between the rotor and stator, and the external torque (load) on the motor. Applying Newton's equation gives: $\tau_{arm} - \tau_{damp} - Q = I_{rot}\dot{\omega}$, where $\tau_{arm} = K_{tor}i_{arm}$ is the electromagnetic

torque produced by the current, and K_{tor} is the torque constant of the motor representing the torque produced per unit ampere of current flowing in the coils, $\tau_{damp} = K_{damp}\omega$ is the torque required to overcome magnetic damping, and K_{damp} is the damping constant representing the torque required to overcome the damping at 1 rad/s, Q is the external torque on the motor exerted by the propeller, and I_{rot} is the rotational moment of inertia of all rotating parts such as the rotor, propeller etc. The propeller inertia is assumed to be distributed uniformly across the propeller disc to avoid calculating complex gyroscopic moments. Putting all these in the moment equation, taking the Laplace transform and solving for the rotational velocity gives:

$$\omega = \frac{K_{tor}i_{arm} - Q}{I_{rot}s + K_{damp}} \quad (4.4)$$

The two equations, (4.3) and (4.4) constitute the BLDC motor model with two states (i_{arm} and ω). A more detailed model may be developed by considering all the three-phases of the motor separately, see e.g. [57], but at the expense of adding two more state variables to the simulation. The presented model is found to be sufficiently accurate and therefore is used in the current work. It has the following parameters: armature resistance R_{arm} and inductance L_{arm} , velocity constant K_{vel} , torque constant K_{tor} , damping constant K_{damp} and rotational inertia I_{rot} of the rotating parts. Inputs to the model are the applied voltage \mathbb{V}_{arm} and the aerodynamic torque Q , while its outputs are the angular velocity ω and the reaction torque $\mathbf{M}_{mot} = -(I_{rot}\dot{\omega} + \tau_{damp})\mathbf{i}$, it exerts on the airframe.

4.4 ESC Model

The main function of an ESC is to run the motor at the user's desired speed. The user issues a PW command to the ESC which is then translated into a voltage applied to the motor armature. Besides this core function, the ESC is also required to limit the surge current when the motor starts from rest. This is because when starting from rest, there is no back EMF to counter the applied armature voltage, and hence a large current flows in the coils.

This initial current is termed as the surge current, which if not limited could burn the motor winding. The ESC has a built-in electronic mechanism that turns on at the start to limit the surge current, and as the motor gains rotational speed, an appreciable back EMF is developed and the mechanism shuts off. Typically, this is achieved within fraction of a second.

Another function present in modern-day ESCs (that may be turned on or off) is the braking mechanism that allows the motor to quickly slow-down when the power is shut-off. If the braking function is turned on, the ESC stops applying armature voltage as soon as the power is shut off. This causes a negative current to flow in the coils (due to the back EMF of the spinning motor) and exert a braking torque on the rotor, thereby slowing down the motor quickly. In contrast, if the braking function is turned off, the ESC will gradually reduce the armature voltage to zero and does not allow a large negative current to flow. In this case, the motor slows down gradually.

Being an electrical/electronic system, the ESC has its own dynamics which may be characterized. However the dynamics of the ESC are fast, and therefore neglected in the present work. More so, the two effects of the ESC discussed above are important only at motor start-up and shut-down, and therefore are also neglected for simplicity. In the current work, the ESC is modeled as a mapping function from the commanded PW input to the desired voltage, which is determined later in Sec. 4.7.1.

4.5 Propeller Aerodynamics

A thruster unit generates thrust due to the aerodynamics of the propeller. Among the several methods that exist in literature for analyzing propellers in their normal working state, blade element momentum theory (BEMT) is a relatively simple but accurate one. Most texts, such as [33], provide expressions to evaluate the thrust and torque, but because of the underlying assumptions such as small inflow angle etc., and the fact that these expressions do not consider oblique flow, these are not used here. Rather, in this work, BEMT has been

applied to a UAV propeller while taking oblique flow into consideration and making fewer simplifying assumptions.

4.5.1 Propeller Frame

A propeller undergoing general motion with an agile UAV will experience a relative flow \mathbf{V}_p which is determined from the aircraft body velocity \mathbf{V}_{cg}^B and body rate $\boldsymbol{\Omega}^B$ as:

$$\mathbf{V}_p = \mathbf{V}_{cg}^B + \boldsymbol{\Omega}^B \times \mathbf{r}_p \quad (4.5)$$

where $\mathbf{r}_p = [r_{p,x}, r_{p,y}, r_{p,z}]^T$ is the position vector of the propeller disc center from the aircraft c.g. measured in the body frame, see Fig. 4.3 (a). The velocity \mathbf{V}_p may be decomposed into an axial component $V_{p,A} = V_{p,x}$ along the propeller rotation axis and an in-plane component $V_{p,IP} = \sqrt{V_{p,y}^2 + V_{p,z}^2}$ in the propeller plane. The angle between \mathbf{V}_p and the propeller rotation axis is called the propeller tilt angle φ_p and may be written as:

$$\varphi_p = \text{atan}(V_{p,IP}/V_{p,A}) \quad (4.6)$$

It is well established from research on helicopter rotors that in forward flight, a rotor behaves as a circular wing with a longitudinal axis joining the disc leading-point (LP; point of disc first contact with the in-plane velocity) to the disc trailing-point (TP; point of last contact). In lieu of this, it is better to analyze the propeller disc in the propeller frame

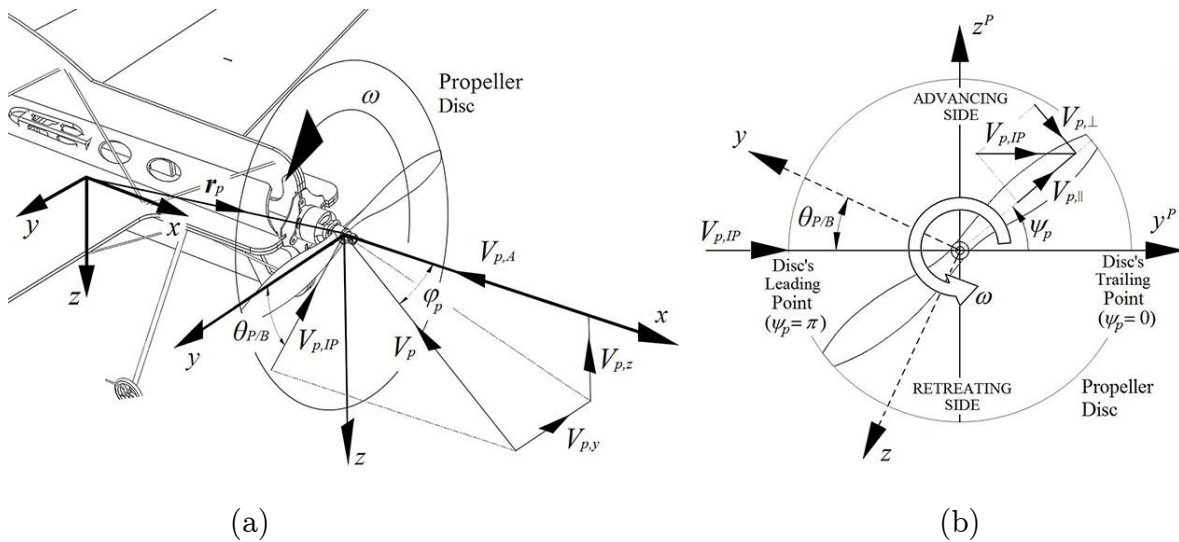


Figure 4.3: (a) A propeller in general forward flight, and (b) propeller frame.

(superscript P): a frame with its origin at the center of the propeller disc, x^P axis aligned with the propeller rotation axis, and y^P axis aligned with the in-plane velocity, as shown in Fig. 4.3 (b). The y^P axis then becomes the longitudinal axis of the propeller disc.

The angular position of the propeller blade is defined by the blade azimuth angle ψ_p , measured from the y^P axis such that the disc LP is represented by $\psi_p = \pi$ while the disc TP lies at $\psi_p = 0$. As the propeller blade rotates from the disc TP to its LP ($\psi_p = 0 \rightarrow \pi$), the blade is said to be “advancing” as it is moving against the in-plane velocity. On its way back from the disc LP to the TP, the blade is said to be “retreating” as it is now moving away from the in-plane velocity.

4.5.2 In-Plane Velocity Components

At any given blade azimuth angle, the in-plane velocity can be resolved along and perpendicular to the propeller blade according to:

$$\begin{aligned} V_{p,\parallel} &= V_{p,IP} \cos \psi_p \\ V_{p,\perp} &= V_{p,IP} \sin \psi_p \end{aligned} \tag{4.7}$$

The parallel in-plane velocity component leads only to skin friction drag along the blade length and is neglected in the present work. The perpendicular in-plane velocity component either supports ($V_{p,\perp} = +ve$) or opposes ($V_{p,\perp} = -ve$) the rotational velocity of the blade depending on whether it is advancing ($\psi_p = 0 \rightarrow \pi$) or retreating ($\psi_p = \pi \rightarrow 2\pi$).

4.5.3 Blade Element Theory

A differential element dr of the propeller blade at a radial distance r from the propeller rotation axis will experience relative flow due to 1) translation: $V_{p,A}$ along the axial direction and $V_{p,\perp}$ in the propeller plane, 2) rotation: ωr in the propeller plane, and 3) the pressure jump across the propeller: V_{ia} in the axial direction (see Fig. 4.4). The velocity induced by a rotating propeller is called the induced velocity, which in general has axial, radial and tangential components. For simplicity, only the axial induced velocity V_{ia} is considered in the present work as it is the most significant among the three [43].

The differential lift, drag and moment, i.e. dL , dD , and dM , acting on the blade element depend on the resultant relative velocity V_R which may be given as,

$$V_R = \sqrt{(V_{p,A} + V_{ia})^2 + (\omega r + V_{p,\perp})^2} \quad (4.8)$$

Moreover from Fig. 4.4, the inflow angle ϕ_{inflow} between the resultant velocity and the propeller plane is,

$$\phi_{inflow} = \text{atan} \left(\frac{V_{p,A} + V_{ia}}{\omega r + V_{p,\perp}} \right) \quad (4.9)$$

The blade section experiences the resultant flow at an effective angle of attack $\alpha' = \theta_p - \alpha_0 - \phi_{inflow}$, where the zero-lift angle α_0 is negative for a positive airfoil camber. The differential lift, drag and moment acting on the blade element are therefore,

$$\begin{aligned} dL &= \frac{1}{2} \rho V_R^2 C_l dA = \frac{1}{2} \rho V_R^2 C_l c dr \\ dD &= \frac{1}{2} \rho V_R^2 C_d dA = \frac{1}{2} \rho V_R^2 C_d c dr \\ dM &= \frac{1}{2} \rho V_R^2 C_{m,ac} c dA = \frac{1}{2} \rho V_R^2 C_{m,ac} c^2 dr \end{aligned} \quad (4.10)$$

where the 2D aerodynamic coefficients (C_l , C_d , and $C_{m,ac}$) are evaluated at the effective angle of attack in the next section. The differential lift and drag are resolved into the instantaneous differential thrust dT_{inst} along the propeller rotation axis, and the instantaneous differential hub force dHB_{inst} in the propeller plane, see Fig. 4.4. The

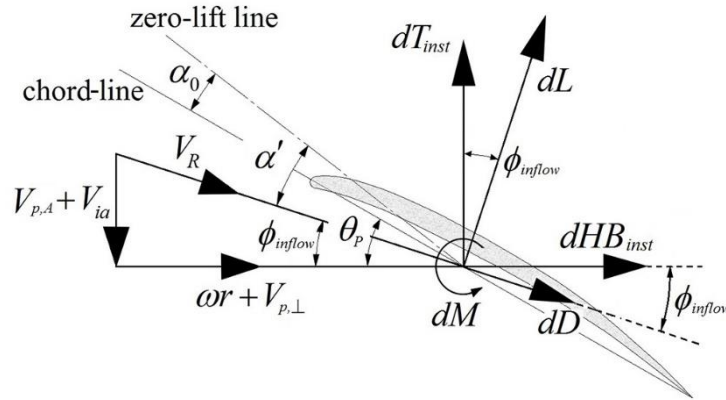


Figure 4.4: Resultant flow to a propeller blade section.

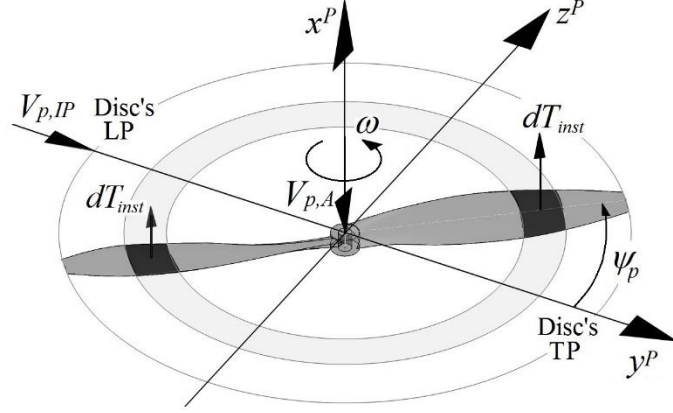


Figure 4.5: Instantaneous thrust of propeller blades.

differential thrust may be written from $dT_{inst} = dL \cos \phi_{inflow} - dD \sin \phi_{inflow}$, and using the definitions of dL and dD from Eq. (4.10) as,

$$dT_{inst} = \frac{1}{2} \rho c V_R^2 (C_l \cos \phi_{inflow} - C_d \sin \phi_{inflow}) dr \quad (4.11)$$

It is noted that the differential thrust given by Eq. (4.11) is an implicit function of the blade azimuth angle. This is because as the blade rotates, i.e. ψ_p changes, it experiences a different $V_{p,\perp}$ according to Eq. (4.7). Thus the blade induces a different axial velocity V_{ia} , which affects V_R as per Eq. (4.8), ϕ_{inflow} as per Eq. (4.9), and differential aerodynamic quantities as per Eq. (4.10), leading to an overall change in the differential thrust. More so, at a given instant, each blade of the propeller will generate a different thrust based on its own azimuth angle as shown in Fig. 4.5.

To determine the blade thrust over a complete revolution, the differential thrust given by Eq. (4.11) is averaged from $\psi_p = 0$ to 2π , i.e. $dT_{avg} = 1/(2\pi) \int_0^{2\pi} dT_{inst} d\psi_p$. Though each blade may generate a different instantaneous thrust, they will all generate the same average thrust. Thus for N propeller blades, the differential thrust is given as,

$$dT = \frac{N}{4\pi} \rho c \int_{\psi_p=0}^{2\pi} V_R^2 (C_l \cos \phi_{inflow} - C_d \sin \phi_{inflow}) d\psi_p dr \quad (4.12)$$

Equation (4.12) represents the differential thrust over an annulus obtained from blade element theory, and primarily consists of two unknowns namely the differential thrust dT

and the induced velocity V_{ia} (included in the V_R , C_l , C_d , and ϕ_{inflow} terms). The induced velocity variation with the blade azimuth angle ψ_p must be prescribed before the integral in Eq. (4.12) can be evaluated.

4.5.4 2D Aerodynamic Coefficients

In the blade element analysis, it is customary to take the aerodynamic coefficients in the linear range only. In the present work however, the aerodynamic coefficients must also be evaluated post-stall because on the retreating side ($\psi_p = \pi \rightarrow 2\pi$), the perpendicular in-plane velocity $V_{p,\perp}$ becomes negative as per Eq. (4.7), reducing the denominator in Eq. (4.9), thus resulting in a large inflow angle and consequently a large effective angle of attack. Hence some retreating blade sections may experience an effective angle of attack greater than their stall angle. A detailed discussion and expressions to evaluate aerodynamic coefficients in the low-alpha and high-alpha regimes are presented in Chap. 3. The relevant expressions are reproduced below:

In the low-alpha regime, i.e. $\alpha_{stall,N} \leq \alpha' < \alpha_{stall,P}$, the coefficients are:

$$\begin{aligned} C_l &= C_{l\alpha} \alpha' \\ C_d &= C_{d,0} \\ C_{m,ac} &= -\pi z_{\max} \end{aligned} \quad (4.13)$$

where $\alpha_{stall,P}$ and $\alpha_{stall,N}$ are the positive and negative stall angles of the airfoil. The moment coefficient is obtained from [33] for a circular arc airfoil with maximum camber ratio z_{\max} .

In the high-alpha regime, i.e. $\alpha' \geq \alpha_{high,S}$, the coefficients are:

$$\begin{aligned} C_n &= C_{d,90} \sin \alpha' / (0.56 + 0.44 \sin \alpha') \\ C_a &= 0.5 C_{d,0} \cos \alpha' \\ C_l &= C_n \cos \alpha' - C_a \sin \alpha' \\ C_d &= C_n \sin \alpha' + C_a \cos \alpha' \\ C_{m,ac} &= -C_n [0.25 - 0.175(1 - 2\alpha'/\pi)] \end{aligned} \quad (4.14)$$

where C_n and C_a are the normal and axial force coefficients acting normal and along the airfoil. The 2D drag coefficient $C_{d,90}$ of a flat plate normal to flow is typically 1.98, and $\alpha_{high,S}$

is the start angle for the high-alpha regime (presently set to 20 deg. for typical thin airfoils of the blade sections). For a given propeller with known C_{la} , $C_{d,0}$, $\alpha_{stall,P}$, and $\alpha_{stall,N}$, the above equations may be intelligently used to cover the full ± 180 deg. angle of attack range of the propeller blade sections, refer to Sec. 3.6.3.

4.5.5 Momentum Theory

In most aerodynamic texts, e.g. McCormick [33], the differential thrust is expressed using momentum theory over an annulus. Using a similar methodology, differential thrust may first be expressed over a segment of the annulus (see Fig. 4.6) as: $dT' = (V_{out} - V_{p,A})d\dot{m}_a$. The velocities far upstream $V_{p,A}$ and far downstream V_{out} are in the axial direction and are related to the axial velocity at the disc by: $V_{disc} = (V_{out} + V_{p,A})/2$, using one-dimensional momentum theory for an incompressible, inviscid and uniform flow [33]. On the other hand, the mass flow rate $d\dot{m}_a$ through the differential segment depends on the total velocity $V_{tot} = \sqrt{(V_{p,A} + V_{ia})^2 + V_{p,IP}^2}$ at the propeller disc, i.e. $d\dot{m}_a = \rho V_{tot} dA = \rho V_{tot} r dr d\psi_p$. Utilizing these definitions and the fact that $V_{disc} = V_{p,A} + V_{ia}$, and integrating from $\psi_p = 0$ to 2π , the differential thrust of an annulus becomes,

$$dT = 2\rho r \int_{\psi_p=0}^{2\pi} V_{ia} \sqrt{(V_{p,A} + V_{ia})^2 + V_{p,IP}^2} d\psi_p dr \quad (4.15)$$

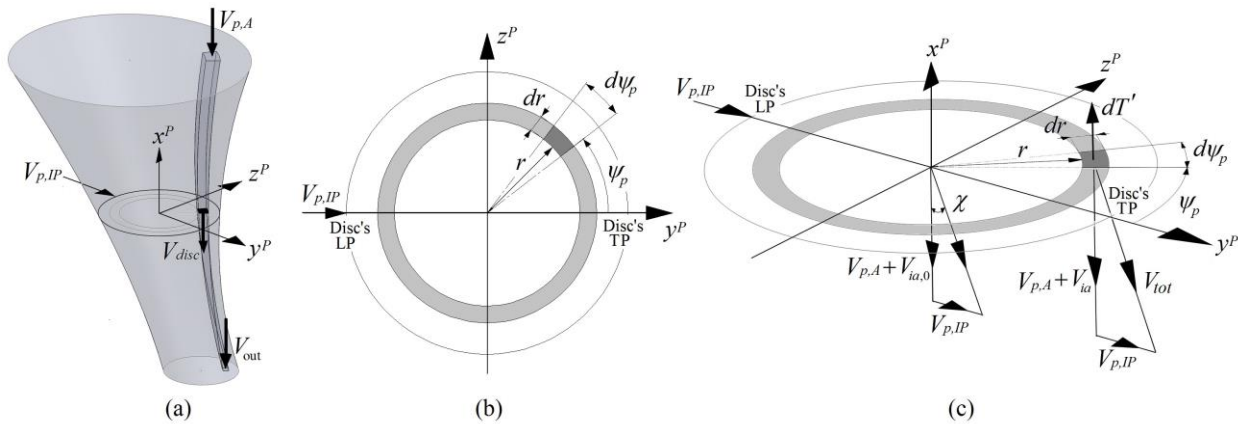


Figure 4.6: (a) Propeller slipstream, (b) differential segment, and (c) mass flow rate.

The above equation gives the differential thrust for an annulus using momentum theory. Equation (4.15) contains two unknowns namely the differential thrust of the annulus dT and the induced velocity V_{ia} , thereby allowing its simultaneous solution with Eq. (4.12). However, as pointed out earlier, V_{ia} is not constant but varies with ψ_p and this variation must be specified for the evaluation of the integrals in Eqs. (4.12) and (4.15) prior to their simultaneous solution.

Finally, it must be realized that when expressing thrust for annuli rather than for the entire disc, it is inherently assumed that these annuli are mutually independent, i.e. the flow from one annulus does not interfere with that from its neighboring annuli. This assumption is largely satisfied for axial flow, but it is satisfied for oblique flow only if the in-plane velocity does not exceed the total axial velocity ($V_{p,A} + V_{ia}$). This condition ensures that the resultant flow is sufficient enough to carry the flow axially far downstream before its sideways interference becomes strong. As an example, in static conditions, i.e. $V_{p,A} = 0$, a typical UAV propeller (10 inch diameter) at around 5000 RPM induces $V_{ia} \approx 8$ m/s. Then Eq. (4.15) will hold for pure side flow (i.e. $\varphi_p = 90$ deg.) until $V_{p,IP} = V_{p,A} + V_{ia} = 8$ m/s. This is therefore a limitation of the propeller model, but one which should be satisfied in most circumstances.

4.5.6 Inflow Model

Variation of the induced velocity V_{ia} with the blade azimuth angle ψ_p can be evaluated using the inflow models developed for helicopter rotors which will be briefly described here. The first and simplest inflow model was proposed by Glauert [73] as a cosine function of the blade azimuth angle: $V_{ia} = V_{ia,0}[1 + K_{ind}(r/R_p)\cos\psi_p]$; where $V_{ia,0}$ denotes the induced velocity at the center, see Fig. 4.6 (c), R_p is the propeller radius, and K_{ind} represents the slope of the induced velocity along the longitudinal axis. This constant is taken to be slightly greater than unity (typically 1.2) such that it gives an upwash at the disc LP ($\psi_p = \pi$) and a downwash at the disc TP ($\psi_p = 0$).

Subsequent works to improve the inflow model were aimed at finding a theoretical value for K_{ind} which was largely left unspecified by Glauert. Using vortex theory, its value was found by Coleman et al. [74] to be $\tan(\chi/2)$, defined in terms of the wake skew angle χ measured between the wake centerline and the propeller rotation axis, see Fig. 4.6 (c). Several other forms for K_{ind} exist in the literature, but in the current work, the value proposed by Pitt and Peters [75]: $K_{ind} = (15\pi/32)\tan(\chi/2)$ will be used as it has been validated against wind tunnel experiments, demonstrating a better match in comparison to other inflow models [76]. Thus the inflow model is written as,

$$V_{ia} = V_{ia,0} \left(1 + \frac{15\pi}{32} \tan\left(\frac{\chi}{2}\right) \frac{r}{R_p} \cos\psi_p \right) \quad (4.16)$$

where $\chi = \text{atan}[V_{p,IP}/(V_{p,A} + V_{ia,0})]$. The wake skew angle is zero for static and axial flow, which gives $K_{ind} = 0$ leading back to uniform induced velocity, i.e. $V_{ia} = V_{ia,0}$. In oblique flow, the wake is skewed, i.e. $\chi > 0$ because of the presence of the in-plane velocity.

4.5.7 Induced Velocity Distribution

Equation (4.16) supplements Eqs. (4.12) and (4.15) so that the two unknowns are the differential thrust dT and the induced velocity at the propeller disc center $V_{ia,0}$. Simultaneous solution of Eqs. (4.12) and (4.15) is carried out to give the induced velocity distribution for an annulus. The process is repeated for all annuli thereby yielding the complete induced velocity distribution $V_{ia}(r, \psi_p)$ at the propeller disc.

4.5.8 Propeller Forces and Moments

Once the induced velocity distribution at the propeller disc is known, the aerodynamic forces and moments can be evaluated using the blade element theory, see Fig. 4.7. First the differential hub force may be derived from its instantaneous value: $dHB_{inst} = dL\sin\phi_{inflow} + dD\cos\phi_{inflow}$ (see Fig. 4.4), by following the procedure outlined in Sec. 4.5.3. This gives a final form for dHB similar to Eq. (4.12):

$$dHB = \frac{N}{4\pi} \rho c \int_{\psi_p=0}^{2\pi} V_R^2 (C_l \sin \phi_{inflow} + C_d \cos \phi_{inflow}) d\psi_p dr \quad (4.17)$$

All other differential forces and moments shown in Fig. 4.7 may be written as,

$$\begin{aligned} dQ &= -dHB r \\ dF_{y^p} &= dHB \sin \psi_p \\ dF_{z^p} &= -dHB \cos \psi_p \\ dM_{y^p} &= dT r \sin \psi_p + dM \cos \psi_p \\ dM_{z^p} &= -dT r \cos \psi_p + dM \sin \psi_p \end{aligned} \quad (4.18)$$

Using Eqs. (4.12) and (4.17), and integrating from hub radius R_h to propeller radius R_p :

$$\begin{aligned} T &= \frac{N}{4\pi} \rho c \sum_{r=R_h}^{R_p} \sum_{\psi_p=0}^{2\pi} V_R^2 (C_l \cos \phi_{inflow} - C_d \sin \phi_{inflow}) \Delta\psi_p \Delta r \\ Q &= -\frac{N}{4\pi} \rho c \sum_{r=R_h}^{R_p} \sum_{\psi_p=0}^{2\pi} V_R^2 (C_l \sin \phi_{inflow} + C_d \cos \phi_{inflow}) \Delta\psi_p r \Delta r \\ F_{y^p} &= \frac{N}{4\pi} \rho c \sum_{r=R_h}^{R_p} \sum_{\psi_p=0}^{2\pi} V_R^2 (C_l \sin \phi_{inflow} + C_d \cos \phi_{inflow}) \sin \psi_p \Delta\psi_p \Delta r \\ F_{z^p} &= -\frac{N}{4\pi} \rho c \sum_{r=R_h}^{R_p} \sum_{\psi_p=0}^{2\pi} V_R^2 (C_l \sin \phi_{inflow} + C_d \cos \phi_{inflow}) \cos \psi_p \Delta\psi_p \Delta r \\ M_{y^p} &= \frac{N}{4\pi} \rho c \sum_{r=R_h}^{R_p} \sum_{\psi_p=0}^{2\pi} V_R^2 [(C_l \cos \phi_{inflow} - C_d \sin \phi_{inflow}) r \sin \psi_p + C_{m.ac} c \cos \psi_p] \Delta\psi_p \Delta r \\ M_{z^p} &= -\frac{N}{4\pi} \rho c \sum_{r=R_h}^{R_p} \sum_{\psi_p=0}^{2\pi} V_R^2 [(C_l \cos \phi_{inflow} - C_d \sin \phi_{inflow}) r \cos \psi_p - C_{m.ac} c \sin \psi_p] \Delta\psi_p \Delta r \end{aligned} \quad (4.19)$$

The above set of equations is comprehensive and is used with the known induced velocity distribution to yield all aerodynamic forces and moments generated by a propeller in general

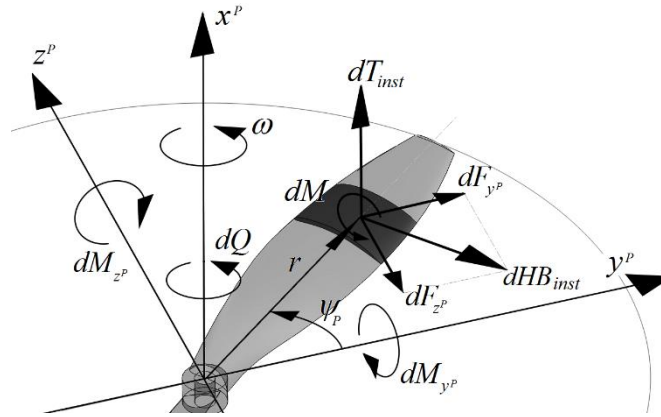


Figure 4.7: Propeller forces and moments.

flow conditions. It may be noted that in static and axial flow conditions, the induced velocity V_{ia} and consequently V_R , ϕ_{inflow} , C_l , C_d and $C_{m,ac}$ are no longer functions of the blade azimuth angle, which leads to $F_{y^p} = F_{z^p} = M_{y^p} = M_{z^p} = 0$.

4.5.9 Propeller Forces and Moments in the Body Frame

Equation (4.19) is a set of aerodynamic forces and moments in the propeller frame described in Sec. 4.5.1. These forces and moments are transformed to the body frame as:

$$\begin{aligned}\mathbf{F}_p^B &= \mathfrak{R}_p^B \left[T, F_{y^p}, F_{z^p} \right]^T \\ \mathbf{M}_p^B &= \mathfrak{R}_p^B \left[Q, M_{y^p}, M_{z^p} \right]^T + \mathbf{r}_p \times \mathbf{F}_p^B\end{aligned}\tag{4.20}$$

The rotation matrix \mathfrak{R}_p^B from the propeller frame to the UAV body frame represents a right-handed rotation of $(\pi - \theta_{P/B})$ about the x axis, see Fig. 4.3.

$$\mathfrak{R}_p^B = \begin{bmatrix} 1 & 0 & 0 \\ 0 & \cos(\pi - \theta_{P/B}) & \sin(\pi - \theta_{P/B}) \\ 0 & -\sin(\pi - \theta_{P/B}) & \cos(\pi - \theta_{P/B}) \end{bmatrix}\tag{4.21}$$

where $\theta_{P/B} = \text{atan}(V_{p,z}/V_{p,y})$. For the propeller moment in Eq. (4.20), the first term accounts for the rotation between the frames while the second term arises since the origin of the propeller frame is at a distance \mathbf{r}_p from the UAV frame. The secondary aerodynamic forces in the y and z direction are called the side force S_F and normal force P_N , while the secondary aerodynamic moments about the y and z axes are called the pitching moment M_P and yaw moment or P-factor N_P . The propeller forces and moments in Eq. (4.20) may be non-dimensionalized into coefficients: $\mathbf{CF}_p = \mathbf{F}_p^B / (\rho n^2 D_p^4)$ and $\mathbf{CM}_p = \mathbf{M}_p^B / (\rho n^2 D_p^5)$, which are functions of the advance ratio $J = V/nD_p$ and propeller tilt angle φ_p .

4.5.10 Working States of the Propeller

The mathematical treatment of the propeller so far is based on its normal working state which assumes either forward flight or stationary condition (like hover) of the UAV. For rearward flight of the agile UAV (e.g. a tail-slide maneuver), the propeller may operate in

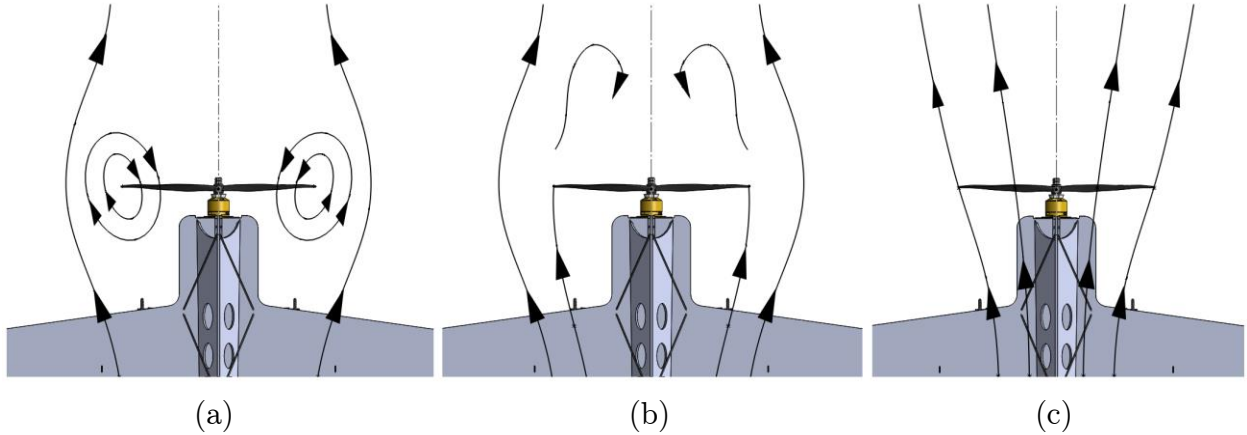


Figure 4.8: (a) Vortex-ring, (b) turbulent-wake, and (c) windmill-brake states.

other states namely the vortex-ring, turbulent-wake and windmill-brake states. These states have been studied in-depth for helicopter rotors for which mathematical treatments may be found in the literature, for e.g. [28].

Normal Working State ($V_{p,A} \geq 0$)

As the name suggests, the propeller normally operates in this state, which is characterized by forward flight or stationary condition of the UAV. In this state, a conventional slipstream is formed around the propeller (see Fig. 4.6) and thus momentum theory holds. Even with the velocities $V_{p,y}$ and $V_{p,z}$, whose effect is only to skew the flow, the slipstream remains well-defined and momentum theory is applicable.

Vortex-Ring, Turbulent-Wake, and Windmill-Brake States ($V_{p,A} < 0$)

Once the UAV is in rearward flight, the reverse flow into the propeller will prevent a slipstream from forming. In fact, if the rearward speed is moderate, the reverse air flow will cause the air induced by the propeller to recirculate into the propeller, as shown in Fig. 4.8 (a). This state in which there exists a toroid-shaped circulatory vortex ring around the propeller disc periphery, is called the vortex-ring state (VRS). The thrust in this state decreases from its static value and fluctuates due to the unsteadiness in the flow. In the absence of a well-defined slipstream, change in velocity and mass flow are not easily defined and thus momentum theory no longer holds.

As the rearward velocity increases, the vortex-ring expands to cover more of the propeller disc and at some point, the vortex-ring collapses creating a turbulent wake on the forward side of the propeller disc, see Fig. 4.8 (b). This is called the turbulent-wake state in which the propeller disc behaves as a circular plate normal to flow (bluff body), and the aerodynamic thrust comes mostly from the drag of this circular plate.

As the rearward velocity increases further, a well-defined slipstream develops again, but now, after passing through the propeller disc the slipstream widens. This state is referred to as the windmill-brake state, shown in Fig. 4.8 (c), and is named so because the flow slows down (brakes) on passing through the propeller disc. However, the slipstream is well-defined and thus momentum theory is applicable again.

During controlled maneuvers of an agile UAV, the rearward speed is never very high for stability reasons. As such, the turbulent-wake and windmill-brake states are unlikely to be encountered, and the propeller may at most operate in the vortex-ring state. Since the momentum theory equation (4.15) does not hold in the VRS, the propeller model presented in the previous sections is not applicable. Although, some models in the literature have been developed to predict the induced velocity distribution in the VRS (e.g. [63]), these lack simplicity and/or are semi-empirical, and therefore those are not used.

In this work, it is proposed that the propeller forces and moments in the vortex-ring state may be determined from the normal working state as follows: from the experimental results of Ref. [61], it is assumed that the drop and fluctuations in thrust (from static value) associated with the VRS are small and may be neglected. Hence, the thrust and torque coefficient ($CF_{p,x}$ and $CM_{p,x}$) in the VRS remain nearly constant at their static ($J = 0$) value. Furthermore, from the experimental results of Theys et al. [64], it is assumed that in VRS, the secondary propeller force and moment coefficients ($CF_{p,y}$, $CF_{p,z}$, $CM_{p,y}$, and $CM_{p,z}$) have the same value as in forward flight.

4.6 Gyroscopic Moments

While spinning about its own axis, the thruster will likely undergo rapid changes in its orientation along with the agile UAV, thus giving rise to the gyroscopic moment: $\mathbf{M}_{gyro} = \mathbf{\Omega}_{thr} \times \mathbf{I}_{thr}\boldsymbol{\omega}_{thr}$. Here $\mathbf{\Omega}_{thr}$ is the rate of change of orientation of the spinning thruster, while the second term represents the angular momentum of the thruster which is the product of its inertia tensor \mathbf{I}_{thr} and spin velocity $\boldsymbol{\omega}_{thr}$. For a typical agile UAV configuration: 1) the thruster is firmly attached to the UAV and therefore $\mathbf{\Omega}_{thr} = \mathbf{\Omega}^B$; 2) the body axes are the principal axes of the thruster, giving $\mathbf{I}_{thr} = \text{diag}(I_{rot}, I_{y,thr}, I_{z,thr})$; and 3) the thruster spins only in the x direction, giving $\boldsymbol{\omega}_{thr} = [\omega, 0, 0]^T$. Substituting all these and solving for the gyroscopic moment gives:

$$\mathbf{M}_{gyro} = I_{rot}\boldsymbol{\omega}[0 \quad r \quad -q]^T \quad (4.22)$$

No new parameter is required to calculate the gyroscopic moment. The rotational inertia I_{rot} is the same as that defined in Sec. 4.3.2, while the rotational speed ω comes from the motor model (Sec. 4.3).

4.7 Experiments and Validation

In this section, the validity of the proposed model is demonstrated against experimental data for the test platform thruster described in Chap. 2. The hardware includes a *RimFire 400 Outrunner* BLDC motor coupled to an *Electrifly PowerFlow* 10x4.5 propeller, powered by a *FlightPower EON-X Lite* LiPo battery and controlled via an *Electrifly Silver Series 25A* brushless ESC unit. Each sub-model has a set of parameters that must be identified for the test hardware prior to validation.

4.7.1 Determination of System Parameters

Battery Parameters

The two parameters of the battery model, z_{batt} and p_{batt} are determined from a simple battery discharge experiment in which the battery is used as a power source to run the RimFire motor while logging the armature voltage. The motor was run at low, moderate and high

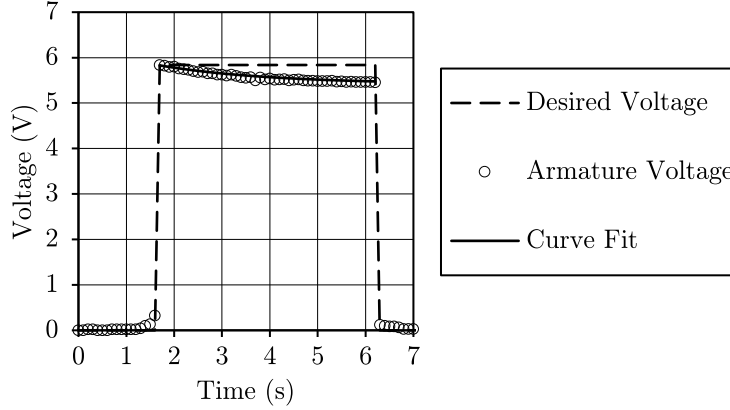


Figure 4.9: Armature voltage drop for moderate discharge rate.

rotational speeds to give different discharge rates of the battery. Armature voltage was observed to drop such that the drop was negligible, moderate and high for the low, moderate and high rotational speeds respectively.

To evaluate the parameters of the battery model, the moderate discharge rate is referenced, following the approach by Gao et al. [113], as shown in Fig. 4.9. The armature voltage is seen to drop to 92.8% of its original value in around 5 s at the moderate discharge rate, which represents the ratio z_{batt}/p_{batt} . The parameter $z_{batt} = 0.4$ is found iteratively such that the simulated drop matches the experimental drop, leading to $p_{batt} = 0.431$. While this process may be repeated for different discharge rates to identify z_{batt} and p_{batt} as functions of variable discharge rates, it is not deemed necessary in this work. This is because a UAV thruster typically operates near moderate speeds for which the above determined set of parameters is sufficient.

BLDC Motor Parameters

The following parameters of the Rimfire motor must be determined: armature resistance and inductance, velocity, torque, and damping constants, and rotational inertia.

Since a BLDC motor does not have carbon brushes or a commutator, its armature resistance R_{arm} is simply the resistance measured at its terminals. Moreover, BLDC motors are three-phase motors for which the measured line-to-line resistance between any two terminals, needs to be transformed into phase resistance using the relationship $R_{phase} = R_{l-l}/2$. For the

Rimfire 400, the line-to-line resistance is measured with an Ohmmeter to be 0.1 Ohms and therefore the armature resistance $R_{arm} = 0.05$ Ohms.

The armature inductance L_{arm} is difficult to measure directly. While an inductance (LCR) meter could be used, measured inductance can be significantly lower than the actual value for three-phase synchronous motors due to mutual magnetic coupling between its phases [118]. Therefore, alternative approaches for measuring inductance were investigated. One approach involves applying a low AC voltage to the motor and measuring its impedance and reactance and with these, the inductance can be calculated. Another approach, which is much simpler, makes use of the relation $L_{arm} = \tau_e R_{arm}$ to calculate inductance. Here, τ_e is the electrical time constant of the motor defined as the time taken for the armature current to reach 63.2% of its steady state value. The Rimfire motor was run at a moderate speed with a current sensor logging armature current. From the logged current data, τ_e was found to be 0.02 s from which L_{arm} was calculated to be 1×10^{-3} H.

The velocity constant, based on its definition, can be expressed mathematically as: $K_{vel} = \mathbb{V}_{back}/\omega$. To find this parameter, the motor was mounted on a drill press and rotated at known speeds while measuring the generated back EMF at steady state as shown in Fig. 4.10. The measured back EMF is the line-to-line voltage and is first converted to phase voltage according to the relation: $\mathbb{V}_{phase} = \mathbb{V}_{l-l}/\sqrt{3}$, and then plotted against the angular velocity, as shown in Fig. 4.10. A linear curve fit of the data gives $K_{vel} = 4.19 \times 10^{-3}$ V.s/rad,

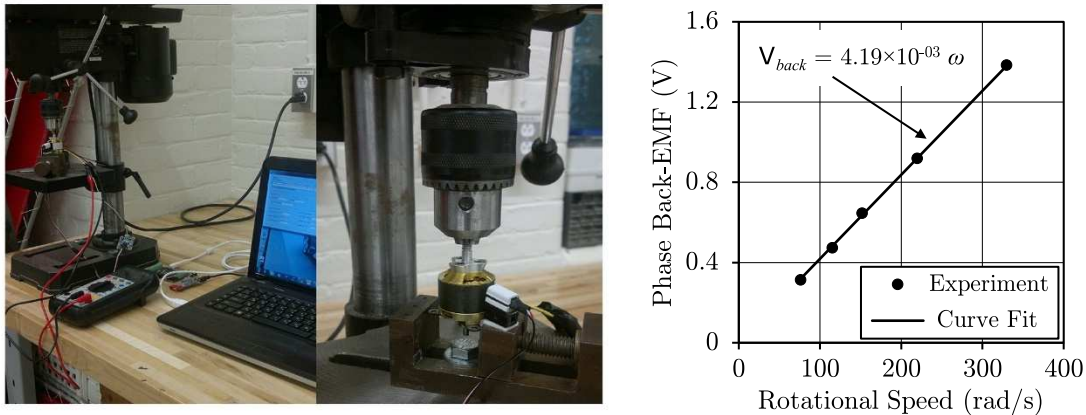


Figure 4.10: Back EMF vs rotational speed.

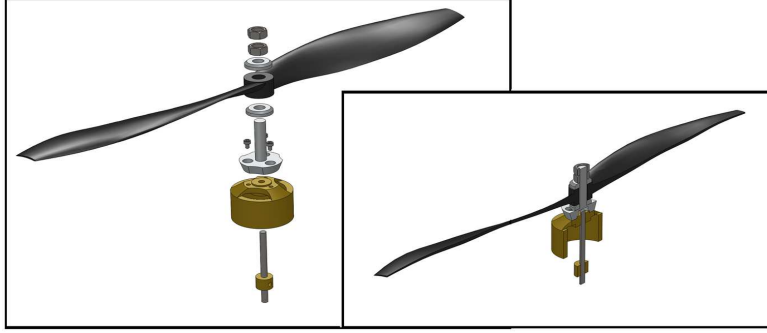


Figure 4.11: CAD model of the thruster.

which is a little lower than that specified by the manufacturer (5.81×10^{-3} V.s/rad). This is not surprising considering that the manufacturer's value is determined theoretically based on the motor design, while the actual value will always be lower due to losses.

Under ideal conditions when there are no frictional or heat losses, the energy conservation on a BLDC motor requires that the mechanical power output must be equal to the electrical power input. This implies that the torque constant is equal to the velocity constant if measured in metric units [115], leading to $K_{tor} = 4.19 \times 10^{-3}$ N.m/A. The damping coefficient K_{damp} is nominally due to viscous bearing friction and has a much smaller effect than other terms in the motor model, and therefore it is presently set to zero.

The rotational inertia I_{rot} of the thruster is the polar moment of inertia of all components that rotate when the motor is running. To determine I_{rot} accurately, all rotating parts of the test platform thruster were modeled in SolidWorks, shown in Fig. 4.11, and from the CAD model, the rotational inertia was evaluated to be 5.71×10^{-5} kg.m².

ESC Parameter

The ESC is modeled as a mapping function from pulse width to desired voltage, see Sec. 4.4. This mapping function is determined by measuring the ESC output voltage for several PW commands. The data is then curve fit with a third order polynomial to give the desired mapping function:

$$\mathbb{V}_{des} = 4.99 \times 10^{-9} PW^3 - 2.66 \times 10^{-5} PW^2 + 4.93 \times 10^{-2} PW - 27.33 \quad (4.23)$$

where PW is the commanded pulse width in μ s and \mathbb{V}_{des} is in volts.

Propeller Parameters

The chord, chordline-pitch angle, zero-lift angle of attack, 2D lift-curve slope, 2D drag coefficient and stall angles can all be measured as functions of the radial position by slicing up the propeller into a number of segments. The Electrify propeller was sliced along the blade at locations $r = [5, 20, 40, 60, 80, 100, 127]$ mm from the rotation axis to give seven cross-sections as shown in Fig. 4.12.

The chord c , maximum thickness ratio t_{max} , maximum thickness location $x_{t,max}$, maximum camber ratio z_{max} and maximum camber location $x_{z,max}$ were measured directly for each of the cross-sections. To calculate the chordline pitch angle θ_p , the vertical leading-edge and trailing-edge distances were measured for each section from a fixed reference as shown in Fig. 4.12. With known chord, θ_p was found for each section using $\theta_p = \text{asin}[(d_{LE} - d_{TE})/c]$. The zero-lift angle of attack can be calculated using $\alpha_0 = -2z_{max}$, an expression derived from the lift coefficient equation of a thin airfoil with circular arc camber line [33].

For simplicity, an average value of the aerodynamic parameters (C_{la} , $C_{d,0}$, $\alpha_{low,E}$) are used. This is done by first finding the mean thickness ratio and a mean camber ratio of all sections, which come out to be 6% and 5.58% respectively. An Eppler-58 airfoil ($t_{max} = 5.6\%$ and $z_{max} = 6.5\%$) is found to be the closest match for which the 2D lift curve slope and 2D drag coefficient are 6.28 and 0.02 respectively. Also the positive and negative stall angles are 12 and -10 deg. respectively.



Figure 4.12: Segmented Electrify 10x4.5 propeller.

TABLE 4.1
ELECTRIFLY 10X4.5 PROPELLER PARAMETERS

Seg. No.	Radial position r (mm)	Chord c (mm)	Chordline pitch angle θ_p (deg.)	Zero-lift angle of attack α_0 (deg.)	2D lift curve slope $C_{l\alpha}$ (per rad)	2D drag coefficient $C_{d,0}$	Stall angle $\alpha_{stall,P}$ (deg.) $\alpha_{stall,N}$ (deg.)	
1	5	12.37	25.00	0				
2	20	16.23	26.50	0				
3	40	22.85	21.89	-9.66				
4	60	28.21	14.39	-8.70	6.28	0.02	12	-10
5	80	28.90	9.80	-7.40				
6	100	26.31	4.75	-10.70				
7	127	13.06	6.59	-8.40				

It must be noted that the aerodynamic parameters vary from the propeller root to tip due to the Reynolds number which, depending on the total velocity, varies from a few hundred (100 to 500) near the root to a few hundred thousand (around 100,000) near the tip. However, airfoil data covering such Reynolds number range is scarce in the literature, and therefore for simplicity, we assume a moderate Reynolds number of 60,000 prevalent throughout the blade length resulting in the constant aerodynamic parameters noted above. Advanced computational techniques like CFD, XFOIL [23] etc., may be employed to yield better airfoil data, but a simple aerodynamics model was preferred in the current work. Table 4.1 lists all the propeller parameters as functions of radial position determined for the test platform propeller.

4.7.2 Experimental Setup and Procedure

A schematic of the experimental setup is shown in Fig. 4.13. The test thruster was mounted on a stand firmly fastened to an ATI Gamma force/torque (F/T) transducer which measures force and torque in the sensor frame (superscript S) with a high resolution (0.028 N in x^S and y^S forces, 0.056 N in the z^S force, and 0.0014 N.m in torque) and sampling rate of 1 kHz. The rotational speed of the motor-propeller combination was measured using the optical RPM sensor from Eagle Tree systems. Battery voltage and current data was also logged. An Arduino board was programmed to send PW signals to the ESC, while data logging was started simultaneously to avoid time-synchronization issues.

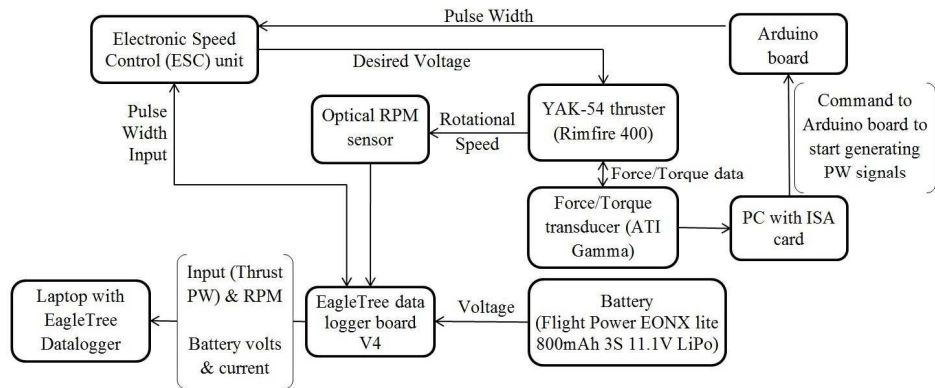


Figure 4.13: Schematic of the experimental setup.

The PW signals were varied from $1050 \mu\text{s}$ to $2000 \mu\text{s}$ in steps of $50 \mu\text{s}$. Each PW was held constant for 10 s in order to achieve steady state. The F/T data from the ATI sensor had noise owing to the thruster stand vibration and sensor noise. Fourier transforms were used to identify a desirable cut-off frequency. A third-order zero-phase Butterworth low-pass filter with a cut-off frequency of 50 Hz, was applied to remove measurement noise.

The thruster force and moment coefficients are calculated using:

$$\begin{aligned} CF_{thr} &= F_{thr}^B / (\rho n^2 D_p^4) \\ CM_{thr} &= M_{thr}^B / (\rho n^2 D_p^5) \end{aligned} \quad (4.24)$$

Under static and axial flow conditions, only thrust coefficient $C_T = T / (\rho n^2 D_p^4)$ and torque coefficient $C_Q = Q / (\rho n^2 D_p^5)$ are defined since the secondary forces and moments are zero.

4.7.3 Steady-State Validation

Steady-state validation of the thruster model is done by comparing the simulated steady-state aerodynamic forces and moments against experimental results. Different flow conditions namely static, axial flow and oblique flow, are treated separately.

Static Condition

The model is run for the test platform thruster under static conditions, i.e. $V = 0$. The simulation results are compared with experimental data in Fig. 4.14. The steady-state thrust and its coefficient are plotted on the left, whereas the steady-state torque and its coefficient

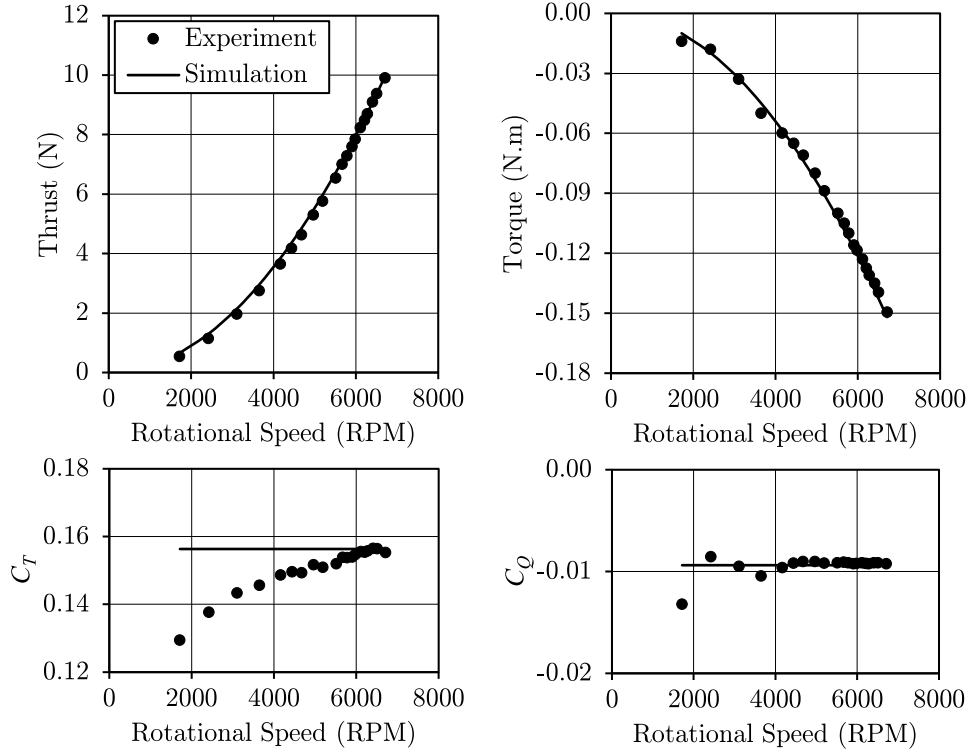


Figure 4.14: Steady-state thrust and torque for Electrify 10x4.5 under static condition.

are plotted on the right. As expected the steady-state thrust and torque are proportional to the square of the rotational speed. This relationship is in fact the basis of the widely used steady-state thruster models discussed at the start of this chapter. An excellent match is seen between the experiments and simulation, thereby validating the thruster model for static conditions. The rms error in thrust and torque are 0.14 N (1.4% of maximum) and 0.003 N.m (1.8% of maximum) respectively.

It may be noted from the bottom plots of Fig. 4.14 that the simulation predicts constant thrust and torque coefficients whereas the experimental data shows an increase in thrust coefficient and decrease in torque coefficient with rotational speed. These variations in the experimental data are attributed to the Reynolds number effect on the aerodynamic coefficients, as also noted by Deters et al. [59], which is not accounted for in the present work. This is acceptable since the discrepancies in thrust and torque coefficients do not correspond to large discrepancies in the actual thrust and torque values, as seen from the upper plots of Fig. 4.14.

Axial Flow Condition

Wind-tunnel experiments for the test platform thruster were not performed to validate axial flow condition results. Instead, validation is carried out against experimental data from the UIUC propeller database [54] which hosts performance data for a large number of propellers pertaining to small UAVs. The *APC 10x4.7 SF* propeller is chosen from that database since it closely resembles the propeller on the test platform. The geometric parameters for the APC propeller can be found in [54] and more comprehensively in [119]. According to the test conditions provided for the APC propeller [54], simulations are run for four rotational speeds: 4014 RPM, 5018 RPM, 6021 RPM, and 6512 RPM. At each rotational speed, the axial velocity is varied to give an advance ratio J ranging from 0 to 1. The results are presented in Fig. 4.15.

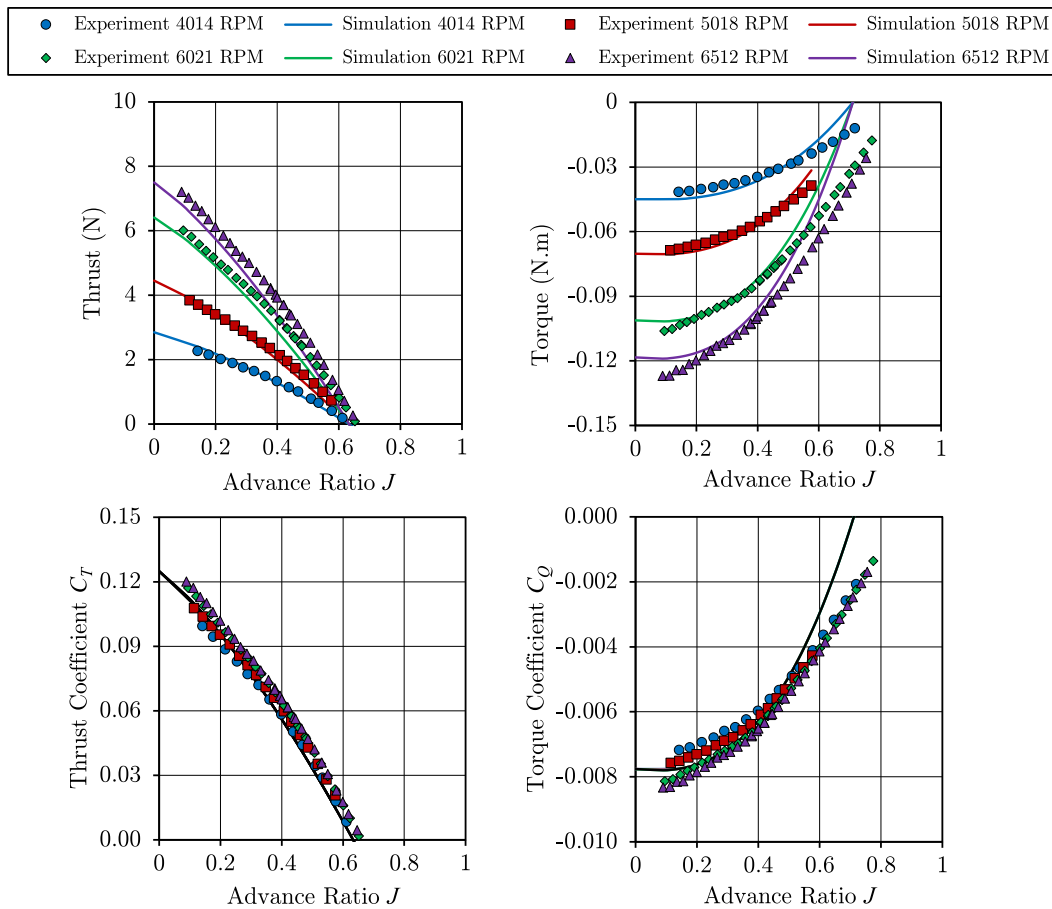


Figure 4.15: Steady-state thrust and torque for APC 10x4.7 SF under axial flow condition.

The effect of forward speed on the thrust and torque is evident from the figure. The thrust drops with advance ratio, becoming zero at around $J = 0.63$, and experimental data supports this. At higher RPMs however, there exists a slight offset between simulated and experimental thrust which will probably disappear if the static condition ($J = 0$) thrust were predicted more accurately. For the torque, the simulation results show a reasonable match with experiments up to an advance ratio of around 0.6, after which the simulation displays a relatively steeper drop until the torque reduces to zero at around $J = 0.7$. By contrast, the experimental torque remains non-zero until $J \approx 0.78$. Improvements like inclusion of the Reynolds number effect, more accurate stall model etc. may result in a better match over a wider range of advance ratio. However it must be noted that a UAV propeller typically operates around $J = 0.4$ and hence the currently employed aerodynamics model is sufficient for the prediction of thrust and torque under typical axial flow conditions.

Variation of the thrust and torque coefficients with advance ratio can be seen in the bottom plots of Fig. 4.15. As opposed to experiments, the simulation predicts that the thrust and torque coefficients collapse onto a single curve. This is expected since the simulation gives constant coefficients with RPM as pointed out earlier in the static results discussion.

Oblique Flow Condition

Again, no wind-tunnel experiments were performed for the test platform thruster and validation of the thruster model in oblique flow condition is carried out using experimental data from the literature. The UIUC database [54] referred in the previous section, lacks experimental data for propellers in oblique flow condition, and therefore another work, by Theys et al. [64] is used in this section for validation. Experimental measurements for the six axis force/torque are provided in [64] for the *Graupner E-Prop 9x5* at various propeller tilt angles and two different wind speeds.

The geometric and aerodynamic parameters for the Graupner propeller are not provided in [64] and therefore these were measured following the procedure outlined in Sec. 4.7.1. More

so, experimental measurements in [64] have been made at fixed motor input voltage which may not correspond to fixed rotational speeds depending on the external flow conditions of

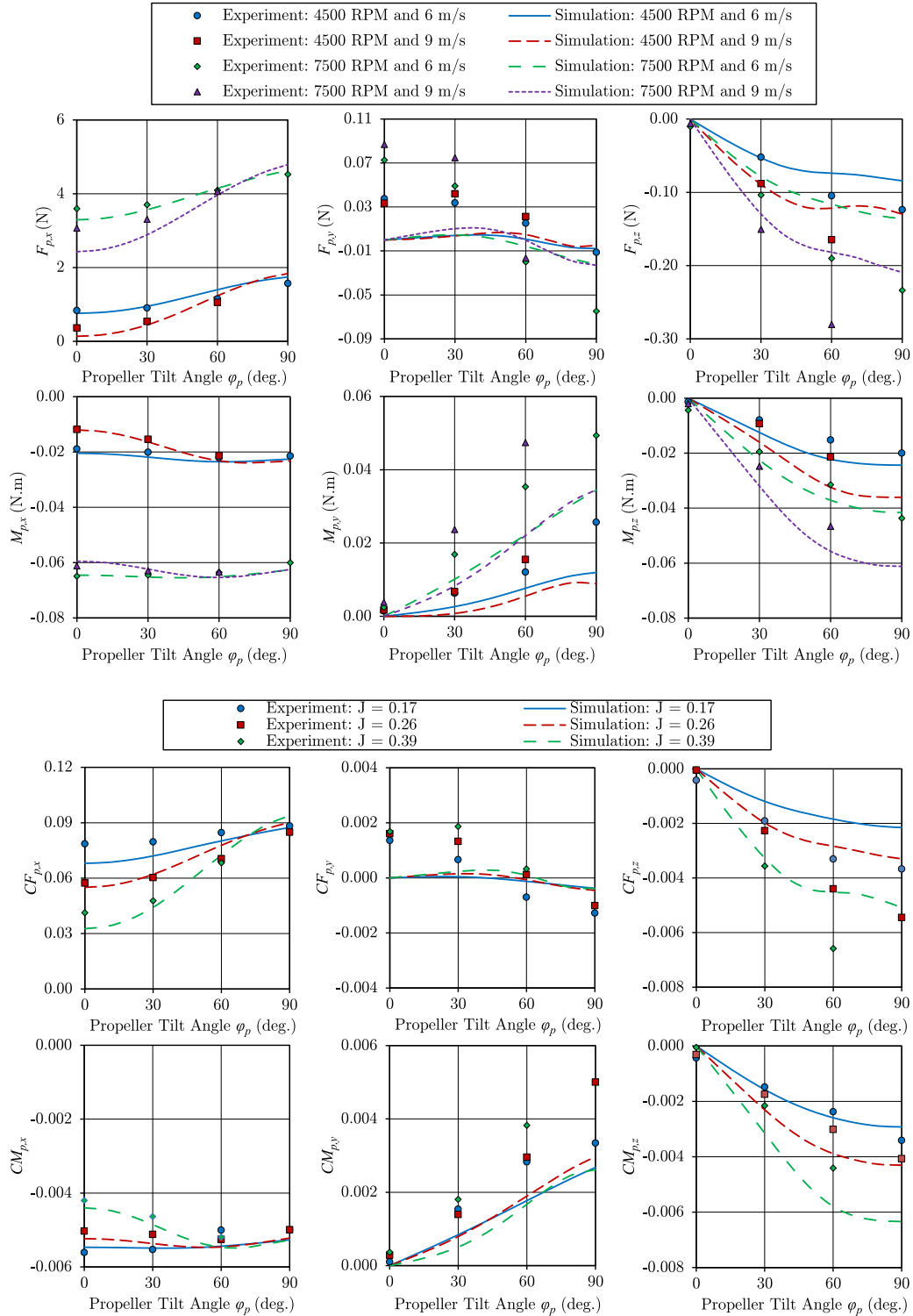


Figure 4.16: Steady-state aerodynamic forces and moments for oblique flow condition.

the propeller. Thus, the force and moment coefficients provided therein are interpolated for the following rotational speeds: 4500 RPM, 6000 RPM, 7500 RPM, and 9000 RPM, which are typical for small UAVs (≤ 2 kg) equipped with 5 – 20 inch propellers. The experiments are carried out at fixed wind speeds of 6 m/s and 9 m/s and various propeller tilt angles in the xz plane, i.e. $\theta_{P/B} = 90$ deg. Simulations are run for these conditions such that at each RPM and wind speed, the propeller tilt angle φ_p is varied from 0 to 90 deg., leading to the results in Fig. 4.16. For clarity, results are shown only for 4500 RPM and 7500 RPM at both 6 m/s and 9 m/s.

It must be noted from the $F_{p,y}$ plot that the simulation predicts near-zero value for all propeller tilt angles, while the experiments show a non-zero $F_{p,y}$ even at $\varphi_p = 0$ deg. This is clearly an indication of misalignment in the experimental setup despite the author's effort to eliminate it [64]. However, since the magnitude of $F_{p,y}$ is quite small, it is presumed that the misalignment may not have drastically affected other measured forces and moments. From the primary aerodynamic thrust and torque ($F_{p,x}$ and $M_{p,x}$) plots, the simulation shows an excellent match with the experimental values with an rms error of 0.25 N (5% of maximum) in $F_{p,x}$ and 0.0014 N.m (2% of maximum) in $M_{p,x}$. For the secondary aerodynamic forces and moments, in general, the simulation results show a good match with experiments up to around 60 deg., beyond which the simulation deviates from experimental results. This is because at higher propeller tilt angles, most of the propeller blade is operating in the stall region of the aerodynamic curves, which only includes a simple stall model and no Reynolds number effect. There might also be some experimental error, as pointed out above. Better results can certainly be achieved by improvements in the aerodynamics model which is not the contribution of the current work.

Even with the simplified aerodynamics model, the maximum discrepancy for $F_{p,z}$ at 90 deg. is 0.04 N at 4500 RPM and 6 m/s, and 0.098 N at 7500 RPM and 6 m/s. The rms error is 0.05 N (17% of maximum). From the $M_{p,y}$ plot, the simulation under-predicts this moment

with an rms error of 0.011 N.m and a maximum error at 90 deg. of 0.014 N.m. From the $M_{p,z}$ plot, the simulation shows a good correlation with experiments with some over-prediction; the rms error is 0.006 N.m and the maximum error at 90 deg. is 0.003 N.m. The force and moment coefficients show similar trends with the propeller tilt angle in Fig. 4.16.

4.7.4 Comparison with Existing Models

It is also worthwhile to compare the presented model with other existing propeller models in the literature against the limited information these models can provide. As alluded earlier, McCormick [33] presents expressions for two secondary aerodynamic quantities (normal force P_N and yaw moment N_p). Comparison is made with McCormick's model in light of the experiments from [64] in the top plots Fig. 4.17. It is evident from P_N and N_p plots that McCormick's model shows a good agreement up to around 30 deg. only, which is expected owing to the small angle assumption involved in deriving these expressions. Also from the

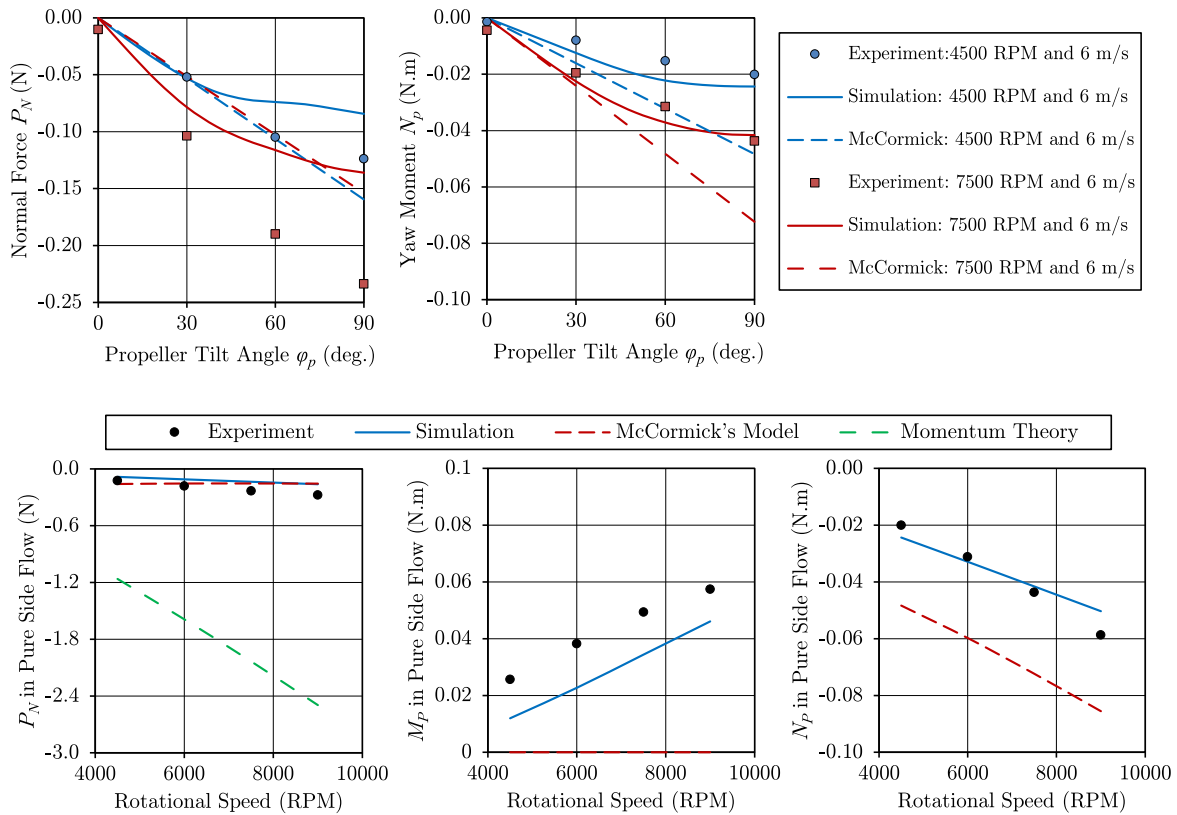


Figure 4.17: Comparison with existing models.

normal force plot, McCormick's model predicts identical results for both 4500 RPM and 7500 RPM indicating that it cannot account for RPM variation correctly.

Momentum theory also can be used to predict the normal force acting on a propeller particularly when the external flow coming purely from the side is turned (not with 100% efficiency) by the propeller disc along its rotation axis. The force required to make this change happen can be determined using the concepts of momentum theory, see for example [66]. For comparison, this force is calculated for the Graupner propeller using momentum theory at 7500 RPM with a 6 m/s pure side flow (i.e. $\varphi_p = 90$ deg.) and assuming 100% efficiency. The results of the current model, McCormick's model and momentum theory are plotted at the bottom of Fig. 4.17 along with experimental measurements from [64]. The current model and McCormick's model are obviously the better choice for the normal force since momentum theory predicts a force 10 times larger than experiments. Moreover, McCormick's model predicts zero pitch moment while momentum theory does not predict the pitch and yaw moment. Figure 4.17 highlights the importance of the presented model over the existing models and theories in the literature for oblique flow.

4.7.5 Analysis and Discussion

The $F_{p,x}$ and $M_{p,x}$ plots of Fig. 4.16 show that the primary aerodynamic thrust and torque increases with the propeller tilt angle, reaching their static condition values in pure side flow (i.e. $\varphi_p = 90$ deg.). This implies that the primary aerodynamic thrust and torque are mainly dependent on the axial component of the external flow, which reduces with increasing propeller tilt angle and becomes zero at 90 deg. Hence in pure side flow, one can expect the performance of a thruster to be similar to that in static conditions. It may further be noted from Fig. 4.16 that in oblique flow, the secondary force $F_{p,y}$ is near-zero, while $F_{p,z}$ is one order of magnitude lower than the primary thrust $F_{p,x}$, and therefore the secondary forces may be neglected depending on the level of accuracy required. On the other hand,

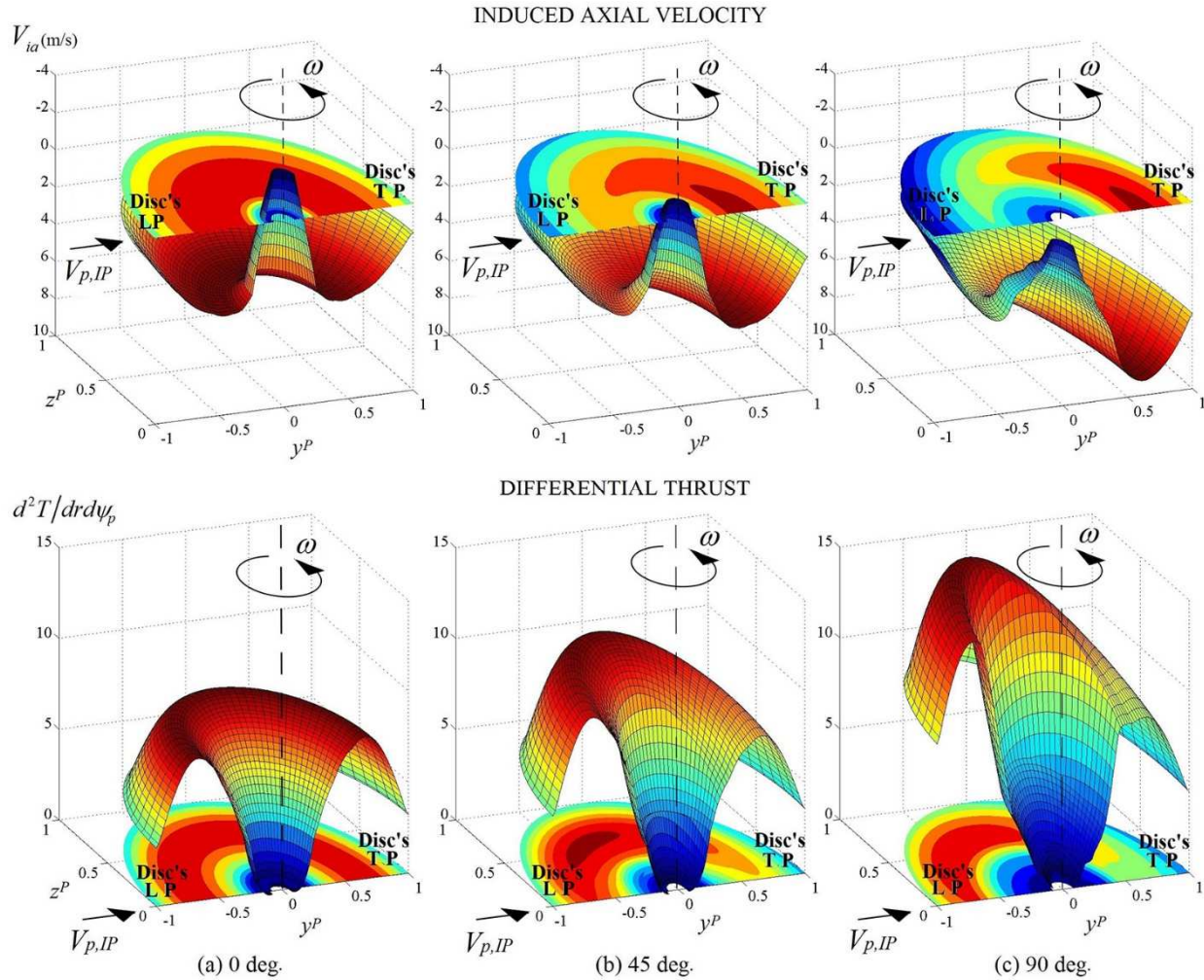


Figure 4.18: Induced velocity and thrust distribution on the propeller disc.

the secondary aerodynamic moments ($M_{p,y}$ and $M_{p,z}$) are of similar order of magnitude as the primary torque $M_{p,x}$, and should not be neglected for thrusters in oblique flow.

It is also worthwhile to plot the induced velocity at the propeller disc and the corresponding differential thrust. This is done in Fig. 4.18 for 7500 RPM and 6 m/s at tilt angles 0 deg., 45 deg. and 90 deg. (for all cases, $\theta_{p/B} = 90$ deg.). The flat semi-disc surface represents the propeller disc with contours of induced velocity and differential thrust shown on it. Also shown simultaneously are 3D plots of the induced velocity and differential thrust. As expected in pure axial flow ($\varphi_p = 0$ deg.), the induced velocity distribution is axisymmetric about the propeller rotation axis. As the propeller tilt angle is increased, the induced velocity

distribution becomes skewed, such that the front half (defined by $-y^P$) of the propeller disc induces less flow as compared to its rear half (defined by $+y^P$), but it remains symmetric about the $x^P y^P$ plane. Only half of the disc is shown in Fig. 4.18.

The differential thrust is also axisymmetric in pure axial flow showing a standard blade loading profile. In oblique flow, the differential thrust retains no symmetry at all; in fact, the peak differential thrust lies in the quadrant defined by $+z^P$ and $-y^P$, see Fig. 4.18 (b) and (c). This lack of symmetry leads to the two moments M_{y^P} and M_{z^P} about the center of the disc which can be visualized from Fig. 4.18 and depicted by Eq. (4.19).

Another plot of interest is Fig. 4.19 wherein the contours of the effective angle of attack experienced by the propeller blade are shown at 7500 RPM and a pure side flow of 6 m/s. Over most of the propeller disc, the effective angle of attack remains positive reaching a maximum of 20 deg. But on the retreating half ($-z^P$) near the disc center, the effective angle of attack becomes highly negative; over -30 deg. This is expected since the in-plane velocity component $V_{p,\perp}$ tends to cancel the rotational velocity ωr on the retreating side (as discussed in Sec. 4.5.2). The effect is most pronounced towards the center since ωr is small due to r being small there. This leads to a large ϕ_{inflow} as per Eq. (4.9), and a large negative α' . Figure 4.19 therefore justifies the use of high angle of attack aerodynamic coefficients in the propeller model.

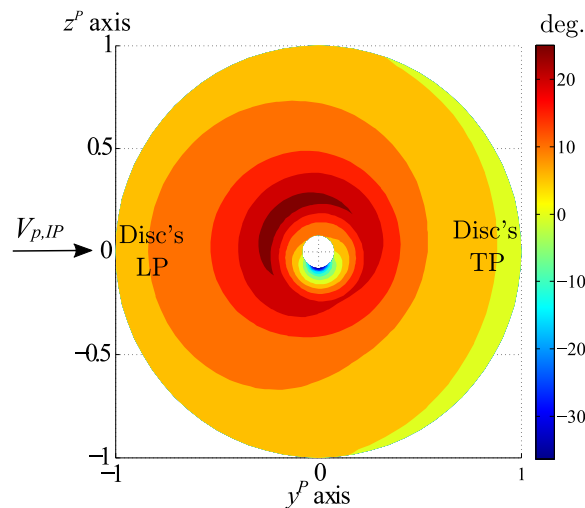


Figure 4.19: Effective angle of attack on the propeller disc.

4.7.6 Dynamic Validation

As stated at the beginning of this chapter, dynamic behavior of the thruster is important for thruster-dominated agile UAVs particularly in transient maneuvers, something which existing steady-state models cannot predict. In fact, this was one of the motivations for the development of the current thruster model. In this section, the dynamic response of the model is validated against experiments using step and random inputs.

Step Signal Response

Several experiments were performed with different step PW inputs to the thruster. Simulations were run for the same step inputs, and the results are compared in Fig. 4.20. As pointed out previously, the F/T data is noisy due to thruster stand vibrations. This can be observed even after filtering, especially in the torque plots. While additional filtering could be done, these plots seem satisfactory for the current purpose of validation. Future experiments will incorporate rubber pads between the thruster stand and the ATI F/T sensor to damp out these vibrations.

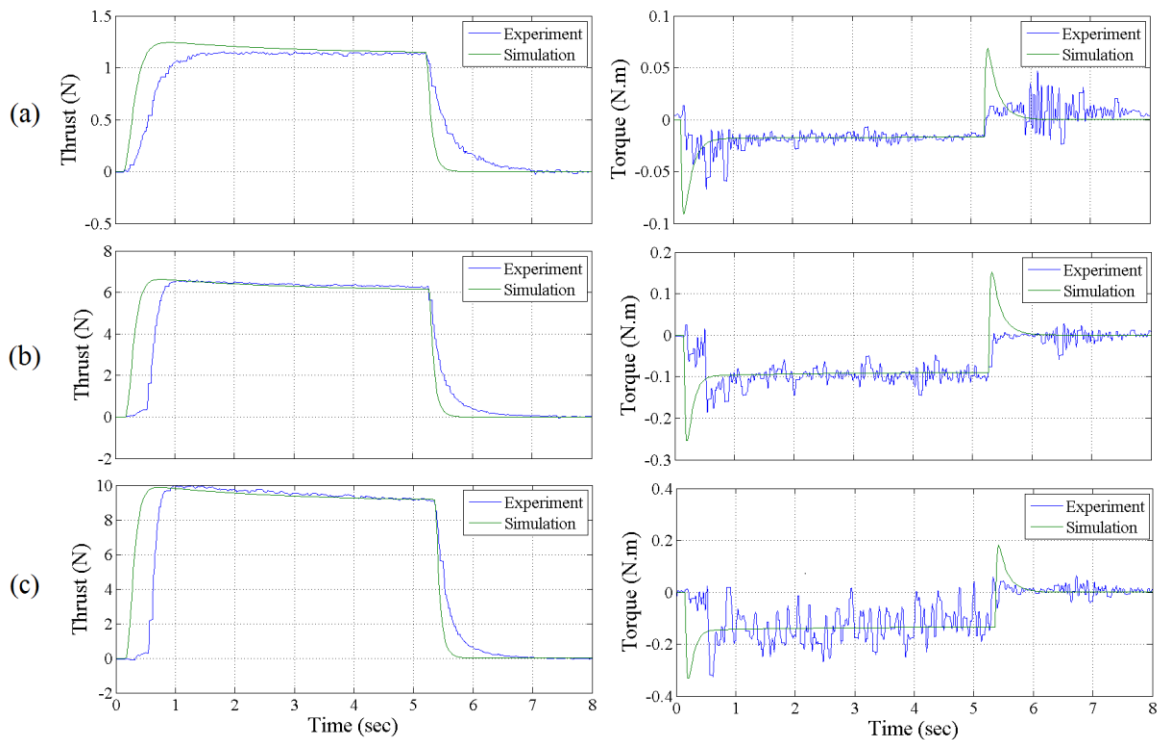


Figure 4.20: Step input response for PW: (a) $1100 \mu\text{s}$, (b) $1500 \mu\text{s}$, and (c) $2000 \mu\text{s}$.

The battery discharge phenomenon is visible in both simulated and experimental results. It is noted that at $PW = 1100 \mu s$, experimental thrust does not show a noticeable drop while the simulated thrust shows a slight drop, implying that the battery model overestimates armature voltage drop at low PWs. At $PW = 1500 \mu s$, the simulation and experiment show approximately the same drop in thrust indicating the battery model to be accurate at moderate PWs. At the highest PW of $2000 \mu s$, the experiment shows more drop in thrust in comparison to the simulation indicating that the battery model underestimates armature voltage drop at high PWs. This behavior is not surprising considering that the battery model does not account for variable discharge rates, as discussed in Sec. 4.7.1.

Further, it is observed that the starting transient response of simulated thrust and reaction torque occur earlier than in the experiment, but exhibit the same shape. This is related to the fact that the motor was started from rest in all experiments. Under these conditions, the ESC limits the surge current and consequently torque is reduced on motor startup, as discussed in Sec. 4.4. The limitation exists from around $t = 0.2$ to 0.5 s, and can be seen as the reduced torque during that time from the plots. Lack of torque at startup causes a deficiency in angular acceleration and results in a delayed rise of angular velocity and thrust. As a result, the starting transient response in thrust is delayed relative to the simulation. Also the ending transients of simulated and experimental thrust and torque are different in Fig. 4.20, where the simulated thrust drops quickly to zero while the experimental thrust shows a more gradual decrease. This is because the braking function of the ESC was turned off in experiments, see the discussion in Sec. 4.4. In this case, the ESC does not allow a reverse current to flow in the armature. Hence no braking torque is applied to slow down the motor, which can be seen from the torque plots.

The problems of motor startup/slowdown might be resolved with the use of programmable ESCs that are available on the market. These may be programmed to release the constraints on startup current and reverse current. However, introduction of additional programmable

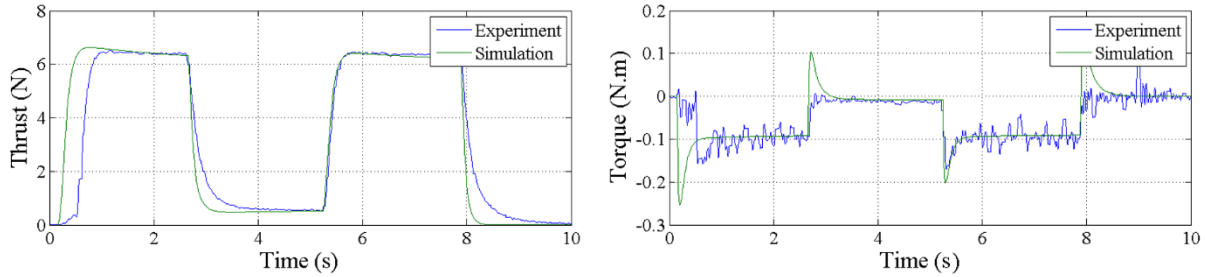


Figure 4.21: Step input response for PW train.

variables would further complicate the dynamic model, and thus a programmable ESC was not used in the current work. To validate the thruster model without startup effects, a second set of experiments was performed in which the motor was started from rest and run at moderate speed ($PW = 1500 \mu s$); then slowed down to the lowest possible speed ($PW = 1050 \mu s$); and then speeding it up once again ($PW = 1500 \mu s$) before finally bringing it to a complete stop. Simulations were run for the same conditions and the results obtained are compared with experiments in Fig. 4.21.

It is seen that the delay in startup torque only exists when the motor starts from rest. In the second acceleration at around $t = 5$ s, the simulated thrust matches closely with the experiment. The ending transients in the thrust/torque curves remain unchanged and the braking function would need to be modeled for the ESC to rectify this. However, even without such a model, the thruster model predicts the dynamic behavior well once the motor has started.

Random Signal Response

Step inputs are unlikely to occur during actual flights where the input would be changing randomly and rapidly. Therefore, the model is validated with random inputs. A random PW signal, recorded during an actual flight, was input to both the model and the thruster on the test stand. The resulting thrust and torque responses of the simulation and experiment are compared in Fig. 4.22.

The simulated thrust and reaction torque are in very good agreement with experimental results. Initially, the simulated thrust matches closely with that obtained in experiment. As

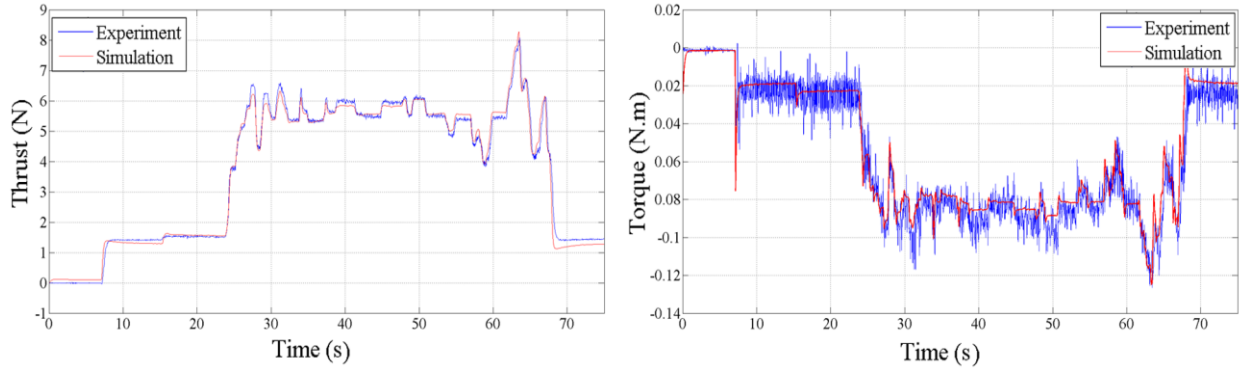


Figure 4.22: Random input response.

time passes, the simulated result starts to diverge; with the simulated thrust always being higher than the experimental thrust. For example at $t = 60$ s, the simulated thrust is 5.63 N while the experimental thrust is 5.45 N, giving an over-prediction of 3.24%. This increasing discrepancy with time is attributed to the fact that the battery model does not have the ability to model capacity fading effects, temperature dependent effects etc., which become important with time.

Propeller Slipstream Effect

Another key aerodynamic component that must be modeled in detail for agile UAVs is the propeller slipstream produced by the thruster, since it provides additional airflow over the aircraft surfaces. This allows the aircraft to maintain lift and control during near-zero forward speed flight like that encountered during vertical takeoff and landing, as well as during aerobatic maneuvers wherein the external flow is largely detached from the aircraft control surfaces. Lift and control under these conditions is achieved primarily by immersing the UAV aerodynamic and control surfaces, entirely or partially, in its propeller slipstream, thereby keeping the surfaces effective at all times, see Fig. 5.1. While the UAV thruster provides the force necessary to keep the aircraft airborne, its propwash provides the airflow over the surfaces to maintain control; these two together allow the UAV to operate in limited spaces and constrained environments such as indoors, caves etc. Hence detailed knowledge of the slipstream velocity is also essential to accurately determine the aerodynamic and control forces/moments on agile UAVs.



Figure 5.1: Propeller slipstream on a small fixed-wing UAV.

Existing slipstream models in the literature [12, 51, 53] are based on conventional theories like the momentum theory, lifting line theory etc., and therefore they consider only acceleration of the air within the slipstream and do not account for the slipstream diffusion with ambient flow. Their application to regions far downstream of the propeller, where diffusion is dominant, is thus questionable. In the UAV research area, the development and effects of the slipstream far downstream of the propeller have never been given due consideration, perhaps because the slipstream is assumed to become too weak due to diffusion to produce any appreciable effect. This may be true for large heavy aircraft but not for agile UAVs that are small and lightweight with relatively powerful thrusters (see Fig. 5.1), and as such their control surfaces far downstream of the propeller (e.g. elevator and rudder) are immersed in a slipstream that is still relatively strong compared to the UAV inertia. In contrast, the diffusion of propeller slipstream (referred to as a propeller jet in marine research area) has been researched thoroughly for marine propellers, where its effects on nearby structures, like seabed scouring etc., is studied [82–84]. Researchers are interested in these effects up to large axial distance of several propeller diameters from the propeller plane, and therefore take into account the diffusion phenomenon using semi-empirical equations developed for marine propellers from detailed experimental investigations. The efforts in this research area are summarized in a review [85].

This chapter presents a mathematical model for the propeller slipstream that accurately predicts the slipstream velocity on propwash-immersed components up to several propeller diameters downstream of the propeller. The axial velocity component is explicitly modeled by taking into account both the acceleration and diffusion phenomenon, while the swirl velocity effect on the UAV is modeled as a reduction on the thruster reaction torque.

The overall slipstream model is presented first followed by a brief discussion on the propeller operating states and slipstream mechanism. Equations for axial slipstream velocity are given in Sec. 5.4, while its semi-empirical coefficients are determined from detailed experiments

in Sec. 5.5. The chapter concludes on model validation and a brief discussion on the entrainment in the slipstream.

5.1 Propeller Slipstream Model

It was pointed out in the previous chapter that the rotating propeller of an agile UAV thruster induces flow in all three directions, i.e. axial, radial and tangential (swirl). Therefore the resulting slipstream contains all three velocity components. The radial and swirl components are small compared to the axial one, and therefore these are not considered explicitly in the propeller slipstream model. Hence the slipstream velocity is along the body x axis only:

$$\mathbf{V}_s = V_s \mathbf{i} \quad (5.1)$$

where V_s is the magnitude of the axial slipstream velocity and is calculated at the aerodynamic center of each YAK54 segment using the equations presented in the next sections. The slipstream velocity for each segment given by Eq. (5.1) is added to Eq. (3.1) to get the total velocity of that segment, and based on the total velocity, angle of attack and aerodynamic coefficients are calculated for that segment, see Sec. 3.1.

5.1.1 Swirl Velocity Effect

Despite the fact that the swirl component is small, it has several effects on the agile UAV with the main one being to counter the thruster reaction moment. This effect is included in the presented model, but other effects, such as delay in stall, increase in maximum lift etc. documented in [90], are small and hence neglected.

For a right-handed propeller, which rotates clockwise when viewed from rear, the swirl velocity gives rise to a positive rolling moment on the aircraft as it causes a downwash on the starboard surfaces and an upwash on the port surfaces. Furthermore, the swirl flow coiling clockwise (when viewed from rear) around the fuselage adds to this effect. Hence the positive roll moment created by the swirl velocity counteracts some of the negative roll moment exerted by the thruster (with a right-handed propeller) on the airframe. This effect

of swirl is included in the propeller slipstream model by reducing $M_{thr,x}$ to 40% of its value. This reduction is typical of an aerobatic UAV configuration as noted in [66].

5.1.2 Time-Dependent Slipstream

Once the induced flow leaves the propeller plane, it is no longer fixed to the UAV airframe, and takes some time before impinging on the aircraft surfaces. This lag is favorable for agile UAVs as in some conditions like hover etc., the UAV is stabilized when small excursions or deviations from these conditions are damped out by the propwash released from the propeller plane at an earlier time. This effect is discussed in-detail and modeled in Refs. [9, 66], however presently this effect is also not included.

5.2 Slipstream in Various Operating States

As discussed in Chap. 4, the propeller of an agile UAV thruster operates, most of the time, in the normal working state (related to forward flight, i.e. $V_{p,A} \geq 0$), but may also enter briefly into other states namely the vortex-ring, turbulent-wake and windmill-brake states (related to rearward flight, i.e. $V_{p,A} < 0$), as a result of a maneuver, accident or wind gust. Each of these states is characterized by a different slipstream structure, see Fig. 4.8.

The slipstream impinges upon the aircraft surfaces in forward flight (normal working state) and also in rearward flight provided that the rearward velocity is not too-high. Presently the limit on rearward velocity is set to 20% of the momentum-averaged induced velocity $V_{ia,avg}$ at the propeller plane in static condition. As the rearward velocity increases beyond this limit, the axial slipstream velocity is counteracted completely by the external reverse flow, and it is unable to reach the aircraft surfaces. Therefore:

$$\mathbf{V}_s = \begin{cases} V_s \mathbf{i} & \text{if } V_{p,A} \geq -0.2V_{ia,avg} \\ 0 & \text{otherwise} \end{cases} \quad (5.2)$$

where $V_{ia,avg}$ may be determined from the momentum theory expression for a propeller [12]: $T = 2\rho A_{disc}(V_{p,A} + V_{ia,avg})V_{ia,avg}$ and using the definition of thrust coefficient $C_T = T/(\rho n^2 D_p^4)$, and setting $V_{p,A} = 0$ for static condition:

$$V_{ia,avg} = 0.798nD_p\sqrt{C_T} \quad (5.3)$$

where D_p is the propeller diameter, n is the rotational speed in rev/s, and C_T is the thrust coefficient. The latter two quantities are taken from the thruster model output from Chap. 4. It may be noted that the same result can be obtained by integrating the $V_{ia} = f(r, \psi_p)$ found in Chap. 4 over the propeller disc.

Similarly, the swirl effect of the reduction to $M_{thr,x}$ exists as long as the rearward speed is low, i.e. $V_{p,A} \geq -0.2 V_{ia,avg}$. At higher rearward speeds, the swirl velocity is unable to impinge upon the aircraft surfaces and hence no reduction is applied to $M_{thr,x}$.

The analysis is further simplified by realizing that in the normal working state, the propeller slipstream and its effect on the UAV is strongest in static condition ($V_{p,A} = 0$). This is because under static condition: 1) the propeller induces maximum flow in the slipstream according to momentum theory, and 2) the propeller slipstream is the only source of flow over the aircraft surfaces. As the forward speed (or advance ratio J) of the propeller increases, the slipstream and its effect weakens because the propeller induces lesser flow and the external flow becomes dominant. In light of this, the equations for the axial slipstream velocity are derived in the next sections based on static condition. The equations applicability to forward flight condition is discussed later in Sec. 5.7.

5.3 Propeller Slipstream Mechanism

Development of equations for the axial slipstream velocity requires an understanding of the two major phenomena that occur within the slipstream – acceleration and diffusion, their cause and effect, and their relative importance in different regions of the slipstream.

5.3.1 Acceleration and Diffusion in the Slipstream

The pressure force associated with the rotating propeller causes the air passing through the propeller plane, to accelerate in all three directions, i.e. axial, tangential (swirl) and radial. As a result of acceleration, the slipstream velocity increases, while the slipstream itself contracts to preserve continuity. On the other hand, air viscosity and turbulence cause

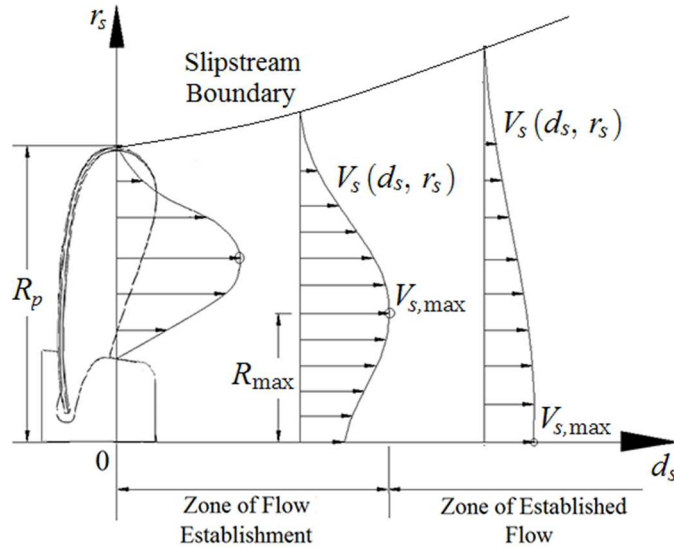


Figure 5.2: Marine propeller jet.

diffusion of the slipstream radially into the ambient flow. The slipstream velocity decreases as a result of momentum transfer from the fast-moving slipstream to the slow-moving ambient flow, and is accompanied by expansion of the slipstream to maintain continuity.

In reality, the two phenomena of acceleration and diffusion occur simultaneously within the slipstream. Their relative importance is key to determining whether the slipstream will contract or expand. Since near the rotating propeller, the pressure force is stronger than the viscous force, acceleration dominates diffusion and therefore contraction occurs near the propeller, as predicted by the classical momentum theory. However, the influence of this pressure force diminishes as the air moves downstream, and at some distance downstream the pressure force becomes weaker than the viscous force and turbulence. Then diffusion dominates, causing the slipstream to expand from that point onwards.

5.3.2 Propeller Jets from Marine Propellers

Before proceeding further, a brief description of marine propeller jets is relevant. A jet produced from a marine propeller is different from a slipstream produced by an aircraft propeller, in that it exhibits little or no contraction and expands continuously starting from the propeller plane, as shown in Fig. 5.2. Absence of contraction in a propeller jet can be

attributed to the marine propeller's low rotational speed, i.e. $\sim 200 - 400$ RPM, in comparison to that of a small aircraft propeller which operates around $5000 - 6000$ RPM. At such low rotational speeds, a small pressure force is developed across a marine propeller, thereby producing negligible acceleration. This is evident from the low velocity induced at the marine propeller plane which is usually of the order of 1 to 2 m/s, as opposed to an aircraft propeller for which it is of the order of 8 to 10 m/s at the propeller plane. Thus in a marine propeller jet, diffusion is dominant starting from the propeller plane and the slipstream exhibits expansion only.

It is well established from research on marine propellers [82–84] that a propeller jet comprises of two distinct zones namely the Zone of Flow Establishment (ZFE) and the Zone of Established Flow (ZEF) as shown in Fig. 5.2. The ZFE is characterized by two maximum velocity peaks, one on either side of the propeller rotation axis (only one peak is shown in Fig. 5.2 since the flow is axisymmetric about the rotation axis). These peaks gradually move inward toward the rotation axis. A certain distance d_{ZFE} (called the length of zone of flow establishment) downstream, these two peaks merge into a single velocity peak located at the rotation axis, and this marks the start of the ZEF. Thereafter, the slipstream velocity decreases in the ZEF as the slipstream diffuses radially outwards until it is no longer distinguishable from the ambient flow.

5.4 Axial Slipstream Velocity

Based on the discussion in Sec. 5.3, equations for the axial slipstream velocity are developed by defining two distinct regions within the slipstream, namely the near-field region and the far-field region shown in Fig. 5.3.

In the near-field region, diffusion is small enough to be neglected compared to the acceleration, and therefore, this region is characterized by slipstream contraction. Conventional theories, such as the momentum theory, hold valid in this region to predict the axial slipstream velocity. By contrast, in the far-field region, acceleration is neglected

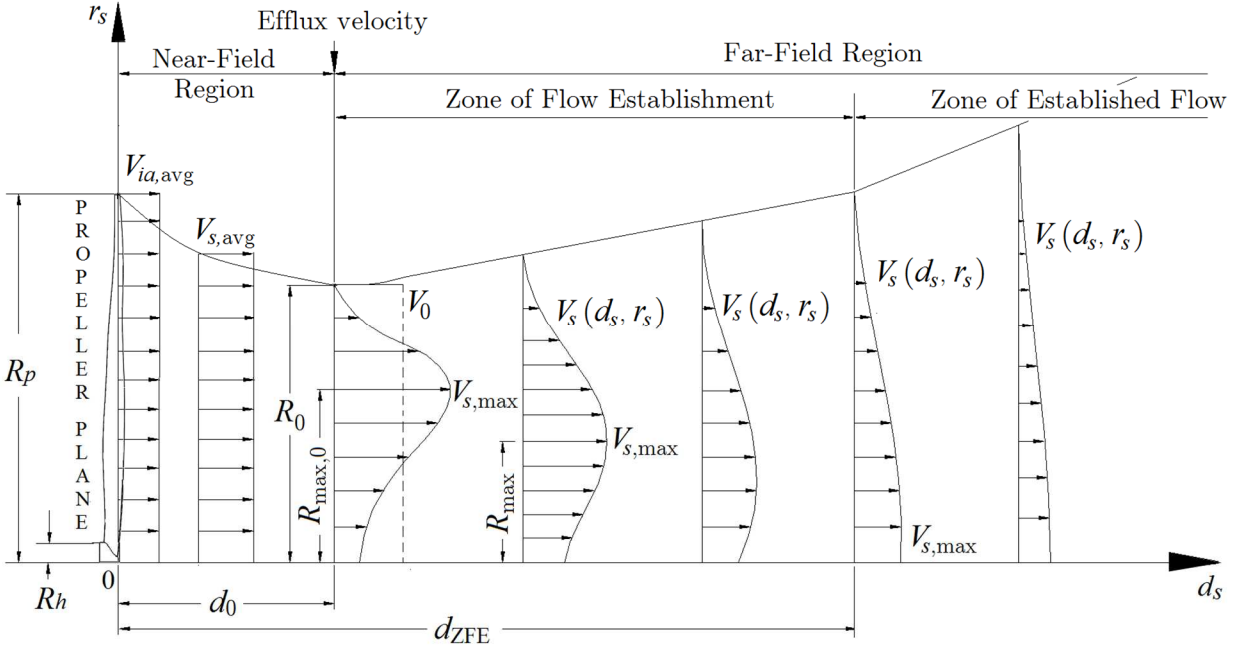


Figure 5.3: Axial slipstream velocity.

and only diffusion is considered, causing slipstream expansion. However, analyzing diffusion, even alone, by treating air as viscous and turbulent in this region is difficult. No simple analytical equations exist in the literature for this purpose and therefore semi-empirical equations, similar to those developed for marine propeller jets, are used to predict the axial slipstream velocity in the far-field region. Use of similar semi-empirical equations for an aircraft propeller slipstream is justified considering that the flow in this case is also incompressible and more so, the density of the fluid is considered explicitly in the equations. However, since viscosity of the fluid is not considered explicitly, the semi-empirical coefficients will be different for a propeller slipstream in air, from those determined experimentally for propeller jets in water. These coefficients represent quantities such as the decay rate of maximum velocity etc., which strongly depend on the fluid viscosity, and therefore must be determined for a propeller slipstream in air through experiments as done later in Sec. 5.4.

A transition plane located at an axial distance d_0 separates the two regions and is termed the efflux plane. Upstream of this plane, the slipstream contracts becoming narrowest at

the efflux plane and expands thereafter, see Fig. 5.3. The slipstream velocity increases starting from the propeller plane in the near-field region, reaches a maximum at the efflux plane, and then decreases downstream until it equals the ambient flow velocity. The momentum-averaged slipstream velocity at the efflux plane is termed the efflux velocity V_0 , and the smallest slipstream radius there is called the contracted radius R_0 .

5.4.1 Slipstream Velocity in the Near-Field Region

The classical momentum theory is known to yield good results in the near-field region of the slipstream where only acceleration is important [13, 87]. From [12], the momentum-averaged slipstream velocity $V_{s,avg}$ at an axial distance d_s from the propeller plane, and the corresponding slipstream radius R_s are given by:

$$V_{s,avg} = V_{ia,avg} \left[1 + \frac{d_s/R_p}{\sqrt{1 + (d_s/R_p)^2}} \right] \quad (5.4)$$

$$R_s = R_p \sqrt{\frac{V_{ia,avg}}{V_{s,avg}}} \quad (5.5)$$

In the above equations, R_p is the propeller radius, and $V_{ia,avg}$ is the momentum-averaged induced velocity at the propeller plane ($d_s = 0$) given by Eq. (5.3).

The increase in slipstream velocity and subsequent reduction in slipstream radius as suggested by Eqs. (5.4) and (5.5), are plotted in Fig. 5.4. Evidently, much of the overall increase in velocity occurs in the vicinity of the propeller, within 1 propeller diameter from the propeller plane, indicating a strong influence of pressure force there. Beyond this axial distance, there is no significant change in slipstream velocity indicating that the pressure force has certainly diminished to a negligible level.

5.4.2 Transition from Near-Field to Far-Field Region

As alluded earlier, the efflux plane that serves as the transition plane from near-field to far-field region is located where the slipstream velocity is maximum. Momentum theory

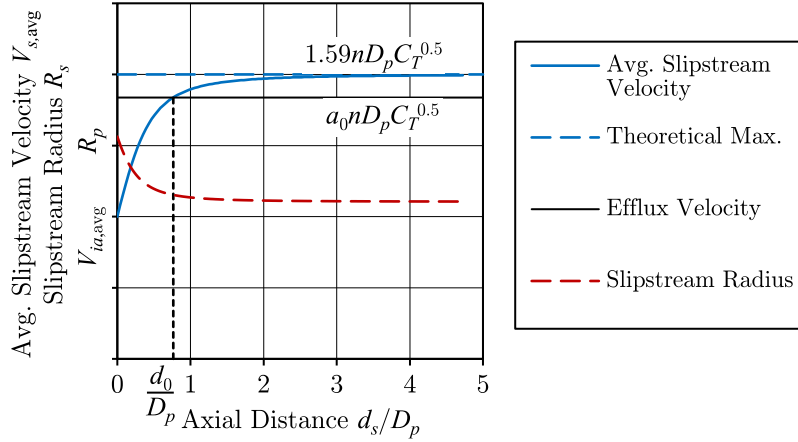


Figure 5.4: Momentum-averaged slipstream velocity and radius.

equation (5.4) predicts that the slipstream velocity will increase to a maximum value of $1.59nD_p C_T^{0.5}$ (i.e. twice of $V_{ia,avg}$) far downstream of the propeller where $d_s \gg R_p$. In reality however, this maximum theoretical value can never be achieved owing to diffusion. Researchers in the marine area have experimentally determined the efflux velocity to be lower than that predicted by the momentum theory, and have subsequently proposed similar equations but with lower coefficients, like $1.33nD_p C_T^{0.5}$ in [83]. The lower coefficients have been determined experimentally for propeller jets in water and thus might not be applicable for a propeller slipstream in air, as pointed out earlier. In lieu of this, a general expression for the efflux velocity is written as,

$$V_0 = a_0 n D_p \sqrt{C_T} \quad (5.6)$$

where the coefficient $a_0 < 1.59$ must be determined experimentally for a propeller slipstream in air. The value of efflux velocity given by Eq. (5.6) is also plotted in Fig. 5.4. The transition from near-field to far-field region occurs at the axial location where the momentum-averaged slipstream velocity, predicted by Eq. (5.4), increases and reaches its maximum efflux value given by Eq. (5.6). Thus the efflux plane location d_0 may be determined by solving:

$$V_{s,avg}(d_0) = V_0 \quad (5.7)$$

Once d_0 is known, the contracted radius at the efflux plane is found from Eq. (5.5) as:

$$R_0 = R_s(d_0) \quad (5.8)$$

Downstream of the efflux plane, the slipstream velocity does not rise any further but rather decreases due to diffusion being dominant thereafter.

5.4.3 Slipstream Velocity in the Far-Field Region

From the efflux plane onwards, the pressure force is sufficiently small to be neglected and only diffusion is considered for the prediction of axial slipstream velocity within the far-field region. As noted earlier, this is not trivial due to the complex nature of the diffusion process, even with the current CFD methods. No relevant work is available in the literature that accounts for the slipstream diffusion for UAVs.

On the other hand, significant work has been done for marine propeller jets to account for their diffusion, which has been summarized in a comprehensive review by Lam et al. [85]. The earliest work can be attributed to Albertson et al. [82] who investigated the induced velocity within a plain water jet using simple momentum theory and characterized the different zones (ZFE and ZEF) within the propeller jet defined in Sec. 5.3.2. Subsequent works by Hamill [83], Stewart [84] etc. improved Albertson's work by modifying the theoretical equations with the help of detailed experiments, and thereby developed semi-empirical equations to predict the induced velocity within different zones of the propeller jet. The general methodology behind the semi-empirical equations is to first determine the variation of maximum induced velocity and its radial position with axial distance, see Fig. 5.2. With these known, the induced velocity profile at any given section is approximated by a Gaussian function. In this manner, the induced velocity is determined as a function of both axial and radial locations throughout the propeller jet.

For a propeller slipstream in air, the semi-empirical equations cannot be used directly since the experimentally determined coefficients in the equations will be different owing to the different fluid. Nonetheless, similar equations can be used but with coefficients determined

from detailed experiments for a propeller slipstream in air. Presented below are the relevant semi-empirical equations with generic coefficients.

The maximum slipstream velocity and its radial position are captured as linear functions of axial distance,

$$V_{s,\max} = V_0 \left(a_1 - b_1 \frac{d_s - d_0}{D_0} \right) \quad (5.9)$$

$$R_{\max} = R_{\max,0} \left(a_2 - b_2 \frac{d_s - d_0}{D_0} \right) \quad (5.10)$$

Here $D_0 = 2R_0$ is the contracted diameter, and $R_{\max,0} = 0.67(R_0 - R_h)$ is the radial position of the maximum slipstream velocity at the efflux plane (see Fig. 5.3), and R_h is the propeller hub radius. Equation (5.10) is valid within the zone of flow establishment, i.e. for $d_s < d_{ZFE}$ only and further downstream R_{\max} will become and remain zero throughout the zone of established flow.

The slipstream velocity profile at any section is approximated by a one-term Gaussian function of the form,

$$V_s = V_{s,\max} \exp \left[- \left(\frac{r_s - R_{\max}}{a_3 R_{\max,0} + b_3 (d_s - d_0 - R_0)} \right)^2 \right] \quad (5.11)$$

The above equation will further simplify for the zone of established flow since $R_{\max} = 0$ there. It may be noted that in contrast to semi-empirical equations for marine propeller jets, the above equations use:

- $(d_s - d_0)$ instead of d_s , since for a propeller slipstream diffusion is dominant starting from the efflux plane ($d_s = d_0$) and not from the propeller plane ($d_s = 0$),
- contracted diameter D_0 instead of propeller diameter D_p , since at the efflux plane the slipstream diameter is smaller than the propeller diameter.

The coefficients $(a_0, a_1, b_1, a_2, b_2, a_3, b_3)$ in Eqs. (5.6) to (5.11) will be determined later from detailed experiments for a propeller slipstream in air. The equations for the axial slipstream velocity involve the same inputs as required by the classical momentum theory, which are:

the propeller radius R_p , hub radius R_h , rotational speed n in rev/s, and thrust coefficient C_T of the propeller.

5.5 Axial Slipstream Velocity Coefficients

In this section, the coefficients in the equations for the axial slipstream velocity are determined from a set of detailed measurements of the slipstream velocity. The experimental setup and procedure are discussed first, followed by the evaluation of the coefficients.

5.5.1 Experimental Setup and Procedure

The experimental setup consists of our test propeller, the *Electrify Powerflow* 10x4.5 (254 mm diameter) attached to the *RimFire 400* BLDC motor as shown in Fig. 5.5. The assembly is mounted on a 38 mm diameter stand (0.38 m high) firmly attached to an ATI Gamma force/torque (F/T) transducer to measure the propeller thrust with a fine resolution. The stand keeps the propeller clear from the ground to avoid any interference between the propeller slipstream and the surroundings.

Three sets of experiments were performed each at a different rotational speed: low (1750 RPM), moderate (5425 RPM) and high (6425 RPM). An Arduino board was used to send pulse width (PW) signals to the motor-propeller assembly to run it at the desired rotational

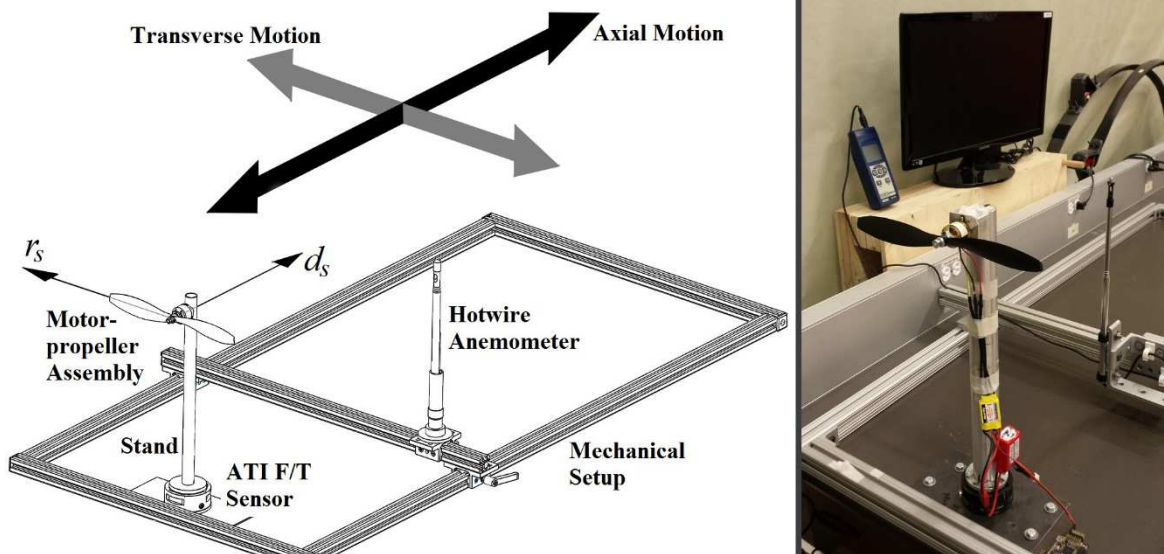


Figure 5.5: Experimental setup.

speed, while the slipstream velocity was measured downstream of the propeller at several axial and radial locations using a *Reed* hotwire anemometer which has a sampling rate of 1 Hz, and a resolution of 0.01 m/s in the range 0.2 – 5 m/s, and 0.1 m/s in the range 5.1 – 25 m/s. The mechanical setup shown in Fig. 5.5 was designed so that the hotwire anemometer could be traversed in the axial as well as radial direction within the slipstream. A comprehensive measurement grid was established with axial locations: $d_s/D_p = [0.08, 0.18, 0.28, 0.35, 0.41, 0.47, 0.57, 0.75, 0.87, 0.98, 1.18, 1.57, 1.97, 2.75, 3.54, 4.33, 5.12]$ measured from the propeller plane, and radial locations: $r_s/R_p = 0$ to 2.91 at 10 mm intervals measured from the rotation axis. Resolution was kept fine in the vicinity of the propeller since the slipstream undergoes rapid change there and also to capture the transition from near-field to far-field region. Furthermore, cubic interpolation of the coarse experimental data was done to obtain a finer spacing of 1 mm in both axial and radial directions.

5.5.2 Determination of the Coefficients

The coefficients in Eqs. (5.6) to (5.11) are determined based on one set of experiments performed at 5425 RPM. At this rotational speed, the propeller was found to generate a thrust $T = 6.43 \pm 0.03$ N, which gives a thrust coefficient of $C_T = 0.1542$. On the other hand, the thruster model developed in Chap. 4 gives a thrust of 6.52 N and a thrust coefficient of 0.1563, which is not too different from experiments and could be used instead.

Coefficient for Efflux Velocity

From experimental data, the slipstream was seen to contract up to an axial distance of $d_0/D_p = 0.764$, and then expand further downstream. Using Eq. (5.7), the coefficient a_0 is determined to be 1.46, and thus Eq. (5.6) becomes:

$$V_0 = 1.46nD_p\sqrt{C_T} \quad (5.12)$$

Subsequently, simplifying Eq. (5.7) and (5.8) for the efflux plane location and contracted radius respectively, results in the following expressions:

$$d_0 = 1.528R_p \quad (5.13)$$

$$R_0 = 0.74R_p \quad (5.14)$$

The efflux velocity is a momentum-averaged quantity and not physically measurable from experimental data. More so, the contracted radius also cannot be found accurately from experimental data as it is difficult to identify the exact boundary of the slipstream. Therefore, using Eqs. (5.12) and (5.14), the efflux velocity and contracted radius are found to be $V_0 = 13.17$ m/s and $R_0 = 93.98$ mm respectively, for use in the next section.

Coefficient for the Semi-Empirical Equations

To determine the coefficients in the semi-empirical equations, three quantities namely maximum slipstream velocity $V_{s,\max}$, its radial position R_{\max} , and the velocity $V_{s,\text{core}}$ at the slipstream core ($r_s = 0$) are extracted from experimental data. As described previously, the cubic interpolation was used to improve spacing to 1 mm in radial direction, yielding a better estimate for $V_{s,\max}$ and R_{\max} as compared to the coarse experimental measurements. The quantities are normalized and plotted as functions of non-dimensional axial distance in Fig. 5.6. A non-dimensional form of the axial distance $(d_s - d_0)/D_0$ is used such that the efflux plane is located at zero of the horizontal axis.

From Fig. 5.6 (b), it is seen that the radial position of the maximum slipstream velocity becomes zero at around $(d_s - d_0)/D_0 = 4.25$. By definition, this marks the end of the zone of flow establishment and therefore $d_{ZFE} = d_0 + 4.25D_0$. More so, from Figs. 5.6 (a) and (b),

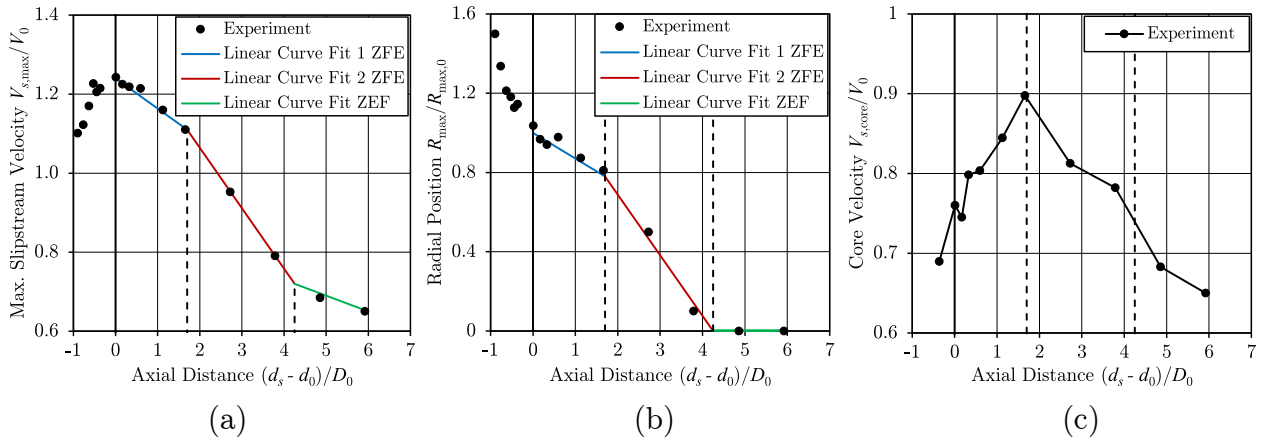


Figure 5.6: (a) Maximum slipstream velocity, (b) its radial location, and (c) velocity at the slipstream core.

within the ZFE itself, the maximum slipstream velocity and its radial position decrease gradually till $(d_s - d_0)/D_0 = 1.7$, and then more rapidly thereafter till the end of the ZFE. Different decay rates before and after this axial distance can be related to the core velocity peaking at that axial distance as shown in Fig. 5.6 (c). A similar observation of two different decay rates within the ZFE has been made in [83] for marine propellers also.

Coefficients in the semi-empirical equations for the maximum slipstream velocity and its radial position are determined by curve fitting Eqs. (5.9) and (5.10) to the experimental data as shown in Figs. 5.6 (a) and (b) respectively. Similarly, coefficients in the semi-empirical equations for slipstream velocity profiles are determined by curve fitting one-term Gaussian functions, Eq. (5.11), to the experimentally measured velocity profiles at three axial locations: two in the ZFE ($d_s/D_p = 0.87$ and 1.97) and one in the ZEF ($d_s/D_p = 4.33$), as shown in Fig. 5.7. The typical profiles of the axial slipstream velocity in the zone of flow establishment are attributed to the propeller hub and the motor, which cause a significantly lower velocity at the rotation axis [82–85, 87]. Furthermore, the experimentally measured velocity profiles are seen to be asymmetric about the peak value; with the asymmetry being most pronounced at the section closest to the propeller plane (see $d_s/D_p = 0.87$), and gradually decreasing with increasing axial distance (see $d_s/D_p = 1.97$), and finally disappearing in the zone of established flow where the slipstream velocity becomes

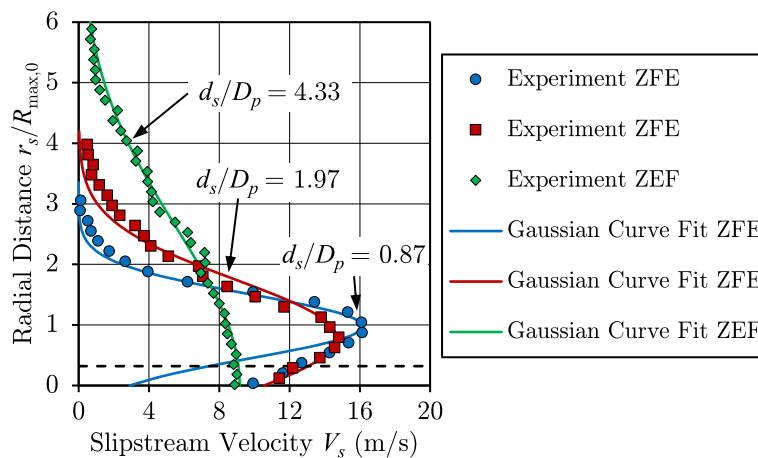


Figure 5.7: Gaussian curve fits to experimentally measured velocity profiles.

symmetric about its peak located at the rotation axis (see $d_s/D_p = 4.33$). A one-term Gaussian function, being symmetric, cannot approximate the asymmetry in the slipstream velocity profiles, but nevertheless it is used in the current work as it is simple and has a physical interpretation. More so, in reality, the slipstream velocity near the rotation axis is of lesser importance because of the aircraft fuselage there, which further justifies the use of one-term Gaussian functions. All the semi-empirical equations obtained from curve fits are presented below.

In the zone of flow establishment, for $d_0 \leq d_s \leq (d_0 + 1.7D_0)$:

$$V_{s,\max} = V_0 \left(1.24 - 0.0765 \frac{d_s - d_0}{D_0} \right) \quad (5.15)$$

$$R_{\max} = R_{\max,0} \left(1 - 0.1294 \frac{d_s - d_0}{D_0} \right) \quad (5.16)$$

$$V_s = V_{s,\max} \exp \left[- \left(\frac{r_s - R_{\max}}{0.8839 R_{\max,0} + 0.1326 (d_s - d_0 - R_0)} \right)^2 \right] \quad (5.17)$$

and for $(d_0 + 1.7D_0) \leq d_s \leq (d_0 + 4.25D_0)$:

$$V_{s,\max} = V_0 \left(1.37 - 0.1529 \frac{d_s - d_0}{D_0} \right) \quad (5.18)$$

$$R_{\max} = R_{\max,0} \left(1.3 - 0.3059 \frac{d_s - d_0}{D_0} \right) \quad (5.19)$$

$$V_s = V_{s,\max} \exp \left[- \left(\frac{r_s - R_{\max}}{0.5176 R_{\max,0} + 0.2295 (d_s - d_0 - R_0)} \right)^2 \right] \quad (5.20)$$

In the zone of established flow, i.e. $d_s \geq d_0 + 4.25D_0$

$$V_{s,\max} = V_0 \left(0.89 - 0.04 \frac{d_s - d_0}{D_0} \right) \quad (5.21)$$

$$R_{\max} = 0 \quad (5.22)$$

$$V_s = V_{s,\max} \exp \left[- \left(\frac{r_s}{0.2411 (d_s - d_0)} \right)^2 \right] \quad (5.23)$$

Equations (5.4) to (5.5), and (5.12) to (5.23) are used to calculate the axial slipstream velocity V_s at any desired location (d_s, r_s) . For each YAK54 segment, the desired location is its aerodynamic center for which:

$$\begin{aligned} d_s &= r_{p,x} - r_x \\ r_s &= \sqrt{(r_{p,y} - r_y)^2 + (r_{p,z} - r_z)^2} \end{aligned} \quad (5.24)$$

where $[r_{p,x}, r_{p,y}, r_{p,z}]^T$ and $[r_x, r_y, r_z]^T$ are the position vectors of the propeller disc center and the segment a.c. measured from the aircraft c.g. in the body frame.

5.6 Validation

A thorough validation of the propeller slipstream model is now undertaken to evaluate its performance for different rotational speeds, geometric characteristics such as diameter, pitch etc., and configurations like pusher, tractor etc. of the propeller. The results are presented in this section.

5.6.1 Validation at Different Rotational Speeds

The model is first validated against other sets of experiments for the same Electrify 10x4.5 propeller. As stated in Sec. 5.5.1, three different sets of experiments were performed for this propeller. While one set of these experiments, done at 5425 RPM, was used in the previous section to determine the semi-empirical coefficients, the other two sets of experiments, done at 1750 RPM and 6425 RPM, are used here for model validation.

A comparison of the entire propeller slipstream is shown in Figs 5.8 (a) and (b) for 1750 RPM and 6425 RPM respectively. In the near-field region, i.e. from the propeller plane ($d_s/D_p = 0$) to the efflux plane ($d_s/D_p = 0.764$), the slipstream model equations (5.4) to (5.5) give a momentum-averaged axial slipstream velocity which is in agreement with the experimentally obtained velocity profiles in this region. Further downstream from the efflux plane, i.e. in the far-field region, the model semi-empirical equations (5.12) to (5.23) give velocity profiles that match the experimentally obtained velocity profiles very well. The overall rms errors in velocity are 0.6 m/s (13% of maximum slipstream velocity) at 1750

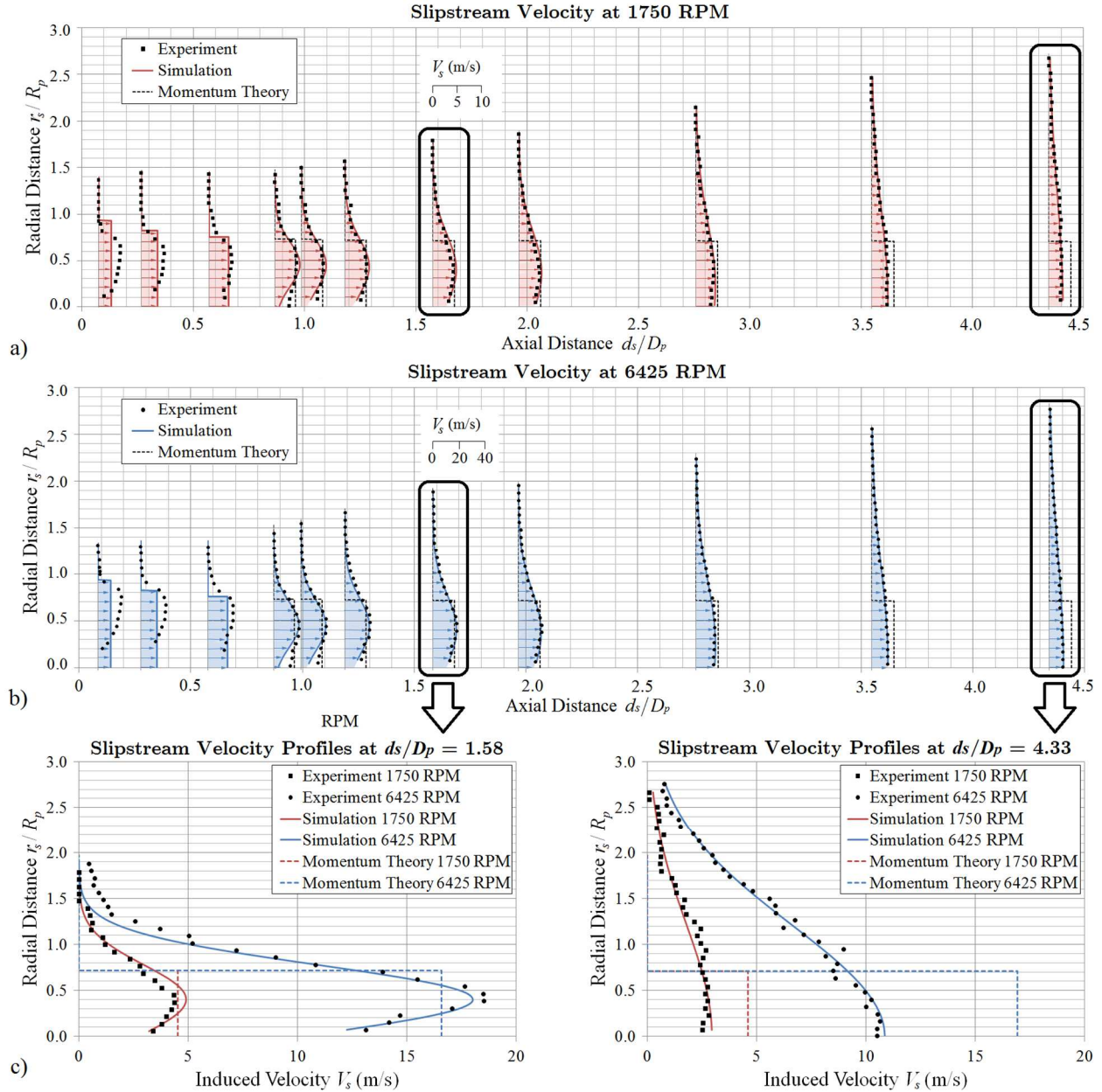


Figure 5.8: Simulation vs experiments at (a) 1750 RPM, and (b) 6425 RPM. Detailed comparison is shown in (c) for $d_s/D_p = 1.58$ (left) and 4.33 (right).

RPM and 2 m/s (12% of maximum slipstream velocity) at 6425 RPM. It can be seen from Figs. 5.8 (a) and (b) that in the zone of flow establishment, the semi-empirical equations under-predict the slipstream velocity near the rotation axis and that the under-prediction vanishes with increasing axial distance. This is expected since the one-term Gaussian functions are unable to approximate the asymmetry in the velocity profiles in the ZFE, as

already discussed. Also shown in Figs. 5.8 (a) and (b) are the predictions of momentum theory in the far-field region (dotted velocity profiles). The discrepancy between the dotted profiles and the experiments with increasing axial distance is evident. Obviously, this is due to the diffusion of the slipstream that is not accounted for by the momentum theory. Plotting the momentum theory predictions show the severity of diffusion in the far-field region of the slipstream, as well as the need for the presented slipstream model that accounts for it.

A detailed comparison is also shown at two axial locations: $d_s/D_p = 1.58$ (left) and 4.33 (right) in Fig. 5.8 (c). Actual values of the slipstream velocity are plotted on the horizontal axis versus normalized radial distance on the vertical axis. A good match is seen between the experiments and simulation at both RPM, thereby validating the propeller slipstream model. As well, this comparison indicates that the empirical coefficients estimated at 5425 RPM are also valid at these higher and lower propeller speeds.

5.6.2 Validation with Different Geometry

The propeller slipstream model is now validated for several other propellers having different geometric characteristics. Using the experimental setup described in Sec. 5.5.1, two other propellers namely APC 11x5.5 (different pitch) and APC 14x4.7 (different diameter) were tested at 3000 RPM and 2815 RPM respectively. Slipstream velocity profiles were measured at two axial locations and are plotted in Fig. 5.9 along with the simulated velocity profiles using the slipstream model. A good match is seen between the model and the experiments with an overall rms error of 0.79 m/s (12% of maximum slipstream velocity) for the APC 11x5.5 propeller and 1 m/s (12% of maximum slipstream velocity) for the APC 14x4.7 propeller. For both propellers, at the location closer to the propeller plane, discrepancy between the model and the experiments can be seen near the rotation axis owing to the previously-explained drawback of the one-term Gaussian functions used in the slipstream

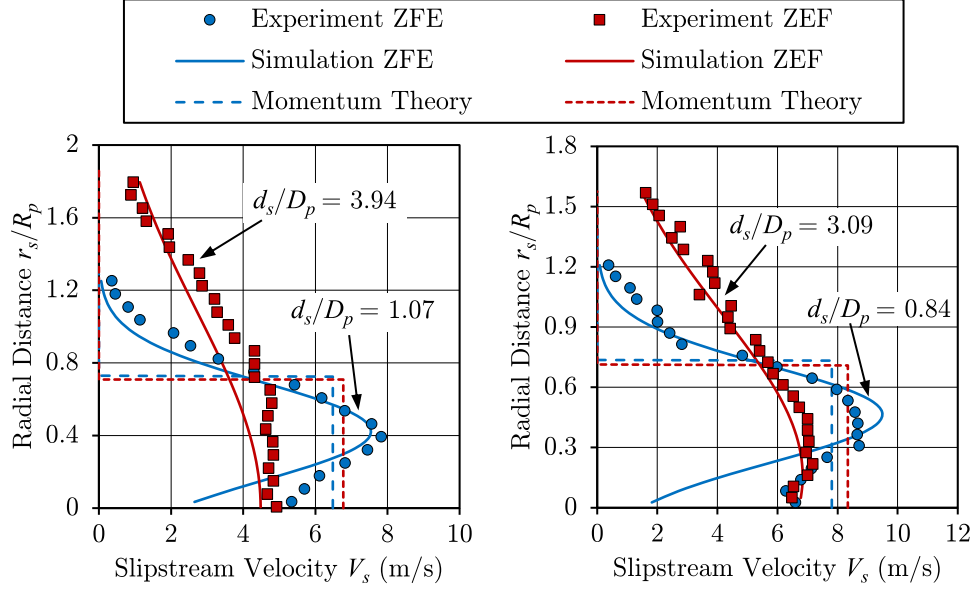


Figure 5.9: Slipstream velocity comparison for APC 11x5.5 (left) and APC 14x4.7 (right).

model. Also shown in Fig. 5.9 are the momentum theory predictions for the slipstream velocity.

5.6.3 Validation with Different Configuration

Further validation of the slipstream model is done in Figs. 5.10 and 5.11 against experimental data from [88] wherein propeller geometry, performance, and slipstream measurements are documented for several commonly used propellers on small/micro UAVs. The slipstream experiments in [88] are done with the propeller arranged in pusher configuration such that the motor is placed upstream of the propeller and thus has no direct influence on the slipstream flow. As a result, there exists higher velocity at the slipstream core, and the velocity profiles in pusher configuration become more asymmetric about the peak value than those in tractor configuration, see Ref. [87]. Experimental data for two propellers namely GWS 9x5 and GWS 5x4.3, is taken from [88] and plotted in Figs. 5.10 and 5.11 respectively. Simulation are run for these propellers using geometry and performance data, also provided in [20], and the results are also plotted in the figures. The simulation results match the experiments very well with overall rms errors in velocity of 1.24 m/s (15% of maximum slipstream velocity) for the GWS 9x5 propeller, and 1.05 m/s

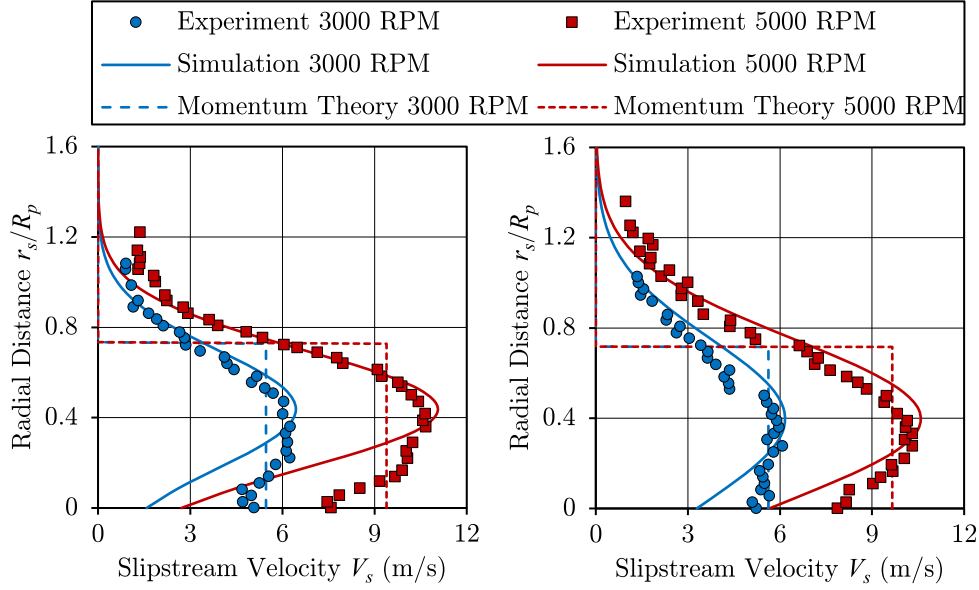


Figure 5.10: Slipstream velocity comparison for GWS 9x5 at $d_s/D_p = 1$ (left) and 1.5 (right).

(15% of maximum slipstream velocity) for the GWS 5x4.3 propeller. As expected, discrepancy near the rotation axis is seen in the zone of flow establishment, since the one-term Gaussian functions used in the model are unable to account for the even-higher asymmetry in the velocity profiles in pusher configuration.

The coaxial contra-rotating propeller arrangement is another common configuration on small UAVs, and in particular on micro air vehicles, and therefore it seems relevant to evaluate the slipstream model for this configuration. In Ref. [87], the performance and

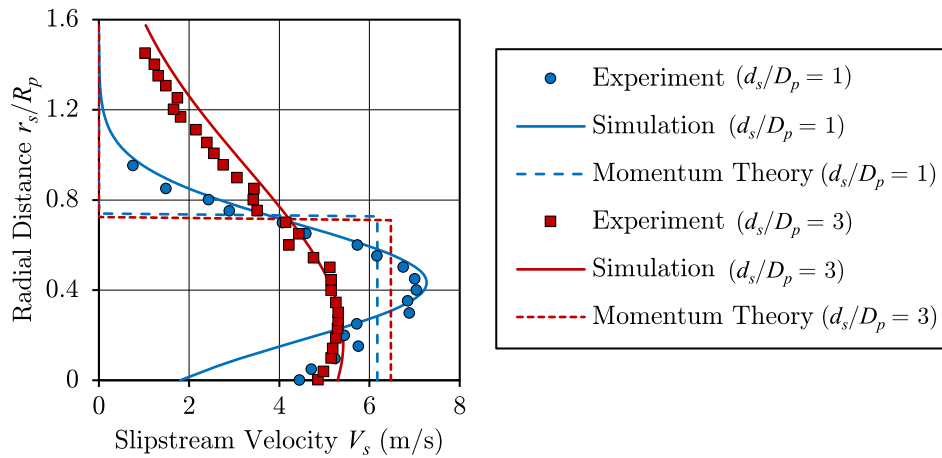


Figure 5.11: Slipstream velocity comparison for GWS 5x4.3.

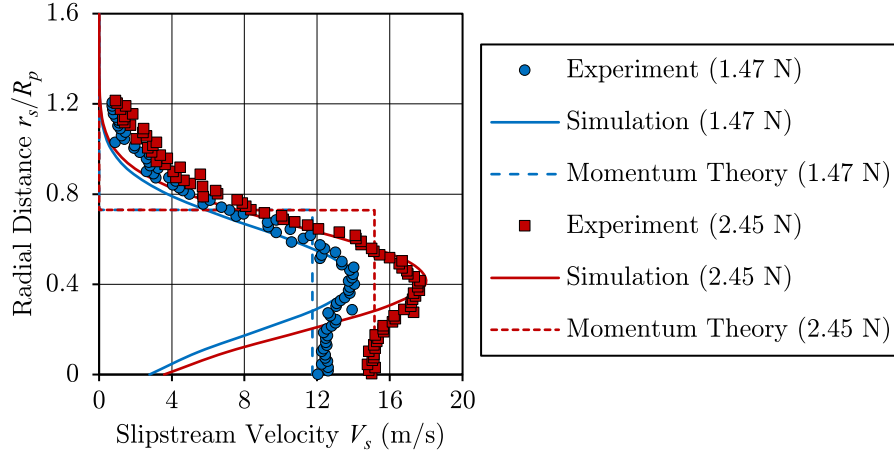


Figure 5.12: Slipstream velocity comparison for coaxial contra-rotating APC propellers.

slipstream velocity profiles are experimentally measured for a coaxial, contra-rotating pair of 140 mm diameter APC propellers (pitch: 114 mm) in both pusher and tractor arrangements. Fig. 5.12 shows the experimentally measured velocity profiles taken from [87], in the pusher arrangement at $d_s/D_p = 0.929$ for two rotational speeds corresponding to $T = 1.47$ N and 2.45 N. Using geometry and performance data also provided in [87], simulation results are plotted in Fig. 5.12. A good match is seen at both RPM except near the rotation axis where the simulation under-predicts the slipstream velocity. As pointed out earlier, this is due to the pusher arrangement of the propeller which causes more asymmetry in the velocity profiles, and thus a relatively larger discrepancy near the rotation axis. It is worth noting from [87], that at $d_s/D_p = 0.5$ and $T = 1.47$ N, the slipstream velocity measured at/near the rotation axis, i.e. $r_s/R_p = 0$ in pusher configuration is significantly higher ($V_s \approx 11$ m/s) than that measured in tractor configuration ($V_s \approx 3$ m/s).

The results shown in all validation tests cover a range of propeller Reynolds numbers (defined as $Re = \rho(0.75R_p\omega)c_{0.75}/\mu$; where $c_{0.75}$ is the chord at 75% blade station, and the rotational speed ω is in rad/s) from around 0.2×10^5 to 1×10^5 . It should be noted that propellers on full scale aircraft operate at Reynolds numbers about one order of magnitude higher. While full scale propellers are not a subject of this work, a cursory check was performed with the slipstream model on an 8.75 ft. diameter propeller using data in [120]

at an axial location $d_s/D_p = 1.6$. A reasonable match was found with an rms error of 1.75 m/s (6.6% of maximum slipstream velocity) at 1000 RPM ($Re \approx 1.5 \times 10^6$), and 4.9 m/s (8.5% of maximum slipstream velocity) at 2200 RPM ($Re \approx 3 \times 10^6$). These results are not shown here as the present work focuses on agile UAVs.

5.7 Analysis and Discussion

In this section, the applicability of the slipstream model to forward flight condition is discussed while also highlighting the importance of the slipstream in the absence of external flow over the aircraft surfaces.

The slipstream model presented in the previous sections is developed based on the assumption that the thruster is static. However, to a certain extent, the model is also applicable to forward flight conditions since one of the inputs to the model, i.e. the thrust coefficient C_T , varies with forward speed (advance ratio) of the aircraft, see Fig. 4.15. When the forward speed increases, C_T decreases and therefore the efflux velocity V_0 given by Eq. (5.12) also decreases. As such, the slipstream velocity distribution, which is based on V_0 , varies with forward speed.

The simulated slipstream velocity at the horizontal tail ($d_s/D_p = 2.8$) of the YAK54 test platform due to the Electrify PowerFlow 10x4.5 propeller running at 4970 RPM is plotted

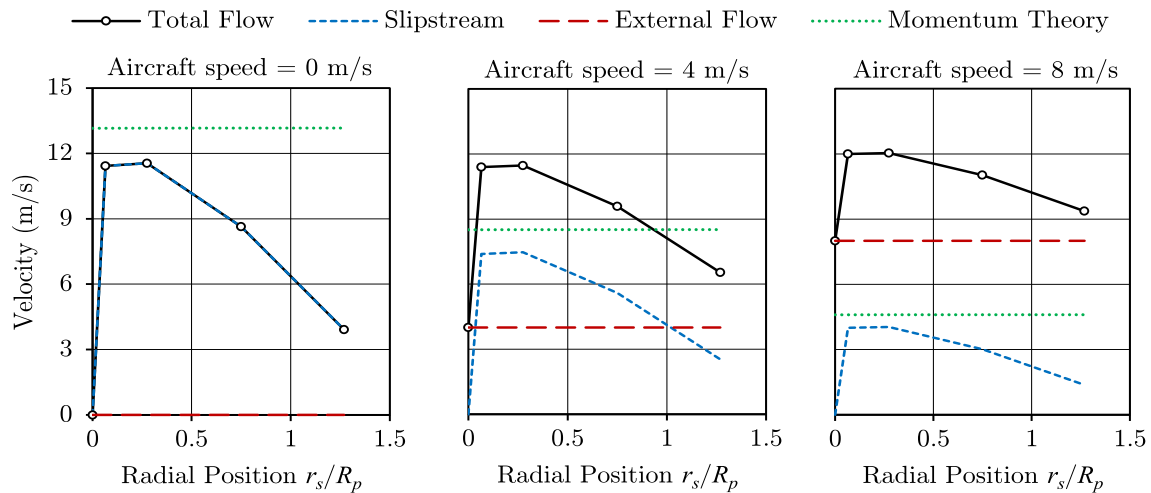


Figure 5.13: Variation of slipstream velocity with aircraft forward speed.

with blue dashed lines in Fig. 5.13. The plots are shown for aircraft forward speeds of 0 m/s (left), 4 m/s (center), and 8 m/s (right). The corresponding advance ratios are $J = 0, 0.19,$ and $0.38,$ for which the thrust coefficients are $0.1563, 0.1263,$ and 0.085 (from the thruster model in Chap. 4) respectively. It can be seen that the slipstream velocity decreases with the aircraft's forward speed. For comparison, the momentum theory predictions are also plotted (green dotted lines), which show a similar decrease in slipstream velocity. Hence, the trend predicted by the presented slipstream model in forward flight matches that of the momentum theory.

Another interesting thing to note from Fig. 5.13 is that during flight of agile UAVs, the total flow velocity (sum of slipstream velocity and external flow velocity) on slipstream-immersed surfaces remains nearly constant. When the aircraft is flying at high forward speed (right plot), most of the total flow is due to the external flow with a small contribution from the slipstream. As the aircraft slows down during maneuvers etc., the slipstream effect becomes more dominant while the external flow diminishes. So much so, that at zero forward speed (left plot), e.g. during a hover maneuver, the total flow velocity comes from the slipstream with little or no external flow. This highlights the importance of the slipstream effect for agile UAVs as it allows, more or less, the same control authority in both conventional and maneuvering flight.

A brief discussion on the entrainment phenomenon in the slipstream is presented here. As pointed out in Sec. 5.3, from the efflux plane onwards, i.e. in the far-field region, the propeller slipstream is acted upon only by the viscous/shear forces and turbulence, and thus the slipstream behaves as a turbulent jet. An essential phenomenon pertinent to turbulent jets is the entrainment of ambient fluid through mixing across the jet boundary, which is responsible for an increase in mass flow rate and the spread of the jet with axial distance [91–93]. Thus, it is worthwhile to look at the mass flow rate \dot{m}_s and entrainment rate Ψ as functions of the axial distance from the propeller plane. The entrainment rate is defined as

the ratio of entrained mass flow rate at any section to the initial mass flow rate at the propeller plane \dot{m}_{s0} , i.e.,

$$\Psi = \frac{\dot{m}_s - \dot{m}_{s0}}{\dot{m}_{s0}} \quad (5.25)$$

The mass flow rate and entrainment rate are plotted in Fig. 5.13 for the test propeller Electrify 10x4.5 propeller at 6425 RPM. The mass flow rate at the propeller plane is calculated using $\dot{m}_{s0} = \rho(\pi R_p^2) V_{ia,avg}$ to be 0.53 kg/s. At sections downstream of the propeller plane, the mass flow is calculated using:

$$\dot{m}_s = 2\pi\rho \sum_{r_s=0}^{R_s} r_s V_s \Delta r_s \quad (5.26)$$

where the slipstream boundary R_s in the far-field region is taken to be the radial location where the slipstream velocity decreases below 1% of $V_{s,max}$.

Both the experiment and simulation show the mass flow rate and entrainment rate to be nearly constant in the near-field region ($d_s/D_p < 0.764$). The offset between simulation and experiments in the near-field region is expected since the slipstream model approximates the velocity profiles with momentum-averaged values in that region, see Fig. 8 (b). In the far-field region, the mass flow rate increases nonlinearly showing considerable entrainment of ambient air by the turbulent slipstream. It is seen that the offset between the simulation

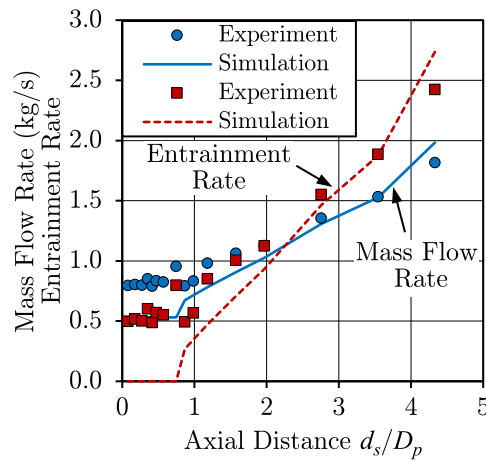


Figure 5.14: Mass flow rate and entrainment rate vs axial distance.

and experiments reduces in the far-field region as the slipstream model better approximates the velocity profiles there. It may be noted that similar values for entrainment rates have also been observed in [92, 93] for turbulent jets.

Chapter 6

Validation

This chapter deals with the validation of the agile UAV model which is assembled by integrating the kinematics & dynamics, aerodynamics, thruster, and slipstream sub-models from the previous chapters. Although each of the sub-models has been validated thoroughly, their combined effects in the agile UAV model needs validation.

Experimental data gathered from actual flight tests would have been ideal for validation. In that case, the model would be run with pilot inputs recorded in flight tests. The simulated response (aircraft states) would then be compared to that measured in flight tests. However, this task becomes challenging when being done in open-loop particularly for inherently unstable systems like agile UAVs, even if the instability is mild. This is because uncertainties and unmodeled effects are always present, and hence some degree of error will exist between the model and real system. In simulation, an open-loop input (or even slightly different initial conditions) to unstable systems will cause this error to propagate over time and eventually dominate the resultant motion.

In light of this, validation based on flight data is not pursued here. However, controller development, closed-loop flight tests, and subsequent flight test validation are recommended for future work. In this chapter, quantitative validation is done via static bench tests in which the entire aircraft is mounted on a force/torque sensor in order to measure the forces and moments generated by the aircraft under different conditions.

A final qualitative validation is also performed via real-time pilot-in-loop simulations where a professional RC pilot, who has experience flying the real aircraft, performs extreme RC maneuvers in the simulator. A discussion on unsteady aerodynamic effects during these maneuvers is also presented at the end of this chapter.

6.1 Agile UAV Dynamics Model

The agile UAV dynamics model is implemented in Matlab/Simulink according to the schematic of Fig. 6.1 for the YAK54 test platform introduced in Chap. 2. The geometric parameters of this test platform required for simulation are given in Table 6.1. The wing and horizontal tail have port and starboard sides which are mirror images of each other, and only the starboard side parameters are stated in Table 6.1.

The kinematics and six-dof equations of motion are presented in Chap. 2 along with the various parameters in the equations, including aircraft mass, moments of inertia, etc. determined for the test platform. The aerodynamic and thruster forces are evaluated from the aerodynamics model presented in Chap. 3 and the thruster model presented in Chap. 4. The slipstream velocity required in the aerodynamics model is calculated using the slipstream model given in Chap. 5.

Inputs to the model are the four PW signals (dashed arrows): one for thrust, and three for control surface deflections (aileron, elevator, and rudder). The thrust PW is input to the thruster model in which it is converted to the desired voltage by the ESC (see Sec. 4.1). The deflection PWs are converted to control surface deflections (δ_a , δ_e , δ_r) for the test platform using input-to-deflection relationships given in Sec. 2.5.3. The model outputs are the aircraft states: UAV body velocity \mathbf{V}_{cg}^B , body rate $\mathbf{\Omega}^B$, attitude e , and position \mathbf{p}^I .

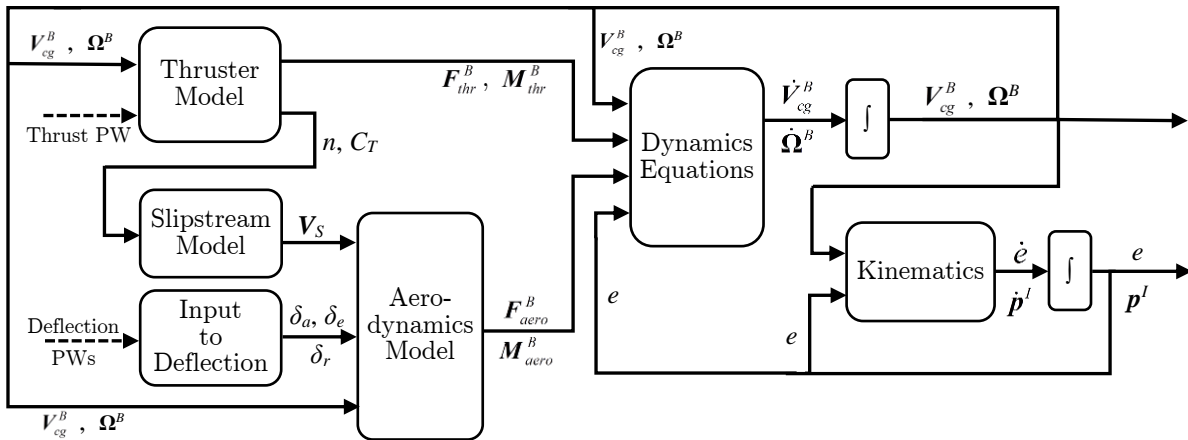


Figure 6.1: Schematic of the agile UAV model.

TABLE 6.1
YAK54 SEGMENTS

	Segment No.	Span (m) b	Chord (m) c	Flap chord (m) c_f	Position vector (m) $\mathbf{r} = [r_x, r_y, r_z]^T$
Wing (Starboard) AR = 1.93	1	0.046	0.278	0	[0.078, 0.023, -0.007]
	2	0.068	0.258	0.109	[0.075, 0.079, -0.007]
	3	0.068	0.233	0.100	[0.072, 0.147, -0.007]
	4	0.089	0.205	0.090	[0.068, 0.225, -0.007]
	5	0.089	0.173	0.078	[0.063, 0.314, -0.007]
	6	0.050	0.064	0	[0.060, 0.384, -0.007]
	7	0.050	0.083	0.083	[-0.011, 0.384, -0.007]
Horizontal Tail (Starboard) AR = 1.26	1	0.016	0.093	0.021	[-0.399, 0.008, -0.007]
	2	0.035	0.138	0.071	[-0.415, 0.035, -0.007]
	3	0.090	0.142	0.086	[-0.427, 0.095, -0.007]
	4	0.040	0.123	0.123	[-0.434, 0.161, -0.007]
Vertical Tail AR = 1.64	1	0.064	0.175	0.125	[-0.500, 0, 0.025]
	2	0.058	0.164	0.114	[-0.497, 0, -0.035]
	3	0.058	0.154	0.104	[-0.494, 0, -0.093]
	4	0.053	0.127	0.127	[-0.505, 0, -0.147]
Fuselage AR = 0.2	1	0.038	0.714	0	[0.080, 0, 0.050]
	2	0.038	0.714	0	[0.080, 0, 0.013]
	3	0.034	0.714	0	[0.080, 0, -0.024]
	4	0.034	0.714	0	[0.080, 0, -0.058]

The entire model is implemented in Simulink with the thruster, aerodynamics and slipstream sub-models as pre-compiled Matlab codes. The dynamics equations are propagated using a variable time-step Runge-Kutta integrator (ODE45). For real-time simulation, the implementation is a bit different, and is discussed later in Sec. 6.3.

6.2 Static Bench Tests

A quantitative validation of the agile UAV model is done via static bench tests, by comparing simulated forces and moments to those obtained through static bench tests.

6.2.1 Experimental Setup

The fully assembled YAK54 was mounted on an ATI Gamma force/torque (F/T) transducer which measures force and torque in the sensor frame (superscript S) with a high resolution (0.028 N in x^S and y^S , 0.056 N in z^S , and 0.0014 N.m in torque) and sampling rate of 1 kHz. The setup is shown in Fig. 6.2. The propwash on the segments a.c. was measured using a

Reed hotwire anemometer which has a sampling rate of 1 Hz and a resolution of 0.01 m/s in the range 0.2 – 5 m/s, and 0.1 m/s in the range 5.1 – 25 m/s. An Arduino board was used to send PW signals to the servos and ESC to produce the desired deflections and run the motor at desired RPM.

Experiments were performed at three RPMs: 1585 (low), 3475 (moderate), and 4900 (high). The three control surfaces were deflected individually as well as in all possible double and triple combinations including aileron-elevator, aileron-elevator-rudder and so on. Post-processing of the F/T data includes: 1) removing measurement noise via a third-order zero-phase Butterworth low-pass filter with a cutoff frequency of 10 Hz, 2) removing the setup drag from the data, and 3) transformation of forces and moments from the sensor frame to the aircraft body frame defined in Sec. 2.1.

6.2.2 Results and Discussion

For simulating the static bench conditions, $[u, v, w]^T$ and $[p, q, r]^T$ were set to zero in the aircraft model. The external force and moment (excluding gravity) acting on the agile UAV are obtained from the simulation and compared with experimental results in the next sections.

Slipstream Velocity

It is also worthwhile to compare the simulated and experimentally measured slipstream velocity at each segment a.c. This is done in Fig. 6.3 for the segments on the wing, horizontal

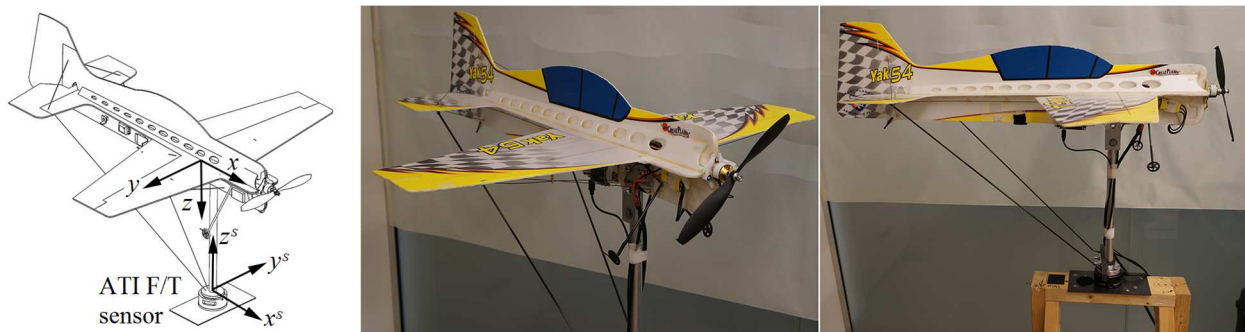


Figure 6.2: Experimental setup.

tail, and vertical tail at 3475 RPM. Experimental measurements were taken at each segment aerodynamic center on both the upper and lower surfaces. For the wing, the slipstream velocity drops to around zero at the fourth segment (on both starboard and port sides) from the wing root, and thereafter remains zero for the remaining three segments on each side; hence velocity is plotted only up to the fourth segment.

For the wing and horizontal tail, it is seen that the slipstream velocity on the upper starboard side is similar to that on the lower port side, and vice versa. This is expected because of the clockwise swirl from the propeller impinges on the upper starboard and lower port sides, increasing the velocity there, but has no effect on the lower starboard and upper port sides. A similar effect of the clockwise swirl can also be seen on the vertical tail: for the first segment which is below the center-line, the slipstream velocity measured on the starboard (right) side is higher than the corresponding port side. For segments that are above the center-line, the velocity measured on the port (left) side is always higher than that on starboard side.

A good match is seen between the simulated and experimental results. Although the slipstream model in Chap. 5 was developed with an isolated propeller, it performs very well in presence of the airframe. The momentum theory predictions for the slipstream velocity

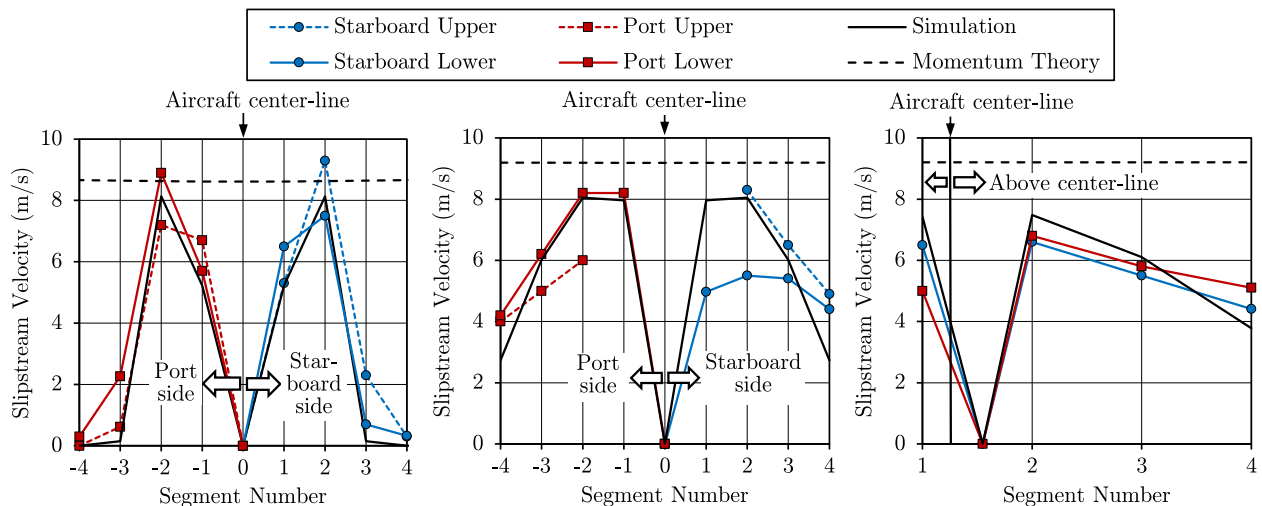


Figure 6.3: Simulated vs experimental slipstream velocity.

are also shown on the plots with a black dashed line. Since momentum theory does not take diffusion into account, it over-predicts slipstream velocity particularly for segments located far-downstream of the propeller such as those on the horizontal and vertical tail.

Individual Deflections

Simulated external forces and moments (excluding gravity) are compared against experiments for individual deflections of the aileron, elevator, and rudder at all three RPMs. The results for the elevator, rudder, and aileron deflection tests are shown in Figs. 6.4 to 6.6. For the elevator, F_y and M_z are not plotted, while for the rudder F_z is not plotted since these are zero for both experiments and simulation. For the same reason, only F_x and M_x are plotted for the aileron. For the aileron tests, the plane was cut as shown in Fig. 6.6 (a) to remove any downwash effect of the wing on the horizontal and vertical tail, so that the force and moment obtained are purely due to aileron deflection. More so, these aileron tests were carried out at relatively lower RPMs, i.e. 1395 RPM, 3125 RPM, and 4422 RPM.

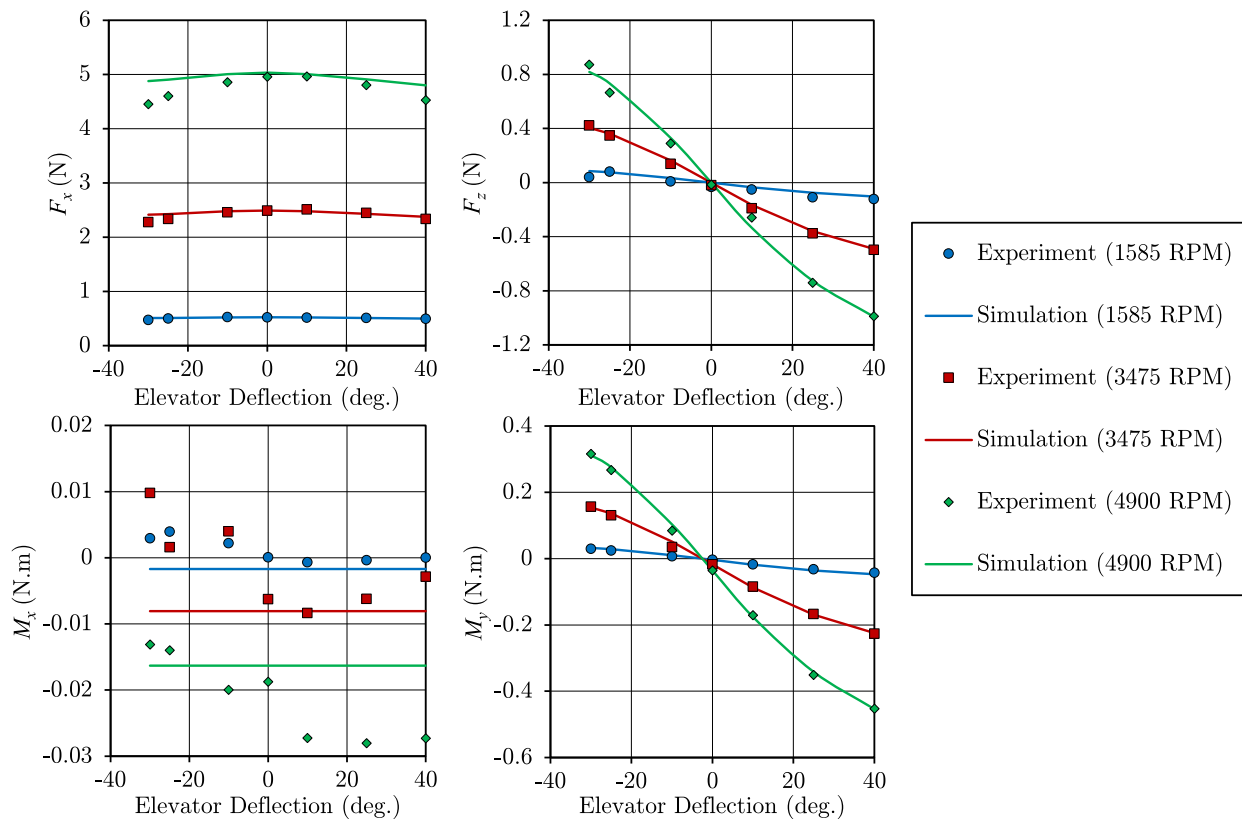


Figure 6.4: Simulated vs experimental force and moment for elevator tests.

From the figures, it is seen that the simulation agrees very well with experiments. The F_x force is equal to the thrust (acting in the $+x$ direction) minus the airframe's aerodynamic drag (acting in the $-x$ direction). On deflecting the control surfaces (whether positive or negative), the drag increases and hence F_x decreases.

From the elevator test results in Fig. 6.4, the F_z force is zero for zero deflection. This is expected for the test platform with all flat plate surfaces that generate no lift at zero angle of attack and deflection. For positive elevator deflections (TE down), the horizontal tail generates a lift force (negative F_z), which gives rise to a negative M_y (pitch) moment. A small pitch moment also exists at zero elevator deflection due to the drag forces of each segment acting at a distance from the c.g. The roll moment M_x is due to the thruster reaction torque minus the swirl effect (see Sec. 5.1.1), which remains unaffected by elevator deflection. The abrupt variations in experimental measurements are attributed to sensor noise and misalignment in the experimental setup.

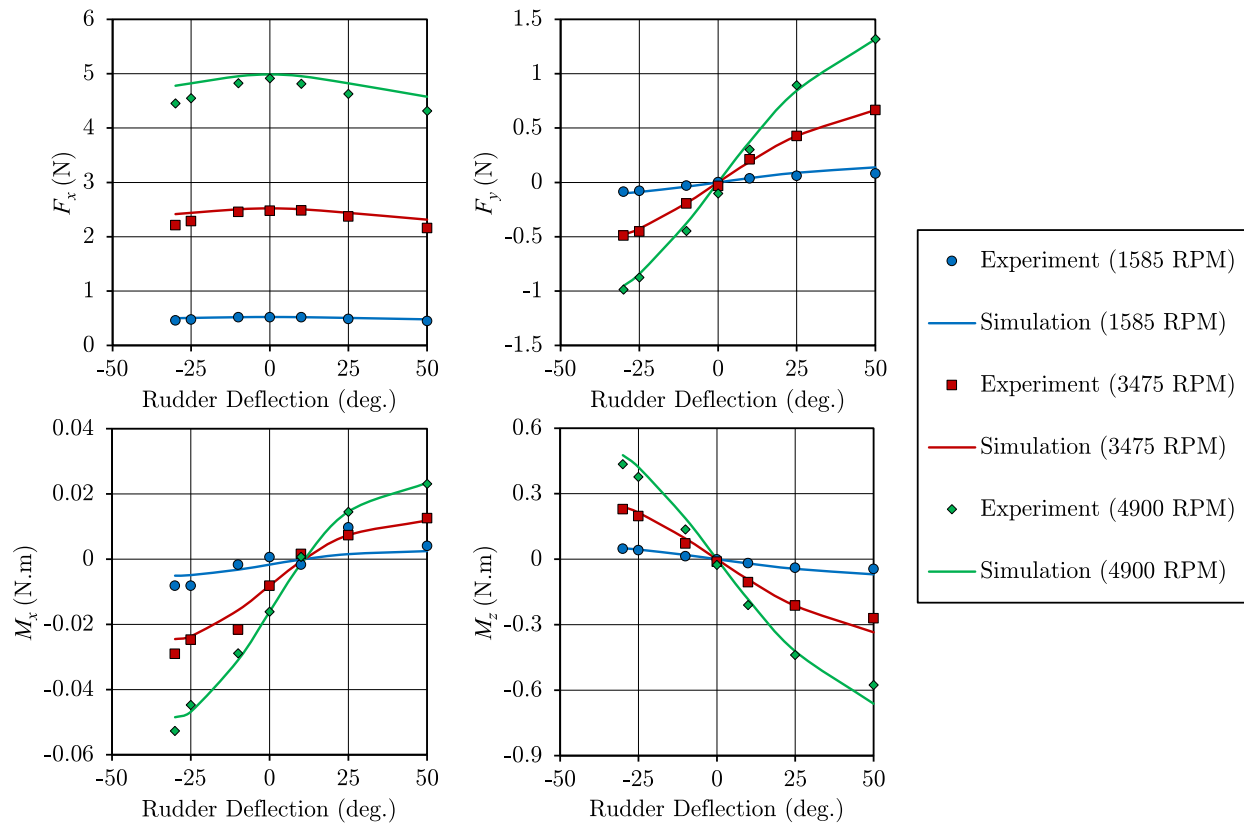


Figure 6.5: Simulated vs experimental force and moment for rudder tests.

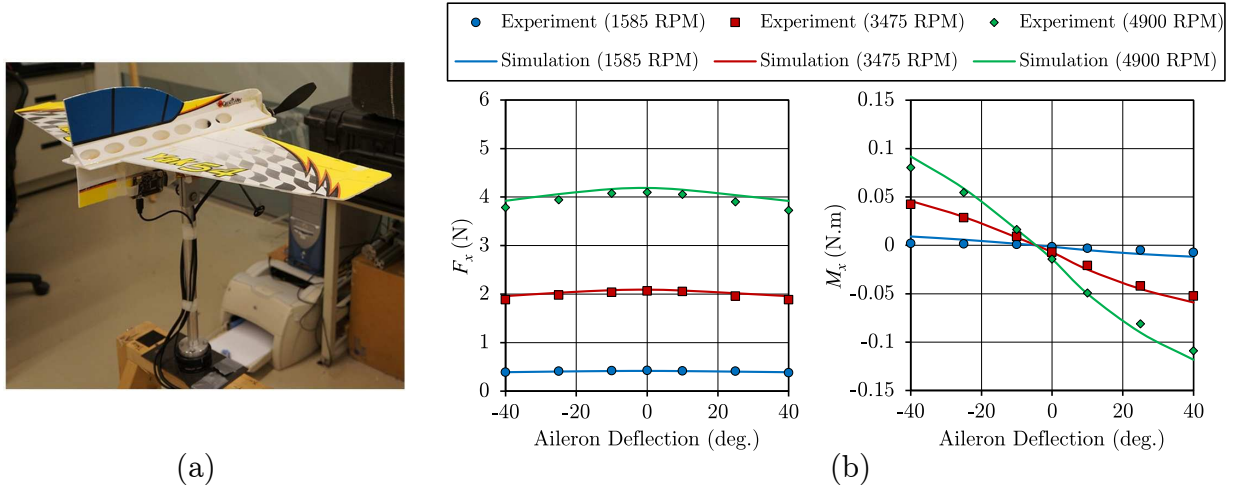


Figure 6.6: (a) Experimental setup, and (b) simulated vs experimental force and moment for aileron tests.

From the rudder test results in Fig. 6.5, the F_y force is zero at zero deflection. For positive rudder deflections (TE left), the vertical tail generates a positive side force F_y , which causes a negative M_z (yaw) moment. At 0 deg. deflection, the roll moment M_x is due to the thruster reaction torque minus the swirl effect as stated previously. For positive rudder deflections, the positive F_y force produces a net positive roll moment since most of the rudder (3 out of 4 segments) is above the aircraft centerline.

From the aileron test results of Fig. 6.6, F_x at zero deflection is lower compared to previous Figs. 6.4 and 6.5. This is expected since the tests were performed at lower RPMs and hence lower thrust values. For the roll moment M_x , the value at zero deflection is due to the thruster reaction torque minus the swirl effect. On positive aileron deflection, the roll moment becomes further negative.

Combined Deflections

To compare aerodynamic interference effects, all possible double and triple deflection combinations such as aileron-elevator, aileron-elevator-rudder were tested at all three RPMs. Herein only the results for aileron-elevator deflection at moderate (3480) RPM are shown in Fig. 6.7. Overall the agreement between simulation and experiments is good.

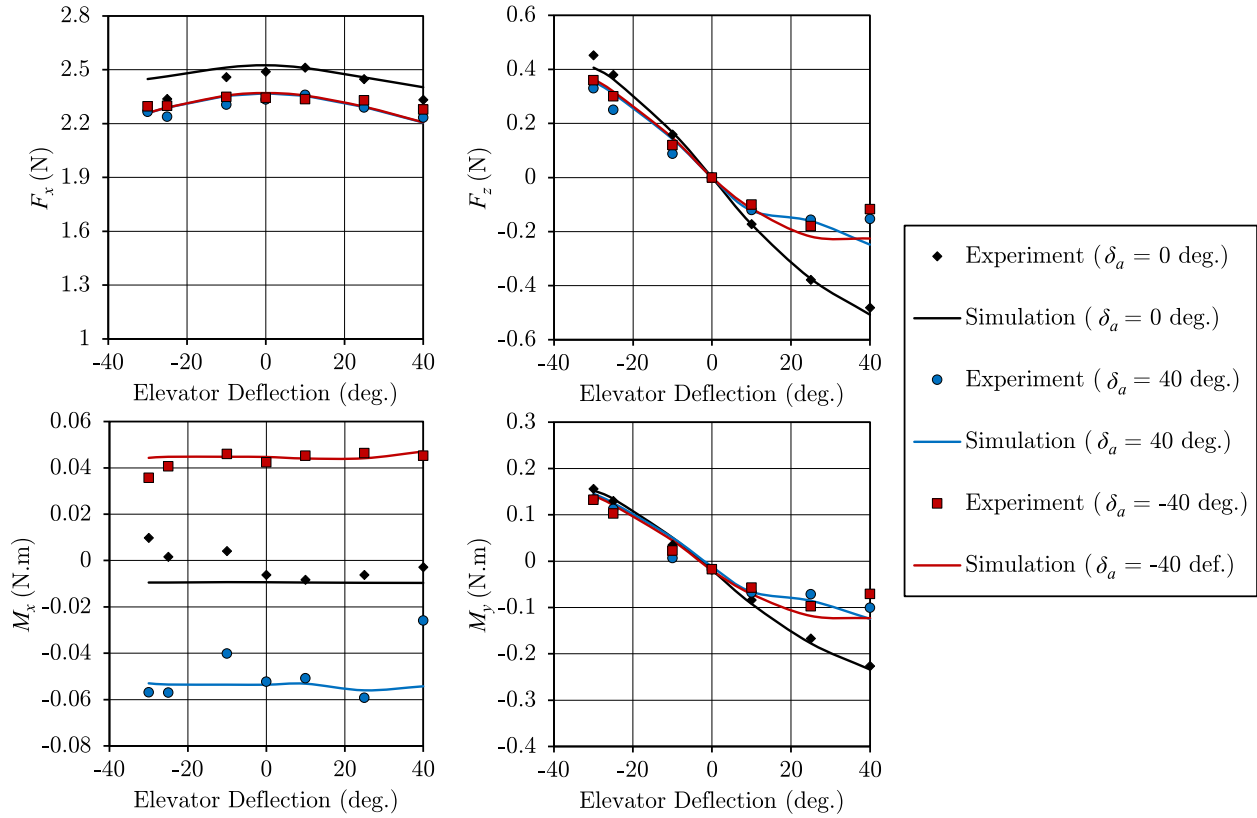


Figure 6.7: Simulated vs experimental force and moment for aileron-elevator tests.

For experiments, the aileron was deflected 0, ± 10 , ± 25 and ± 40 deg., and at each aileron deflection, the elevator was deflected from -30 to $+40$ deg. Figure 6.7 shows the force/moment variation with elevator deflection for $\delta_a = -40$ deg. (minimum), 0 deg. and $+40$ deg. (maximum).

The F_x results for $\delta_a = \pm 40$ deg. are offset (lower) from those at $\delta_a = 0$ deg., simply because of the additional drag associated with aileron deflection. The roll moment M_x for $\delta_a = 0$ deg. is solely due to thruster reaction torque minus swirl effect, but at $\delta_a = +40$ deg., there is an additional negative roll moment due to aileron deflection. Similarly, at $\delta_a = -40$ deg., there is a net positive roll moment since the aileron deflection produces a positive roll moment that overcomes the negative reaction torque of the thruster.

From the F_z and M_y plots, it is evident that the elevator is less efficient in producing lift force (and consequently pitch moment) with ailerons deflected. This is expected since aileron

deflection produces some lift on the wing, thereby causing a downwash on the horizontal tail, reducing its angle of attack and lift.

6.3 Real-Time Pilot-In-Loop Simulations

As a final validation, the simulation was set up to run in real-time with the pilot-in-loop. A professional RC pilot who has experience flying the actual YAK54 test platform, tested the simulator by flying various RC maneuvers including harrier, knife-edge, inverted spins etc. His overall comments were that the simulation behaves much like the real aircraft.

6.3.1 Simulation Environment

In order to set up a real-time pilot-in-loop simulation, some additional steps were taken which are briefly discussed below.

- Firstly, it was ensured that all the sub-models of the agile UAV model are able to run in real-time, i.e. they do not involve intensive iterations. Since real-time simulation was one of the goals from the onset of this work, most sub-models were suitable for real-time implementation and therefore were embedded directly into the overall UAV simulation. The propeller part of the thruster model, however, is iterative, and therefore it was run offline for the test platform propeller (Electrifly PowerFlow 10x4.5) for a range of advance ratios: $J = 0$ to 1, and propeller tilt angles: $\varphi_p = 0$ to 180 deg. The resulting propeller force and moment coefficients \mathbf{CF}_p , $\mathbf{CM}_p = f(J, \varphi_p)$ are stored as look-up tables called the propeller maps. During simulation, the advance ratio and propeller tilt angle are calculated, and the coefficients are looked up from the propeller maps using these values. Then these are converted into the propeller force and moment (refer to Chap. 4) to be used in the UAV model.
- A standard RC joystick was incorporated in the simulation to allow pilot inputs. The joystick inputs were normalized from 0 (minimum joystick position) to 1 (maximum joystick position), and then linearly transformed to PW inputs such that

0 on the joystick represents $PW = 1000 \mu s$, 0.5 on the joystick is $1500 \mu s$, and 1 on the joystick represents $2000 \mu s$.

- One important component of the pilot-in-loop simulation is the visual interface for the pilot. Since RC pilots fly small aircraft by relying on their position/orientation with reference to the environment, they need a realistic visual feedback that contains scenery, objects etc. In this work, X-Plane – a highly customizable commercial simulator, was used to provide the necessary visual feedback to the pilot. A 3D model of the YAK54 was made using its own airplane maker. A plugin written in C++ was installed in X-Plane to turn off its physics and instead, take position, orientation and control surface deflection data from external source (in this case the output of our simulation in Simulink). Similarly, a C++ code was read via Simulink S-function to export simulation data to X-Plane.

6.3.2 Simulated Maneuver Results

Flight simulation results for several well-known maneuvers flown by the pilot are presented here. Each maneuver is discussed briefly in terms of the aircraft states and trajectory. In the figures that follow, the aircraft trajectory is shown by the colored line where the color represents progression of time: blue color is the start of the flight while the red color marks the end. Also an outline of the YAK54 with corresponding attitude is drawn along the trajectory at different time steps. For each maneuver, the scale and time step are stated in the description as well as in the figure caption.

For ease of understanding:

- 1) The position is specified in the inertial North-East-Down (NED) frame, such that the position p_D is positive downwards. All flights start at $[p_N, p_E, p_D]^T = [0, 0, 0]^T$.
- 2) Aircraft attitude is plotted in terms of Euler angles instead of quaternions. This is done by transforming the quaternions (obtained from simulation) to Euler angles using the relationships provided in Chap. 2.

- 3) Aircraft velocity is plotted in terms of the total velocity V_{cg} , angle of attack α and sideslip angle β instead of body velocity. These are obtained from the body velocity as follows: $V_{cg} = (u^2 + v^2 + w^2)^{0.5}$, $\alpha = \text{atan2}(w, u)$, and $\beta = \text{asin}(v/V_{cg})$.
- 4) Control inputs are plotted in terms of aileron, elevator, and rudder deflections (δ_a , δ_e , and δ_r), and thruster RPM (δ_t) instead of PW signals.

The list of maneuvers flown also includes those presented in Refs. [16, 17, 66]. These references are the only known works wherein aircraft state and trajectory data is presented for several well-known RC maneuvers. Although that data is also produced by a simulation, it is found to be realistic by RC professional pilots having over 30 years of experience. Here comparison will be made against these works wherever necessary.

Tail-slide Maneuver

A simulated tail-slide maneuver is shown in Fig. 6.8 with the aircraft drawn at a scale of 3.3 times actual size, and a time step of 0.7 s. The relevant aircraft states are plotted in Fig. 6.9. The aircraft starts in a nose up position with the following initial conditions taken from [16]: $[u, v, w]^T = [p, q, r]^T = [p_N, p_E, p_D]^T = [0, 0, 0]^T$, and $[\phi, \theta, \psi]^T = [180, 88, 0]^T$ deg. No control inputs are given during this maneuver, i.e. $\delta_a = \delta_e = \delta_r = 0$ deg. and $\delta_t = 0$ RPM.

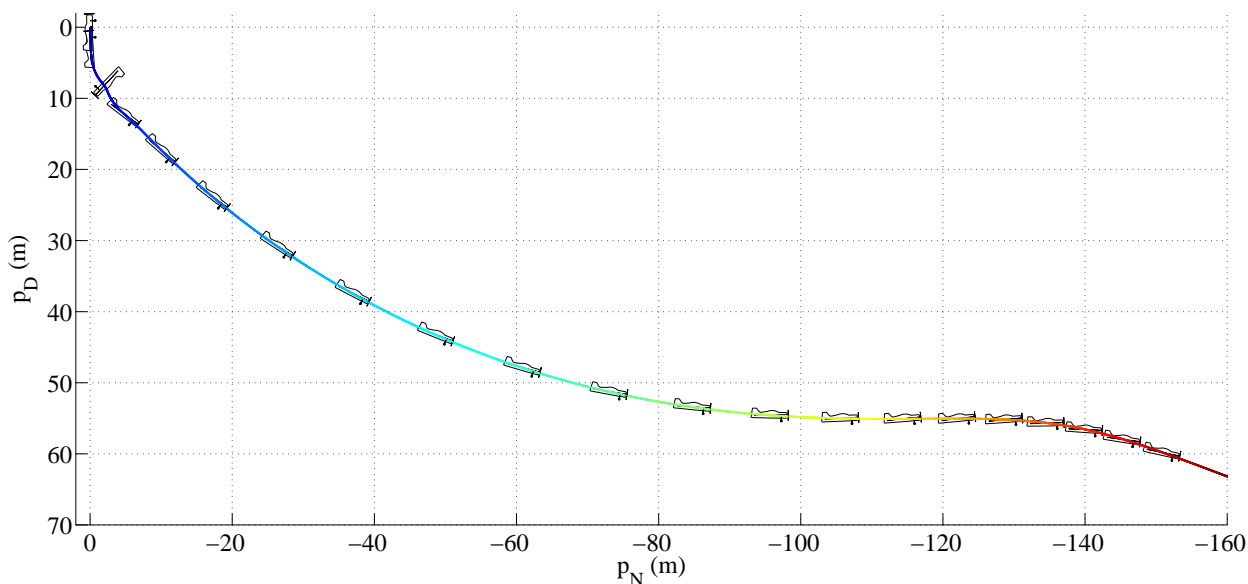


Figure 6.8: Tail-slide maneuver (aircraft scale = $3.3 \times$ actual size; time step = 0.7s).

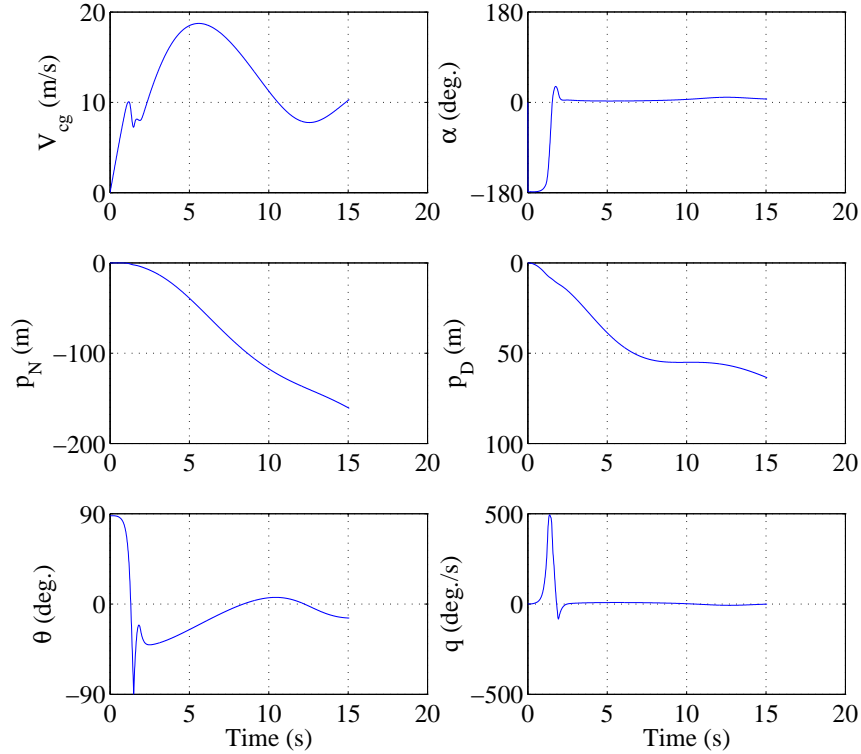


Figure 6.9: Aircraft states for the tail-slide maneuver.

Since the aircraft is statically unstable in this position, it moves briefly in the rearward direction before it “nose-flips” towards the ground at around $t = 1$ s due to the large pitch rate. During this flipping: the velocity drops slightly, the pitch angle passes through -90 deg., and the angle of attack becomes positive. Thereafter, the aircraft glides and enters its phugoid mode. The aircraft states in Fig. 6.9 show similar trends to those observed in [16]. Some difference in magnitudes are expected since the test platform used in this work (with a mass of 465 g) is almost twice as heavy as the aircraft used in [16].

Harrier Maneuver

Figures 6.10 and 6.11 show a high angle of attack flight flown by the pilot in the simulator. The aircraft scale is set to 2.5 times actual size drawn at every 1.5 s. It is commonly referred to as a harrier maneuver in RC parlance. The maneuver is characterized by slow forward flight wherein the aircraft operates in the post-stall regime and hence most of the aircraft weight is supported by the thruster. It must be noted that such post-stall flight is only possible due to the high thrust-to-weight ratio of the UAV.

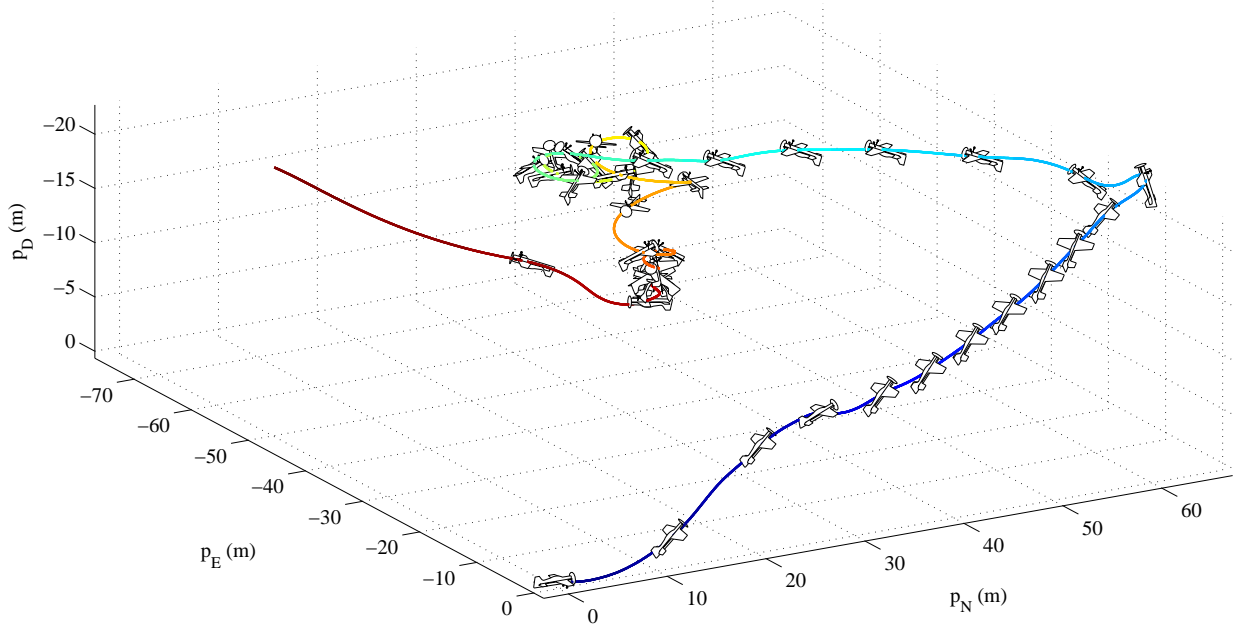


Figure 6.10: Harrier maneuver (aircraft scale = $2.5 \times$ actual size; time step = 1.5 s).

The aircraft starts with the following initial conditions: $[u, v, w] = [2, 0, 0]^T$ m/s, and $[p, q, r]^T = [p_N, p_E, p_D]^T = [\phi, \theta, \psi]^T = [0, 0, 0]^T$. The pilot first brings the aircraft to a higher altitude ($p_D = -10$ m) and then at $t = 5$ s, inputs a negative δ_e (-12 deg.) to pitch up the aircraft into an upright harrier maneuver which is characterized by a roll of 0 deg. and a large pitch of ~ 45 deg. As the UAV pitches up, much of the thrust (vertical component) goes to support the aircraft weight, and only a small horizontal component is left to keep the aircraft moving forward. Hence V_{cg} decreases from around 10 m/s to 4 m/s. The upright harrier maneuver is maintained for around 10 s. During the entire maneuver, small fluctuations in roll exist which are constantly being compensated by the pilot. Although small, these can be seen in the roll rate as well as the aileron input plots. This phenomenon called wing-rock is commonly encountered in the real world.

At $t \approx 15$ s, the pilot increases the elevator deflection (to -30 deg.) to pitch the aircraft over. This can be seen in the θ plot as the pitch rises to 90 deg. and over. The pilot quickly stops the aircraft from falling over to the other side by giving a positive δ_e (+15 deg.). Thereafter the aircraft enters the inverted harrier ($\phi = 180$ deg., and $\theta \approx 40$ deg.) which is maintained

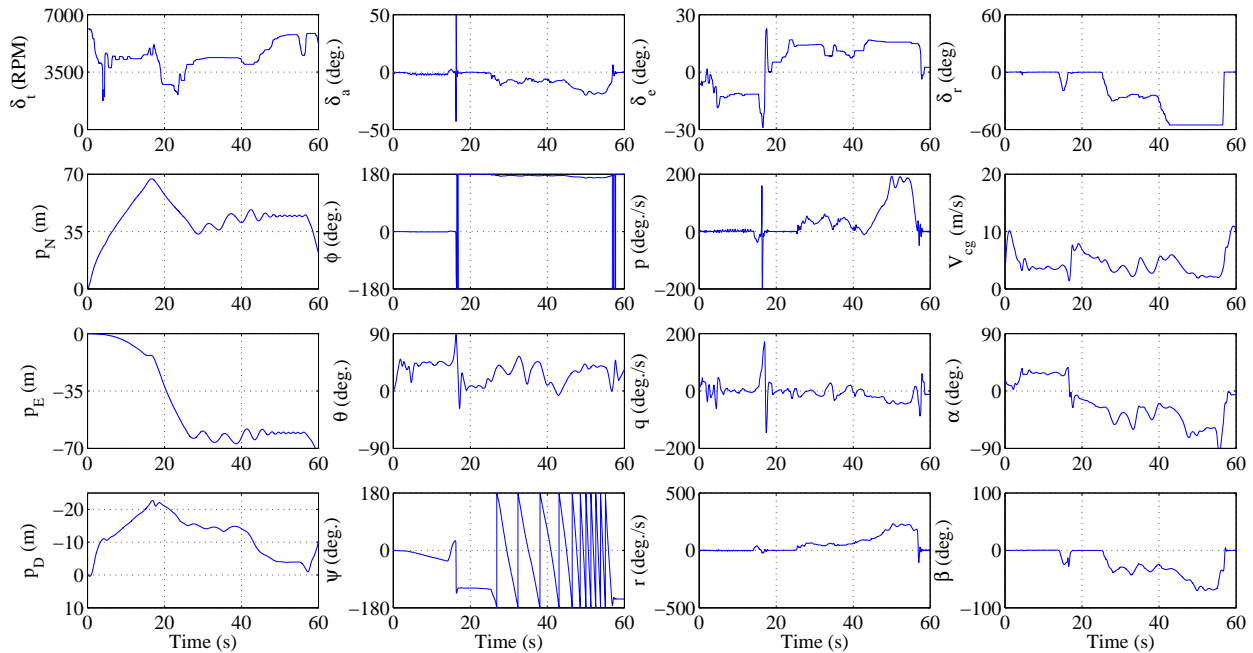


Figure 6.11: Aircraft states for the harrier maneuver.

for another 10 s. The angle of attack is negative for this part of the maneuver. It can be seen from the roll rate and aileron input plots that, as compared to the upright harrier flight, the roll fluctuations are reduced. Again, this is commonly observed in real-world.

At around 25 s, rudder input ($\delta_r = -28$ deg.) is given. While in an inverted harrier, the aircraft starts spinning in a circle of ~ 6 m diameter. This can be seen from the sinusoidal trajectory of the p_N and p_E positions, as well as from the ψ plot. As expected, the aircraft experiences sideslip ($\beta \approx -32$ deg.) during spinning.

After 4 turns (at around 42 s), the rudder input is increased to -53 deg. causing the aircraft to spin into a tighter circle of ~ 1 m diameter. The sideslip increases to around -70 deg. Due to the large drag incurred by the rudder, the aircraft loses some altitude. The drop in altitude is arrested by increasing the thruster input to around 5780 RPM. After 7 turns, the rudder input is relieved and the pilot pulls the aircraft out of the maneuver into inverted flight.

Hover Maneuver

One of the most popular RC maneuver is the hover maneuver in which the pilot brings the aircraft into a stationary nose up position. The thrust is just enough to balance the weight

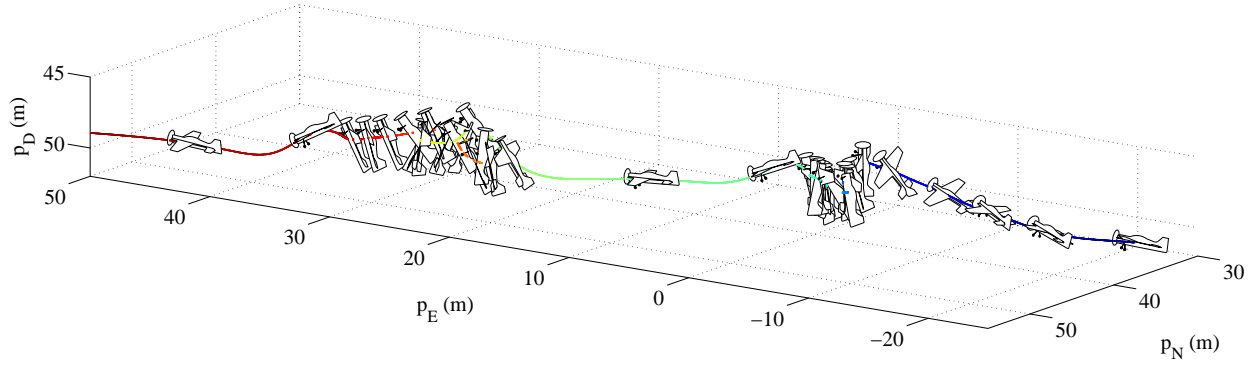


Figure 6.12: Hover maneuver (aircraft scale = $2.5 \times$ actual size; time step = 0.9 s).

of the aircraft, while the slipstream from the thruster keeps the control surfaces effective. Some aileron input is required to stop the aircraft from rolling due to thruster's reaction torque.

Figures 6.12 and 6.13 show the hover maneuver flown by the pilot in simulation. The aircraft is drawn at every 0.9 s with a scale of 2.5 times actual size. At around $t = 3$ s, the pilot pitches up the aircraft by giving a negative δ_e (~ -20 deg.) and increases the thruster input from around 3500 RPM to 4500 RPM since the thruster has to support all the aircraft weight in the hover. The pitch angle reaches 90 deg. and the aircraft velocity drops from 8

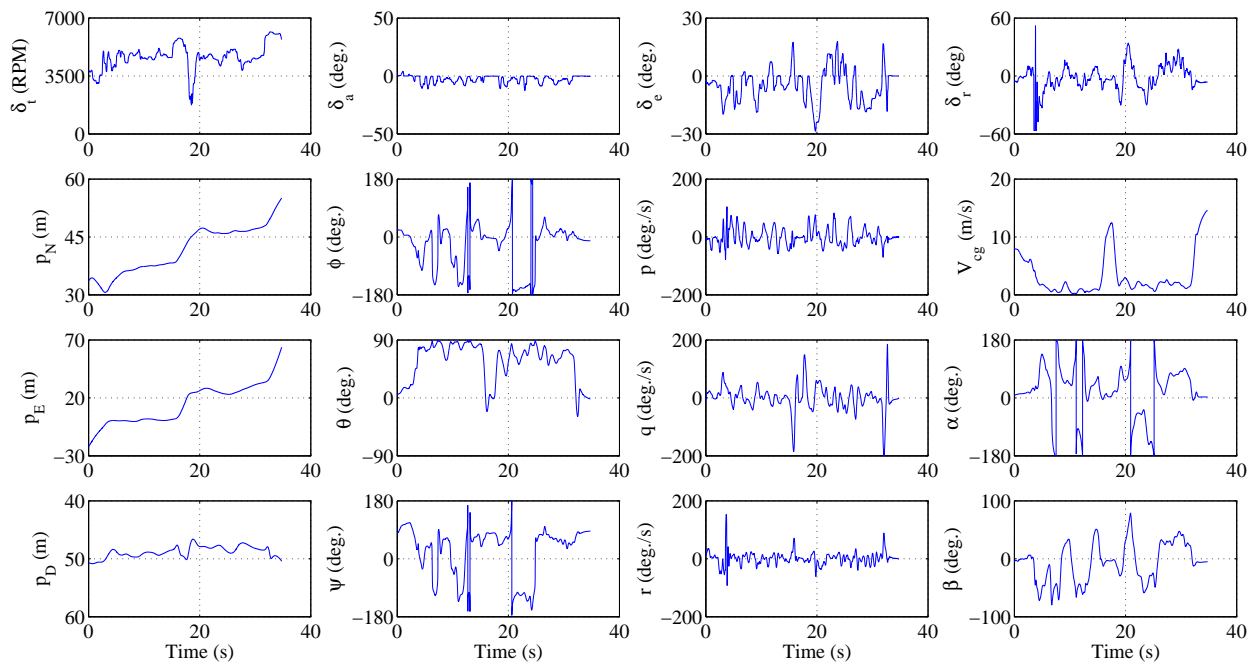


Figure 6.13: Aircraft states for the hover maneuver.

m/s to nearly zero. Thereafter the pilot maintains this pitched-up nose position for approximately 12 s. Continuous negative aileron inputs ($\delta_a \approx -10$ deg.) are required to counter the negative reaction torque of the thruster.

At around 15 s, the pilot transitions back to level flight by giving a quick positive elevator input (~ 18 deg.) and decreasing thruster input. The pitch angle drops to zero, while the velocity peaks to 12 m/s. After briefly flying in level flight, the pilot transitions into a hover maneuver for a second time at $\sim t = 18$ s. Again the pitch angle increases to 90 deg., while the velocity becomes nearly zero. The hover position is maintained for another 12 s, before transitioning back into level flight and flying away.

During both hover maneuvers, the positions, p_N , p_E , and p_D , of the aircraft do not change much. This means that an agile UAVs can easily operate in limited spaces and constrained environments e.g. indoors, caves etc.

Knife-Edge Maneuver

The next maneuver flown by the pilot in simulation is the knife-edge maneuver shown in Fig. 6.14 along with the respective states in Fig. 6.15. The aircraft scale in Fig. 6.14 is set to 2.5 times actual size, while the time step is set to 1 s. The aircraft starts from level flight

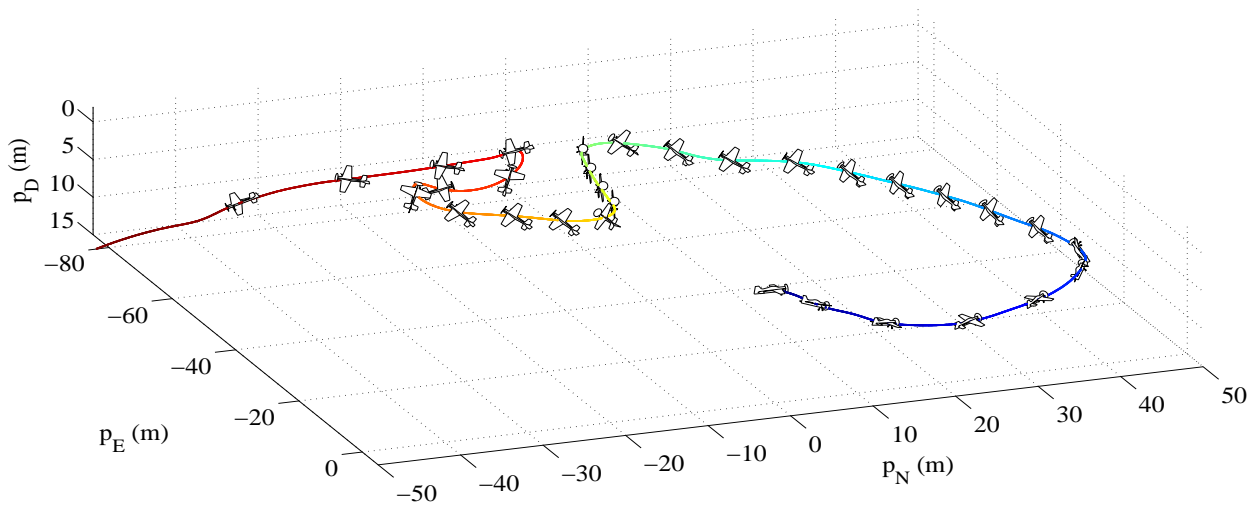


Figure 6.14: Knife-edge maneuver (aircraft scale = $2.5 \times$ actual size; time step = 1 s).

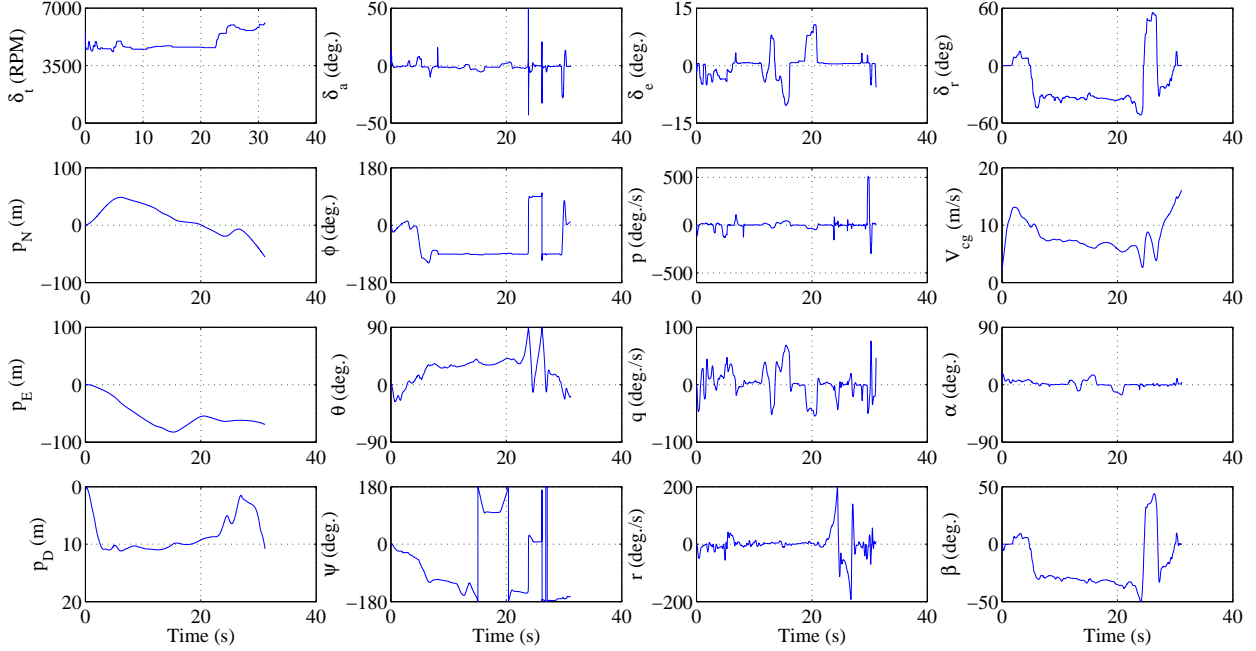


Figure 6.15: Aircraft states for the knife-edge maneuver.

with the following initial conditions: $[u, v, w] = [2, 0, 0]^T$ m/s, and $[p, q, r]^T = [p_N, p_E, p_D]^T = [\phi, \theta, \psi]^T = [0, 0, 0]^T$.

The pilot first brings the aircraft to a lower altitude ($p_D = 10$ m) before turning left and gracefully merging into a knife-edge maneuver by giving a positive δ_a (+10 deg.) at around $t = 4$ s. The aircraft reaches a roll angle of -90 deg, which is the characteristic of the knife-edge maneuver. As soon as the aircraft enters into the knife-edge, the functions of the elevator and rudder are exchanged, i.e. the elevator controls yaw and the rudder controls pitch. Hence a large rudder input of around $\delta_r = -35$ deg. is given and maintained to keep the nose pitched up at $\theta \approx 30$ deg. More so, the thruster input is kept constant at ~ 4600 RPM throughout the maneuver.

It is noted by the pilot that while in a knife-edge, the aircraft tends to roll, and he had to continuously give aileron inputs to maintain the roll at -90 deg. This is in contrast to his experience with the real aircraft. This is due to the flow shadowing effect of the fuselage on the leeward wing (starboard wing in this maneuver) which is not modeled in the current work. Owing to this effect, the leeward wing on the real aircraft has disrupted flow due to

the fuselage, making it less efficient in generating aerodynamic forces. Refer to [16, 17] for more details on this effect. Hence in simulation, where this effect is not modeled, the leeward wing efficiently generates aerodynamic forces that leads to the roll tendency in the aircraft. However, the roll tendency is quite small and requires a very small aileron input ($\delta_a \approx -1.5$ deg.) to keep the aircraft stable in the knife-edge.

At around $t = 14$ s, a negative elevator deflection $\delta_e = -10$ deg. is given to turn (yaw) the aircraft left, followed by a positive δ_e (+10 deg.) at around $t = 18$ s to turn the aircraft right. Finally, the pilot performs a Cuban-8 while in knife-edge at $t = 22$ s. Full negative rudder input (-52 deg.) is given so that the pitch angle increases and reaches 90 deg. Thruster input is simultaneously increased to 5600 RPM to support the aircraft weight. Then a full positive rudder input (+55 deg.) is given quickly to stop the aircraft from falling on the other side. Again the pitch angle rises to 90 deg., and this time a negative rudder input (-30 deg.) is given to stop the falling aircraft.

The pilot exits the knife-edge maneuver at $t = 29.5$ s by giving a negative aileron deflection (~ -28 deg.) to bring the roll angle back to 0 deg. and set the aircraft into level flight.

Rolling Harrier Maneuver

Another interesting maneuver is the rolling harrier maneuver shown in Figs. 6.16 and 6.17. The aircraft is drawn 1.43 times actual size at every 0.8 s. This maneuver starts off as a harrier followed by a constant roll rate while maintaining a pitch up nose through a combination of elevator and rudder inputs. As the UAV rolls, it passes through several phases: upright harrier ($\phi = 0$ deg.), knife-edge ($\phi = \pm 90$ deg.) and inverted harrier ($\phi = \pm 180$ deg.). The elevator and rudder inputs are continuously exchanged in relation to the UAV's roll angle, such that in harrier, pitch is controlled solely by elevator and yaw is controlled by rudder, but in knife-edge, pitch is controlled by the rudder whereas the yaw is controlled by the elevator.

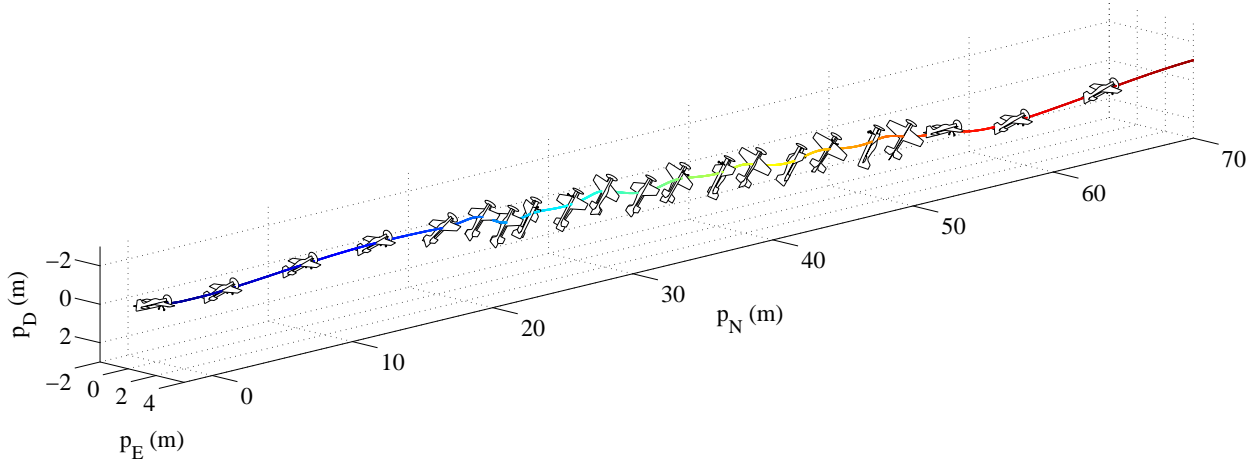


Figure 6.16: Rolling harrier maneuver (scale = $1.43 \times$ actual size; time step = 0.8 s).

The aircraft starts in level flight with the following initial conditions: $[u, v, w] = [5, 0, 0]^T$ m/s, and $[p, q, r]^T = [p_N, p_E, p_D]^T = [\phi, \theta, \psi]^T = [0, 0, 0]^T$. From level flight, a negative elevator input ($\delta_e = -35$ deg.) is given at $t = 3$ s. The aircraft pitches up (positive q) into a harrier position with $\theta \approx 48$ deg. Since much of the thrust goes to support the aircraft weight, V_{cg} decreases from around 6 m/s to 3 m/s.

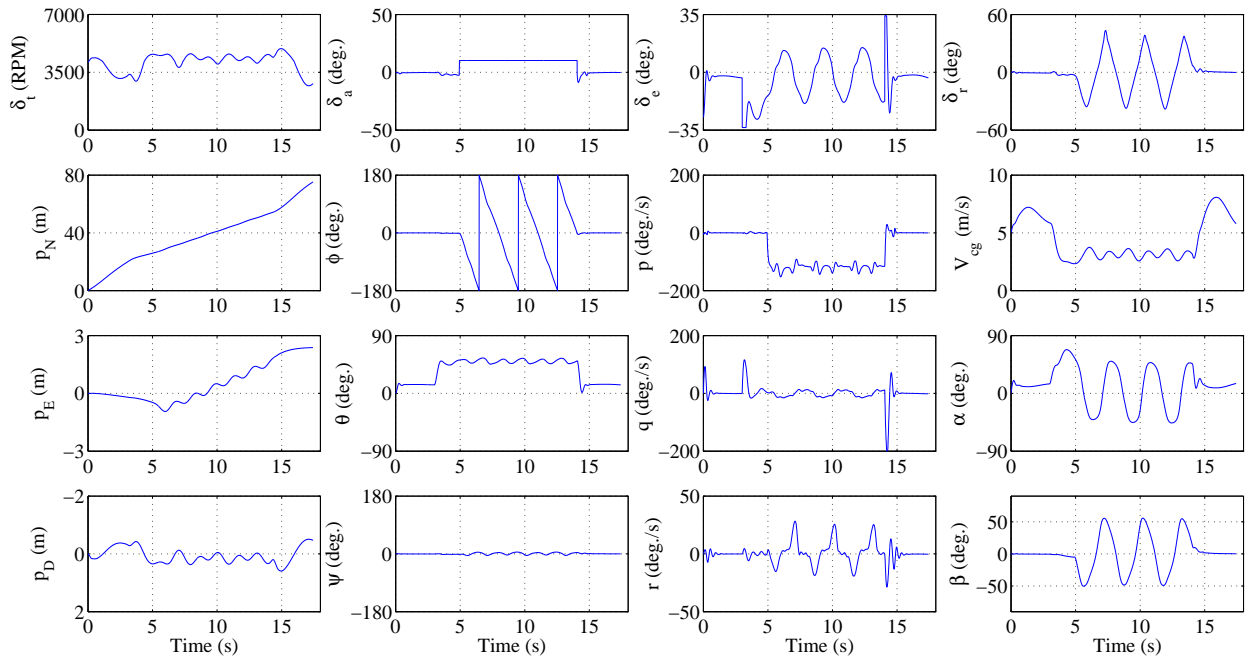


Figure 6.17: Aircraft states for the rolling harrier maneuver.

Then at $t = 5$ s, a positive aileron deflection ($\delta_a = +10$ deg.) is given and maintained to create a roll rate of around $p = -120$ deg./s, and the UAV starts rolling (see the ϕ plot). As the UAV rolls, θ is maintained at ~ 50 deg. by continuously-exchanging elevator and rudder inputs. As the UAV completes three rolls (at $t \approx 14$ s), the aileron input is relieved, reducing the roll rate to $p = 0$ deg./s, and the elevator input is reduced to bring the aircraft back into level flight ($\theta = 14$ deg.).

Blender/Inverted Spin Maneuver

A more dynamic maneuver called the blender/ inverted flat spin is flown by the pilot in the simulation as shown in Fig. 6.18 with the aircraft scale of 1.67 times actual size drawn at every 0.7 s. The aircraft starts in level flight

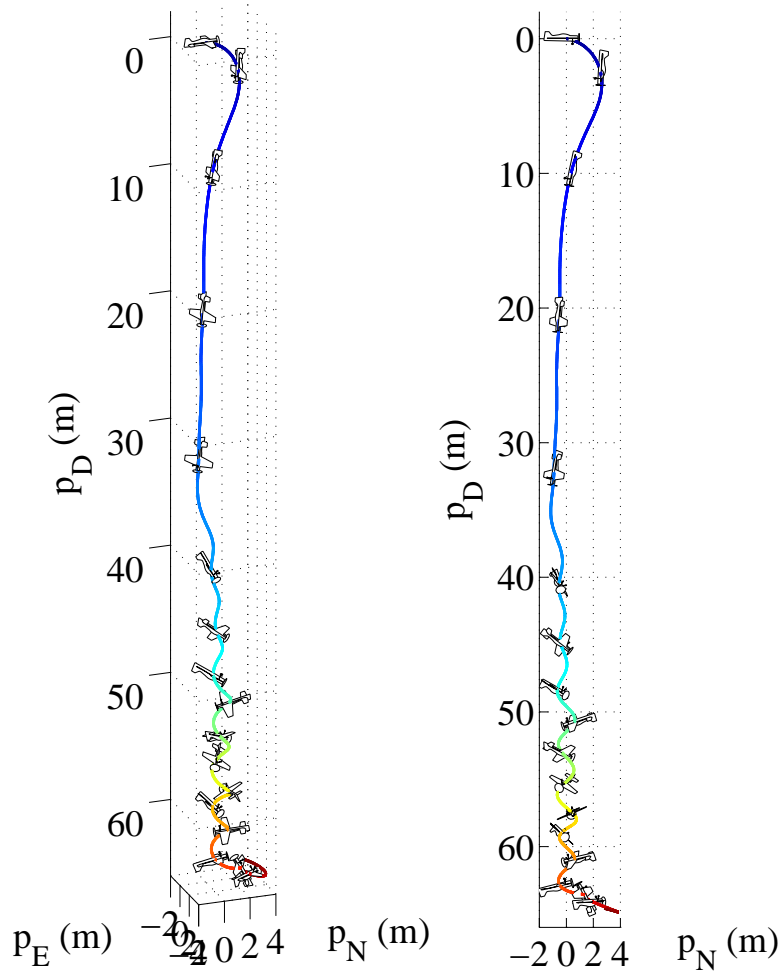


Figure 6.18: Blender/inverted spin maneuver (scale = 1.67; time step = 0.8 s).

with the following initial conditions: $[u, v, w] = [2, 0, 0]^T$ m/s, and $[p, q, r]^T = [p_N, p_E, p_D]^T = [\phi, \theta, \psi]^T = [0, 0, 0]^T$.

The pilot starts by giving a large positive δ_e (17 deg.) to nose dive the aircraft towards the ground, and as this is happening, a maximum right aileron input ($\delta_a = +50$ deg.) is given at $t = 1.7$ s to start a fast roll (see the roll rate plot; $p = -800$ deg./s). Due to this the aircraft gains tremendous angular momentum along the roll direction in less than a second. In RC parlance, this is the blender stage of the maneuver.

At $t = 2.5$ s, full positive elevator and rudder inputs ($\delta_e = +34$ deg. and $\delta_r = -57$ deg.) are quickly given (and maintained) so that the tremendous momentum along the roll direction is transferred to the yaw direction. This can be seen in the roll rate and yaw rate plots; p reduces while r increases. Due to the elevator deflection, the aircraft nose pitches up to $\theta \approx -20$ deg. The aileron input is gradually reduced, and the aircraft settles into a steady state where it spins inverted in a tight circle (~ 1 m diameter) while slowly coming down ($V_{cg} \approx 5$ m/s), and the overall effect is dramatic. From the ψ plot of Fig. 6.19, it can be seen that once in inverted spin, the aircraft spins at steady rate of ~ 0.75 rotations/s. This stage of

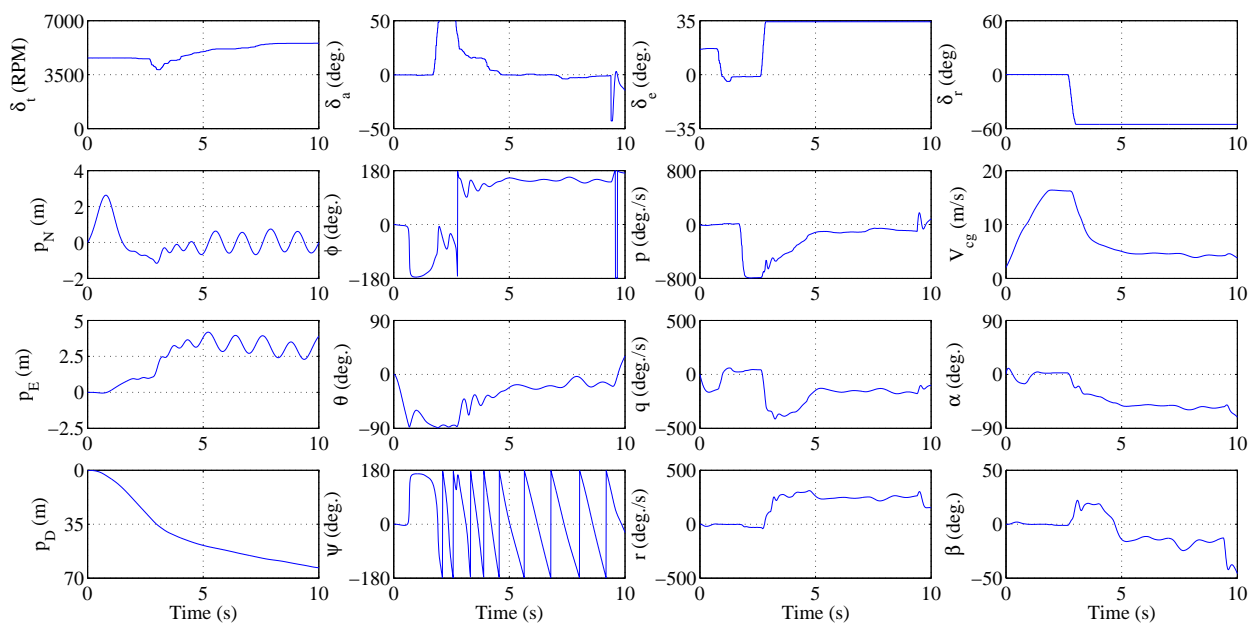


Figure 6.19: Aircraft states for the blender/inverted spin maneuver.

the maneuver is the inverted spin. To exit the maneuver, the pilot relieves the elevator and rudder inputs, and increases thrust to pull out of the maneuver.

This maneuver covers an entire class of maneuvers as its spin part can take many forms with slight variations of the control inputs. For example, the spin would be upright rather than inverted if a negative full elevator deflection was given at $t = 2.5$ s. Also, the pitch during the spin can be controlled with thrust; increasing thruster input will cause the nose to pitch up (from -20 deg. in Fig. 6.19) making the UAV descend even slower.

6.4 Unsteady Aerodynamic Effects during Maneuvers

A detailed discussion and mathematical analysis on unsteady aerodynamics was undertaken in Chap. 3, and it was pointed out that even the most aggressive maneuvers could be treated as quasi-steady. Hence it is worthwhile to look at the unsteady aerodynamic effects during the maneuvers performed by the pilot in simulation.

The unsteadiness is characterized by the reduced frequency parameter k_r , see Chap. 3, Sec. 3.5.1. For an aircraft, it may be defined based on its rate of change of angle of attack $\dot{\alpha}$ (for unsteadiness in the longitudinal plane) and its rate of change of sideslip $\dot{\beta}$ (for unsteadiness in the lateral direction). Therefore:

$$\begin{aligned} k_\alpha &= \dot{\alpha}\bar{c}/2V_{cg} \\ k_\beta &= \dot{\beta}\bar{c}/2V_{cg} \end{aligned} \tag{6.1}$$

where \bar{c} is the mean aerodynamic chord of the wing, and for the YAK54 aircraft it is found to be 0.221 m. For each maneuver, the angle of attack α and sideslip β are differentiated using a central finite-difference scheme to give $\dot{\alpha}$ and $\dot{\beta}$, which are then used to calculate the reduced frequencies from Eq. (6.1) for those maneuvers.

Figure 6.20 plots the reduced frequencies for three maneuvers: harrier, knife-edge and blender/inverted spin discussed previously. These three are particularly chosen because the first one (harrier) will reveal the unsteadiness in the longitudinal plane, the second one (knife-edge) will reveal the unsteadiness in the lateral plane, while the last one

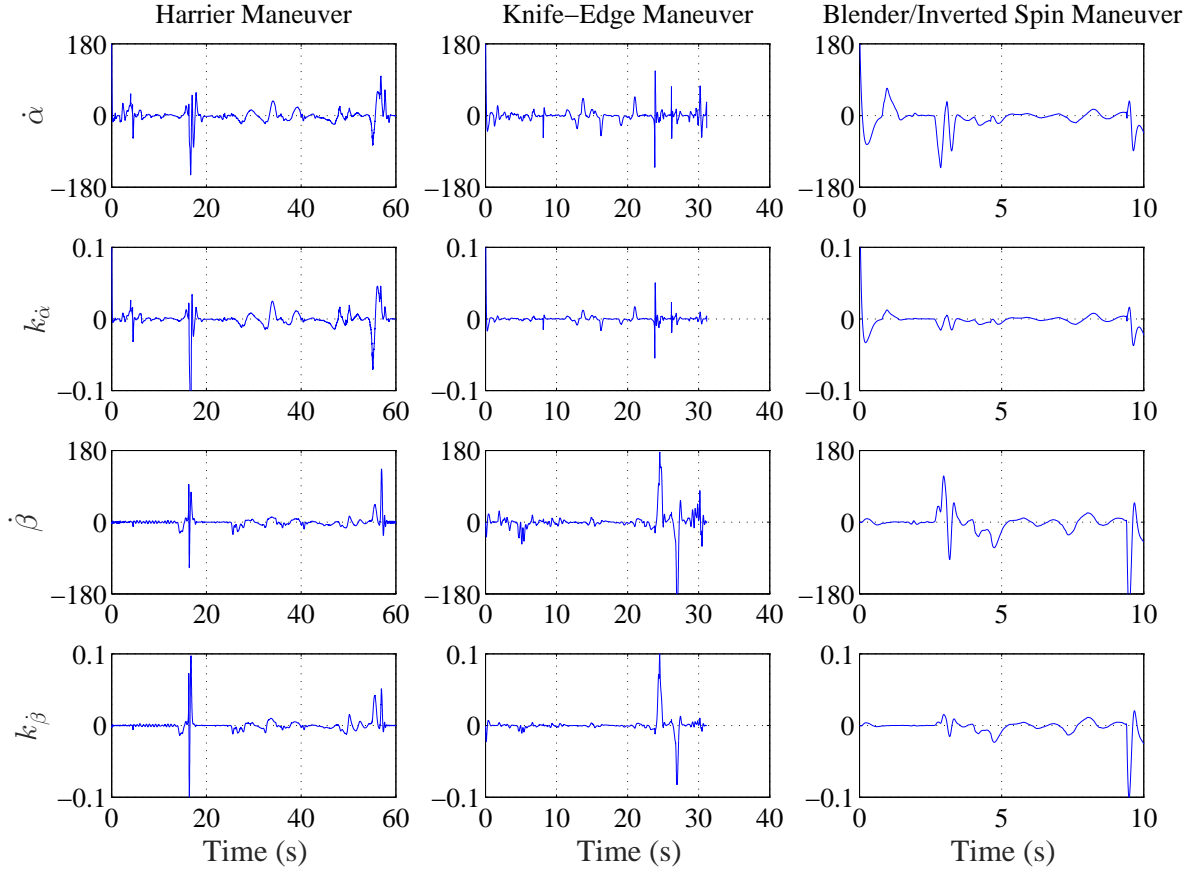


Figure 6.20: Reduced frequencies during various maneuvers.

(blender/inverted spin) is typically considered a highly dynamic maneuver [16, 17]. The rate of change of angle of attack and sideslip are also shown. It can be seen from the $k_{\dot{\alpha}}$ and $k_{\dot{\beta}}$ plots that for most part of all these maneuvers, the reduced frequencies remain well below ± 0.05 and hence the aerodynamics can be treated as quasi-steady [28].

For the harrier maneuver, the reduced frequency $k_{\dot{\alpha}}$ (and $k_{\dot{\beta}}$) exceeds ± 0.05 at $\sim t = 15$ s when the pilot quickly pitches up the aircraft to go from the upright harrier into an inverted harrier. For the knife-edge maneuver, $k_{\dot{\beta}}$ exceeds ± 0.05 between $t = 24$ to 27 s (two opposite peaks seen in the $k_{\dot{\beta}}$ plot), during the Cuban-8 turn performed in the lateral plane. For the blender/inverted spin also, $k_{\dot{\beta}}$ exceeds ± 0.05 as the pilot tries to exit from the inverted spin into inverted level flight near $t = 9$ s. However in all cases, the reduced frequencies exceed the critical value only for less than 1 second.

Chapter 7

Conclusions

The main goal of this work was to develop a nonlinear six degree-of-freedom model for agile fixed-wing UAVs that demonstrate exceptional aerobatic capabilities over the full flight envelope, i.e. ± 180 deg. angle of attack and sideslip range. Such capabilities stem from the unique configuration of these UAVs which includes low aspect ratio surfaces with big control surfaces and large deflections, high thrust-to-weight ratio and strong slipstream effects.

In this work, the challenging task of modeling agile UAVs has been undertaken through first principles. System identification techniques which are now gaining popularity for small UAVs, are deemed unsuitable for agile UAVs because exhaustive experimental testing would be required to identify a general agile UAV model applicable over the full flight envelope. On the other hand, the model presented in this work, based on first principles, is applicable to the general class of agile UAVs for their entire working envelope.

The current work focused on modeling three main areas of the agile UAV: aerodynamics, thruster dynamics and propeller slipstream effects. Traditionally, these individual areas are also considered/modeled for conventional UAVs but with many simplifications. Unfortunately, for agile UAVs, existing simple models fail to capture their behavior over the full flight envelope. In light of this, effort was vested in the current work to improve and expand existing models and even propose novel models in the areas of interest.

Quaternion attitude representation is found suitable keeping in view of the maneuverability requirement of agile UAVs. This is particularly important for some maneuvers like hover, perching etc., where the pitch is essentially 90 deg. and the Euler angle representation fails due to its mathematical singularity (gimbal lock).

The test platform used in the current work is the YAK54 Electric 3D Aerobat – an off-the-shelf high performance RC plane with three control surfaces (ailerons, elevator and rudder) and a thruster. The mass, center of gravity, and geometric parameters were measured physically, while the inertial properties were evaluated from a detailed CAD model developed in SolidWorks.

A thorough validation of the agile UAV model is undertaken for this test platform against experimental data collected from static bench tests in which the test platform was mounted on an ATI Gamma force/torque transducer to capture forces and moments acting on the aircraft at various rotational speeds of the thruster, and control surface deflections. For the same conditions, the simulated forces and moments showed an excellent agreement with experiments.

A final qualitative validation is also done by configuring the simulation to run in real-time with the pilot-in-loop. A professional RC pilot who has experience flying the real aircraft tested the simulator, and found it to be realistic. Many real-world phenomena such as wing-rock, stable flight in inverted harriers etc. were captured by the simulation. As well, the aircraft states for several well-known RC maneuvers follow similar trends to those presented in the literature [16, 17, 65].

There were some instances where the pilot found the simulated aircraft to behave differently than the real one; for e.g. during a knife-edge maneuver, the simulated aircraft has a roll tendency which is not experienced in real observations. Such differences arise because of the unmodeled effects like flow-shadowing etc. However, the difference in behavior is found to be subtle and is corrected/compensated by very small pilot inputs.

The concluding remarks specific to each area of interest are given below, followed by future works and recommendations at the end of this chapter.

7.1 Aerodynamics

The detailed aerodynamics model presented in the current work is based on a component breakdown approach as opposed to the conventionally-used stability derivatives approach. The aircraft components are broken down into a number of segments each having its own aerodynamics that are modeled in this work. The aerodynamics model features low-alpha and high-alpha aerodynamics, low aspect ratio and large control surface deflection effects, aerodynamic interactions, as well as quasi-steady and unsteady aerodynamics. Hence the aerodynamics model is suitable for agile UAVs that perform extreme aerobatic maneuvers over the full flight envelope, i.e. ± 180 deg. angle of attack and sideslip range.

Polhamus' theory is used to account for low aspect ratio (AR) in the low-alpha regime and it is found to be sufficiently accurate for AR as low as 0.167. More so, the stall phenomenon is included by incorporating the effects of trailing-edge separation and leading-edge vortex breakdown. These effects are characterized by semi-empirical coefficients, which at present are determined for various AR from experimental works in the literature. Finally, the effect of control surface deflection is modeled using standard methods [33] in the low-alpha regime, and an "equivalent flat plate" approach proposed for the high-alpha regime.

Unsteady aerodynamic effects are also included with the help of existing well-known models. The main time-dependent effects included are: the added mass, the circulatory response, and the dynamic leading-edge vortex breakdown and trailing-edge separation. From the simulated maneuvers (some of which are extremely dynamic) flown by the pilot, it is shown that the aerodynamics during most part of these maneuvers can be treated as quasi-steady and only at some instances the unsteady effects become important and that too for very short duration (less than a second). In light of this, unsteady effects may be neglected depending on the application; an exception to this is the aggressive pitch-up maneuver where the unsteady effects are large.

7.2 Thruster Dynamics

A thruster dynamics model that predicts six-axis forces and moments under all flow conditions namely static, axial flow, oblique flow and reverse flow, is presented in this work. It considers all the components (battery, ESC, BLDC motor, and propeller) of a typical electric-powered UAV thruster. Unlike most models available in the literature that are steady-state, the current model also predicts the dynamic response of the thruster by incorporating the battery and BLDC motor dynamics into the system. A detailed mathematical analysis of the propeller is undertaken in order to predict its aerodynamic forces and moments under the aforementioned flow conditions.

The model parameters are identified for the test platform thruster. In general, the thruster model predicts both the steady-state and dynamic response very well. For static and axial flow conditions, the match between simulation and experiments is very good, while for oblique flow some discrepancy exists between simulation and experiments (only for the secondary thruster forces and moments). Nonetheless, the presented thruster model is shown to be better than existing models.

It is found that in general forward flight conditions, the thruster side force is one order of magnitude smaller than its thrust, while the thruster secondary (pitch and yaw) moments are of similar order of magnitude as its reaction torque. Although the thruster side force is small, it cannot be neglected for agile UAVs, because it acts as a damping force and keep the aircraft stabilized in certain maneuvers like the hover.

7.3 Propeller Slipstream Effect

In this work, a mathematical model for the propeller slipstream is presented. Effects of the two slipstream components: swirl and axial, are considered. While the swirl slipstream velocity is not explicitly determined, its main effect of counteracting the thruster reaction torque is included. On the other hand, the axial slipstream velocity is determined explicitly

using a novel model proposed in the current work. Its effect on the UAV surfaces is then accounted for by adding it to the segment total velocity.

In contrast to the conventional models based on momentum theory etc., the novel model for the axial slipstream velocity takes into account both the acceleration and diffusion occurring within the slipstream. As such, it is applicable up to several propeller diameters downstream of the propeller plane. The semi-empirical coefficients of the model are determined from a set of experiments performed with the test platform thruster.

The model is thoroughly validated against experiments performed in this work, as well as against experimental data taken from various sources in the literature. Different rotational speeds, geometry, and configurations are considered for validation, and the model is found to be extremely good in all conditions. It is worthwhile to mention that the simplicity of the presented model matches that of the momentum theory, and therefore it is suitable for most UAV applications.

7.4 Future Works and Recommendations

This thesis covered various topics related to the dynamics modeling of agile fixed-wing UAVs. As such, limited effort could be vested on the individual topics. The following future works are recommended to carry the research further.

- Validation against flight test data could not be performed in the current work, since it requires closed-loop flight test data. Such validation is recommended for future work. This includes development of a data-acquisition system, controllers, performing closed-loop flight tests, and may also involve state estimation from the raw flight data.
- Many new approaches have been proposed in the literature to achieve autonomous maneuvering of small fixed-wing UAVs. These include nonlinear control laws, adaptive methods such as neural networks etc., and machine learning approaches. The agile UAV model presented in this work can be used to validate these various

approaches and possibly to identify the best approach for autonomous full-envelope aerobatics.

- A real-time implementation of the agile UAV model has been realized in this work. This will serve as a useful platform for path/motion planning and controller development. The model can be used in conjunction with existing motion planning algorithms for maneuver construction and trajectory generation. Furthermore, the platform may be used to develop controllers for autonomous aerobatic flight.
- A pilot-in-loop implementation has been developed in this work. A hardware-in-loop simulation could be established by connecting the real aircraft's actuators and sensors to the simulation. This could then be used in closed-loop testing of future controllers prior to actual closed-loop flight tests, and would be helpful to foresee and resolve any issues with the control strategy and/or implementation.

The following improvements to the presented model may also be carried out in future.

- The time constants for quasi-steady and unsteady aerodynamics may be experimentally determined. This will require dynamic testing of the UAV airfoil sections in the wind-tunnel since such data is scarce in the literature.
- Wind-tunnel experiments could be performed to identify the effect of control surface deflection at high angles of attack. A particularly important effect that needs characterization is the efficiency of the control surface when deflected into the wake of its parent surface.
- In Chap 3., wind-tunnel testing could only be performed for the starboard wing. A similar wind-tunnel testing of the entire aircraft is recommended. This can prove useful for identifying various aerodynamic effects, as well as for quantitative validation.
- Only the axial component of the induced velocity was considered while developing the thruster model in Chap. 4. The analysis can be extended to include the swirl

component. Not only will it be beneficial for more-accurate thruster forces/moment predictions, but it will also be useful in analyzing the swirl flow effect of the propeller slipstream.

- The propeller slipstream model presented in Chap. 5 predicts the axial slipstream velocity up to far downstream of the propeller. This model can be expanded to also predict the rotational (swirl) slipstream velocity. It would be required to perform the necessary experiments, and identifying semi-empirical equations for the swirl velocity.
- The propeller slipstream model, as implemented in the present work, predicts that the airspeed at the control surfaces remains nearly constant, irrespective of the forward speed of the aircraft (see Sec. 5.7). Wind tunnel experiments should be performed to verify this important result.

References

- [1] E. G. Dickes, J. N. Ralston, and K. P. Lawson, "Application of Large-Angle Data for Flight Simulation," AIAA Paper 2000-4584, Aug. 2000.
- [2] O. J. Boelens, "CFD Analysis of the Flow around the X-31 Aircraft at High Angle of Attack," *Aerospace Science and Technology*, vol. 20, no. 1, pp. 38-51, 2012.
- [3] V. Klein, and E. A. Morelli, *Aircraft System Identification: Theory and Practice*, AIAA, Reston, VA, 2006.
- [4] P. Ciecinski, and J. Pieniazek, "Identification of a UAV Model for Control," *Robot Motion and Control*, K. R. Kozlowski (Ed.), Springer, London, 2009, pp. 13-22.
- [5] B. Johnson, and R. Lind, "High Angle-of-Attack Flight Dynamics of Small UAVs," AIAA Paper 2009-61, Jan. 2009.
- [6] H. Wu, D. Sun, and Z. Zhao, "Model Identification of a Micro Air Vehicle in Loitering Flight Based on Attitude Performance Evaluation," *IEEE Transactions on Robotics*, vol. 20, no. 4, pp. 702-712, 2004.
- [7] W. E. Green, and P. Y. Oh, "A MAV That Flies Like an Airplane and Hovers Like a Helicopter," in *Proc. IEEE/ASME Int. Conf. on Advanced Intelligent Mechatronics*, Monterey, CA, USA, July 24-28, 2005, pp. 693-698.
- [8] W. E. Green, and P. Y. Oh, "A Hybrid MAV for Ingress and Egress of Urban Environments," *IEEE Transactions on Robotics*, vol. 25, no. 2, pp. 253-263, 2009.
- [9] A. Frank, J. S. McGrew, M. Valenti, D. Levine, and J. P. How, "Hover, Transition, and Level Flight Control Design for a Single-Propeller Indoor Airplane," AIAA Paper 2007-6318, Aug. 2007.
- [10] E. N. Johnson, A. Wu, J. C. Neidhoefer, S. K. Kannan, and M. A. Turbe, "Flight-Test Results of Autonomous Airplane Transitions Between Steady-Level and Hovering Flight," *Journal of Guidance, Control and Dynamics*, vol. 31, no. 2, pp. 358-370, 2008.
- [11] K. J. Krogh, "Developing a Framework for Control of Agile Aircraft Platforms in Autonomous Hover," M. S. Thesis, Dept. of Aeronautics and Astronautics, University of Washington, Washington, USA, 2009.
- [12] B. W. McCormick, *Aerodynamics of V/STOL Flight*, Dover, New York, 1999.
- [13] R. H. Stone, "Aerodynamic Modeling of the Wing-Propeller Interaction for a Tail-Sitter Unmanned Air Vehicle," *Journal of Aircraft*, vol. 45, no. 1, pp. 198-210, 2008.

- [14] D. Kubo, "Study on Design and Transitional Flight of Tail-Sitting VTOL UAV," in *Proc. 25th Congress of Int. Council of the Aeronautical Sciences*, Hamburg, Germany, Sept. 3-8, 2006.
- [15] S. Roy, A. Moreau, and M. Grosbois, "Modeling and Simulation of a Forward-Swept Wing, Vertical Takeoff or Landing & Thrust Vected Remotely Piloted Vehicle," in *Proc. Canadian Aeronautics and Space Institute Annual General Meeting on Aircraft Design and Development Symposium*, Toronto, ON, Canada, 2007.
- [16] M. S. Selig, "Modeling Full-Envelope Aerodynamics of Small UAVs in Realtime," AIAA Paper 2010-7635, Aug. 2010.
- [17] M. S. Selig, "Real-Time Flight Simulation of Highly Maneuverable Unmanned Aerial Vehicles," *Journal of Aircraft*, vol. 51, no. 6, pp. 1705-1725, 2014.
- [18] "FS One, Precision RC Flight Simulator," Software, Ver. 2, InertiaSoft, Champaign, IL, 2014.
- [19] M. F. Sobolic, "Agile Flight Control Techniques for a Fixed-Wing Aircraft," M. S. Thesis, Dept. of Aeronautics and Astronautics, Massachusetts Institute of Technology, MA, USA, June 2009.
- [20] D. V. Uhlig, and M. S. Selig, "Determining Aerodynamic Characteristics of a Micro Air Vehicle Using Motion Tracking," *Journal of Aircraft*, vol. 50, no. 5, pp. 1481-1490, 2013.
- [21] R. Cory, and R. Tedrake, "Experiments in Fixed-Wing UAV Perching," AIAA Paper 2008-7256, Aug. 2008.
- [22] W. Hoburg, and R. Tedrake, "System Identification of Post Stall Aerodynamics for UAV Perching," AIAA Paper 2009-1930, April 2009.
- [23] M. Drela, "XFOIL: An Analysis and Design System for Low Reynolds Number Airfoils," *Low Reynolds Number Aerodynamics*, T. J. Mueller (Ed.), Springer, New York, 1989, pp. 1-12.
- [24] J. L. Tangler, "Insight into a Wind Turbine Stall and Post-Stall Aerodynamics," *Wind Energy*, vol. 7, no. 3, pp. 247-260, 2004.
- [25] S. F. Hoerner, and H. V. Borst, *Fluid-Dynamic Lift: Practical Information on Aerodynamic and Hydrodynamic Lift*, 2nd ed., 1985. Ch. 5, 17, 21.
- [26] C. Lindenburg, "Stall Coefficients," presented at the *IEA Symposium on the Aerodynamics of Wind Turbines*, NREL, CO, USA, Dec. 4-5, 2010.

- [27] S. Young, and F. Donald, "Blade Section Lift Coefficients for Propellers at Extreme Off-Design Conditions," Hydromechanics Directorate Research and Development Report No. CRDKNSWC/HD-1205-02, Carderock Div., Naval Surface Warfare Center, Maryland, Dec. 1997.
- [28] J. G. Leishman, *Principles of Helicopter Aerodynamics*, 2nd ed., Cambridge Aerospace Series, New York, 2006.
- [29] T. J. Mueller, and G. E. Torres, "Aerodynamics of Low Aspect Ratio Wings at Low Reynolds Numbers With Applications to Micro Air Vehicle Design and Optimization," Report No. UNDAS-FR-2025, University of Notre Dame, Nov. 2001.
- [30] G. E. Torres, "Aerodynamics of Low Aspect Ratio Wings at Low Reynolds Numbers With Applications to Micro Air Vehicle Design," Ph. D. Dissertation, Dept. of Aerospace and Mechanical Engineering, University of Notre Dame, IN, USA, April 2002.
- [31] T. J. Mueller, and J. D. DeLaurier, "Aerodynamics of Small Vehicles," *Annual Review of Fluid Mechanics*, vol. 35, no. 1, pp. 89-111, 2003.
- [32] A. Pelletier, and T. J. Mueller, "Low Reynolds Number Aerodynamics of Low-Aspect-Ratio, Thin/Flat/Cambered-Plate Wings," *Journal of Aircraft*, vol. 37, no. 5, pp. 825-832, 2000.
- [33] B. W. McCormick, *Aerodynamics, Aeronautics, and Flight Mechanics*, 2nd ed., Wiley, New York, 1995.
- [34] E. C. Polhamus, "Predictions of Vortex-Lift Characteristics by a Leading-Edge-Suction Analogy," *Journal of Aircraft*, vol. 8, no. 4, pp. 193-199, 1971.
- [35] E. C. Polhamus, "A Concept of the Vortex Lift of Sharp-Edge Delta Wings Based on a Leading-Edge-Suction Analogy," NASA TN D-3767, 1966.
- [36] J. E. Lamar, "Extension of Leading-Edge-Suction Analogy to Wings with Separated Flow around the Side Edges at Subsonic Speeds," NASA TR R-428, 1974.
- [37] P. Cosyn, and J. Vierendeels, "Numerical Investigation of Low-Aspect-Ratio Wings at Low Reynolds Numbers," *Journal of Aircraft*, vol. 43, no. 3, pp. 713-722, 2006.
- [38] M. Okamoto, and A. Azuma, "Aerodynamic Characteristics at Low Reynolds Numbers for Wings of Various Planforms," *AIAA Journal*, vol. 49, no. 6, pp. 1135-1150, 2011.
- [39] G. K. Ananda, "Aerodynamic Performance of Low-to-Moderate Aspect Ratio Wings at Low Reynolds Numbers," M. S. Thesis, Dept. of Aerospace Engineering, University of Illinois at Urbana-Champaign, IL, USA, 2012.

- [40] X. Ortiz, D. Rival, and D. Wood, "Forces and Moments on Flat Plates of Small Aspect Ratio with Application to PV Wind Loads and Small Wind Turbine Blades," *Energies*, vol. 8, no. 1, pp. 2438-2453, 2015.
- [41] G. A. Williamson, "Experimental Wind Tunnel Study of Airfoils with Large Flap Deflections at Low Reynolds Numbers," M. S. Thesis, Dept. of Aerospace Engineering, University of Illinois at Urbana-Champaign, IL, USA, 2012.
- [42] T. Theodorsen, "General Theory of Aerodynamic Instability and the Mechanism of Flutter," NACA TR 496, 1935.
- [43] J. G. Leishman, and K. Q. Nguyen, "State-Space Representation of Unsteady Airfoil Behavior," *AIAA Journal*, vol. 28, no. 5, pp. 836-844, 1990.
- [44] J. G. Leishman, and G. L. Crouse, "State-Space Model for Unsteady Airfoil Behavior and Dynamic Stall," AIAA Paper 89-1319-CP, April 1989.
- [45] M. Goman, and A. Khrabrov, "State-Space Representation of Aerodynamic Characteristics of an Aircraft at High Angles of Attack," *Journal of Aircraft*, vol. 31, no. 5, pp. 1109-1115, 1994.
- [46] D. Fischenberg, "Identification of an Unsteady Aerodynamic Stall Model from Flight Test Data," AIAA Paper 95-3438-CP, Aug. 1995.
- [47] D. Fischenberg, and R. V. Jategaonkar, "Identification of Aircraft Stall Behavior from Flight Test Data," RTO MP-11 Paper No. 17, March 1999.
- [48] J. N. Dias, and F. A de Almeida, "High Angle of Attack Model Identification without Air Flow Angle Measurements," AIAA Paper 2013-4980, Aug. 2013.
- [49] S. L. Brunton, and C. W. Rowley, "Empirical State-Space Representations for Theodorsen's Lift Model," *Journal of Fluids and Structures*, vol. 38, no. 1, pp. 174-186, 2013.
- [50] R. W. Beard, and T. W. McLain, *Small Unmanned Aircraft: Theory and Practice*, Princeton University Press, New Jersey, 2012.
- [51] T. J. Mueller, J. C. Kellogg, P. G. Ifju, and S. V. Shkarayev, *Introduction to the Design of Fixed-Wing Micro Air Vehicles: Including Three Case Studies*, AIAA, Reston, VA, 2007.
- [52] P. Castillo, R. Lozano, and A. E. Dzul, *Modelling and Control of Mini-Flying Machines*, Springer, London, 2005.
- [53] R. Lozano (Ed.), *Unmanned Aerial Vehicles: Embedded Control*, Wiley, New York, 2010.

- [54] J. B. Brandt, R. W. Deters, G. K. Ananda, and M. S. Selig, "UIUC Propeller Data Site," available at: <http://m-selig.ae.illinois.edu/props/propDB.html> (accessed Jan. 03, 2016).
- [55] R. W. Deters, and M. S. Selig, "Static Testing of Micro Propellers," AIAA Paper 2008-6246, Aug. 2008.
- [56] P. Pounds, R. Mahony, and P. Corke, "Design of a Static Thruster for Microair Vehicle Rotorcraft," *Journal of Aerospace Engineering*, vol. 22, no. 1, pp. 85-94, 2009.
- [57] R. Martinez-Alvarado, F. J. Ruiz-Sanchez, A. Sanchez-Orta, and O. Garcia-Salazar, "Dynamic Response of BLDC-Thruster for Small Scale Quadrotors Under Aerodynamic Load Torque," in *Proc. IEEE International Autumn Meeting on Power, Electronics and Computing (ROPEC)*, Itapúa, Mexico, Nov. 5-7, 2014.
- [58] P. Peddiraju, "Development and Validation of a Dynamics Model for an Unmanned Finless Airship," M. Eng. Thesis, Dept. of Mechanical Engineering, McGill University, QC, Canada, 2010.
- [59] R. W. Deters, G. K. Ananda, and M. S. Selig, "Reynolds Number Effects on the Performance of Small-Scale Propellers," AIAA Paper 2014-2151, June 2014.
- [60] D. V. Uhlig, and M. S. Selig, "Post Stall Propeller Behavior at Low Reynolds Numbers," AIAA Paper 2008-407, Jan. 2008.
- [61] O. R. Shetty, and M. S. Selig, "Small-Scale Propellers Operating in the Vortex Ring State," AIAA Paper 2011-1254, Jan. 2011.
- [62] J. G. Leishman, M. J. Bhagwat, and S. Ananthan, "Free-Vortex Wake Predictions of the Vortex Ring State for Single-Rotor and Multi-Rotor Configurations," in *Proc. AHS International 58th Annual Forum*, Montreal, QC, Canada, June 11-13, 2002, vol. 1, pp. 642-671.
- [63] C. Chen, and J. V. R. Prasad, "Simplified Rotor Inflow Model for Descent Flight," *Journal of Aircraft*, vol. 44, no. 3, pp. 936-944, 2007.
- [64] B. Theys, G. Dimitriadis, T. Andrienne, P. Hendrick, and J. De Schutter, "Wind Tunnel Testing of a VTOL MAV Propeller in Tilted Operating Mode," in *Proc. Int. Conf. on Unmanned Aircraft Systems (ICUAS)*, Orlando, FL, USA, May 27-30, 2014, pp. 1064-1072.
- [65] K. Tehrani, "Propellers in Yawed Flow at Low Speeds," M. S. Thesis, Dept. of Aerospace Engineering, University of Illinois at Urbana-Champaign, IL, USA, 2006.

- [66] M. S. Selig, "Modeling Propeller Aerodynamics and Slipstream Effects on Small UAVs in Realtime", AIAA Paper 2010-7938, Aug. 2010.
- [67] R. E. Pendley, "Effect of Propeller-Axis Angle of Attack on Thrust Distribution over the Propeller Disc in Relation to Wake-Survey Measurement of Thrust," NACA ARR No. L5J02B, 1945.
- [68] H. B. Freeman, "The Effect of Small Angles of Yaw and Pitch on the Characteristics of Airplane Propellers," NACA Report No. 389, pp. 523-531, 1932.
- [69] T. W. K. Clarke, "Effect of Side Wind on a Propeller," British A.C.A. R&M No. 80, 1913.
- [70] R. G. Harris, "Force on a Propeller Due to Sideslip," British A.C.A. R&M No. 427, 1918.
- [71] H. S. Ribner, "Propellers in Yaw," NACA ARR No. 3L09, 1943.
- [72] J. L. Crigler, and J. Gilman, "Calculation of Aerodynamic Forces of a Propeller in Pitch or Yaw," NACA TN-2585, 1952.
- [73] H. Glauert, "A General Theory of the Autogyro," British A.R.C. R&M No. 1111, 1926.
- [74] R. P. Coleman, A. M. Feingold, and C. W. Stempin, "Evaluation of the Induced Velocity Field of an Idealized Helicopter Rotor," NACA ARR No. L5E10, 1947.
- [75] D. M. Pitt, and D. A. Peters, "Theoretical Prediction of Dynamic Inflow Derivatives," *Vertica*, vol. 5, no. 1, pp. 21-34, 1981.
- [76] R. T. N. Chen, "A Survey of Nonuniform Inflow Models for Rotorcraft Flight Dynamics and Control Applications," NASA TM-102219, 1989.
- [77] M. F. Islam, A. Akinturk, B. Veitch, and P. Liu, "Performance Characteristics of Static and Dynamic Azimuthing Podded Propulsor," in *Proc. First International Symposium on Marine Propulsors*, Trondheim, Norway, June 22-24, 2009, pp. 482-492.
- [78] H. Amini, and S. Steen, "Experimental and Theoretical Analysis of Propeller Shaft Loads in Oblique Inflow," *Journal of Ship Research*, vol. 55, no. 4, pp. 268-288, 2011.
- [79] M. George, and E. Kisielowski, "Investigation of Propeller Slipstream Effects on Wing Performance," U.S. Army Aviation Materiel Laboratories, USAAVLABS Technical Report 67-67, Fort Eustis, Virginia, Nov. 1967.
- [80] D. P. Witkowski, A. K. H. Lee, and J. P. Sullivan, "Aerodynamic Interaction between Propeller and Wings," *Journal of Aircraft*, vol. 26, no. 9, pp. 829-836, 1989.

- [81] R. M. Ardito Marretta, "Different Wing Flowfields Interaction on the Wing-Propeller Coupling," *Journal of Aircraft*, vol. 34, no. 6, pp. 740-747, 1997.
- [82] M. L. Albertson, Y. B. Dai, R. A. Jensen, and H. Rouse, "Diffusion of a Submerged Jet," Transcript of the A.S.C.E. Paper No. 2409, 115, pp. 639-697, 1950.
- [83] G. A. Hamill, "Characteristics of the Screw Wash of a Manoeuvring Ship and the Resulting Bed Scour," Ph. D. Dissertation, Queen's University of Belfast, Northern Ireland, 1987.
- [84] D. P. J. Stewart, "Characteristics of a Ships Screw Wash and the Influence of Quay Wall Proximity," Ph. D. Dissertation, Queen's University of Belfast, Northern Ireland, 1987.
- [85] W. Lam, G. A. Hamill, Y. C. Song, D. J. Robinson, and S. Raghunathan, "A Review of the Equations Used to Predict the Velocity Distribution within a Ship's Propeller Jet," *Ocean Engineering*, vol. 38, pp. 1-10, 2011.
- [86] B. J. Gamble, "Experimental Analysis of Propeller Interactions with a Flexible Wing Micro-Air-Vehicle," M. S. Thesis, Dept. of Aeronautics and Astronautics, Air Force Institute of Technology, Wright-Patterson AirForce Base, OH, USA, 2006.
- [87] S. Shkarayev, J. Moschetta, and B. Bataille, "Aerodynamic Design of Micro Air Vehicles for Vertical Flight," *Journal of Aircraft*, vol. 45, no. 5, pp. 1715-1724, 2008.
- [88] R. W. Deters, "Performance and Slipstream Characteristics of Small-Scale Propellers at Low Reynolds Numbers," Ph. D. Dissertation, Dept. of Aerospace Engineering, University of Illinois at Urbana-Champaign, IL, USA, 2014.
- [89] R. W. Deters, G. K. Ananda, and M. S. Selig, "Slipstream Measurements of Small-Scale Propellers at Low Reynolds Numbers," AIAA Paper 2015-2265, June 2015.
- [90] G. K. Ananda, R. W. Deters, and M. S. Selig, "Propeller-Induced Flow Effects on Wings of Varying Aspect Ratio at Low Reynolds Numbers," AIAA Paper 2014-2153, June 2014.
- [91] F. P. Ricou, and D. B. Spalding, "Measurements of Entrainment by Axisymmetrical Turbulent Jets," *Journal of Fluid Mechanics*, vol. 11, no. 1, pp. 21-32, 1961.
- [92] S. H. Park, and H. D. Shin, "Measurements of Entrainment Characteristics of Swirling Jets," *Int. Journal of Heat and Mass Transfer*, vol. 36, no. 16, pp. 4009-4018, 1993.
- [93] A. M. Falcone, and J. C. Cataldo, "Entrainment Velocity in an Axisymmetric Turbulent Jet," *Journal of Fluid Engineering*, vol. 125, no. 4, pp. 620-627, 2003.

- [94] E. W. M. Roosenboom, A. Heider, and A. Schroder, "Investigation of the Propeller Slipstream with Particle Image Velocimetry," *Journal of Aircraft*, vol. 46, no. 2, pp. 442-449, 2009.
- [95] E. W. M. Roosenboom, and A. Schroder, "Flowfield Investigation at Propeller Thrust Reverse," *Journal of Fluids Engineering*, vol. 132, pp. 1-8, 2010.
- [96] E. W. M. Roosenboom, A. Sturmer, and A. Schroder, "Advanced Experimental and Numerical Validation and Analysis of Propeller Slipstream Flows," *Journal of Aircraft*, vol. 47, no. 1, pp. 284-291, 2010.
- [97] W. Fu, J. Li, and H. Wang, "Numerical Simulation of Propeller Slipstream Effect on a Propeller-Driven Unmanned Aerial Vehicle," *Procedia Engineering*, vol. 31, pp. 150-155, 2012.
- [98] H. Xu, Z. Ye, and A. Shi, "Numerical Study of Propeller Slipstream Based on Unstructured Overset Grids," *Journal of Aircraft*, vol. 49, no. 2, pp. 384-389, 2012.
- [99] J. B. Kuipers, *Quaternions and Rotation Sequences: A Primer with Applications to Orbits, Aerospace and Virtual Reality*, Princeton University Press, New Jersey, 1999.
- [100] W. F. Phillips, *Mechanics of Flight*, 2nd ed., Wiley, New Jersey, 2010.
- [101] "YAK54 Electric 3D Aerobat," Electrify by Great Planes, Champaign, IL. Available at <http://www.electrify.com/discontinued/gpma1131.html> (last accessed: Jan. 05, 2016).
- [102] A. Lussier-Desbiens, A. T. Asbeck, and M. R. Cutkosky, "Landing, Perching and Taking Off from Vertical Surfaces," *Int. Journal of Robotics Research*, vol. 30, no. 3, pp. 355-370, 2011.
- [103] "UIUC Airfoil Data Site," available at <http://m-selig.ae.illinois.edu/ads.html> (last accessed Jan. 05, 2016).
- [104] I. H. Abbott, and A. E. Von Doenhoff, *Theory of Wing Sections: Including a Summary of Airfoil Data*, Dover, New York, 1959.
- [105] G. E. Torres, and T. J. Mueller, "Low-Aspect-Ratio Wing Aerodynamics at Low Reynolds Numbers," *AIAA Journal*, vol. 42, no. 5, pp. 865-873, 2004.
- [106] R. D. Blevins, *Applied Fluid Dynamics Handbook*, Macmillan, ON, Canada, 1984.
- [107] R. E. Sheldahl, and P. C. Klimas, "Aerodynamic Characteristics of Seven Symmetrical Airfoil Sections Through 180-Degree Angle of Attack for Use in Aerodynamic Analysis of Vertical Axis Wind Turbines," Report No. SAND80-2114, Sandia Laboratories, Albuquerque, March 1981.

- [108] A. W. Bloy, and D. G. Roberts, "Aerodynamic Characteristics of the NACA63-215 Aerofoil for Use in Wind Turbines," *Wind Engineering*, vol. 17, no. 2, pp. 67-75, 1993.
- [109] M. H. Hansen, M. Gaunaa, and H. A. Madsen, "A Beddoes-Leishman Type Dynamic Stall Model in State-Space and Indicial Formulations," Report No. Risø-R-1354(EN), Risø National Laboratory, Roskilde, Denmark, June 2004.
- [110] J. W. Larsen, S. R. K. Nielsen, and S. Krenk, "Dynamic Stall Model for Wind Turbine Airfoils," *Journal of Fluids and Structures*, vol. 23, no. 7, pp. 959-982, 2007.
- [111] D. H. Hodges, and G. A. Pierce, *Introduction to Structural Dynamics and Aeroelasticity*, Cambridge University Press, 2002, pp. 201-206.
- [112] R. T. Jones, "Operational Treatment of the Non-Uniform Lift Theory in Airplane Dynamics," NASA TN-667, 1938.
- [113] L. Gao, S. Liu, and R. A. Dougal, "Dynamic Lithium-Ion Battery Model for System Simulation," *IEEE Transactions on Components and Packaging Technologies*, vol. 23, no. 3, pp. 495-505, 2002.
- [114] O. Erdinc, B. Vural, and M. Uzunoglu, "A Dynamic Lithium-Ion Battery Model Considering the Effects of Temperature and Capacity Fading," in *Proc. IEEE Int. Conf. Clean Electrical Power*, Capri, Italy, June 09-11, 2009, pp. 383-386.
- [115] M. McClure, "A simplified approach to DC motor modeling for dynamic stability analysis," Texas Instruments, Dallas, Texas, Application Rep. SLUA076, July 2000.
- [116] A. S. O. Al-Mashakbeh, "Proportional integral and derivative control of brushless DC motor," *European Journal of Scientific Research*, vol. 35, no. 2, pp. 198-203, 2009.
- [117] M. O. Ali, S. P. Koh, and K. H. Chong, "Design a PID controller of BLDC motor by using hybrid genetic-immune," *Modern Applied Science*, vol. 5, no. 1, pp. 75-85, 2011.
- [118] W. L. Soong, *Inductance Measurements for Synchronous Machines, Power Engineering Briefing Note Series*, Adelaide, Australia: Univ. Adelaide, May 2008.
- [119] T. Tsadok, Thruster Modeling for Small Unmanned Aerial Vehicles with Coaxial-Rotors," M. S. thesis, Dept. Mechanical Engineering, McGill Univ., Canada, 2014.
- [120] L. B. Salters, "Velocity Distributions Measured in the Slipstream of Eight-Blade and Six-Blade Dual-Rotating Propellers at Zero Advance," NACA RM-L55D21, Langley Aeronautical Lab., Langley Field, VA, June 1955.